

Studies on Dynamics and Sound Transmission  
Loss of Thick Smart Cylindrical Composite  
Structures

by

Vahid Rabbani

A Thesis submitted to the Faculty of Graduate Studies of  
The University of Manitoba  
in partial fulfillment of the requirements of the degree of

DOCTOR OF PHILOSOPHY

Department of Mechanical Engineering  
University of Manitoba  
Winnipeg, MB, Canada

Copyright © 2020 by Vahid Rabbani

## Abstract

Sound Transmission Loss (STL) describes the accumulated decrease in the sound intensity as waves spread outward from a source or through specific areas. In order to reduce the sound transmission from the cylinder, an acoustic quieting process needs to be implemented. One of the most efficient ways to reduce sound transmission is using piezoelectric materials. Piezoelectric materials can be applied to reduce transmitted noise from different structures versus damping approaches when it is difficult to completely dampen structural vibrations via passive methods. The primary aim of the present study is to analyze the dynamic characteristics of infinitely long, thick, piezo-laminated cylindrical structures with functionally graded material properties for vibration suppression and control of sound transmission losses.

Two thick shell models were developed to consider the effects of anisotropy and piezoelectricity on the STL. In the first model, an exact Three Dimensional (3D) piezoelectric model is built to investigate the free vibration of an arbitrary thick triclinic piezoelectric hollow cylinder. The effects of different anisotropic piezoelectric properties (i.g orthotropic piezoelectric, monoclinic piezoelectric, triclinic piezoelectric, ...) on the dispersion curve of natural frequencies were studied. In the second model, the estimation of STL due to the piezoelectric effects is studied for a thick-walled piezo-composite cylindrical shell excited by an oblique incident plane wave. Parameter studies are conducted to investigate the effects of piezoelectric material properties, piezoelectric polarization direction, shell thickness ratio, electrical boundary conditions, and Functionally Graded Piezoelectric Material (FGPM) on

the sound transmission loss due to the piezoelectricity. These two models were used as the fundamental workspace.

These two initial models enable us to explore deeper and study the effect of feedback control strategy for the enhancement of STL. The active control strategy is achieved by sending the control signal from the distributed piezoelectric sensor layer through a controller to drive the external piezoelectric actuators. Comprehensive numerical studies are carried out to investigate the sound transmission loss of controlled and uncontrolled piezo-composite cylinders as well as the effect of closed-loop gain. The second model was also used to increase STL by using the different sizes and arrangements of piezoelectric electrodes. The study shows that increasing the number of electrodes may not necessarily provide higher soundproofing abilities. However, the level of sound isolation can be adjusted by using the proper size of the electrode.

Finally, in order to go one more step deeper, considering the fluid-solid shear interaction, a new 3D elastic model incorporating the piezoelectricity and fluid viscosity is developed to simulate the dynamics and STL of a thick shell submerged in a viscous fluid. The Navier-Stokes equation is employed to describe the surrounding viscous acoustic medium as well as the internal acoustic cavity. Parametric studies are carried out to investigate the effect of fluid viscosity (dynamic viscosity and bulk viscosity), shell anisotropy, and piezoelectric boundary conditions on the sound transmission loss. The results show that the magnitude of STL linearly increases as the value of bulk and dynamic viscosities increases, which results in providing a better soundproofing ability.

# Acknowledgments

First and foremost, I would like to express my deepest gratitude to my advisor Dr. Nan Wu for his unfailing support of my Ph.D. research and for his dedication, patience, inspiration, devotion, and vast knowledge. His immense knowledge and charming personality helped me through this research and writing of my candidacy report. He worked actively to provide me with protected academic funds and time to pursue my academic aims. I could not have imagined having a better supervisor and mentor for my Ph.D. program.

Besides my advisor, I am especially indebted to the members of my Dissertation Committee, Professor Xihui Liang, and Professor Pooneh Maghoul, for their constructive comments, encouragement, professional guidance, and continuous encouragement. Their offices were always open whenever I encountered a trouble spot or had a question about my research. Without their passionate assistance and valuable input, this research could not have been successfully conducted. As my mentors, they taught me more than I could ever give them credit here.

I would like to express my sincere thanks to my fellow labmates and friends in the vibration and acoustics lab: Dr. Mohammad Hodaei, Miad Jarrahi, Mehdi Allaei, Shahriar Bagheri, Alireza Keshmiri, Hossein Bisheh, Xin Wang for their unconditional help, stimulating discussions and supports.

Besides, I must express my profound gratitude to my parents and my siblings for giving me unfailing support and continuous encouragement throughout my years of study and through the process of researching and writing this research. This accomplishment would not have been possible without them.



Finally, this research was conducted, thanks to financial support from Natural Sciences and Engineering Research Council of Canada (NSERC), the University of Manitoba, and Research Manitoba. We would like to thank CMC Microsystems for the products and services that eased this study.

# List of Tables

4.1	Mechanical and electrical properties of the constituent materials. . .	58
5.1	Mechanical properties of $Ba_2NaNb_5O_{15}$ , PZT4, and Aluminum. . .	91
5.2	Piezoelectric coupling and dielectric permittivity constants for axially and radially polarized piezoelectric materials. . . . .	91
5.3	Acoustics properties of Water and Air. . . . .	93
8.1	Acoustic parameters for several Newtonian fluids at $25^{\circ}C$ . . . . .	159
8.2	Viscosity of Glycerol solution in different temperatures ([1]). . . . .	161

# List of Figures

2.1	An idealized model of inclined incidence Transmission Loss (TL) through a barrier. . . . .	11
2.2	STL spectrum through a cylindrical structure. The cylinder absorbed the incident energy at 455 Hz (see green dotted line). . . . .	13
4.1	Schematic of thick an-isotropic smart piezoelectric cylinder . . . . .	51
4.2	Non-dimensional wave phase velocity $\Upsilon$ versus the non-dimensional axial wave number $\xi$ for $(b-a)/a=0.05$ . . . . .	59
4.3	Non-dimensional wave phase velocity $\Upsilon$ versus the non-dimensional axial wave number $\xi$ for $(b-a)/a=0.5$ . . . . .	60
4.4	Non-dimensional wave phase velocity, $\Upsilon$ , versus the non-dimensional axial wave number, $\xi$ , for selected piezoelectric materials material $n=0$ and $(b-a)/a=0.5$ . . . . .	61
4.5	Non-dimensional wave phase velocity, $\Upsilon$ , versus the non-dimensional axial wave number, $\xi$ , for $n=1$ and $(b-a)/a=0.5$ . . . . .	62
4.6	First lowest natural frequencies $\omega$ versus the circumferential wave number $n$ for selected axial wave number $\xi$ and $(b-a)/a=0.5$ . . .	64

4.7a	Natural frequencies $\omega$ versus the non-dimensional wave number $\xi$ for selected lowest natural frequency with $n=0$ and $(b-a)/a = 0.5$ . . .	66
4.7b	Natural frequencies $\omega$ versus the non-dimensional wave number $\xi$ for selected lowest natural frequency with $n=0$ and $(b-a)/a = 0.5$ . . .	67
4.8	Cut-off frequency of the lowest natural frequencies $\omega$ versus the non- dimensional axial wave number $\xi$ for $n = 0$ and $(b-a)/a = 0.5$ . . .	69
5.1	Problem Configuration. . . . .	73
5.2	STL validations. . . . .	90
5.3	Cylinder TL comparison between the current study and Finite Element Method (FEM) (COMSOL MULTIPHYSICS) for the thin, moderately thick, and very thick thicknesses ( $h_a = 0.1\text{ m}, 0.25\text{ m}, 0.5\text{ m}$ ). The cylinder is assumed to be made of a single layer of axially polarized non-graded Lead Zirconate Titanate (PZT) <sup>4</sup> filled and surrounded by air, excited by a normal incident plane wave while the short-circuited boundary condition is applied at the inner and outer surfaces of the cylinder. . . . .	92
5.4	FEM modeling of the problem using COMSOL MULTIPHYSICS <sup>®</sup> . . .	94
5.5	Mesh modeling of the problem using COMSOL MULTIPHYSICS <sup>®</sup> . . .	95

5.6	Effect of piezoelectric layer on the STL of the piezocylinder. The cylinder is filled with air and submerged in the water. The elastic layer of the cylinder is made of Aluminum, while the piezoelectric layer is axially polarized ( $r_{in} = 1.8\text{ m}$ , $r_a = 1.9\text{ m}$ and $r_{ex} = 2\text{ m}$ ). The short-circuited boundary condition was applied at the internal and external surfaces of the piezoelectric cylinder. . . . .	96
5.7	STL versus the frequency for different piezoelectric polarization, when the cylinder is filled with air and submerged in water subjected to different angles of the plane incident waves. The cylinder is made of Aluminum and PZT4 with $r_{in} = 1.8\text{ m}$ , $r_m = 1.9\text{ m}$ and $r_{ex} = 2\text{ m}$ . The cylinder is filled and surrounded by air, and the short-circuited boundary condition is enforced at the inner and outer surface of the piezoelectric cylindrical shell. . . . .	98
5.8	Accumulated cylinder TL versus the thickness ratio between the piezo-layer and host material, $\delta = \frac{h_a}{h_o}$ , for the selected incident angles. The cylinder is made of Aluminum, and radially polarized PZT4 ( $r_{in} = 1.8\text{ m}$ and $r_{ex} = 2\text{ m}$ ) surrounded and filled with air-fluid while the short-circuited boundary condition was enforced at the inner and outer surface of the piezoelectric layer. . . . .	99
5.9	Cylinder TL versus the frequency for the short and open circuited electrical boundary conditions. The cylinder is radially polarized, made of PZT4 piezoelectric material and Aluminum ( $r_{in} = 1.8\text{ m}$ , $r_m = 1.9\text{ m}$ and $r_{ex} = 2\text{ m}$ ), filled and surrounded with air acted upon by a plane normal incident wave. . . . .	102

5.10	Variation of STL as a function of frequency for the selected material gradient profiles ( $\mu = 0.2, 1, 5$ ). The cylinder is axially polarized, made of FGPM perfectly bonded to the internal shell made of aluminum ( $r_{in} = 1.8\text{ m}$ , $r_m = 1.9\text{ m}$ , and $r_{ex} = 2\text{ m}$ ), filled with air and fully submerged in the water acted upon by a normal plane incident wave.	104
5.11	STL spectrum for the selected acoustic fluids. The cylinder is axially polarized, made of PZT4 perfectly bonded to the internal shell made of aluminum ( $r_{in} = 1.8\text{ m}$ , $r_m = 1.9\text{ m}$ , and $r_{ex} = 2\text{ m}$ ), insonified by a normal plane incident wave, filled with and submerged in water/air.	105
6.1	Schematic of feedback controller for piezo-laminated cylindrical shell.	113
6.2	Comparison of STL with FEM (COMSOL MULTIPHYSICS) for a tri-layer piezoelectric cylinder. The cylinder is assumed to be made of axially polarized PZT4 ( $r_{in} = 1.95\text{ m}$ , $r_s = 1.98\text{ m}$ , $r_a = 1.99\text{ m}$ , $r_{ex} = 2\text{ m}$ ) with closed-loop electrical boundary condition applied to both of the sensor and actuator layers whereas the core layer is made of Aluminum material. The structure is surrounded and filled with air and excited by a normal incident plane wave ( $\alpha = \pi/2$ ).	118
6.3	Convergence study for selected incident wave frequencies and different angles of an acoustic incident plane wave. The piezo-composite cylinder is assumed to be made of radially polarized PZT4, filled and submerged in water.	121

6.4	Variation of converged truncated mode number with respect to the frequency for selected angles of incident waves. The piezo-composite cylinder is assumed to be made of radially polarized PZT4, surrounded and filled with water. . . . .	122
6.5	STL spectra of the radially polarized piezo-composite cylinder for four different angles of incident waves, based on the negative feedback control strategy with four different gain controls. . . . .	123
6.6	STL spectra of the axially polarized piezo-composite cylinder for four different angles of incident waves, based on the negative feedback control strategy with four different gain controls. . . . .	127
7.1	Schematic diagram of smart piezo-laminated cylinder embedded with discrete electrodes submerged in an inviscid acoustic fluid excited by an arbitrary oblique incident plane wave. . . . .	133
7.2	Comparison of STL with finite element method (COMSOL MULTIPHYSICS) for a piezo-composite cylinder. The cylinder is assumed to be made of radially polarized PZT4 ( $r_{in} = 1.8\text{ m}$ , $r_a = 1.9\text{ m}$ , $r_{ex} = 2\text{ m}$ ) with closed-loop electrical boundary condition applied to the internal layer of the actuator, whereas the external layer of the piezoelectric cylinder is attached to $90^\circ$ electrode at the top with the external electrical potential of 1 V as excitation. The core layer of piez-composite cylinder is made of Aluminum material. The structure is surrounded and filled with air and excited by a normal incident plane wave ( $\alpha = \pi/2$ ). . . . .	137

- 7.3 Sound transmission loss through a piezo-composite cylinder for different electrical potential excited by a normal incident plane wave. The cylinder is made of Aluminum and radially polarized Pzt4 ( $r_{in} = 1.8\ m$  and  $r_{ex} = 2\ m$ ) surrounded and filled with air-fluid. The piezoelectric cylinder is considered to be grounded in its internal surface. . . . . 139
- 7.4 Sound transmission loss through a piezo-composite cylinder for different sizes of electrodes excited by a normal incident plane wave. The cylinder is made of Aluminum and radially polarized Pzt4 ( $r_{in} = 1.8\ m$  and  $r_{ex} = 2\ m$ ) surrounded and filled with air-fluid with external electrical potential of 1 V as excitation. The piezoelectric cylinder is considered to be grounded in its internal surface. . . . . 142
- 7.5 The sound transmission loss through a piezo-composite cylinder at different positions of the electrode patch in relation to an incident plane wave. The cylinder is made of Aluminum and radially polarized Pzt4 ( $r_{in} = 1.8\ m$  and  $r_{ex} = 2\ m$ ) surrounded and filled with air-fluid while the internal surface of the cylinder is grounded . . . . . 143
- 7.6 Sound transmission loss through a piezo-composite cylinder for different asymmetric patches of electrodes, excited by a normal incident plane wave. The size of the top electrode is equal to  $\beta = \pi/3$  while the size of the asymmetric electrode is equal to  $\beta' = \pi/12$  . The cylinder is made of Aluminum and radially polarized Pzt4 ( $r_{in} = 1.8\ m$  and  $r_{ex} = 2\ m$ ) surrounded and filled with air-fluid while the piezoelectric cylinder is considered to be grounded in its internal surface . . . . . 146



7.7	Sound transmission loss through a piezo-composite cylinder for different arrangements of electrodes, excited by a normal incident plane wave. The size of all electrodes is equal to $\beta = \pi/6$ . The cylinder is made of Aluminum and radially polarized Pzt4 ( $r_{in} = 1.8\text{ m}$ and $r_{ex} = 2\text{ m}$ ) surrounded and filled with air-fluid. In addition, the electrodes are supplied with an external electrical potential of 1 V as excitation. In addition, the internal surface of the cylinder is grounded.	149
8.1	Schematic diagram of a smart piezo-composite cylinder submerged in a viscous fluid excited by an oblique incident plane wave. . . . .	155
8.2	Flowchart diagram followed for the calculation of STL. . . . .	160
8.3	STL comparison between Flugge-Lure-Byrne thin walled theory as presented in [2] and the current study for three different incident angles ( $\alpha = \pi/6; \pi/3; \pi/2$ ) at Mach=0 for a cylinder submerged in an inviscid fluid. . . . .	161
8.4	Angular distributions of the scattering patterns of pressures at a far-field for a brass cylinder submerged in glycerine at $77^\circ\text{F}$ ( $\Re[k_c]r_{in} = 0.1$ ) . . . . .	162

8.5	STL comparison between the current study and FEM model for a piezo-composite cylinder, filled and submerged in Glycerol at $40^{\circ}C$ . The cylinder is assumed to be made of a single layer of Aluminium coated with radially polarized PZT4 piezoelectric material. Besides, the cylinder is excited by a normal incident plane wave while the open-loop electrical boundary condition is enforced at the internal and external surface of the cylinder. . . . .	163
8.6	STL comparison between inviscid and viscous model at different frequency spectra for the short-circuited electrical boundary conditions. The cylinder is excited by a normal incident plane wave ( $\alpha = \pi/2$ ). The core layer of the cylinder is made of Aluminum, while the piezoelectric layer is made of radially polarized PZT4 ( $r_{in} = 19$ mm, $r_a = 20$ mm and $r_{ex} = 21$ mm). The Piezo-composite cylinder is filled with and submerged in Glycerol at $0^{\circ}C$ . . . . .	166
8.7	STL versus dynamic viscosity for a cylinder submerged in glycerol at $0^{\circ}C$ . The cylinder is made of a single layer of Aluminum excited by a normal incident plane wave with the amplitude of 1 Pa ( $r_{in} = 19$ mm, $r_a = 20$ mm). . . . .	169
8.8	Comparison of the effect of dynamic viscosity and bulk viscosity on the STL of the cylinder submerged in glycerol. The cylinder is made of a single layer of Aluminum excited by a normal incident plane wave with the amplitude of 1 Pa ( $r_{in} = 19$ mm, $r_a = 20$ mm). The frequency of the incident plane wave is set to 100 kHz . . . . .	170

8.9	Effect of fluid temperature on the STL through a piezo-composite cylinder at different frequency spectra for the short circuited electrical boundary conditions; the cylinder is excited by a normal incident plane wave ( $\alpha = \pi/2$ ). The core layer of the cylinder is made of Aluminum, while the piezoelectric layer is made of radially polarized PZT4 ( $r_{in} = 19$ mm, $r_a = 20$ mm and $r_{ex} = 21$ mm). The Piezo-composite cylinder is filled with and submerged in Glycerol at different temperatures ( $T = 0^{\circ}\text{C}$ , $\mu = 9390$ cp, $\lambda = 12000$ cp; $T = 40^{\circ}\text{C}$ , $\mu = 234$ cp, $\lambda = 238$ cp). . . . .	172
8.10	Effect of anisotrpicity of actuator layer on the STL spectra for the short-circuited piezo-composite cylinder submerged in Fluorocarbon (FC-75) at $25^{\circ}\text{C}$ at different frequency ranges. The cylinder is excited by a normal incident plane wave ( $\alpha = \pi/2$ ) with a pressure amplitude of 1 Pa. The elastic layer of the cylinder is made of Aluminum, while three different actuator layers are considered to be made of isotropic, orthotropic, or triclinic materials. The triclinic case is constitute of one layer of Lithium niobate ( $LiNbO_3$ ), and the second type of layer is made of Lithium tantalate ( $LiTaO_3$ ) ( $r_{in} = 19$ mm, $r_a = 20$ mm and $r_{ex} = 100$ mm). The mechanical and electrical properties of the triclinic piezoelectric materials are given in Table 4.1. The cylinder is also considered to be short-circuited at both its external and internal layers. . . . .	175

- 8.11 Comparison of the effect of anisotropy on the STL of a piezo-laminated cylinder submerged in Fluorocarbon (FC-75) at 25°C for different ranges of dynamic viscosity. The frequency of the incident plane wave is set to 250 kHz. The core layer of the cylinder is made of Aluminum, while the external layer is made of anisotropic piezoelectric material constituting of one layer of Lithium niobate ( $LiNbO_3$ ), and the second type of layer is made up of Lithium tantalate ( $LiTaO_3$ ) ( $r_{in} = 19$  mm,  $r_a = 20$  mm and  $r_{ex} = 100$  mm). The cylinder is considered to be short-circuited on both its external and internal layers. The cylinder is excited by a normal incident plane wave ( $\alpha = \pi/2$ ) with a pressure amplitude of 1 Pa. The mechanical and electrical properties of the triclinic piezoelectric materials are given in Table 4.1. [3]. . . . . 176
- 8.12 Comparison of viscous and inviscid models for the effect of piezoelectric boundary conditions on the STL spectra for the short-circuited and open-circuited piezo-composite cylinder submerged in glycerin at 0°C at different ranges of frequencies. The cylinder is excited by a normal incident plane wave ( $\alpha = \pi/2$ ) with the pressure amplitude of 1 Pa. The core layer of the cylinder is made of Aluminum, while the external layer is made of radially polarized PZT4 ( $r_{in} = 19$  mm,  $r_a = 20$  mm and  $r_{ex} = 30$  mm). . . . . 178

8.13 Comparison of the effect of different electrical boundary conditions on the STL of piezo-laminated cylinder submerged in the Oil at 25°C for a different range of dynamic viscosity. The frequency of the incident plane wave is set to 400 kHz. The elastic layer of the cylinder is made of Aluminum, while the external layer is made of radially polarized PZT4 ( $r_{in} = 19$ mm, $r_a = 20$ mm and $r_{ex} = 30$ mm). The cylinder is excited by a normal incident plane wave ( $\alpha = \pi/2$ ) with a pressure amplitude of 1 Pa. . . . .	180
---	-----

# List of Abbreviations

2D	Two Dimensional. 15, 35
3D	Three Dimensional. i, 5, 8, 15–18, 29, 32, 35, 36, 41, 49, 50, 72, 88–90, 106, 110, 129, 162, 180
ACD	Active Damping Control. 31
BEM	Boundary Element Method. 21
FEM	Finite Element Method. vii, ix, xiii, 26, 72, 92, 107, 108, 117, 118, 163–165
FGM	Functionally Graded Material. 8, 73, 103, 184
FGPM	Functionally Graded Piezoelectric Material. i, ix, 4, 8, 30, 73, 104, 184
GA	Genetic Algorithms. 18, 20
LQG	Linear Quadratic Gaussian. 20
NSGA	Non-dominated Sorting Genetic Algorithm. 18
ODE	Ordinary Differential Equations. 114
PLM	Perfectly Matched Layer. 93, 117, 118, 164
PZT	Lead Zirconate Titanate. vii–x, 23, 60, 62, 63, 91, 92, 94, 97–99, 101–105, 107, 116–119, 121, 122, 124, 126
SONAR	Sound Navigation RAnging. 14, 23, 25

STL	Sound Transmission Loss. i, ii, vi–x, xii–xvi, xxiv, xxvi–xxviii, 3–10, 12–16, 18–20, 28, 30–32, 71, 72, 86, 90, 96, 98, 102–106, 109, 111, 113, 117–119, 122–129, 133, 135, 152, 153, 159–173, 175–182, 184–187
TL	Transmission Loss. vi–viii, 2, 11, 13–16, 19, 31, 72, 86–92, 96, 97, 99–103, 106–108, 116, 125, 126

# Nomenclature

$(h/R)$	Thickness ratio
$\alpha$	Incident wave angle
$\delta$	Thickness ratio between the piezoelectric layer and the host material
$u_i$	Lagrangian particle acceleration
$\epsilon_{ij}$	Second-order dielectric permittivity tensors
$\epsilon_{kl}$	Cauchy–Green strain tensor
$\eta$	Structural damping
$\Lambda(\bar{r}_i)$	Volume fraction of the material in the i-th layer
$\mathfrak{i}$	Imaginary unit
$\mu$	Power of gradient profile
$\omega$	Circular frequency
$\phi$	Electrical potential
$\Pi_I$	Incident acoustic power



$\Pi_T$	Transmitted acoustic power
$\boldsymbol{\nu}$	The fluid velocity
$\Psi$	Non-dimensional natural frequency
$\rho$	Density of elastic layer
$\rho_{ex}$	External fluid density
$\rho_{in}$	Internal fluid density
$\rho_{pz}$	Density of piezoelectric
$\sigma_{ij}$	Cauchy–Green stress tensor
$\mathbf{I}$	Unit tensor
e	Exponential function
$\theta$	Circumferential cylindrical coordinate
$\Upsilon$	Non-dimensional wave phase velocity
$\zeta$	Axial wave number
$A$	Domain of integration over the surface of the cylinder
$c_{ex}$	Traveling speed of sound in the external fluid
$C_{ijkl}$	Fourth-order elasticity tensor
$c_{in}$	Traveling speed of sound in the cavity
$D_i$	Electrical displacement vector

$E_i$	Electrical field vector
$e_n$	Unit base vector
$e_{ijk}$	Third-order piezoelectric tensors
$f_i$	Body force
$h$	Thickness of the shell
$H_n^1(x)$	Hankel function of the first kind
$H_n^2(x)$	Hankel function of the second kind
$J_n(x)$	Bessel function of the first kind
$k$	Closed-loop gain
$N$	Value of truncated constant
$n$	Circumferential wave number
$n_j$	Unit-length direction vector
$n_{pz}$	Number of piezoelectric sub-layers
$P^I$	Incident wave pressure
$P^R$	Reflected wave pressure
$P^T$	Transmitted wave pressure
$p_0$	Amplitude of the incident wave pressure
$Q_f$	Free charge density

$R$	Radius of the shell
$s$	Specific entropy
$t_i$	Cauchy stress vector at a traction surface
$TL$	Transmission Loss
$V$	Spatial state vectors
$z$	Axial cylindrical coordinate

# Contents

List of Tables	v
List of Figures	vi
List of Abbreviations	xvii
Nomenclature	xix
Contents	xxiii
<b>1 Introduction</b>	<b>1</b>
1.1 The Big Picture . . . . .	1
1.2 Thesis Statement and Objectives . . . . .	4
1.2.1 Thesis Statement . . . . .	4
1.2.2 Objectives . . . . .	5
1.3 Organization of this study . . . . .	8

<b>2</b>	<b>Literature Survey</b>	<b>10</b>
2.1	Transmission Loss . . . . .	11
2.1.1	What Is Transmission Loss? . . . . .	11
2.2	A Comprehensive Review on The STL Through Cylindrical Shells .	13
2.3	A Comprehensive Review on The Sound Isolation Techniques for Cylindrical Shells . . . . .	17
2.4	Introduction of Piezoelectricity . . . . .	21
2.4.1	A Brief History of Piezoelectricity . . . . .	21
2.4.2	Basic Principles of Piezoelectricity . . . . .	24
2.4.3	Anisotropic Piezoelectric Cylinder and Its Applications . .	24
2.4.4	A Review on The Dynamic Study of Anisotropic Piezoelectric Cylinder . . . . .	25
2.5	Review on The STL Through Viscous Fluid . . . . .	28
2.6	Objectives, Contributions, Applications and Discussions . . . . .	29
<b>3</b>	<b>Fundamental Theories of Elasticity and Acoustics</b>	<b>34</b>
3.1	Introduction to The Three Dimensional Theory of Elasticity . . . .	35
3.1.1	Limitation of Linear Three Dimensional Theory of Elasticity	41
3.2	Inviscid Acoustic Field Equations . . . . .	43
3.3	Viscous Acoustic Model . . . . .	45

<b>4</b>	<b>Three-Dimensional Free Vibration Analysis of Triclinic Piezoelectric Hollow Cylinder</b>	<b>49</b>
4.1	Mathematical Modelling . . . . .	51
4.1.1	Problem Description of Triclinic Piezoelectric Hollow Cylinder	51
4.1.2	State Space Method . . . . .	54
4.2	Traction Boundary Conditions and Final Solution . . . . .	56
4.3	Validations . . . . .	59
4.4	Case Studies . . . . .	62
4.5	Conclusions . . . . .	69
<b>5</b>	<b>Sound Transmission Through a Thick-Walled FGM Piezo-laminated Cylindrical Shell Filled with and Submerged in Compressible Fluids</b>	<b>71</b>
5.1	Problem Description of Sound Transmission Through a Piezo-laminated cylinder . . . . .	73
5.1.1	External Acoustic Medium . . . . .	74
5.1.2	Internal Acoustic Medium . . . . .	76
5.2	Structural Modelling: Elasticity and Piezoelasticity . . . . .	77
5.2.1	Functionally Graded Laminated Model . . . . .	78
5.2.2	Kinematic Assumptions . . . . .	79
5.2.3	Conservation Laws . . . . .	79
5.3	Spatial State Vectors and Ultimate Transfer Function . . . . .	80

5.3.1	Ultimate Transfer Matrices . . . . .	83
5.4	Fluid-solid Coupling and Electrical Boundary Conditions . . . . .	84
5.4.1	Fluid-solid Interaction . . . . .	84
5.4.2	Electrical Boundary Conditions . . . . .	85
5.5	Final Solution . . . . .	86
5.5.1	STL . . . . .	86
5.6	Model Validation . . . . .	87
5.7	Results and discussion . . . . .	95
5.8	Conclusion . . . . .	106
<b>6</b>	<b>Active Broadband STL Control Through an Arbitrary Thick Smart Piezo-composite Cylinder</b>	<b>109</b>
6.1	Problem Description for STL Control Through an Smart Piezo-composite Cylinder . . . . .	111
6.2	Sensor Layer Modeling . . . . .	113
6.2.1	Modal Spatial State Equations . . . . .	114
6.2.2	Boundary Conditions and Controller Implementation . . . . .	115
6.3	Model Validation . . . . .	116
6.4	Results and discussion . . . . .	119
6.5	Conclusions . . . . .	129

<b>7</b>	<b>Effect of Electrode Size and Configuration on the Sound Transmission Loss of Smart Piezo-laminated Structures</b>	<b>131</b>
7.1	Problem Description for Different Size and Configuration of Electrodes	132
7.2	Mathematical Modeling . . . . .	133
7.2.1	Electro-mechanical Boundary Conditions . . . . .	134
7.3	Model Validation . . . . .	135
7.4	Results and Discussion . . . . .	138
7.4.1	Voltage effect . . . . .	139
7.4.2	Electrode size effect . . . . .	140
7.4.3	Electrode location effect . . . . .	144
7.4.4	Electrode asymmetric effect . . . . .	144
7.4.5	Electrode number effect . . . . .	147
7.5	Conclusions . . . . .	150
<b>8</b>	<b>Effect of Fluid Viscosity on the Sound Transmission Loss of Smart Piezo-laminated Structures</b>	<b>152</b>
8.1	Problem Description For Transmission Loss in Viscous Fluid . . . .	154
8.1.1	Viscous Acoustic Model . . . . .	155
8.1.2	Electro-mechanical Boundary Conditions . . . . .	158
8.2	Model Validation . . . . .	158
8.3	Results and discussion . . . . .	165
8.3.1	Effect of Viscosity on STL . . . . .	165



8.3.2	Effect of temperature on the STL . . . . .	170
8.3.3	Effect of anisotropy on the STL considering fluid viscosity	173
8.3.4	Effect of piezoelectricity on the STL with the viscous fluid .	177
8.4	Conclusions . . . . .	180
<b>9</b>	<b>Conclusions and Future Works</b>	<b>183</b>
9.1	Conclusions . . . . .	183
9.2	Possible Future Works . . . . .	186
	<b>Appendices</b>	<b>192</b>
	<b>Appendix A</b>	<b>193</b>
A.1	Anisotropic Piezoelectric Constitutive Model . . . . .	193
A.2	Differential Operator . . . . .	193
A.3	Kinematic Relations . . . . .	194
A.4	Conservation Laws . . . . .	194
A.5	Modal Coefficient Matrices . . . . .	195
A.6	Final System of Linear Algebraic Equation . . . . .	199
	<b>Appendix B</b>	<b>199</b>
B.1	Constitutive Relations . . . . .	199
B.1.1	Constitutive relation of the orthotropic materials . . . . .	199
B.1.2	Constitutive relation of axially polarized piezoelectric materials	200

B.1.3	Constitutive relation of radially polarized piezoelectric materials	200
B.2	Matrix Operators . . . . .	201
B.3	Modal Coefficient Matrices . . . . .	202
B.3.1	Elastic Modal Coefficient Matrices . . . . .	202
B.3.2	Modal Matrix of Axially Polarized Piezoelectric Material . .	203
B.3.3	Modal Matrix of Radially Polarized Piezoelectric Materials	205
B.4	Final Solution . . . . .	208
B.4.1	Short Circuited and Active Electrical Boundary Conditions	208
B.4.2	Open Circuited Electrical Boundary Condition . . . . .	210
B.4.3	Feedback Control With a Closed-loop Gain Amplifier . . . .	211
<b>Appendix C</b>		<b>212</b>
C.1	Final Solution of Viscous Model . . . . .	212
C.1.1	Open Circuited Electrical Boundary Conditions . . . . .	212
C.1.2	Short Circuited Electrical Boundary Condition . . . . .	222
<b>Bibliography</b>		<b>226</b>

# Chapter 1

## Introduction

*"Invention is the most important product of man's creative brain. The ultimate purpose is the complete mastery of mind over the material world, the harnessing of human nature to human needs."*

---

Nikola Tesla

### 1.1 The Big Picture

Dynamic studies of thick smart cylindrical composite structures have a widespread application in nondestructive testing, underwater acoustics, diagnostic ultrasound, noise abatement in the fuselage, and marine applications (Caresta [4], Krakters et al. [5]). Prediction of steady-state behavior of fluid-coupled structures has been the subject of current research as the most external excitations, or acoustic pressure signals in many technological and engineering applications are of a harmonic nature. Particularly, fluid-solid interaction in submerged cylindrical structures experiencing

an oblique incident shock wave or wide-band acoustic excitation is a difficult multi-physics problem of fundamental importance that has been extensively studied over the past few decades (Hasheminejad and Mousavi-Akbarzadeh [6], Iakovlev et al. [7, 8]).

Attenuation of transmission loss (TL) from such structures based on conventional passive control methods in most cases is insufficient due to the deterioration of the damping characteristics of such treatments under temperature and frequency deviations aside from the cost of including substantial weight or volume to the vibrating structure (Hasheminejad and Keshavarzpour [9], Hasheminejad and Kazemirad [10]). New developments in the area of smart material technology along with the considerable enhancement in the computational power of microcomputers have paved the way for an efficient mechanism to diminish vibration and acoustic emission of vibrating structural systems (Crawley and De Luis [11], Hasheminejad and Alaei-Varnosfaderani [12], Hasheminejad and Keshavarzpour [13]). Specifically, the coupled electro-mechanical properties of piezoelectric materials embedded into the mechanical structures give the structure the ability to convert electrical energy to mechanical energy and vice versa. These materials are suitable for exploiting as piezoelectric sensor and actuator layers in a wide range of industrial applications in active vibration and noise control. Such an intelligent structure would allow the use of a closed-loop control system for vibration and sound suppression.

In general, when the sound waves impinge on the wall of a cylinder, the sound wave attenuates because of the boundary layer effects. These losses can be significant when the structure is quite small compared to the surrounding media and submerged in a viscous fluid. Although the inviscid acoustic model is very efficient to study

the sound transmission loss (STL) in many cases, there are some cases that the inviscid model may fail to accurately predict the STL. For instance, if the structure is submerged in a fluid with a high level of viscosity, the loss of sound waves is caused by fluid viscosity and heat exchange. In the vicinity of borders, these losses are particularly significant. Such losses become very significant when the dimension of the structure is similar to the boundary layer thickness [14]. Obviously, the inviscid model can not capture such losses, so it becomes necessary to develop a model that can take into account such losses. It should also be mentioned that in some circumstances, wave propagation happens in a narrow gap due to the presence of a fluid's viscosity, which cannot be ignored [15]. A narrow slit or enclosure in a hearing aid, a small transducer, etc, are examples of such a situation [15].

While browsing through the literature, although the effects of the fluid viscosity on the sound transmission loss through thin/thick smart cylindrical structures is often overlooked, some scholars pay attention to the effects of viscosity on the sound transmission in the cylindrical structures [16, 17, 18], and some comprehensive studies on the piezoelectricity benefiting STL have also been conducted in non-viscous media [19, 20]. However, the compound effects of an-isotropic piezoelectricity and fluid viscosity on the STL while the structure is submerged in the viscous fluid were not considered and well discussed. In addition, the effect of piezoelectric materials on the active and passive STL control from smart structures is often overlooked. Besides, the effect of piezoelectric anisotropy was not considered during the operation of the intelligent system. Both piezoelectricity and fluid viscosity have obvious effects on wave behaviors in a cylindrical shell, and the coupled and interacted piezoelectricity and fluid viscosity could bring different understanding/findings on

STL that has not been revealed before. Therefore, designing a model that can deal with an-isotropic piezoelectric crystal and also take into account the effects of inevitable fluid viscosity in wave propagation is very important in acoustic quieting or sound utilization applications. Such a model can also help in predicting the dynamics of nano and micro-electromechanical systems as fluid viscosity plays an important role at nano and micro scales.

## 1.2 Thesis Statement and Objectives

### 1.2.1 Thesis Statement

The main focus of this study is to investigate the interaction between the incident plane waves and the smart piezo-composite hollow cylinder to provide active control strategies for sound isolation enhancement of the cylindrical structures submerged in either an inviscid or viscous fluid. The aim is to mitigate the transmitted sound into the cylinder by decreasing the internal sound intensity, using a control strategy to provide smart structures with better acoustic performances. This will be achieved by using the proposed Vibro-Acoustics model to investigate the effects of piezoelectric material properties, effects of size and configurations of piezoelectric electrode patches, piezoelectric polarization direction, shell thickness ratio, electrical boundary conditions, and FGPM on the STL due to the piezoelectricity. Besides, comprehensive numerical studies are carried out to investigate STL of the controlled and uncontrolled piezo-composite cylinder as well as the effect of closed-loop gain. In addition, the structure is submerged in a viscous fluid in order to study the effect of viscosity on the STL through the piezo-composite hollow cylinder.

### 1.2.2 Objectives

The main goals of this study are classified into two sub-objectives as follows.

#### Objectives for Mathematical Modeling

1. To establish an accurate closed-form mathematical model of the Vibro-acoustics behavior of a smart piezo-composite cylinder. This model should:
  - (a) consider the specific continuum-mechanical model of three-dimensional 3D exact theory of elasticity and piezo-elasticity rather than approximate shell theories for all ranges of thicknesses and frequencies;
  - (b) be able to model cylinders made of fully anisotropic or triclinic materials (the most general form of anisotropic materials without any axis of material symmetry);
  - (c) modeling the propagation of waves through the internal cavity and infinitely large domain of external surrounding fluid using the classical Helmholtz equation;
  - (d) including the fully coupled fluid-structural interactions by considering the equilibrium of the radial stress with the fluid pressure at the inner/outer surfaces of the piezo-composite cylinder in addition to considering the continuity of the normal fluid and solid displacements at the interior/exterior surfaces;
  - (e) the model should be able to obtain an analytical solution for calculation of STL;

- (f) the intelligent structure model should be able to integrate with a closed-loop control system for the enhancement of STL;
  - (g) the closed-loop control strategy should be able to provide a significant wave isolation effect at the resonant frequencies;
  - (h) the model should be able to take into account the viscosity of the surrounding fluid and the internal cavity in order to predict the sound wave attenuation due to the effect of the boundary layers;
  - (i) the model should be able to consider different sizes and configurations of electrode patches
2. To use the developed model and study STL through a smart cylinder under different conditions (i.e., perform parametric studies).

### **Objectives for Investigations**

1. To investigate the effect of anisotropy on the natural frequency of the thick-walled piezoelectric cylinder;
2. To investigate the effect of different electrical boundary conditions on the STL and determine a better one for the different range of frequencies;
3. To investigate the effect of different piezoelectric materials and functionality of material properties on the STL and specifying which materials provide the best sound isolation performance for a different range of frequencies;
4. To investigate the effect of different piezoelectric polarization at different angles of the plane incident waves;



5. Investigation of the optimal thickness ratio between the piezo-layer and host material;
6. Performing convergence study for selected incident wave frequencies and different angles of an acoustic incident plane wave;
7. Studying the effect of different gain controls on the STL;
8. Studying the effect of different sizes and configurations of electrode patches on the STL
9. Studying the compound effects of an-isotropic piezoelectricity and fluid viscosity on the STL while the structure is submerged in the viscous fluid.

### 1.3 Organization of this study

The specific organization of this study is outlined as follows. First, a definition of STL and its importance will be provided. Then, a comprehensive review of the STL through cylindrical shells is given. Next, different isolation techniques for cylindrical shells are discussed. In addition, a brief history of piezoelectricity, along with the basic principles of piezoelectricity, is discussed in chapter 2. Finally, a comprehensive review of the STL through a viscous fluid will be given.

In chapter 3, the basic theory of 3D elasticity is discussed and explained. Additionally, the basic principles of acoustic theory in viscous and inviscid fluids are comprehensively explained.

In chapter 4, the free vibration of the general model of an anisotropic piezoelectric material with all possible material constants is analytically modeled and studied to cover a broad range of anisotropic piezoelectric materials. Then the validity of the proposed model was checked against other literature's results. Next, the effect of anisotropy on the wave dispersion curves of the piezoelectric cylinder is discussed in the case studies section. Finally, the concluding remarks are listed.

In chapter 5, the general model presented in chapter 4 is used and extended to investigate sound transmission through a thick-walled Functionally Graded Material (FGM) piezo-laminated cylindrical shell filled with and submerged in compressible inviscid fluids. Parameter studies are conducted to investigate the effects of piezoelectric material properties, piezoelectric polarization direction, shell thickness ratio, electrical boundary conditions, and FGPM on the STL due to the piezoelectricity.

The passive STL control given in chapter 5 has many advantages. There were,

however, some drawbacks, such as the fact that the passive method could not provide high STL at resonance frequencies. In addition, there are not many ways to provide the desired sound isolation at a specific frequency. In chapter 6 we probe deeper into this issue and used active STL control to solve this problem. In chapter 6, the previous study was utilized to realize better STL especially at the resonance frequencies of the structure through a feedback control of piezo-composite cylinder. The active control strategy is achieved by sending a control signal from the distributed piezoelectric sensor layer through a controller with a certain feedback gain to drive the external piezoelectric actuators. The mechanical stress generated by the piezo-actuator layer cancels the parts of the input incident wave to enhance the STL.

In chapter 7, the effect of different sizes and configurations of piezoelectric patches are discussed.

The previous studies on STL with smart composite thick shell are all based on non-viscosity assumption. To consider the viscosity and piezoelectric coupling effect on STL, the content in chapter 8 is proposed. In chapter 8, the Navier-Stokes equation is employed to study the effect of the fluid viscosity on the STL. Parametric studies are carried out to investigate the effect of fluid viscosity (dynamic viscosity and bulk viscosity), shell anisotropy, and piezoelectric boundary conditions on the STL through a piezo-composite cylinder submerged in a viscous fluid.

Lastly, the concluding remarks and future work are given in chapter 9.

# Chapter 2

## Literature Survey

*"Is it right to probe so deeply into Nature's secrets? The question must here be raised whether it will benefit mankind, or whether the knowledge will be harmful."*

---

Pierre Curie

The multidisciplinary nature of sound isolation and noise reduction by a piezoelectric element, in particular, makes the topic to be approached by a large group of audience from a different scientific branch of knowledge. Therefore, the goals of this chapter are to cover basic principles of piezoelectricity and research that have been carried out in the areas of anisotropic piezoelectric materials modeling, investigating the effects of piezoelectric material on STL along with a thorough review of recent developments and techniques for acoustic enhancement of smart cylindrical structures with a short description of STL.

## 2.1 Transmission Loss

### 2.1.1 What Is Transmission Loss?

TL typically defines the cumulative reduction in the waveform energy as a wave transmits through a barrier or a given area, such as the different variety of structures [21]. TL is a broad terminology in many branches of science, such as acoustics, optics, electrical science. In optics, it refers to attenuation of sunlight or X-rays when they transmit through water, air, or any other media [22]. In electrical engineering, TL is defined as the electrical power loss along an electrical cable [23]. Here, however, we focused our study on the transmission of acoustic waves. Three different phenomena may occur when sound waves impinge on a solid structure, as illustrated in Figure 2.1 [24].

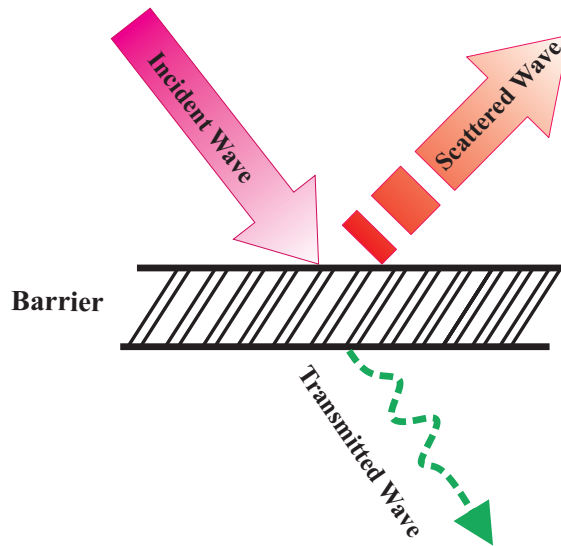


Figure 2.1: An idealized model of inclined incidence TL through a barrier.

Some portion of acoustic pressure waves can be reflected off an obstacle while the rest of it can be transmitted through the barrier or absorbed and dissipated by converting to thermal energy [25]. STL evaluates the performance of acoustic obstacles for industrial applications [24]. It can be described as the ratio of acoustic energy transmitted through an acoustic barrier to the acoustic energy of the incident wave [24, 26]. It can be defined as [24]

$$TL = 10 \log_{10} \left( \frac{\Pi_I}{\Pi_T} \right), \quad (2.1)$$

in which  $\Pi_I$  and  $\Pi_T$  are incident and transmitted acoustic power, respectively. Furthermore,  $\log_{10}(x)$  indicates the common logarithm with base 10. STL is very much dependent on the frequency (see Figure 2.2)[26]. It is not dependent on the sound source [26]. Keeping in mind Equation 5.32, the higher the STL of an acoustic treatment has, the better it will work in regard to sound attenuation [26]. In Figure 2.2, the y-axis shows how many dB the acoustic treatment attenuates the incoming acoustic intensity. For instance, in Figure 2.2, it is evident that at 445 Hz, the cylinder reduces the incident acoustic energy by 33 dB as shown by the green line, whereas, at 377 Hz, the cylinder does not significantly reduce the incident acoustic energy as shown by the purple line (see Figure 2.2). This also shows that the STL is highly dependent on the frequency of the incoming incident wave.

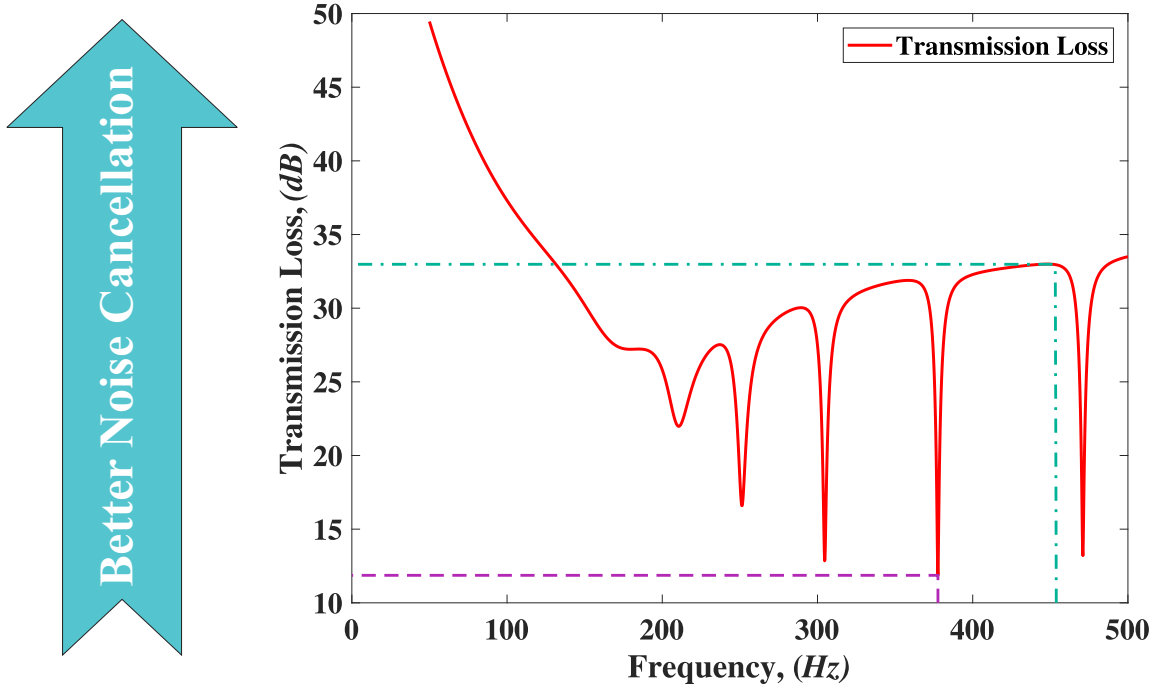


Figure 2.2: STL spectrum through a cylindrical structure. The cylinder absorbed the incident energy at 455 Hz (see green dotted line).

## 2.2 A Comprehensive Review on The STL Through Cylindrical Shells

Structural dynamic behavior and its TL from cylindrical and spherical objects have been a subject of researchers' interest from the late nineteen century within different branches of physics such as acoustics, electromagnetic, geology, and quantum (Furutsu [27], Li and Zhang [28], Zhou et al. [29], Suematsu and Imai [30], Jiang and Georgakopoulos [31], Dong and Wang [32], Goubau [33], Young and Crocker [34], Oba and Finette [35], Bisheh and Wu [36], Moore and Lyon [37], Chen et al. [38], Hasheminejad et al. [39, 40], Bisheh and Wu [41, 42, 43, 44], Lu-miao et al. [45], Qin et al. [46, 47], Wang et al. [48], Kang et al. [49]).

The appeal is due to its wide range of applications in different branches of applied physics. STL through cylindrical structure stays as a hot topic due to its manufacturing feasibility and wide range of industrial applications, examples of which are

- *Noise reduction*, in air conditioning and ventilation systems (Choy et al. [50]);
- *Aviation*, in predicting airborne noise from a fuselage (Wang and Crocker [51]);
- *Underwater acoustics*, design of transducer arrays in cylindrical Sound Navigation Ranging (SONAR) systems (Sastry and Munjal [52], Li and Hua [53]);
- *Noise control*, in an aircraft's cabin (Koval [2], Flodén et al. [54]);
- *Muffler*, design such as expansion volume types (Tao and Seybert [55], Wu and Wan [56]).

Several studies have been carried out in this area to cover the essential needs of these industrial applications. Many researchers focused on the classical shell theories to study the TL through an isotropic cylindrical shell. Among these researchers, Smith Jr [57] used the thin cylindrical elastic shell theories along with the method developed by Lax and Feshbach [58] in order to measure the acoustic impedance of an infinite cylindrical shell subjected to normal incident acoustic waves. Due to the limitations of shell theory, the solution was only valid when the radial thickness of the shell is of the same order of the shell vibration wavelength. Later on, White [59] used the concept of average energy and energy flow to study the same problem



for a finite-length cylindrical shell. The results showed that the acoustic isolation properties subjected to a random incident plane wave are approximately independent of the incident angle.

Koval [2] developed the work done by Smith Jr [57] to include the effects of different acoustic's fluid properties, Mach number, and internal pressurization on the STL of oblique incident plane waves through a thin shell. The results showed that the TL is not affected by the Mach number when the wave incident angle is normal. Koval [60] extended his previous work to consider the effect of orthotropy on the STL of airborne noise. While the TL was shown to be very sensitive to the ratio of circumferential to axial elastic modulus, it was nearly unaffected by the change in the shear modulus. Later on, the model was developed to investigate the effect of the fiber orientation in the acoustic isolation of a laminated composite circular cylindrical shell (Koval [61]). Numerical results demonstrated that the laminated composite shell can reduce the noise transmission at low frequencies, while their performance may degrade in the high-frequency ranges.

Narayanan and Shanbhag [62] used the thin shell theory to study TL and the structural response of a layered cylindrical shell with unconstrained damping and a sandwich shell with constrained damping treatment by consideration of axisymmetric modes. Significant improvement of sound transmission characteristics was achieved for a layered cylindrical shell by appropriate choice of the modulus of elasticity and thickness of the damping layer. Later on, Blaise et al. [63] extended Koval's work ([60]) to calculate the diffuse field transmission coefficient. His previous work was extended in order to compare the STL through the 3D and Two Dimensional (2D) models. The main aim was to investigate the limitations of the 2D model (Blaise

and Lesueur [64]).

Tang et al. [65] have studied the effects of the incident angle, Mach number, structural loss factor, and the ratio between the core thickness and the total thickness of the cylinder on the STL from a cylindrical sandwich shell with a honeycomb core. In addition, the effects of shear and rotation of sandwich shell were considered, and the results showed that the transmission of shear waves will result in the TL reduction for the high-frequency range. Lee and Kim [66] both experimentally and analytically studied the sound transmission through an infinite cylindrical shell excited by an oblique incident plane wave. Love's thin shell theory was utilized to model the cylinder structure. It was shown that, despite the significant simplification of the problem, the theoretical model can still be employed as an effective tool in practical design. Ghinet et al. [67] used symmetrically laminated composite shells and discrete layer shell theory to investigate the diffuse field TL of infinite cylindrical shells. The validity of the two models was compared against the experimental results.

The 3D theory of elasticity has also been used to investigate the STL from the thick isotropic cylindrical shell. Among these researchers, Sastry and Munjal [52] utilized the transfer matrix approach to study the effect of cylinder thickness, layer material characteristics, and surrounding media on the wave scattering from a thick multi-layered infinite cylindrical shell in the case of the normal plane incident wave. Later on, Hosseini-Toudeshky et al. [68] used the same theory to investigate the sound transmission through a thick hollow cylindrical shell with fixed-end boundary condition in the case of the plane wave, monopole, and dipole sources. Recently, Magniez et al. [69] employed a mixed 3D-shell analytical model to investigate the sound transmission through a cylindrical sandwich shell. The mixed 3D-shell cylinder

was composed of thin orthotropic layers and an isotropic core layer. The first was described with the first-order shear deformation theory, while the latter was modeled with the 3D theory of elasticity.

## 2.3 A Comprehensive Review on The Sound Isolation Techniques for Cylindrical Shells

Dynamics modeling and analysis of composite structures, as well as the sound isolation behaviors of these structures, are vital issues in the evaluation and enhancement of their dynamics and acoustic properties. Designing, studying and enhancement of different composite engineering materials or structures and the associated sound isolation method and techniques have been widely investigated by many scholars (Li and Zhang [28], Dong and Wang [32], Young and Crocker [34], Oba and Finette [35], Moore and Lyon [37], Hasheminejad et al. [39, 40], Bisheh and Wu [36, 41, 70, 43, 44], Bisheh et al. [71], Lu-miao et al. [45], Wang et al. [48], Kang et al. [49], Daneshjou et al. [72], Chronopoulos et al. [73]). One common consideration of vibration/acoustics isolation is the analysis of different boundary conditions connecting engineering mediums and structures. Accounting for non-classic boundary conditions commonly encountered in engineering applications, plates, and shells under general boundary conditions have been extensively studied using the artificial spring technique. Different types of orthogonal polynomials and modified Fourier series functions were commonly employed to expand displacement fields, accounting for general boundary conditions. For those expansion functions, Qin et al. [74] developed a unified solution and compared the computational efficiency and convergence

rates of different expansion functions, upon which a series of studies were conducted on rotating plate-shell combinations [75], CNT and graphene reinforced composite shells [76, 77]. Regarding the vibration/acoustics isolation techniques, the most common technique that has been widely investigated is based on the passive sound isolation technique by adding absorption treatments to the main structure such as using shunt piezoelectric, viscoelastic, blocking masses, and porous materials (Fu et al. [78, 79], Pietrzko and Mao [80]).

Numerous studies used poroelastic materials to improve the sound attenuation of cylinders ([81, 82, 83]). Lee et al. [84] utilized a multi-wave characterization of the poroelastic materials in which the strongest wave is considered among the two dilatational and rotational waves in order to study the STL through a doubled panel lined with a poroelastic layer. Magniez et al. [85] used 3D Biot's theory of poroelasticity mixed with classical first-order shear deformation theory to investigate the STL through a composite cylinder with a poroelastic core. Umnova et al. [86] studied STL through a finite periodic array of a rigid cylinder with and without the poroelastic absorber. Ramezani and Saghafi [87] used the Genetic Algorithms (GA) to optimize the STL through a composite double-walled circular cylindrical shell lined with poroelastic materials. Daneshjou et al. [88] used Biot's theory of poroelasticity to investigate the STL through the sandwich cylindrical shell with a poroelastic core excited by an incident plane wave. Talebitooti et al. [82] utilized Non-dominated Sorting Genetic Algorithm (NSGA) along with classical first-order shear deformation theory to optimize sound attenuation through a sandwich circular cylindrical shell lined with a poroelastic material. Talebitooti et al. [89] used 3D Biot's theory of poroelasticity to investigate the effect of compressed poroelastic materials on the

sound attenuation of a sandwich cylindrical shell lined with poroelastic core and air gap insulation for different boundary conditions. The results show that using poroelastic covering improves the overall sound attenuation of periodic arrays of cylinders.

Some scholars used other passive methods such as a shunted piezoelectric system, constrained-layer damping treatment, added mass, and air gap flow for sound mitigation purposes. Ahmadian and Jeric [90] utilized shunted piezoceramic materials to increase the sound attenuation from a plate with and without constrained-layer damping materials. Gardonio et al. [91] used blocking masses to reduce the coupling between the structural vibration modes and the incident plane waves in order to reduce the STL through a honeycomb cylinder filled with air. Liu and He [92] studied the effect of external mean flow on the sound attenuation of a double-walled circular cylindrical shell lined with porous materials. Yu and Chuanbo [93] studied the effect of air gap flow on the STL through a double-walled sandwich cylinder excited by a random incident wave. The study showed that the air gap flow enhances the sound isolation properties of the cylinder near the critical frequency. Oliazadeh et al. [94] used statistical energy analysis to investigate the effect of sound-absorbing materials on the STL of cylindrical shells. Yu and Chuanbo [93] used the reinforcement angles of the orthotropic layers as an optimization parameter to reduce the transmitted sound through the sandwich cylindrical shells. The results show that the optimization technique is effective at low frequencies. Smart composite structures have also been used for the TL enhancement of different engineering structures.

New advancements in the field of intelligent materials, in addition to an important improvement in high-speed electronic computing machines, paved the way for dealing

with airborne sound control problems ([95, 96, 97]). In general, intelligent materials, such as piezoelectric materials along with a suitable control strategy can significantly enhance the vibration suppression of the structure by modification of damping and stiffness in a controlled manner ([98]). The use of piezoelectric materials for vibration suppression proposes a very applicable option due to low energy consumption, easy implementation, and being lightweight ([98]).

Many researchers applied a different technique for active vibration control of STL through cylindrical structures. Jones and Fuller [99] utilized the unstiffened cylindrical model in conjunction with multi-control forces exerted directly on the surface of the cylinder to actively control the STL through cylindrical shells excited by external monopole sources. Later on, he used piezoelectric actuators bonded to the cylinder to study the active control of internal sound in model aircraft fuselage ([100]). Sun et al. [101] used a distributed piezoelectric actuator to actively control the interior sound radiation and vibration of the aircraft fuselage. Wang and Vaicaitis [102] employed Galerkin-like approximation method and patches of the piezoelectric actuator in conjunction with velocity and sound pressure rate feedback control strategy to control the vibration of a simply supported composite cylindrical shell due to random point force inputs. Lin et al. [103] used Flugge's shell theory and a pair of piezoelectric actuators and sensors along with a Linear Quadratic Gaussian (LQG) control strategy to control the vibration of cylindrical panel excited by external forces acting on the surface of the panel. Henry and Clark [104] used velocity and pressure feedback control strategy to control structural-acoustic vibration through a rigid-wall cylindrical enclosure with a curved panel. Li et al. [105] used a numerical approach and GA to optimize the location of piezoelectric patches to control the

structural-acoustic noise of a thin finite circular cylindrical shell with a longitudinal floor partition excited by a mechanical force. They neglected the mass of actuators and sensors. Bernardini et al. [106] used Boundary Element Method (BEM), which is a numerical method for solving linear partial differential equations to reduce the tonal noise of an elastic thin cylindrical shell and longitudinal stringers modeled as a beam with arbitrary cross-section excited by two pulsating monopole sources.

## 2.4 Introduction of Piezoelectricity

### 2.4.1 A Brief History of Piezoelectricity

*“The crystals that have one or more axes with dissimilar ends, i.e., the hemihedral [semi-symmetrical] crystals with oblique faces, possess a particular physical property of giving rise to two electric poles of opposite signs at the extremities of these axes when they undergo a change in temperature: This phenomenon is known as pyroelectricity. We have found a new method for developing polar electricity in these same crystals, which consists of subjecting them to variations in pressure along their hemihedral axes”,(Jacques et Pierre Curie, 1880, p.15, [107]).*

With these words, on 2 August 1880, two brothers, Jacques and Pierre Curie, reported to the French Academy of Sciences about their finding of the direct piezoelectric effect [107]. Two brothers put together their knowledge of crystal structures and pyroelectricity (i.e., the capacity of certain materials to produce temporary voltage when experiencing a change in the temperature) to model the behavior of piezoelectric crystals such as Rochelle salt (sodium potassium tartrate tetrahydrate),

topaz, quartz, tourmaline [108]. According to *Encyclopaedia Britannica*, piezoelectricity is described as “the generation of electric charge in a substance by mechanical stress that changes its shape, and a proportional change in the shape of a substance when voltage is applied” [107, 109]. However, the finding and early observation by Curie brothers explain only the direct effect “the generation of electric charge by mechanical stress” [107]. Nonetheless, the Curies failed to predict the existence of the reverse process. The generation of strain and/or stress by applying the voltage is known as converse piezoelectric effects [107, 110]. While the Curies established their piezoelectric explanation based on the reciprocal effect of pyroelectricity that was explained by Thomson’s hypothesis of inner polarization, yet, they did not notice the likelihood of a piezoelectric converse effect [107]. Undoubtedly, it was difficult and delicate to measure the converse effect experimentally [107]. The converse piezoelectric effect was theoretically predicted by Jonas Ferdinand Gabriel Lippmann in 1881 [107]. He used basic thermodynamic concepts to prove the converse piezoelectric effect mathematically [110]. The Curies soon endorsed Lippmann’s finding [111]. Lippmann’s theoretical approach to piezoelectricity bears no resemblance to the mechanistic method of Jacques and Pierre Curie. However, this dissimilarity didn’t stop the brothers from gaining experimental evidence that electro-elasto-mechanical deformations in piezoelectric crystals are completely reversible [111]. Piezoelectricity stayed something of a laboratory interest for many years later, although it was a crucial element in Pierre and Marie Curie’s 1898 discovery of Radium and Polonium [112]. Additional work has been done to investigate and describe the properties of crystals that show piezoelectricity [113].

The publication of Woldemar Voigt’s *Lehrbuch der Kristallphysik* in 1910 delin-



eated twenty different natural crystal groups, having the ability to show piezoelectric properties and the piezoelectric constants were rigorously established using tensor analysis [114]. Perhaps, the early practical application of piezoelectric material date back to world war I when French physicist Paul Langevin and his assistant employed SONAR technique (i.e., Sound Navigation RAnging known as SONAR is a method that uses sound propagation underwater to interact, navigate with or trace an object such as submarine) to track down marine vessels [115]. The device was a transducer consisted of two steel plates covering a thin quartz crystal and a hydrophone to receive the reflected sound waves. By sending a high-frequency acoustic pulse from the piezoelectric device, one can measure the distance to the object by calculating the time needed to detect the reflected acoustic waves that are scattered from the surface of the object [115]. It wasn't until after world war I that the design of the detector was completed. A major breakthrough in piezoelectric research happened during World War II when many different countries such as USA, Russia, and Japan conducted research which led to the discovery of a new class of synthetic materials known as ferroelectrics (i.e., a feature of unique nonconducting crystals that exhibit natural electric polarization that can be reversed when exposed to the external electrical field) [116, 117, 118]. This class of materials has piezoelectric coupling constants several times greater than natural materials [116, 117, 118]. These intensive researches paved the way for the discovery of barium titanate ( $\text{BaTiO}_3$ ) and PZT during and after World War II [119]. Barium titanate ( $\text{BaTiO}_3$ ) is a ferroelectric ceramic material that was separately developed by different research groups from Russian, USA, and Japan simultaneously whereas, PZT discovered by scientists at Tokyo Institute of Technology in 1952 [119]. PZT exhibits a greater piezoelectric

coefficient of almost 250 PC/N and can resist harsh environment, which makes it an ideal candidate for many industrial applications [119]. Over the next few decades, new advanced piezoelectric materials with different applications were developed and explored [120]. Piezoelectric devices are an indispensable part of our daily life. Nowadays, piezoelectric materials are used in many home appliances such as washing machines, cigarette lighters, printers, guitars, etc [121, 122, 123, 124]. However, future researches need to be done to develop new piezoelectric technologies.

## 2.4.2 Basic Principles of Piezoelectricity

### 2.4.3 Anisotropic Piezoelectric Cylinder and Its Applications

The exceptional electro-mechanical coupling properties of piezoelectric materials plays a preeminent role in the advancement of various electro-mechanical equipment (Shodja and Ghazisaeidi [125], Arnau et al. [126], Jalili [127], Park and Shrout [128], Brown [129], Anderson and Hagood [130], DeReggi et al. [131]). These applications can be classified as

- *Nondestructive testing*, which utilizes piezoelectric transducers in intelligent monitoring of infrastructure such as pressure vessels, natural gas pipelines, railways, roads and bridges (Giurgiutiu and Cuc [132], Krautkrämer and Krautkrämer [133], Rose [134], Bickerstaff et al. [135], Chapagain et al. [136], Boucher [137], Kobayashi and Jen [138, 138]). Also, oxyborate piezoelectric crystals are used in condition monitoring in high temperatures such as turbines and furnaces (Yu et al. [139, 140], Zhang et al. [141, 142], Yu et al. [143]);

- *Underwater acoustics*, which applies piezoelectric hydrophone in modern towed SONAR array for underwater surveillance (Brown et al. [144]);
- *Diagnostic ultrasound*, which uses a small piezoelectric transducer placed within the cylinder frequently used for the *in-vivo* ultrasound tomography for early detection of malignant lesions such as in breast and prostate tissues (Opieliński et al. [145], Opielinski et al. [146], Yang et al. [147]). Furthermore, cylindrical piezoelectric balloons under internal pressure have been utilized in the *in-vivo treatment* of distal flow and angina and myocardial hypoperfusion issues (Vidal Denham and Rice [148]);
- *Sensors and actuators*, which use piezoelectrics for active vibration and noise control of smart structures (Tzou and Gadre [149], Riley et al. [150], Zhuk and Guz [151], Zhao et al. [152], Kirichok [153], Kozlov and Karnaukhova [154], Hasheminejad and Keshavarzpour [9], Hasheminejad and Alaei-Varnosfaderani [95, 12], Hasheminejad et al. [155], Shur et al. [156], Yang et al. [157]). Furthermore, they have been extensively utilized to increase the bending stiffness of structures in order to resist high buckling loads beyond what it can normally tolerate (Thompson and Loughlan [158]).

#### 2.4.4 A Review on The Dynamic Study of Anisotropic Piezoelectric Cylinder

Among all different shapes of engineering structures, the hollow cylindrical shape has attracted much attention and been recommended where acoustic directivity, simplicity, and size constraints are the primary design concerns (Rabbani et al.

[3]). Thus, numerous studies have been carried out on the dynamic behavior of piezoelectric cylinder (Hasheminejad and Keshavarzpour [9], Hasheminejad and Alaei-Varnosfaderani [12, 95], Hasheminejad et al. [159], Chen et al. [160], Hasheminejad and Rajabi [161], Hasheminejad et al. [155], Tzou [162], Ding et al. [163]). Piezoelectric cylinders are applied not only to structural engineering but also to biomechanics. Experimental studies on the human body have proved that the bone structure has mechanical anisotropy and piezoelectric properties (Jayasuriya et al. [164]).

Numerous studies on the free vibration analysis of a piezoelectric cylindrical shell with some degrees of anisotropy have been done by using fully numerical methods such as FEM as well as analytical approaches. The current review, however, is focused merely on the analytical and semi-analytical approaches. The analytical solutions are based on two different methods in describing the elastic deformation of a shell: one is based on the thin shell theories, whereas the other uses the exact theory of linear elasticity. A brief review of the most related studies on the application of the thin shell theory to study the free vibration of piezoelectric structures is given next.

Numerous investigations on the free vibration of different piezoelectric structures have been conducted by utilizing different thin shell theories (Bisheh and Wu [41]). Haskins and Walsh [165] used the traditional shell theory to investigate the free vibration of the transversely isotropic hollow piezoelectric cylindrical shell. Their numerical results obtained for the radially polarized piezoelectric cylindrical shell displayed a good agreement with experimental data in the case of a very small thickness. Drumheller and Kalnins [166] employed shell theories to develop

an analytical solution for free vibration of piezoelectric cylindrical shells. Their proposed model can also satisfy both mechanical and electrical governing equations within the border of shell theories. Babaev et al. [167] utilized thin shell theory to investigate the dynamic response of a radially polarized cylindrical piezoelectric shell filled and submerged with the acoustic fluid, excited by electrical signals. Babaev and Savin [168] used Kirchhoff-Love theory to study the transient vibroacoustic response of two infinitely long coaxial piezoelectric cylinders excited by a time-dependent electrical signal. Tzou and Zhong [169] proposed a generic linear shell theory to investigate the dynamic response of thin or moderately thick piezoelectric cylinders. The suggested piezoelectric shell theory is so general that it can be employed for other engineering structures, such as the sphere, plate, panel, etc. Sheng and Wang [170] used Hamilton's principle and Maxwell's equation along with the first-order shear deformation theory to study the thermo-elastic vibration of the moderately thick functionally graded piezoelectric shell under thermal loading and electrical voltage. Studies based on the exact theory of linear elasticity are reviewed next.

Earlier research by the exact theory of linear piezoelectricity has attracted more attention due to its capability for obtaining accurate results while the thickness of the cylinder can vary from thin to extremely thick along the radius. Kapuria et al. [171] presented an analytical approach to calculate the harmonic response of a simply supported orthotropic piezoelectric cylinder subjected to non-axisymmetric electromechanical loads. The inverse technique was used to determine the applied pressure to the shell from the electrical voltage measured between the inner and outer radius of the piezoelectric cylinder. Chen and Shen [172] used the power series expansion method to study both direct and inverse piezoelectric effects on the free

vibration of a finite length orthotropic piezoelectric circular cylindrical shell. Chen et al. [160] developed a closed-form solution by using the piezoelectricity, the state space method, and the transfer matrix approach to study the free vibration of an arbitrarily thick functionally graded orthotropic piezoelectric hollow cylinder filled with ideal fluid. Shlyakhin [173] utilized the vector eigenfunction expansion method to find a closed-form solution for the dynamic vibration of a radially polarized orthotropic piezoelectric cylinder. More recently, Wang et al. [174] both theoretically and experimentally investigated the free vibration of a finite quartz cylinder using the Rayleigh-Ritz method and Chebyshev polynomials.

## 2.5 Review on The STL Through Viscous Fluid

The backgrounds and discussion of the STL through a piezo-laminated cylinder with some level of anisotropy submerged in an ideal fluid was discussed section 2.2. Although the inviscid acoustic model is very efficient to study the STL in many cases, there are some cases that the inviscid model may fail to accurately predict the STL. For instance, if the structure is submerged in a fluid with a high level of viscosity, the loss of sound waves is caused by fluid viscosity and heat exchange. In the vicinity of borders, these losses are particularly significant. Such losses become very significant when the dimension of the structure is similar to the boundary layer thickness [14]. Obviously, the inviscid model can not capture such losses, so it becomes necessary to develop a model that can take into account such losses. It should also be mentioned that in some circumstances, wave propagation happening in a narrow gap due to the presence of a fluid's viscosity, which cannot be ignored [15]. A narrow slit or enclosure in a hearing aid, a small transducer, etc. are examples of such a situation

[15]. Actually, many attempts have been made to include viscosity in the wave propagation through the structure in viscous fluids. The boundary value problem affected by the interaction of a plane sound wave with (thermo)elastic solid cylinders and spheres submerged in (thermo)viscous fluid was studied by Lin and Raptis [16] through both analytical and numerical approaches. Later, the same authors presented a general scattering theory for an incident plane sound wave obliquely exciting a thin, elastic circular rod submerged in an unconfined viscous fluid [17]. Hasheminejad and Safari [18] used 3D dimensional theory of elasticity to study the scattering by isotropic spherical and cylindrical shells immersed in and filled with viscous compressible fluids.

## 2.6 Objectives, Contributions, Applications and Discussions

From the literature review given in subsection 2.4.4 and to the best of the author's knowledge, there are numerous studies on the vibration of a cylindrical shell with some degrees of anisotropy where most of them are transversely isotropic (Haskins and Walsh [165]) and orthotropic (Shlyakhin [173], Chen et al. [160], Kapuria et al. [171]). The need for improvement in a piezoelectric element's sensitivity, however, requires the development of materials with stronger anisotropy such as lead Lithium Tantalate, Lithium Niobate, and Oxyborate crystals of  $YCa_4O(BO_3)_3$  (YCOB) as indicated in previous studies, for example, Kar-Gupta and Venkatesh [175], Yu et al. [139], Han and Yan [176], Luo et al. [177]. Dynamic and vibration characteristics analysis of these components is obviously an essential element in

their design, no matter whether they are employed as sensors or actuators. The aforementioned comprehensive literature review suggests that a dispersion analysis of a fully anisotropic hollow cylindrical piezoelectric shell is yet to be addressed. Consequently, the specific novelties and highlights of this research are

- monoclinic material with one symmetry plane;
- fully anisotropic or triclinic materials are the most general form of anisotropic materials without any axis of material symmetry;
- using the exact theory of elasticity rather than approximate shell theories for all ranges of thicknesses and frequencies.

The solution of such problems includes complexity because of the system of the coupled partial differential equation along with satisfying the boundary conditions on the internal and external surface of the cylinder. These complexities can increase when the cylinder is made of an anisotropic material.

Besides, for the STL through the cylinder, a survey of the literature given in section 2.2, however, shows that almost no study has been done on the STL from a thick orthotropic hollow piezo-composite cylindrical shell excited by an oblique plane incident wave. Thus, investigating the effects of piezoelectric material properties, piezoelectric polarization direction, shell thickness ratio, electrical boundary conditions, and FGPM on the STL is also an objective of the current study.

This study can expediently help acoustics engineers to use piezoelectric layers to design cylindrical structures with remarkable sound transmission control characteristics. Such smart structures have extensive applications in noise control in the



fuselage (Krakers et al. [5]) and marine applications (Caresta [4]). In addition, by coupling a piezoelectric sensor to the current structure, an Active Damping Control (ACD) strategy can be implemented to increase the sound insulation enhancement for a wide range of frequencies (Hasheminejad et al. [39]). Moreover, the extensive numerical data can help as a dependable benchmark for checking other numerical methods, particularly in the case of a lack of experimental data.

In addition, the preceding review given in section 2.3 showed that the majority of the previous works used numerical approximation methods to control the structural-acoustic vibration of a cylinder, which always suffer from discretization errors. The numerical solutions, given the discretization of the PDEs, can lead to some inaccuracy in high-frequency ranges ([178]). In addition, some scholars used pressure feedback velocity to measure the pressure inside the cylinder, which required installing a pressure sensor inside the cylinder. Installing a pressure sensor inside a cylinder is very costly and conveys complicated implementation. Besides, the majority of works that have been published in this area are focused on the membrane or thin shell theories. As the thickness of the cylinder increases, the results provided by even high order shell theories become inaccurate, especially at higher frequencies ([179]). Furthermore, some scholars used passive control strategies, which are easier to be realized. While the passive control strategy showed less TL efficiency at the resonance frequencies, the new work is aimed at improving the STL at the resonance frequencies ([19]).

Furthermore, the review given in section 2.5 showed although the effects of the fluid viscosity on the STL through thin/thick smart cylindrical structures is often overlooked, some scholars pay attention to the effects of viscosity on the sound

transmission in the cylindrical structures [16, 17, 18], and some comprehensive studies on the piezoelectricity benefiting STL have also been conducted in non-viscous media [19, 20]. However, the compound effects of an-isotropic piezoelectricity and fluid viscosity on the STL while the structure is submerged in the viscous fluid were not considered and well discussed. As introduced before, both piezoelectricity and fluid viscosity have obvious effects on wave behaviors in a cylindrical shell, and the coupled and interacted piezoelectricity and fluid viscosity could bring different understanding/findings on STL that has not been revealed before. Therefore, designing a model that can deal with an-isotropic piezoelectric crystal and also take into account the effects of inevitable fluid viscosity in wave propagation is very important in acoustic quieting or sound utilization applications. Such a model can also help in predicting the dynamics of nano and micro-electromechanical systems as fluid viscosity plays an important role at nano and micro scales.

The purpose of the current work is to tackle the above-mentioned limitations by introducing the active control process of the piezoelectric layers and studying its effect on the enhancement of the STL through a thick cylindrical structure, especially at resonance frequencies. The current work benefits from the 3D theory of elasticity and piezoelectricity to give highly accurate results even in high-frequency ranges. This study takes advantage of the direct piezoelectric effect, which uses the piezoelectric layer as a sensor and can easily be implemented with minimal modification of the original structure compared to other pressure sensors. The current solution also gives more accurate and reliable results compared to other numerical approaches.

In addition, the current model can be used to send multimedia data such as video and pictures to underground tunnels. We know that underground transmission of

radio frequency is not feasible. For digital data transmission, it is possible to utilize an acoustic waveguide that transmits modulated sounds. With our current model, we can find a specific frequency in which the magnitude of sound transmission loss is very low to make sure that the majority of acoustic incident waves are transmitted through the elastic medium. This research can be used to decrease the sound transmission through the air-plane fuselage as aircraft noise exposure leads to an increased risk of hearing-related diseases. Excessive vibration due to sound transmission into the fuselage also can cause failure in electronic chips which can lead to catastrophic air-plane crashes. Lastly, the current model if submerged in water could be used for condition monitoring of the oil and gas pipelines that are located at the bottom of the ocean. By sending a plane wave incident wave and studying the scattered wave from the pipeline, engineers could use ultrasonic imaging to perform a preventative maintenance examination of pipelines. The objective of this inspection is to identify corrosion, cracks, and other defects that may cause catastrophic failure of the structure. The current model also can be used as benchmark to check the validity of numerical solutions.

## Chapter 3

# Fundamental Theories of Elasticity and Acoustics

*"A theory can be proved by  
experiment; but no path leads from  
experiment to the birth of a  
theory.."*

---

Albert Einstein

In this Chapter, the equation governing a linear elastic body can be established by three tensor partial differential equations. These three equations include the Lagrangian description of the equation of motion, infinitesimal strain-displacement, and linear algebraic constitutive relations. Constitutive equations for the elastic body are the equations that relate the secondary field variables such as stress tensor to the primary field variable, such as strain tensor. In addition, the basic principles of acoustic theory for viscous and inviscid fluids are comprehensively explained.

### 3.1 Introduction to The Three Dimensional Theory of Elasticity

In the continuum study of solid mechanics, there are two major theories that study the deformation of the elastic cylinder under applied forces. The first theory is the shell theory, whereas the second one is the theory of elasticity. Here,  $h$  is the thickness of the shell, whereas  $R$  indicates the radius of the shell. Besides, the thickness ratio can be shown by  $(h/R)$ . A 3D body can be referred to as a shell if the thickness/radius ratio of the cylinder is small enough compared to unity [180, 181]. A shell considered to be thin when the thickness ratio is  $h/R \leq 1/20$  [182]. All shell theories under-predict the radial displacement and the classical shell theory of Donnell gives unacceptable results even for a shell with thickness  $h/R=1/20$  [183]. In order for a linear theory to accurately describe the behavior of the shell structure, their vibration amplitude must be smaller than  $1/10$  of their thickness [182]. The shell theories take advantage of this geometric property to reduce a 3D problem to a 2D problem [181]. 3D theory of elasticity is a mathematical model to study the stress and deformation of solid materials due to arbitrary sets of loads and boundary conditions [184]. The advantage of the theory of elasticity over the shell theories is that as the thickness/radius ratio of the cylinder increases, the results provided by the shell theories become highly inaccurate, especially in higher vibration frequencies. In contrast, the 3D theory of elasticity can deal with a full 3D structure with an arbitrary thickness ratio [179]. Besides, there are many different types of shell theories. Based on their type and orders, they can give a finite number of natural frequencies. However, the 3D theory of elasticity gives

infinite numbers of natural frequencies with no loss of accuracy, especially in the high-frequency ranges. For instance, Cooper-Naghdi shell theory provides the first fifth natural frequencies, whereas the 3D theory of elasticity can give infinite natural frequencies. In modeling scattering problem using the shell theories, one cannot distinguish the reflection of waves from the inner and outer surface of the cylinder, and the boundary condition should be applied to the middle surface of the shell, while in the 3D theory of elasticity, the boundary conditions are defined on the real internal and external surface of the cylinder [185]. Usually, in the dynamic equation of thin shell theories, only the first parts of the dispersion curves of some first modes of the 3D theory of elasticity will be properly modeled [185]. It is evident that when the shell theories are used to model a scattering problem, the peripheral modes of the higher-order, which can not be described by these theories, could not be generated [185]. Considering the advantages of the theory of elasticity, this theory is used to study the current problem. The equation governing a linear elastic body using the 3D theory of elasticity can be established by three tensor partial differential equations [184]. These three equations include the Lagrangian description of the equation of motion, infinitesimal strain-displacement, and linear algebraic constitutive relations. Here, we assumed that the deformation in the solid media is very small so that we can neglect the squares of the displacement gradients, and the stresses do not reach the yield point in the material [184]. Such assumptions are reasonable in many real-life engineering problems and are used extensively in engineering design and applications [186]. Even considering these simplifications, seeking an analytical solution assuming the linearized elasticity can not be obtained for complicated geometries [184]. It is very beneficial to mention the equations of

linearized elasticity for use in the later chapters. The strain-displacement relations in the direct tensor form that is independent of the choice of the coordinate system are given here [184]

$$\boldsymbol{\epsilon} = \frac{1}{2}[\nabla \mathbf{u} + (\nabla \mathbf{u})^T + (\nabla \mathbf{u})^T(\nabla \mathbf{u})], \quad (3.1)$$

in which,

$$\boldsymbol{\epsilon} = \begin{bmatrix} \epsilon_{rr} & \epsilon_{r\theta} & \epsilon_{rz} \\ \cdot & \epsilon_{\theta\theta} & \epsilon_{\theta z} \\ \cdot & \cdot & \epsilon_{zz} \end{bmatrix},$$

where,  $\mathbf{u} = [u_r \ u_\theta \ u_z]^T$  and  $\nabla$  is the gradient operator. When the deformation is very small ( $|\nabla \mathbf{u}| \ll 1$ ), the nonlinear term in the Equation 3.1 can be omitted and the linearized form of the infinitesimal strain tensor can be defined as ([187])

$$\boldsymbol{\epsilon} = \frac{1}{2}[\nabla \mathbf{u} + (\nabla \mathbf{u})^T]. \quad (3.2)$$

Lagrangian description of the equation of motion is the second set of equations in the theory of elasticity. It is an expression of Newton's second law under the assumption that the Green's strain and stress tensors as  $\boldsymbol{\gamma}$  and  $\boldsymbol{\sigma}$  are symmetric. The tensor form of Lagrangian description of the equation of motion in the absence of body forces can be given as ([187])

$$\nabla \cdot \boldsymbol{\sigma}^T = \rho \frac{\partial^2 u}{\partial t^2}. \quad (3.3)$$

in which,  $\rho$  is the spatial density of the material.

The third set of tensor equations is the constitutive equations. Constitutive equations are the equations that relate the secondary field variables such as stress

tensor to the primary field variable, such as strain tensor ([187]). Constitutive equations can not be obtained from physical principles because they are associated with the physical properties of a medium ([187]). The constitutive model can be validated against the experimental data ([187]). The general form of the constitutive equation for elastic materials can be written as ([188, 189])

$$\boldsymbol{\sigma} = \mathbf{C} : \boldsymbol{\epsilon}, \quad (3.4)$$

in which,  $\mathbf{C}$  is the elastic stiffness tensor of the material and “:” represents the inner product of two second-order tensors. Matrix  $\mathbf{C}$  can be different for various materials depending on the certain material symmetry. If we apply strain positive energy condition, the fourth-order elastic stiffness tensor,  $\mathbf{C}$ , becomes  $6 * 6$  matrix [188]. Depending on the number of symmetry planes, matrix  $\mathbf{C}$  can be classified into eight fundamental groups. The following symbols are used to indicate the relation between the elements [188].

- \*                      nonzero elements
- \* \_\_\_\_\_ \*            equal elements
- \* \_\_\_\_\_ \*            equal but opposite elements
- indicates  $C_{66} = (C_{11} - C_{12})/2$

- **Isotropic materials** with infinite number planes of symmetry [188]



$$\mathbf{C} = \begin{bmatrix} * & * & * & 0 & 0 & 0 \\ . & * & * & 0 & 0 & 0 \\ . & . & * & 0 & 0 & 0 \\ . & . & . & \bullet & 0 & 0 \\ . & . & . & . & \bullet & 0 \\ . & . & . & . & . & \bullet \end{bmatrix}$$

- **Cubic Materials** have 9 planes of symmetry

$$\mathbf{C} = \begin{bmatrix} * & * & * & 0 & 0 & 0 \\ . & * & * & 0 & 0 & 0 \\ . & . & * & 0 & 0 & 0 \\ . & . & . & * & 0 & 0 \\ . & . & . & . & * & 0 \\ . & . & . & . & . & * \end{bmatrix}$$

- **Transversely Isotropic or Hexagonal Materials**

$$\mathbf{C} = \begin{bmatrix} * & * & * & 0 & 0 & 0 \\ . & * & * & 0 & 0 & 0 \\ . & . & * & 0 & 0 & 0 \\ . & . & . & * & 0 & 0 \\ . & . & . & . & * & 0 \\ . & . & . & . & . & \bullet \end{bmatrix}$$

- **Tetragonal Materials** have 5 planes of symmetry

$$\mathbf{C} = \begin{bmatrix} * & * & * & 0 & 0 & 0 \\ . & * & * & 0 & 0 & 0 \\ . & . & * & 0 & 0 & 0 \\ . & . & . & * & 0 & 0 \\ . & . & . & . & * & 0 \\ . & . & . & . & . & * \end{bmatrix}$$

- **Trigonal Materials** have 3 planes of symmetry

$$\mathbf{C} = \begin{bmatrix} * & * & * & * & 0 & 0 \\ . & * & * & * & 0 & 0 \\ . & . & * & 0 & 0 & 0 \\ . & . & . & * & 0 & 0 \\ . & . & . & . & * & * \\ . & . & . & . & . & \bullet \end{bmatrix}$$

- **Orthotropic Materials** have 3 planes of symmetry

$$\mathbf{C} = \begin{bmatrix} * & * & * & 0 & 0 & 0 \\ . & * & * & 0 & 0 & 0 \\ . & . & * & 0 & 0 & 0 \\ . & . & . & * & 0 & 0 \\ . & . & . & . & * & 0 \\ . & . & . & . & . & * \end{bmatrix}$$

- Monoclinic Materials have one planes of symmetry

$$\mathbf{C} = \begin{bmatrix} * & * & * & 0 & * & 0 \\ . & * & * & 0 & * & 0 \\ . & . & * & 0 & * & 0 \\ . & . & . & * & 0 & * \\ . & . & . & . & * & 0 \\ . & . & . & . & . & * \end{bmatrix}$$

- Triclinic Materials, No symmetry planes

$$\mathbf{C} = \begin{bmatrix} * & * & * & * & * & * \\ . & * & * & * & * & * \\ . & . & * & * & * & * \\ . & . & . & * & * & * \\ . & . & . & . & * & * \\ . & . & . & . & . & * \end{bmatrix}.$$

Here, the study is focused on the most general form of material, which is the triclinic materials with no planes of symmetry. The solution procedure for the coupled partial differential equations over an elastic domain will be given in the next chapter.

### 3.1.1 Limitation of Linear Three Dimensional Theory of Elasticity

The limitation of of linear 3D theory of elasticity is that the deformation in the solid media is very small in comparison with the dimensions of the structure so that

we can neglect the squares of the displacement gradients, and the stresses do not reach the yield point in the material. Do not make a distinction between the second Piola–Kirchhoff stress tensor  $S$  and the Cauchy stress tensor  $\sigma$  and between the current coordinates  $x$  and the material coordinates  $X$  [190]. The current model can be used when the stiffness, strength, ductility, and other properties are not sensitive to the rate of deformation (indirect dependence on time), the loading rate, the strain or stress history, temperature, and heating or cooling rate [190]. We also consider that removing the loading reverts the sample to its original shape and the strain disappears [190]. Elastic behavior is characterized by this characteristic. At some point along the stress-strain curve, the sample does not return to its original state, and some permanent plastic deformation occurs. The current model is not able to predict the behavior of the structure beyond its elastic limit [190]. We also consider that the body is continuous and without any void [191]. The physical quantities in the body, such as stresses, strains, and displacements, can only be translated into continuous functions of coordinates in space under this assumption [191]. As long as the dimensions of the body and the distances between neighboring particles are very large, however, these assumptions will not lead to significant errors [191]. In addition the body is considered to be homogeneous. This implies that elastic constants are independent of the location within the body [191]. As a result, one can analyze the body’s basic structure from an isolated volume, and then apply the results to the entire structure [191].

## 3.2 Inviscid Acoustic Field Equations

The compressible fluid motion in which the pressure does not constrain the flow so that the volume of fluid elements is changeable (i.e., the material derivative of the density is not negligible) can be described by conservation of mass, momentum and energy laws. The mass conservation law for a compressible fluid can be written as (Rienstra and Hirschberg [192])

$$\frac{\partial \rho}{\partial t} + \nabla \cdot (\rho \boldsymbol{\nu}) = 0, \quad (3.5)$$

in which the  $\rho$  is the fluid density, and  $\boldsymbol{\nu}$  is the fluid velocity. The conservation of momentum for a fluid particle can also be written as (Rienstra and Hirschberg [192])

$$\rho \frac{\partial \boldsymbol{\nu}}{\partial t} + \nabla \cdot (\mathbf{P}) + \rho \boldsymbol{\nu} \cdot \nabla \boldsymbol{\nu} = f, \quad (3.6)$$

where  $\mathbf{P}$  and  $f$  are the fluid stress tensor, and the external force density, respectively. For an inviscid fluid the fluid stress tensor can be related to the pressure,  $p$  as (Rienstra and Hirschberg [192])

$$\mathbf{P} = p \mathbf{I},$$

in which  $\mathbf{I}$  is the unit tensor. The energy conservation law for the isentropic fluid when the viscous dissipation and the heat conduction are negligible can be written as

$$\frac{\partial s}{\partial t} + \boldsymbol{\nu} \cdot \nabla s = 0, \quad (3.7)$$

in which  $s$  is the specific entropy. Using the equation of state, the isentropic speed of sound,  $c$  can be obtained as

$$c = \sqrt{\left(\frac{\partial p}{\partial \rho}\right)_s}. \quad (3.8)$$

The density,  $\rho'$ , and velocity,  $\boldsymbol{\nu}'$  fluctuations associated with the wave propagation in the acoustic phenomena, are very small. Using the linearized approximation of Equation 3.5, Equation 3.6 and Equation 3.7, and neglecting the second-order terms in the perturbations the governing equations for a quiescent fluid in the absence of body forces can be written as

$$\frac{\partial \rho'}{\partial t} + \rho_0 \nabla \cdot \boldsymbol{\nu}' = 0, \quad (3.9a)$$

$$\rho_0 \frac{\partial \boldsymbol{\nu}'}{\partial t} + \nabla p' = 0, \quad (3.9b)$$

$$\frac{\partial s'}{\partial t} = 0, \quad (3.9c)$$

in which  $s'$  is the entropy fluctuation. The fluid constitutive Equation 3.8 can also be simplified as

$$p' = c_0^2 \rho'. \quad (3.10)$$

Now by taking the time derivative of Equation 3.9a along with taking the divergence of Equation 3.9b and subtracting the equations, one can (Rienstra and Hirschberg [192])

$$\nabla^2 p' - \frac{\partial^2 \rho'}{\partial t^2} = 0, \quad (3.11)$$

substituting Equation 3.10, into Equation 3.11, the acoustic wave equation governing the small acoustics fluctuations through a compressible, homogeneous, isentropic and frictionless fluid may be written around the equilibrium pressure as

$$\frac{\partial^2 p'}{\partial t^2} - c_0^2 \nabla^2 p' = 0. \quad (3.12)$$

Equation 3.12 will be used in the next chapters to model the external acoustic medium and the internal cavity.

### 3.3 Viscous Acoustic Model

Using the linearized form of the Navier-Stokes equation for a non-heat-conducting viscous compressible fluid, the governing equations for viscous acoustic medium in the absence of body forces can be written as [184, 18]

$$\frac{\partial \rho}{\partial t} + \nabla \cdot (\rho \mathbf{v}) = 0, \quad (3.13a)$$

$$\mu \nabla^2 \mathbf{v} + \left( \frac{1}{3} \mu + \lambda \right) \nabla (\nabla \cdot \mathbf{v}) - \nabla p = \rho \frac{\partial \mathbf{v}}{\partial t}, \quad (3.13b)$$

where  $\rho$ ,  $\mathbf{v}$ ,  $\mu$  and  $\lambda$  represent the mass density of fluid, velocity vector, shear and bulk coefficient of viscosities, respectively. In addition,  $p$  indicates the acoustic pressure of the viscous fluid and  $\nabla^2 = \frac{\partial^2}{\partial r^2} + \frac{1}{r} \frac{\partial}{\partial r} + \frac{1}{r^2} \frac{\partial^2}{\partial \theta^2} + \frac{\partial^2}{\partial z^2}$ . For a barotropic fluid, the equation of the state is independent of the temperature. Thus, the fluid pressure is only a function of the fluid density. Consequently, the equation of state for a barotropic fluid can be written as ([184])

$$p = c^2 \rho, \quad (3.14)$$

in which  $c$  is the speed of sound. By combining Equation 3.13 and Equation 3.14, a single equation in terms of fluid velocity can be obtained as ([18])

$$\frac{\mu}{\rho} \nabla^2 \frac{\partial \mathbf{v}}{\partial t} + \frac{1}{\rho} \left( \frac{1}{3} \mu + \lambda \right) \nabla \left( \nabla \cdot \frac{\partial \mathbf{v}}{\partial t} \right) + c^2 \nabla (\nabla \cdot \mathbf{v}) - \frac{\partial^2 \mathbf{v}}{\partial t^2} = 0. \quad (3.15)$$

Using the Helmholtz decomposition, the velocity field can be decomposed into the longitudinal (irrotational) and transverse (solenoidal) vector components as ([193])

$$\mathbf{v} = -\nabla\phi + \nabla \times \boldsymbol{\psi}, \quad (3.16)$$

where  $\phi$  is a scalar function and  $\boldsymbol{\psi} = \psi_r \hat{\mathbf{e}}_r + \psi_\theta \hat{\mathbf{e}}_\theta + \psi_z \hat{\mathbf{e}}_z$  in which  $\hat{\mathbf{e}}_r$ ,  $\hat{\mathbf{e}}_\theta$  and  $\hat{\mathbf{e}}_z$  are the orthogonal unit vectors in the radial, tangential, and axial directions, respectively. By applying the gradient and curl operators to the scalar function  $\phi$  and vector  $\boldsymbol{\psi}$ , the radial, axial, and tangential velocity components can be given in terms of potential functions in the viscous acoustic medium as [16]

$$v_r = -\frac{\partial\phi}{\partial r} + \frac{1}{r} \frac{\partial\psi_z}{\partial\theta} - \frac{\partial\psi_\theta}{\partial z}, \quad (3.17a)$$

$$v_\theta = -\frac{1}{r} \frac{\partial\phi}{\partial\theta} + \frac{\partial\psi_r}{\partial z} - \frac{\partial\psi_z}{\partial r}, \quad (3.17b)$$

$$v_z = -\frac{\partial\phi}{\partial z} + \frac{\partial(r\psi_\theta)}{r\partial r} - \frac{\partial\psi_r}{r\partial\theta}. \quad (3.17c)$$

Substituting Equation 3.16 into Equation 3.15, making use of solenoidal vector field ( $\nabla \cdot \boldsymbol{\psi} = 0$ ), the fully uncoupled wave equations in a viscous fluid can be deduced as ([194])

$$\frac{\partial^2\phi}{\partial t^2} = \left[ c^2 + \frac{1}{\rho} \left( \frac{4}{3}\mu + \lambda \right) \frac{\partial}{\partial t} \right] \nabla^2\phi, \quad (3.18a)$$

$$\frac{\partial\psi_i}{\partial t} = \frac{\mu}{\rho} \nabla^2\psi_i; \quad i = r, \theta, z. \quad (3.18b)$$

Since the acoustic incident wave is considered to have a single wavelength and frequency (monochromatic wave), the solution of Equation 3.18 can be expressed in



the form of [18]

$$\phi(r, \theta, z, t) = \mathbb{R} [\phi(r, \theta, z, \omega)e^{-\mathfrak{i}\omega t}] , \quad (3.19a)$$

$$\psi(r, \theta, z, t) = \mathbb{R} [\psi(r, \theta, z, \omega)e^{-\mathfrak{i}\omega t}] , \quad (3.19b)$$

where  $\mathbb{R}[\mathbb{Z}]$  gives the real part of the complex number  $\mathbb{Z}$  and  $\mathfrak{i} = \sqrt{-1}$ . Substituting Equation 3.19 into Equation 3.18, by making use of harmonic functions, after some algebraic manipulations, the wave equations can be simplified as follows [18]

$$\nabla^2 \phi + \kappa_c^2 \phi = 0, \quad (3.20a)$$

$$\nabla^2 \psi + \kappa_s^2 \psi = 0, \quad (3.20b)$$

in which  $\kappa_s$  and  $\kappa_c$  are the complex shear and compressional wave numbers, respectively, known as [195]

$$\kappa_s = (1 + \mathfrak{i}) \sqrt{\frac{\omega \rho}{2\mu}}, \quad (3.21a)$$

$$\kappa_c = \left( \frac{\omega}{c} + \mathfrak{i} \frac{\omega^2}{2\rho c^3} \left( \frac{4}{3}\mu + \lambda \right) \right). \quad (3.21b)$$

Here, the basic equations governing a linear elastic are discussed and explained. These basic equations will be used in chapters 4, 6 and 7 to model the elastic layer of the cylinder. However, in order to be able to model the piezoelectric layer, the constitutive equations and the equilibrium of electrical charge should be added to the constitutive laws of elastic body. The description of constitutive equation for the piezoelectric layer will be explained in section 4.1.1 and the modified constitutive law for the piezoelectric layer will be explained in section 4.1.1. Please note that the kinematic assumption for both the elastic layer and piezoelectric layer will be

the same. After modeling the piezoelectric layer by the 3D theory of elasticity, this model will be used in chapter 4, 5, 6 and 7 to model the actuator and sensor layers.

## Chapter 4

# Three-Dimensional Free Vibration Analysis of Triclinic Piezoelectric Hollow Cylinder

*“If you want to find the secrets of  
the universe, think in terms of  
energy, frequency, and vibration.”*

---

Nikola Tesla

Piezoelectric materials are anisotropic materials, which means they do not have the same properties in all directions. As discussed in the section 3.1 majority of the shell and even the 3D theory of elasticity model used isotropic or transversely isotropic piezoelectric materials to study the vibration of piezoelectric cylinders (Haskins and Walsh [165]). While using those models can make the problem solution easier, it may cause inaccuracy in the results especially in piezoelectric materials with stronger anisotropy such as lead Lithium Tantalate, Lithium Niobate, and Oxyborate crystals of  $YCa_4O(BO_3)_3$  (YCOB). Thus, studying these materials needs

to adopt a new model that can handle such a level of anisotropy. The main aim of this chapter is to adopt a mathematical model that is capable of handling the most general form of anisotropic piezoelectric materials, which are known as triclinic materials with 21 independent elastic parameters. The 3D theory of piezoelectricity is used to model the triclinic piezoelectric materials. Unlike the shell theory of piezoelectricity, the piezoelectricity theory can handle 3D structures with no loss in accuracy of final results in higher frequency ranges. Its results also can be very accurate as the thickness to radius ratio of the cylinder increases.

Thus, the main aim of this chapter is to develop an analytical model to study, discuss, and explain the free vibration of a triclinic infinite cylinder in order to fill the gap in the current literature. The suggested solution is very fundamental, in view of the classical structural problem. The proposed method can also offer an analytical foundation for exploiting the potential ability of triclinic piezoelectric material in intelligent cylindrical structures. It can also be used as a benchmark for comparison to other results achieved by numerical or semi-analytical methods. The specific organization of this chapter is outlined as follows. The mathematical modeling section is developed based on the theory of linear piezoelectricity. This includes the constitutive relations of the exact 3D elastic medium, kinematic assumptions, conservation laws, traction boundaries, and solution assembly. Next, the traction boundary conditions and final solution are obtained. Then the validity of the proposed model was checked against other literature's results. Next, the effect of anisotropy on the wave dispersion curves of the piezoelectric cylinder is discussed in the case studies section. Finally, the concluding remarks are listed.

## 4.1 Mathematical Modelling

A detailed description of the problem is given first. It is important to note that the current approach is applicable to any fully anisotropic material and different piezoelectric polarization cases (i.e., radially, axially, and circumstantially polarized).

### 4.1.1 Problem Description of Triclinic Piezoelectric Hollow Cylinder

In this chapter, we develop an analytical model to study the free vibration of a triclinic infinite piezoelectric cylinder. An infinitely long piezoelectric cylindrical shell is modeled by a fully triclinic anisotropic assumption. The cylindrical shell is made of a triclinic piezoelectric material with an internal and external radius of  $a$  and  $b$ , respectively, as shown in Figure 8.1. Constitutive relations are given next.

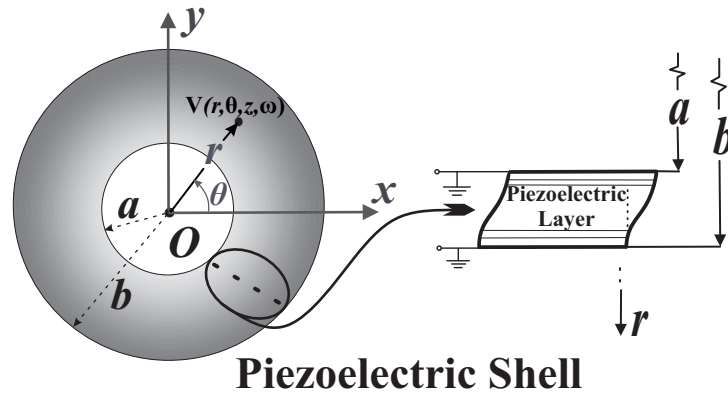


Figure 4.1: Schematic of thick an-isotropic smart piezoelectric cylinder .

## Constitutive Relations

The general, linear, anisotropic constitutive relations for piezoelectricity can be written as (Chopra and Sirohi [196])

$$\sigma_{ij} = \mathbb{C}_{ijkl}\epsilon_{kl} - e_{ijk}E_k, \quad D_i = e_{ikl}\epsilon_{kl} + \kappa_{ij}E_j, \quad (4.1)$$

where,  $e_{ijk}$ ,  $\sigma_{ij}$ , and  $\epsilon_{kl}$ , are the third-order piezoelectric tensors, second-order Green-Cauchy stress, and strain tensor, which have 18, 6, and 6 independent parameters, respectively.  $\mathbb{C}_{ijkl}$  and  $\kappa_{ij}$  are the fourth-order elasticity and second-order dielectric permittivity tensors measured under the conditions of zero electric and strain fields, which have up to 21 and 6 independent parameters, respectively. Thus a comprehensive description of a triclinic piezoelectric material involves the recognition of all 45 independent constants. The expanded matrix form of Equation 4.1 is given in section A.1. Furthermore,  $E_i$ , and  $D_i$  represent the electrical field and the electrical displacement vectors, respectively. The electrical field,  $E_i$ , can be defined by using an electrical potential,  $\phi$ , such that

$$E_i = -\phi_{,i}, \quad (4.2)$$

where,  $_{,i} \equiv \vec{\nabla}$  is the forward gradient operator in cylindrical coordinates, which is given in section A.2. The kinematic assumptions will be discussed next.

## Kinematic Assumptions

The  $\epsilon_{ij}$  is the Lagrangian finite strain tensor in which its linearized form for infinitesimal deformations,  $u_i$ , turns into

$$\epsilon_{ij} = \frac{1}{2}(u_{i,j} + u_{j,i}), \quad (4.3)$$

where  $u_i$  indicates an infinitesimal deformation. Moreover,  $_{,i} \equiv \vec{\nabla}$ , and  $_{,j} \equiv \overleftarrow{\nabla}$  are forward and backward Nabla operators. The expanded matrix form of Equation 4.3 is given in section A.3. The Conservation Laws will be discussed next.

## Conservation Laws

Conservation of linear momentum for a differential element can be expressed as

$$\sigma_{ij,j} + f_i - \rho \ddot{u}_i = 0, \quad (4.4)$$

where,  $f_i$ ,  $\rho$ , and  $\ddot{u}_i$  are a body force, unperturbed material density, and the Lagrangian particle acceleration, respectively. The first term, the divergence of the stress tensor, is determined by the inner product of the second-order stress tensor with the cylindrical gradient operator, which is given in section A.2. The expanded form of Equation 4.4 can be found in Equation A.4.1.

The electrostatic charge equilibrium of a piezoelectric material can be expressed as

$$D_{i,i} = Q_f, \quad (4.5)$$

where,  $Q_f$  is the free charge density. Hence the equilibrium conditions for a piezoelectric material are satisfied by the implementation of both Equation 4.4 and Equation 4.5. The expanded form of Equation 4.5 is given in Equation A.4.2. The traction boundaries are given next.

## Traction Boundaries

The mechanical boundary conditions require the continuity of traction forces,  $t_i$ , and displacement  $u_i$  vectors. The traction force can be defined as

$$t_i = \sigma_{ij} n_j, \quad (4.6)$$

where,  $t_i$  and  $n_i$  are the Cauchy stress vector at a traction surface and unit-length direction vector, respectively. The mixed mechanical and electrical boundary conditions, under the assumption of perfect bonding, require the continuities of displacement  $u_i$ , traction force  $t_i$ , electric potential,  $\phi_i$ , and the electrical displacement  $D_i$ . As the center of the cylindrical coordinate is located at the center-line of the shell,  $e_n \equiv e_r$ , hence,

$$t = \sigma_{rr}e_r + \sigma_{r\theta}e_\theta + \sigma_{rz}e_z, \quad (4.7)$$

where  $e_n$  is the unit base vector. The solution assembly will be discussed next.

#### 4.1.2 State Space Method

The field's variables can be expanded in terms of trigonometric functions in the circumferential  $\theta$  and axial  $z$  directions in a cylindrical coordinate, such that

$$\mathbf{V} = \sum_{n=-\infty}^{\infty} \mathbf{V}_n e^{i(\zeta z + n\theta - \omega t)}, \quad (4.8)$$

in which  $n$ ,  $e$ ,  $\zeta$ , and  $\omega$  are the circumferential wave number, the exponential function, the axial wave number, and the circular frequency, respectively. Furthermore  $\mathbf{V} \equiv \mathbf{V}(r, \theta, z, \omega)$  is spatial *state vectors* and  $\sqrt{-1} = -1$ . The modal components of the aforementioned state vector,  $\mathbf{V}_n(r, \omega)$ , are

$$\mathbf{V}_n(r, \omega) = \left\{ \begin{array}{c} u_r^n(r, \omega) \\ u_\theta^n(r, \omega) \\ u_z^n(r, \omega) \\ \sigma_{rr}^n(r, \omega) \\ \sigma_{r\theta}^n(r, \omega) \\ \sigma_{rz}^n(r, \omega) \\ D_r^n(r, \omega) \\ \phi_n(r, \omega) \end{array} \right\}. \quad (4.9)$$



After performing a tedious task of substituting modal expansions given in Equation 4.9 into Equation 4.1, Equation 4.2, Equation 4.3 and Equation 4.4 along with the application of orthogonality properties of trigonometric functions in the absence of a body force,  $f_i$ , and electrical charge density,  $Q_f$ , a *modal state space* of the system emerges can be written as

$$\frac{d\mathbf{V}_n(r, \omega)}{dr} = \mathbf{\Xi}_n(r, \omega)\mathbf{V}_n(r, \omega), \quad n = -\infty, \dots, -1, 0, 1, \dots, +\infty, \quad (4.10)$$

where  $\mathbf{\Xi}_n(r, \omega)$  is a  $8 \times 8$  modal coefficient matrix whose elements are given in section A.5.

A general analytical solution of Equation 4.10 is not straightforward when  $\mathbf{\Xi}$  is position-dependent. Consequently, an approximate laminated model is adopted as Ding and Chen [197]. Subsequently, the piezoelectric thickness is assumed to be composed of  $n_{pz}$  perfectly bonded sub-layers with equal thicknesses of  $\hat{h} = (b-a)/n_{pz}$ . The elements of matrix  $\mathbf{\Xi}_n(r, \omega)$  is assumed to be constant and equal to the values at the mid-surfaces  $\bar{r}_k = (r_k + r_{k-1})/2$  because of very small thickness of each sub-layer,  $\hat{h} \ll 1$ . Accordingly, each layer's solution to Equation 6.1b is

$$\mathbf{V}_n(r, \omega) = e^{((r-r_{k-1})\mathbf{\Xi}_n(\bar{r}_k, \omega))}\mathbf{V}_n(r_{k-1}, \omega), \quad r_{k-1} \leq r \leq r_k, \quad (4.11)$$

$$r_{k-1} = a + (k-1)\hat{h}, \quad r_k = a + k\hat{h}, \quad k = 1, 2, \dots, n_{pz}.$$

Evaluating the latter equations for the  $k^{th}$  layer leads to

$$\mathbf{V}_n(r_k, \omega) = e^{(\mathbf{\Xi}_n(\bar{r}_k, \omega)\hat{h})}\mathbf{V}_n(r_{k-1}, \omega). \quad (4.12)$$

The global transfer matrix is obtained, next, by enforcing the continuity of  $\mathbf{V}_n$  between all interfaces. Then the modal components of the state variables,  $\mathbf{V}_n$ , at the outer and inner radii are related through the global transfer matrices,  $\mathbf{\Theta}_n$ , such that

$$\mathbf{V}_n(b, \omega) = \mathbf{\Theta}_n(\omega) \mathbf{V}_n(a, \omega), \quad (4.13)$$

$$\mathbf{\Theta}_n(\omega) = \prod_{k=1}^{n_{pz}} \mathbf{e}^{(\mathbf{\Xi}_n(\bar{r}_k, \omega) \hat{h})}, \quad (4.14)$$

for the piezoelectric layer where  $\mathbf{\Theta}_n(\omega)$  is  $8 \times 8$  ultimate transfer matrix, respectively. The traction boundary conditions and the final solution will be discussed next.

## 4.2 Traction Boundary Conditions and Final Solution

The tangential and normal stresses at the internal and external surfaces of the piezoelectric cylinder can be easily expressed as Chen and Ding [198]:

$$t_n \equiv \begin{Bmatrix} \sigma_{rr}^n(r, \omega) \\ \sigma_{r\theta}^n(r, \omega) \\ \sigma_{rz}^n(r, \omega) \end{Bmatrix} = \begin{Bmatrix} 0 \\ 0 \\ 0 \end{Bmatrix}, \quad r = a, b. \quad (4.15)$$

The short-circuit electrical boundary condition at the inner and outer surfaces of the piezoelectric cylinder can be written as

$$\phi_n(r, \omega)|_{r=a} = \phi_n(r, \omega)|_{r=b} = 0. \quad (4.16)$$

Next, by substitution of boundary conditions (Equation 4.15 and Equation 4.16) into the global transfer function (Equation 4.13), it is obtained,

$$\begin{Bmatrix} u_r(b, \omega) \\ u_\theta(b, \omega) \\ u_z(b, \omega) \\ 0 \\ 0 \\ 0 \\ D_r(b, \omega) \\ 0 \end{Bmatrix} = \mathbf{\Theta}_n(\omega) \begin{Bmatrix} u_r(a, \omega) \\ u_\theta(a, \omega) \\ u_z(a, \omega) \\ 0 \\ 0 \\ 0 \\ D_r(a, \omega) \\ 0 \end{Bmatrix}. \quad (4.17)$$

By rearranging the system of Equation 4.17, the homogeneous linear system of algebraic equations can be written as

$$\mathbf{A}\mathbf{x} = \mathbf{0}_{8 \times 1}, \quad (4.18)$$

where,  $\mathbf{0}_{8 \times 1}$  is a zero vector. The expanded form of Equation 4.18 can be found in section A.6. By solving the eigenvalue problem of Equation 4.18, a non-trivial frequency-domain equation of triclinic piezoelectric cylinder is obtained as

$$|\mathbf{A}| = 0, \quad (4.19)$$

in which  $|\mathbf{A}|$  is the determinant of matrix  $\mathbf{A}$ .

	$C_{ij}$	<i>PZT4</i>	<i>LiBnO<sub>3</sub></i>	<i>LiTaO<sub>3</sub></i>	<i>YCa<sub>4</sub>O(BO<sub>3</sub>)<sub>3</sub></i>	<i>Triclinic</i>
$C_{ij}$ ( $10^{11} N/m^2$ )	$C_{11}$	1.39	2.45	2.33	1.551	2.385
	$C_{12}$	0.78	0.75	0.80	0.142	0.768
	$C_{13}$	0.74	0.75	0.47	0.422	0.633
	$C_{14}$	0	0	0.11	0	0.06
	$C_{15}$	0	0	0	0	0.028
	$C_{16}$	0	0	0	0	0.005
	$C_{22}$	1.39	2.03	2.75	1.451	2.412
	$C_{23}$	0.74	0.53	0.80	-0.051	0.637
	$C_{24}$	0	0	0	0	-0.027
	$C_{25}$	0	0.09	0	-3.5	-0.010
	$C_{26}$	0	0	0	0	-0.002
	$C_{33}$	1.15	2.03	2.330	1.244	2.177
	$C_{34}$	0	0	-0.11	0	-0.027
	$C_{35}$	0	0.09	0	0.016	-0.019
	$C_{36}$	0	0	0	0	-0.003
	$C_{44}$	0.256	0.75	0.94	0.29	0.860
	$C_{45}$	0	0	0	0	0.057
	$C_{46}$	0	0.09	0	0.007	0.055
	$C_{55}$	0.256	0.6	0.93	0.478	0.843
	$C_{56}$	0	0	0.11	0	0.053
	$C_{66}$	0.305	0.6	0.94	61.4	0.764
$e_{ij}$ ( $C/m^2$ )	$e_{11}$	0	1.3	0	0.14	-0.614
	$e_{12}$	0	0.2	0	0	0.117
	$e_{13}$	0	0.2	0	-0.47	0.122
	$e_{14}$	0	0	0	0	-0.053
	$e_{15}$	12.7	0	-1.6	-0.07	-0.727
	$e_{16}$	0	0	-2.6	-2.6	-1.252
	$e_{21}$	0	0	0	0	-0.1
	$e_{22}$	0	0	-1.9	-1.9	-0.906
	$e_{23}$	0	0	0	0	0.044
	$e_{24}$	12.7	-2.5	0	0.13	-1.433
	$e_{25}$	0	0	0	0	-0.094
	$e_{26}$	0	3.7	0	0.49	1.908
	$e_{31}$	-5.2	0	-1.6	-0.11	-0.811
	$e_{32}$	-5.2	-2.5	0	-0.36	-1.202
	$e_{33}$	15.1	2.5	1.6	0.15	2.043
	$e_{34}$	0	0	-2.6	-2.6	-1.274
	$e_{35}$	0	3.7	0	-0.23	2.046
	$e_{36}$	0	0	0	0	0.045
$\epsilon_{ij}$ ( $10^{-11} F/m$ )	$\kappa_{11}$	650	25.7	36.3	8.540	31.753
	$\kappa_{12}$	0	0	0	0	-0.089
	$\kappa_{13}$	0	0	0	0.840	1.780
	$\kappa_{22}$	650	38.9	38.1	10.443	-2.123
	$\kappa_{23}$	0	0	0	0	-2.123
	$\kappa_{33}$	560	38.9	36.3	8.451	43.846
$\rho$ ( $kg/m^3$ )	$\rho$	7500	4700	7450	3310	6075

Table 4.1: Mechanical and electrical properties of the constituent materials.

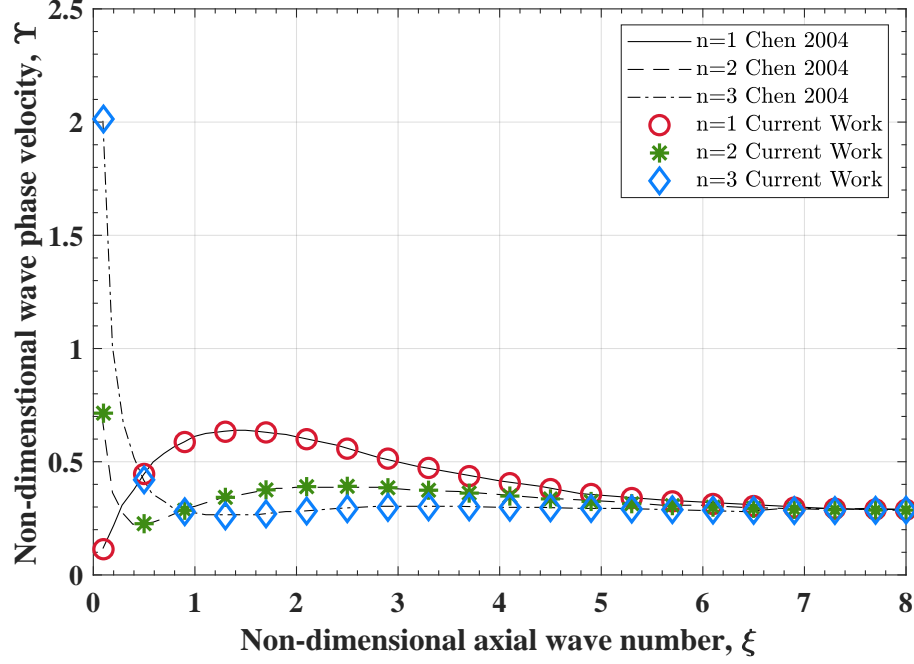


Figure 4.2: Non-dimensional wave phase velocity  $\Upsilon$  versus the non-dimensional axial wave number  $\xi$  for  $(b-a)/a=0.05$ .

### 4.3 Validations

Due to the wide range of different configurations and parameters offered in the problem formulation, while keeping in mind the computational cost and restrictions, we should focus on some logically selected model configurations. In order to show that the proposed model can handle very thick geometries, the inner and outer radius of the piezo-composite cylinder are considered as  $a = 1 \text{ m}$  and  $b = 1.5 \text{ m}$ .

A general MATLAB<sup>®</sup> parallel code was established in order to determine the final global transfer matrix  $\Theta_n$  as well as attaining matrix determinant (Equation 4.19). The calculation was performed on the cluster of Intel<sup>®</sup> Xeon<sup>®</sup> Processor E5-2630 v4 desktop computer (15M Cache, 2.30 GHz, 7.20 GT/s), which benefits from parallel core technology for multi-threaded applications. By utilizing Matlab Parallel

Computing Toolbox, we optimized our code to be able to exploit the full processing power of multicore desktops by executing applications on 40 workers (MATLAB computational engines) that run locally.

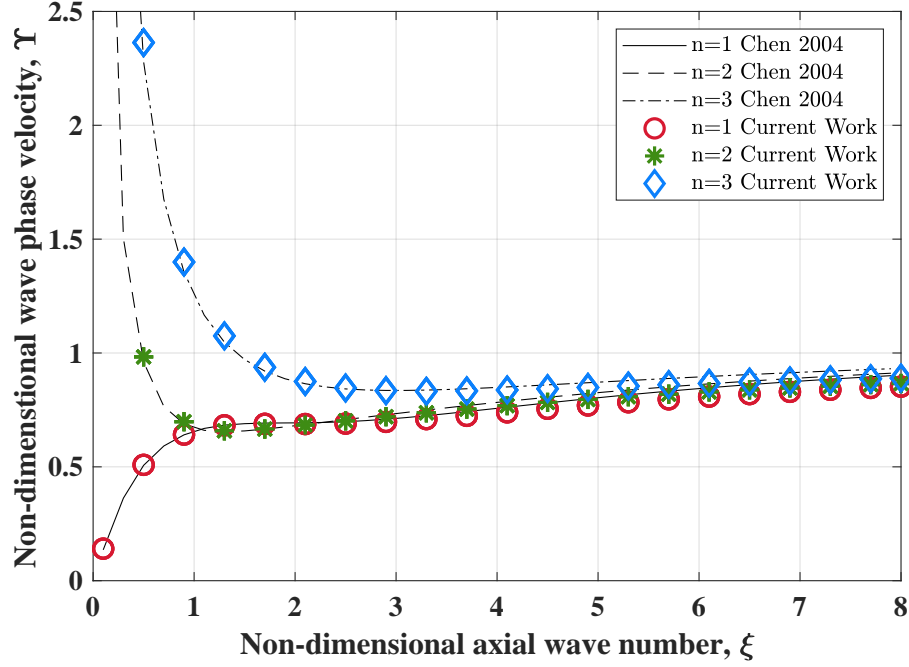


Figure 4.3: Non-dimensional wave phase velocity  $\Upsilon$  versus the non-dimensional axial wave number  $\xi$  for  $(b-a)/a=0.5$ .

Before addressing the main result, the overall accuracy of the proposed solution shall be studied. First, the cylinder is assumed to be fabricated from non-graded PZT4. The material properties of PZT4 were provided in Table 4.1. In order to satisfy the convergence of the final global transfer matrix of the cylindrical piezoelectric cylinder, we used thirty ( $n_{pz} = 30$ ) sub-layers to calculate the final global transfer matrix. The lowest non-dimensional natural frequency,  $\Psi = \omega a \sqrt{\frac{\rho}{C_{44}}}$ , was determined. Then, the non-dimensional wave phase velocity  $\Upsilon = \frac{\Psi}{\xi}$  versus the non-dimensional axial wave number  $\xi = \frac{\zeta}{a}$  were depicted in Figure 4.2 and Figure 4.3

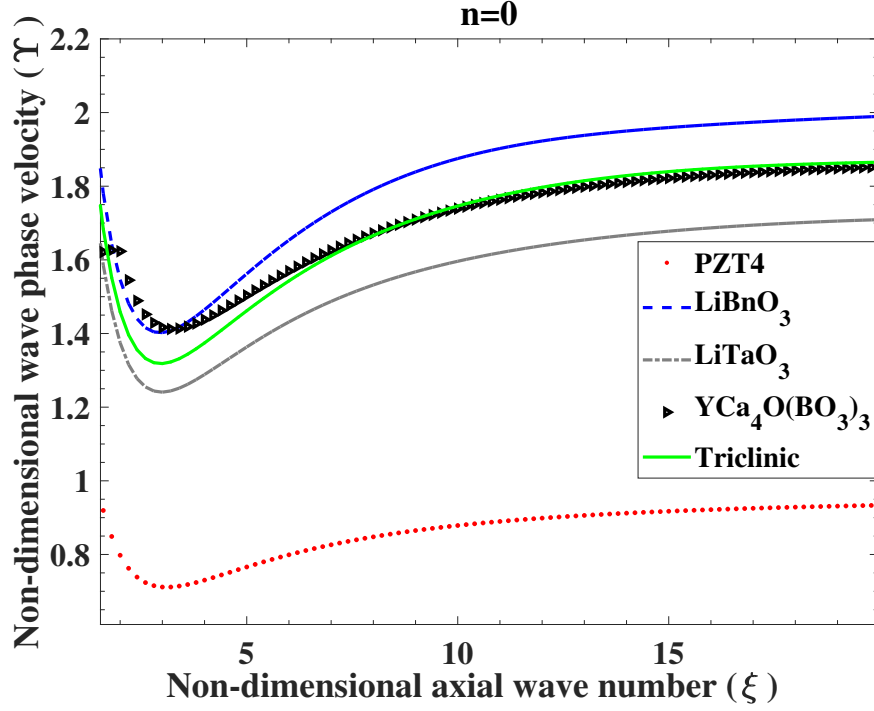


Figure 4.4: Non-dimensional wave phase velocity,  $\Upsilon$ , versus the non-dimensional axial wave number,  $\xi$ , for selected piezoelectric materials material  $n=0$  and  $(b-a)/a = 0.5$ .

for a relatively thin  $\frac{(b-a)}{a} = 0.05$  and thick  $\frac{(b-a)}{a} = 0.5$  hollow cylinder, respectively.

The outputs, as shown in Figure 4.2 and Figure 4.3, display an excellent agreement with Chen et al. [160]. The case studies will be discussed next.

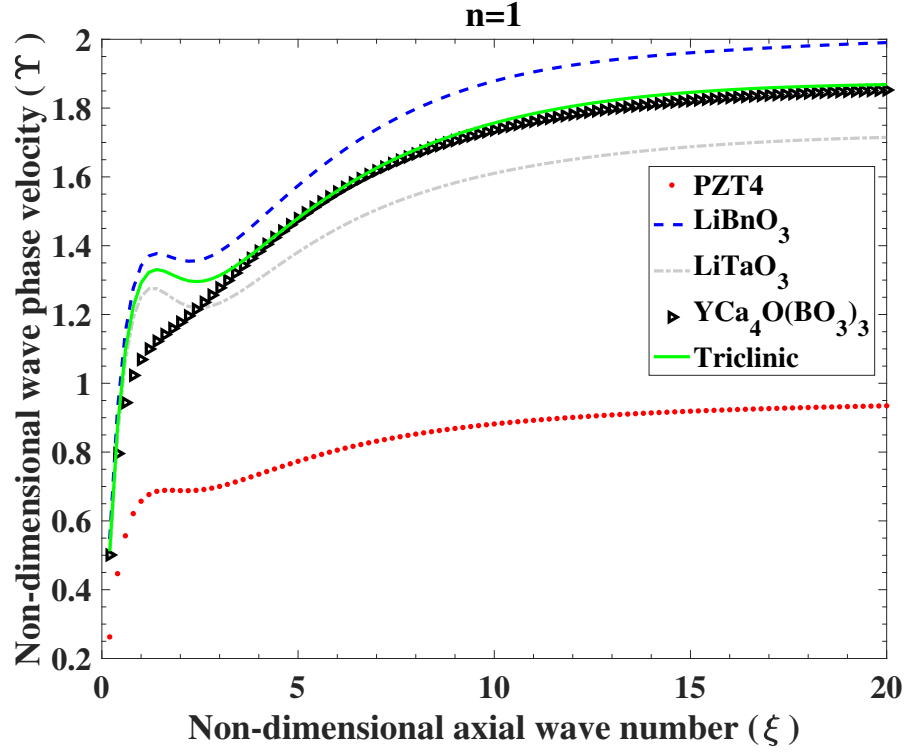


Figure 4.5: Non-dimensional wave phase velocity,  $\Upsilon$ , versus the non-dimensional axial wave number,  $\xi$ , for  $n=1$  and  $(b - a)/a = 0.5$ .

## 4.4 Case Studies

The configuration and material selection is based on the thick case, which has been addressed in section 4.3. Figure 4.4 and Figure 4.5 show the dispersion curves of the non-dimensional wave phase velocity  $\Upsilon$  versus the non-dimensional axial wavenumber  $\xi$  for the five different piezoelectric materials, as listed in Table 4.1. Although all the plots finally become almost invariant at high wavenumbers larger than 15, it is obvious that there is a significant difference between the dispersion curves of the PZT cylinder with the other materials. The dispersion curve of the PZT cylinder becomes rapidly invariant with the increase in the axial wavenumber, while the dispersion



curves for the other anisotropic materials become gradually constant with relatively higher values of non-dimensional wave phase velocities. Since the PZT material is classified as the orthotropic piezoelectric materials, however, the other curves belong to the monolithic or triclinic piezoelectric materials, which show a different pattern compared to the conventional orthotropic PZT material. This observation shows that the previous proposed theoretical methods for orthotropic piezoelectric materials can not be simply extended to monolithic or triclinic piezoelectric materials, which need to take into consideration a higher number of non-zero material constants. The non-dimensional wave phase velocities of triclinic material are found to have a significant difference with other anisotropic materials as well.

Figure 4.6 shows the dispersion curves of the lowest natural frequencies  $\omega$  versus the circumferential wave number  $n$  for the triclinic and the orthotropic piezoelectric materials for selected axial wave numbers  $\xi$ . The triclinic material used in Table 4.1 is made up one layer of  $LiNbO_3$  with the crystalline Z-axis along  $z$  and the crystalline Y-axis along  $r$  and the second layer is made up  $LiTaO_3$  with the crystalline X-axis along  $z$  and the crystalline Y along  $r$ , in order to show the triclinic effect on the wave behavior (see Akcakaya and Farnell [199]). In order to make the results of triclinic and orthotropic materials comparable, the orthotropic material used in Figure 4.6, Figure 4.7 and Figure 4.8 are made up of the same triclinic material by putting all the nonzero constants to zero in the way that it changes from a triclinic material to an orthotropic piezoelectric, for example, PZT4. Regarding Figure 4.6, the circumferential wave number has a significant effect on the natural frequencies of both triclinic and orthotropic materials. It is axiomatic that there is a more severe difference between the natural frequencies of the two materials in

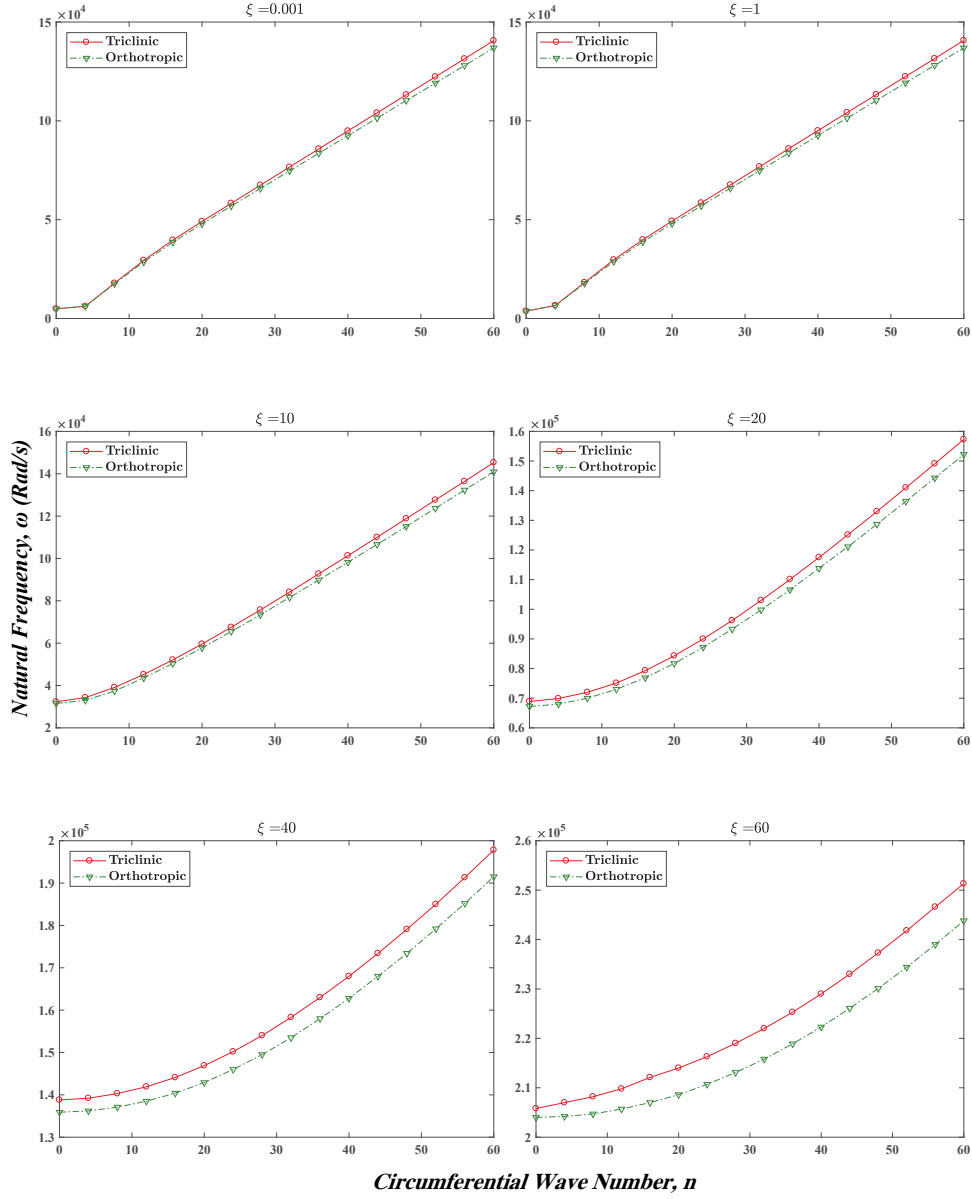


Figure 4.6: First lowest natural frequencies  $\omega$  versus the circumferential wave number  $n$  for selected axial wave number  $\xi$  and  $(b - a)/a = 0.5$ .

higher circumferential wavenumber, regardless of the value of the axial wavenumber. Also, the difference in the natural frequencies of the two materials depends on the

value of the axial wavenumber. As it is clearly seen from Figure 4.6, as the value of the axial wavenumber  $\xi$  increases from 0.001 to 60, the difference between the natural frequencies of the two materials becomes bigger. In addition, for the lower axial wave number such as  $\xi = 0.001$  and high circumferential wave number, for example,  $n = 60$ , the difference between the natural frequencies of the two materials is considerable, and the natural frequency of the triclinic material is higher than the one of orthotropic material by  $580 \text{ Rad/s}$ . Likewise, for the lowest circumferential wave number  $n = 0$  and higher axial wavenumber  $\xi = 60$ , the natural frequency difference is also noteworthy, and the natural frequency of the triclinic material is higher than the one of orthotropic material by  $3100 \text{ Rad/s}$ . The difference between the natural frequencies of triclinic and orthotropic materials is due to the fact that the triclinic material has more non-zero material constants, which results in consideration of more stress terms with a given strain vector. It can also be concluded that the conventional orthotropic model of the piezoelectric cylinder, including a lower number of material constants, can only be used to capture the lowest natural frequency of the totally anisotropic piezoelectric cylinder when both axial wave number and circumferential wave number are relatively low. In other words, the triclinic model proposed in this research, which considers all possible constants should be used to study the triclinic piezoelectric cylinder for higher axial wave numbers or higher circumferential wave numbers because the natural frequency of the orthotropic model deviates from the triclinic model, obviously.

Figure 4.7a and Figure 4.7b display the dispersion curves of the natural frequency versus the non-dimensional axial wavenumber  $\xi$  for selected lowest natural frequencies while the circumferential wave number is equal to zero. Results for the twelve selected

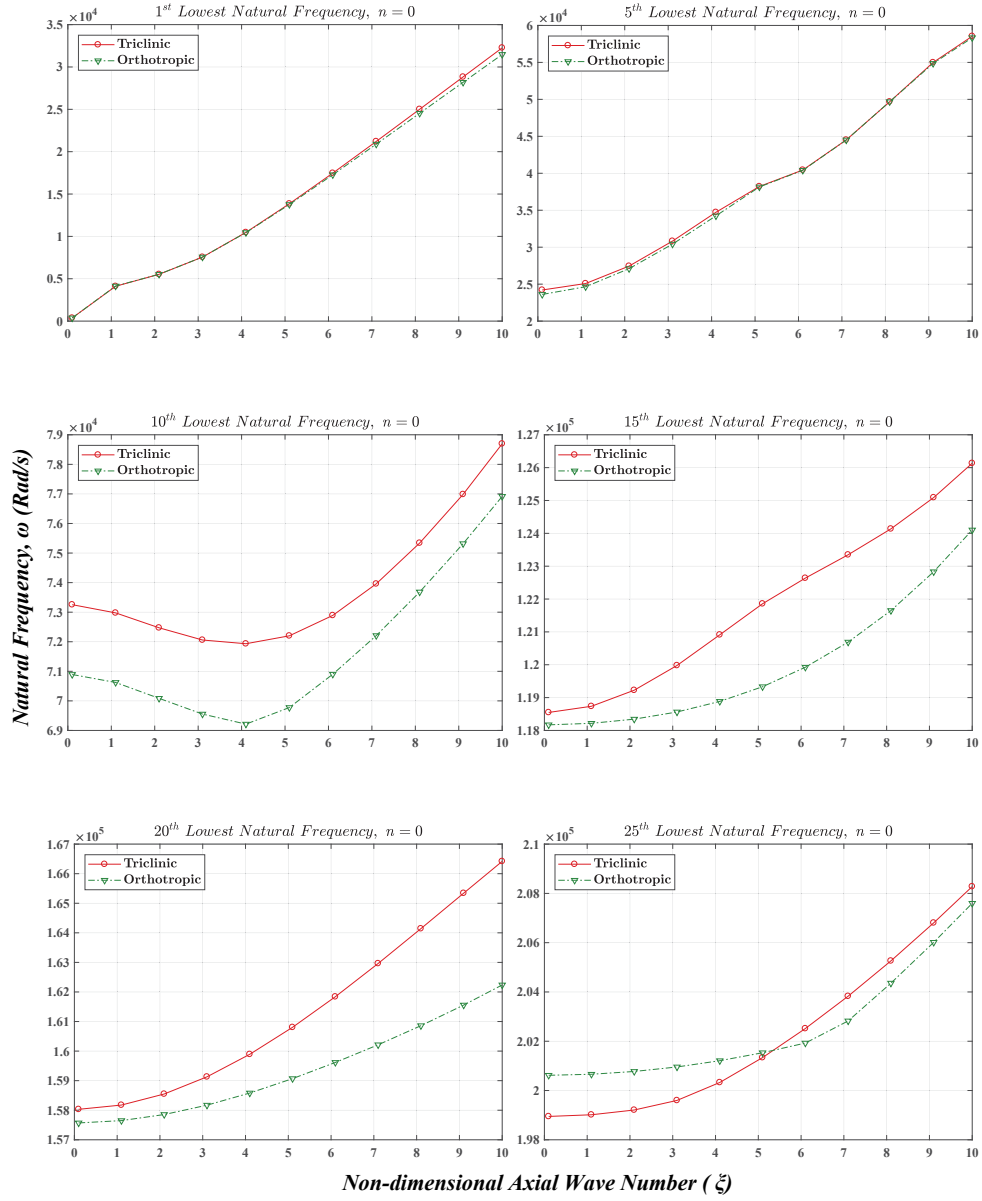


Figure 4.7a: Natural frequencies  $\omega$  versus the non-dimensional wave number  $\xi$  for selected lowest natural frequency with  $n=0$  and  $(b-a)/a = 0.5$ .

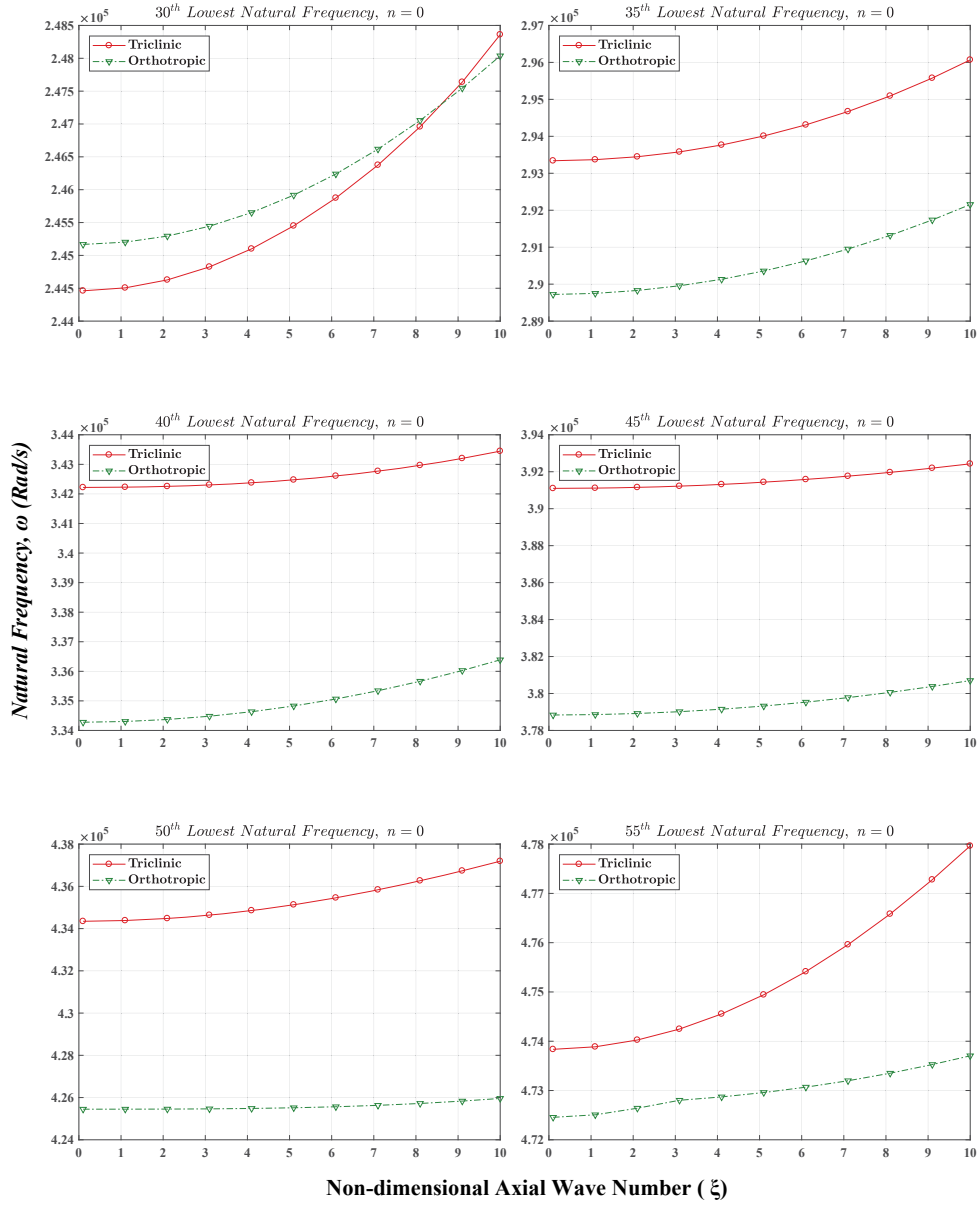


Figure 4.7b: Natural frequencies  $\omega$  versus the non-dimensional wave number  $\xi$  for selected lowest natural frequency with  $n=0$  and  $(b - a)/a = 0.5$ .

natural frequencies show that the difference between the natural frequencies of the two materials is very small for the first lowest natural frequency. However, for higher natural frequencies, the difference between the natural frequencies of two materials becomes gradually bigger, and the two plots become completely different in higher natural frequencies, such as shown in the figure, for the 55-th lowest natural frequency, and the natural frequency of triclinic material is higher than the one of orthotropic material by  $4300 \text{ Rad/s}$ . This observation indicates that the conventional orthotropic model of the piezoelectric cylinder with a lower number of non-zero material constants can only be used to model the anisotropic piezoelectric materials when the value of the natural frequency is relatively small. So, the value of the lowest natural frequency is the third important factor after the circumferential wave number and the axial wavenumber when the orthotropic model is utilized to predict the dynamic behavior of triclinic piezoelectric materials.

Figure 4.8 shows the cut-off frequency of the first eight natural frequencies,  $\omega$ , versus the non-dimensional axial wave number,  $\xi$ , for the circumferential wave number  $n = 0$ . It can be seen that the difference between the dispersion curves of orthotropic and triclinic materials increases when the fundamental frequencies order change to higher values. For instance, while the two plots are exactly matched in the first and second-order frequencies, a significant difference can be observed in the  $7_{th}$  and  $8_{th}$  order frequencies.

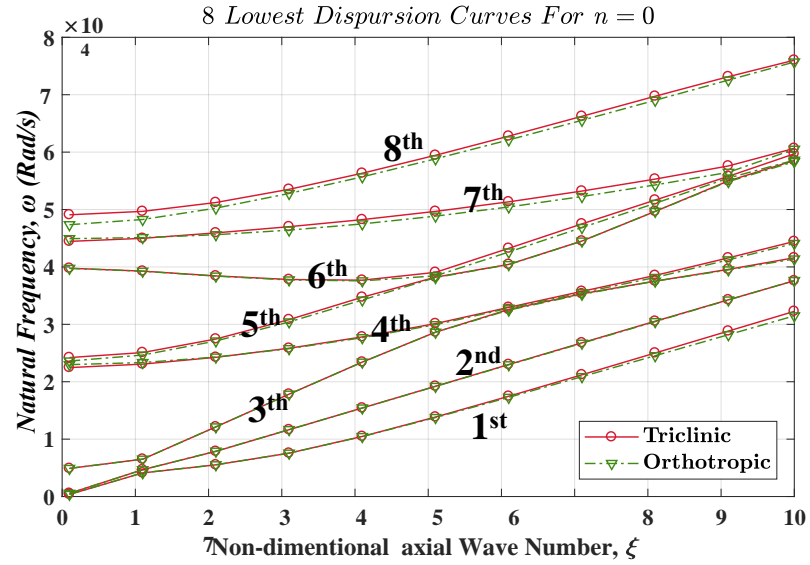


Figure 4.8: Cut-off frequency of the lowest natural frequencies  $\omega$  versus the non-dimensional axial wave number  $\xi$  for  $n = 0$  and  $(b - a)/a = 0.5$ .

## 4.5 Conclusions

The state-space method, transfer matrix approach along with appropriate state vector expansion are utilized to study the free vibration of an arbitrary thick, infinitely long triclinic hollow piezoelectric cylinder. The free vibration of the most general form of an anisotropic piezoelectric material with all possible material constants is analytically modeled and studied to cover a broad range of anisotropic piezoelectric materials. The main findings of this chapter are as follows

- The orthotropic model can only be used to model triclinic piezoelectric materials when the circumferential wave number, axial wave number, and the value of the lowest natural frequency are all relatively small.
- The results of the orthotropic piezoelectric model can not be extended to

investigate the behavior of the triclinic piezoelectric materials in high-frequency ranges.

- The difference between the dispersion curves of orthotropic and triclinic materials increases when the fundamental frequencies order change to higher values.

Because no assumption was considered for stress and displacement fields, the output results can be used as a benchmark to investigate the accuracy of different shell models, semi-numerical and numerical solutions. As part of future works, the proposed model can also be easily used to study the free vibration of a functionally graded anisotropic material. Furthermore, due to considering all the possible material constants for the general anisotropic piezoelectric, the model is able to investigate the natural frequencies of monolithic piezoelectric material. The model can be extended to studies of multi-layers anisotropic piezoelectric structures. In addition, it can be used to investigate the effect of different polarization directions on the natural frequencies of general anisotropic piezoelectric materials.



## Chapter 5

# Sound Transmission Through a Thick-Walled FGM Piezo-laminated Cylindrical Shell Filled with and Submerged in Compressible Fluids

*“Mathematics reveals its secrets only  
to those who approach it with pure  
love, for its own beauty”*

---

Archimedes

When a sound wave strikes on a barrier, some of it reflects back to the original medium, and some may be transmitted through the barrier. An index is essential to be defined, in order to measure the capability of the sound absorber in blocking the sound transmission from the external fluid to the internal environment. That index is known as STL. STL is the best quantification for benchmarking the acoustic performance of any acoustic treatment. In the past few years, STL from cylindrical objects has been a subject of researchers' interest due to the wide range of engineering

applications and their manufacturing feasibility. Several studies have been carried out in this area to cover the essential needs of these industrial applications [57, 59]. Many researchers focused their study on finding new materials to increase the STL from the cylindrical structures. The most common materials that were used for this purpose are viscoelastic and poroelastic materials. However, the use of intelligent materials such as piezoelectric materials in STL through cylindrical structures is often overlooked. Piezoelectric materials offer advantages such as durability, high energy density, low cost, compactness, and low weight which give them the potential to replace classical poroelastic and viscoelastic sound treatments [200]. The current work is aimed at using piezoelectric materials in order to investigate their effects on the STL through the cylinder. In this work, the estimation of STL due to the piezoelectric effects, as attenuation of acoustic waves, is studied for a thick-walled piezo-composite cylindrical shell excited by an oblique incident plane wave. The wave propagation through the hollow cylinder was achieved by using the state space method and transfer matrix approach within the context of the 3D theory of elasticity. The STL expression was obtained by performing the exact integration over the internal surface of the cylinder. Finally, the accuracy of the presented analytical solution was cross-checked with the simplified model in various literature. Due to a lack of available results for the TL of the piezoelectric cylinder in literature, a finite element package has been used to check the result of a purely piezoelectric cylindrical shell. The final results display an impressive agreement between the FEM and the proposed analytical solution.

## 5.1 Problem Description of Sound Transmission Through a Piezo-laminated cylinder

In this section, the structure given in chapter 4 is modified and used to study the sound transmission loss from a thick orthotropic hollow piezo-composite cylindrical shell excited by an oblique plane incident wave.

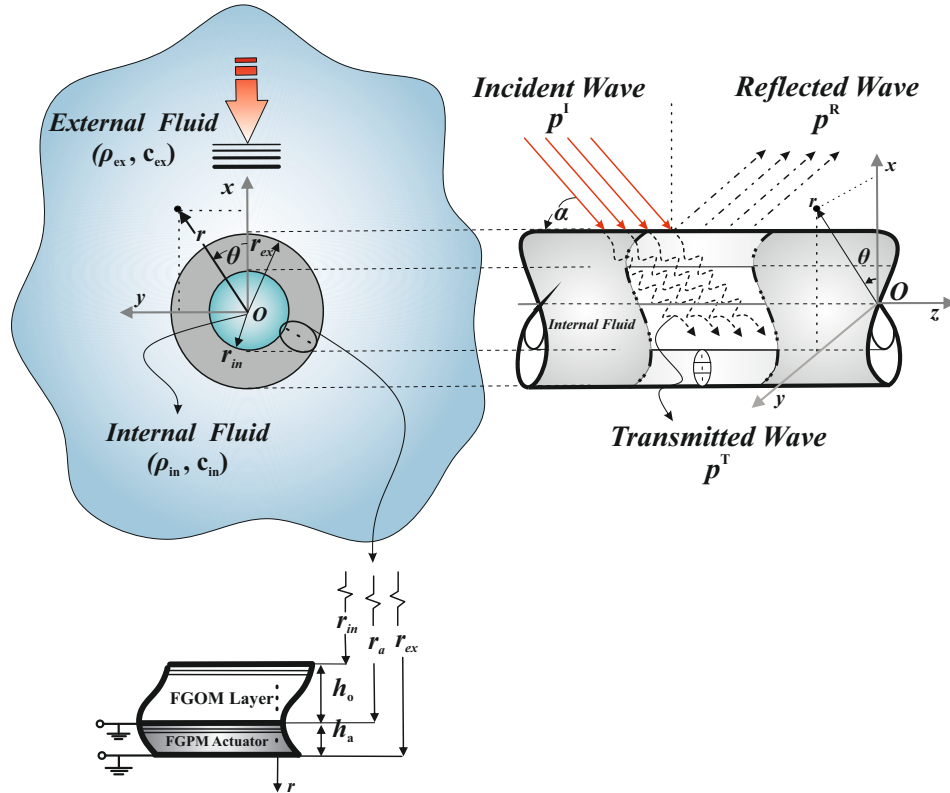


Figure 5.1: Problem Configuration.

Let us consider an infinite laminated piezo-composite cylindrical shell with FGM property, as depicted in Figure 8.1. The cylinder is made of a FGM of total thickness  $h_o = r_a - r_{in}$ , perfectly matched to an outer radially polarized FGPM of the total thickness  $h_a = r_{ex} - r_a$ . The infinite cylinders are assumed to be submerged in

and filled with ideal compressible fluids of densities  $\rho_{ex}$ , and  $\rho_{in}$ , respectively. The infinite cylindrical shell is excited by an incoming oblique incidence plane wave with an arbitrary angle,  $\alpha$ . Acoustic field equations will be discussed next.

### 5.1.1 External Acoustic Medium

Since the external acoustic field is affected by the incident and refracted waves, using Equation 3.12, the external acoustic wave equation can be expressed as [65]

$$c_{ex}\nabla^2(p^I + p^R) - \frac{\partial^2(p^I + p^R)}{\partial t^2} = 0, \quad (5.1)$$

where  $c_{ex}$ ,  $p^I$ , and  $p^R$  are the traveling speed of sound in the external fluid, the incident pressure wave, and the refracted pressure wave, respectively. Furthermore,  $\nabla^2 = \frac{\partial^2}{\partial r^2} + \frac{1}{r}\frac{\partial}{\partial r} + \frac{1}{r^2}\frac{\partial^2}{\partial \theta^2} + \frac{\partial^2}{\partial z^2}$  is the Laplacian operator in the cylindrical coordinate.

The harmonic incident plane wave pressure,  $p^I$  can be written as [201]

$$p^I(r, \theta, z, \omega) = \sum_{n=0}^{\infty} p_0 \varepsilon_n (-\mathbf{i})^n J_n(k_r^{ex} r) \cos(n\theta) e^{\mathbf{i}(\omega t - k_z^{ex} z)}, \quad (5.2)$$

where  $\omega$ ,  $p_0$ ,  $n$ ,  $\alpha$  and  $J_n(x)$  are circular frequency, the magnitude of the incident wave pressure, the circumferential wave number, incident wave angle and Bessel function of the first kind, respectively. Furthermore,  $p_n^I(r) = p_0 \varepsilon_n (-\mathbf{i})^n J_n(k_r^{ex} r)$  and

$$\varepsilon_n = \begin{cases} 1 & n = 0, \\ 2 & n \geq 1. \end{cases}$$

where,

$$k_r^{ex} = k_{ex} \sin(\alpha), \quad (5.3a)$$

$$k_z^{ex} = k_{ex} \cos(\alpha). \quad (5.3b)$$

Moreover,  $k_{ex} = \omega/c_{ex}$  and  $\mathfrak{i} = \sqrt{-1}$ . The reflected wave can also be expressed as

$$p^R(r, \theta, z, \omega) = \sum_{n=0}^{\infty} A_n(\omega) H_n^2(k_r^{ex} r) \cos(n\theta) e^{\mathfrak{i}(\omega t - k_z^{ex} z)}, \quad (5.4)$$

where

$$p_n^R(r, \omega) = A_n(\omega) H_n^2(k_r^{ex} r).$$

$A_n(\omega)$  and  $H_n^2(x)$  are an unknown modal constant and Hankel function of the second kind, respectively (Yuan et al. [202]).

### 5.1.2 Internal Acoustic Medium

The governing equation of the acoustic cavity can be expressed using Equation 3.12 as (Pierce and Smith [203])

$$c_{in} \nabla^2 p^T - \frac{\partial^2 p^T}{\partial t^2} = 0, \quad (5.5)$$

where  $c_{in}$  is the traveling speed of sound in the cavity. The modal expansion of internal pressure can be written as

$$p^T(r, \theta, z, \omega) = \sum_{n=0}^{\infty} B_n(\omega) H_n^1(k_r^{in} r) \cos(n\theta) e^{i(\omega t - k_z^{in} z)}, \quad (5.6)$$

$$p_n^T(r, \omega) = B_n(\omega) H_n^1(k_r^{in} r),$$

where,  $B_n(\omega)$ ,  $H_n^1$ ,  $k_r^{in}$ , and  $k_z^{in}$  are unknown modal constants, Hankel function of the first kind, radial, and axial wave numbers, respectively. Since the internal and external acoustic waves are both driven by one incident-traveling wave, the axial wavenumber inside and outside of the cylinder are equivalent  $k_z^{in} = k_z^{ex} = k_z$ . Furthermore, it's straightforward to show

$$k_r^{in} = \sqrt{k_{in}^2 - (k_z^{in})^2}, \quad (5.7)$$

in which,  $k_{in} = \omega/c_{in}$ .

## 5.2 Structural Modelling: Elasticity and Piezoelectricity

The generalized linear constitutive equations relating the stress components  $(\Sigma_{ij}, \sigma_{ij})$  to the relevant strain components  $(\Gamma_{ij}, \gamma_{ij})$  for the functionally graded orthotropic and piezoelectric layers can be written as [196]

$$\boldsymbol{\sigma} = \mathbf{c} \boldsymbol{\gamma}, \quad (5.8)$$

$$\boldsymbol{\Sigma} = \mathbf{C} \boldsymbol{\Gamma} - \mathbf{e} \mathbf{E}, \quad (5.9)$$

where,  $\mathbf{c}$  and  $\mathbf{C}$  are the elasticity matrices of the orthotropic and piezoelectric materials, respectively, measured under the condition of zero electric voltage. The elasticity matrices can have a maximum of 21 independent constants. Likewise,  $\mathbf{e}$  is the piezoelectric coupling matrix for zero strain field conditions. This matrix has a maximum of 18 independent parameters. Furthermore,  $\boldsymbol{\sigma}$  and  $\boldsymbol{\Sigma}$  represent the Green-Cauchy stress vector for the orthotropic and piezoelectric material, whereas the  $\boldsymbol{\gamma}$  and  $\boldsymbol{\Gamma}$  stand for the Green-Cauchy strain vector of the orthotropic and piezoelectric material, respectively.

Additionally,  $\mathbf{E}$  denotes the electric-field vector. The expanded form of Equation 5.8 is given in subsection B.1.1. Moreover, the expanded form of piezoelectric constitutive relation, Equation 5.9, for the axially and radially polarized piezoelectric materials are presented in subsection B.1.2 and subsection B.1.3, respectively.

The electrical field vector  $\mathbf{E}$  can be related to the electrical potential,  $\phi$ , in which

[36]

$$\mathbf{E} = -\vec{\nabla}\phi, \quad (5.10)$$

where, the nabla symbol,  $\vec{\nabla}$  denotes the gradient operator in the cylindrical coordinates. The direct piezoelectric effect can be written as [204]

$$\mathbf{D} = \mathbf{e}^T \boldsymbol{\Gamma} + \boldsymbol{\epsilon} \mathbf{E}, \quad (5.11)$$

in which  $\mathbf{D}$  and  $\boldsymbol{\epsilon}$  are the electrical displacement vector and dielectric permittivity tensor, respectively. The maximum independent parameters of the dielectric permittivity tensor are 6. The expanded form of Equation 5.11 for the axially and radially polarized piezoelectric materials is described in Equation B.1.3 and Equation B.1.5, respectively. The functionally graded laminated model is given next.

### 5.2.1 Functionally Graded Laminated Model

In order to include the functionality of materials properties in the constitutive relation, a laminated model should be adopted. By employing the simple rule of mixture, the mechanical and electrical properties of the constituent materials within the  $i$ -th layer of the laminated cylinder can be advantageously expressed as [160]

$$\xi^i = \Lambda(\bar{r}_i)\xi_1 + [1 - \Lambda(\bar{r}_i)]\xi_2, \quad (5.12)$$

where  $\Lambda(\bar{r}_i)$  is the volume fraction of the material in the  $i$ -th layer and  $\xi$  could be any material properties such as  $\epsilon, \rho, e, c, \text{etc.}$  In addition, subscript 1 and 2 show the material properties in the inner and outer layer of the shell, respectively. The gradient profile of the associated materials can be described by the following assumption for the volume fraction of the material across the cylinder radius as [205, 206, 76]

$$\Lambda(r) = \left(1 - \frac{r - a_o}{h_p}\right)^\mu, \quad o = in, a; \quad p = o, a, \quad (5.13)$$



in which  $a_0$ ,  $h_p$ , and  $\mu$  are the inner radius of the cylinder, thickness along the radial axis, and power of gradient profile.

### 5.2.2 Kinematic Assumptions

The Green-Cauchy strain vectors of the orthotropic layer,  $\boldsymbol{\gamma}$ , and piezoelectric layers,  $\boldsymbol{\Gamma}$  are associated with the pertinent material displacement vectors via the linearized kinematic relation as [207]

$$\boldsymbol{\gamma} = \mathbf{K}\mathbf{u}, \quad (5.14)$$

$$\boldsymbol{\Gamma} = \mathbf{K}\mathbf{U}, \quad (5.15)$$

where,  $\mathbf{u} = [u_r \ u_\theta \ u_z]^T$  and  $\mathbf{U} = [U_r \ U_\theta \ U_z]^T$  are the elastic and piezoelectric Lagrangian displacement, respectively. Furthermore, the matrix operator  $\mathbf{k}$  is described in Equation B.2.1. The conservation laws are employed next.

### 5.2.3 Conservation Laws

The conservation of linear momentum and electrical charge equilibrium in the absence of free charge density and body forces for a differential element can be expressed as

$$\mathbf{m} \boldsymbol{\sigma} = \rho \ddot{\mathbf{u}}, \quad (5.16)$$

$$\mathbf{M} \begin{bmatrix} \boldsymbol{\Sigma} \\ \mathbf{D} \end{bmatrix} = \rho_{pz} \begin{bmatrix} \ddot{\mathbf{U}} \\ 0 \end{bmatrix}, \quad (5.17)$$

where  $\rho$  and  $\rho_{pz}$  are the unperturbed material density of elastic and piezoelectric materials, respectively. Moreover, double dot, “ $\ddot{\phantom{x}}$ ” denotes twice differentiation respect

to time. The expanded form of matrix operators ( $\mathbf{m}, \mathbf{M}$ ) are given in Equation B.2.2 and Equation B.2.3, respectively.

### 5.3 Spatial State Vectors and Ultimate Transfer Function

The modal transformed spatial state vectors associated with the orthotropic,  $\mathbf{v}$ , and piezoelectric layers,  $\mathbf{V}$ , may advantageously be expressed in terms of the trigonometric functions in the form of

$$\mathbf{v} = \sum_{n=0}^{\infty} \begin{pmatrix} u_r^n(r, \omega) \cos(n\theta) \\ u_\theta^n(r, \omega) \sin(n\theta) \\ u_z^n(r, \omega) \cos(n\theta) \\ \sigma_{rr}^n(r, \omega) \cos(n\theta) \\ \sigma_{r\theta}^n(r, \omega) \sin(n\theta) \\ \sigma_{rz}^n(r, \omega) \cos(n\theta) \end{pmatrix} e^{i(\omega t - k_z z)}, \quad (5.18a)$$

$$\mathbf{V} = \sum_{n=0}^{\infty} \begin{pmatrix} U_r^n(r, \omega) \cos(n\theta) \\ U_\theta^n(r, \omega) \sin(n\theta) \\ U_z^n(r, \omega) \cos(n\theta) \\ \Sigma_{rr}^n(r, \omega) \cos(n\theta) \\ \Sigma_{r\theta}^n(r, \omega) \sin(n\theta) \\ \Sigma_{rz}^n(r, \omega) \cos(n\theta) \\ D_r^n(r, \omega) \cos(n\theta) \\ \phi_n(r, \omega) \cos(n\theta) \end{pmatrix} e^{i(\omega t - k_z z)}, \quad (5.18b)$$

in which  $\omega$ ,  $n$  and  $k_z^{\text{ex}}$  are angular frequency, circumferential and axial external wave number, respectively. Subsequently, the modal components of the aforementioned state vectors,  $\mathbf{v}_n(r, \omega)$  and  $\mathbf{V}_n(r, \omega)$  described in Equation 5.18a and Equation 5.18b

can be written as

$$\mathbf{v}_n(r, \omega) = \begin{Bmatrix} u_r^n(r, \omega) \\ u_\theta^n(r, \omega) \\ u_z^n(r, \omega) \\ \sigma_{rr}^n(r, \omega) \\ \sigma_{r\theta}^n(r, \omega) \\ \sigma_{rz}^n(r, \omega) \end{Bmatrix}, \quad \mathbf{V}_n(r, \omega) = \begin{Bmatrix} U_{r,n}(r, \omega) \\ U_{\theta,n}(r, \omega) \\ U_{z,n}(r, \omega) \\ \Sigma_{rr,n}(r, \omega) \\ \Sigma_{r\theta,n}(r, \omega) \\ \Sigma_{rz,n}(r, \omega) \\ D_r^n(r, \omega) \\ \phi_n(r, \omega) \end{Bmatrix}. \quad (5.19)$$

Now, by performing an exhausting task of substituting Equation 5.18a and Equation 5.18b into Equation 5.8, Equation 5.9, Equation 5.11, Equation 5.14 and Equation 5.15 along with benefiting from the orthogonality of trigonometric functions, the modal state-space relations for the elastic and piezoelectric layer accordingly emerge as

$$\frac{d\mathbf{v}_n(r, \omega)}{dr} = \mathbf{g}_n(r, \omega)\mathbf{v}_n(r, \omega), \quad (5.20a)$$

$$\frac{d\mathbf{V}_n(r, \omega)}{dr} = \mathbf{G}_n(r, \omega)\mathbf{V}_n(r, \omega), \quad (5.20b)$$

where  $\mathbf{g}_n(r, \omega)$  is  $6 \times 6$  modal coefficient matrix whose elements are given in Equation B.3.1, whereas  $\mathbf{G}_n(r, \omega)$  is  $8 \times 8$  modal coefficient matrix whose arrays for the axially and radially polarized piezoelectric materials are provided in subsection B.3.2 and subsection B.3.3, respectively. The details of the solution procedure for Equation 6.1 is given in subsection 4.1.2. By subsequent employment of state space method, the modal components of the state variables at  $i^{th}$  sub-layer can be related to the one at  $(i-1)^{th}$  sub-layer as

$$\mathbf{v}_n(r_i, \omega) = \exp\left(\mathbf{g}_n(\bar{r}_k, \omega)\hat{h}_o\right)\mathbf{v}_n(r_{i-1}, \omega), \quad (5.21a)$$

$$\mathbf{V}_n(r_i, \omega) = \exp\left(\mathbf{G}_n(\bar{r}_k, \omega)\hat{h}_a\right)\mathbf{V}_n(r_{i-1}, \omega). \quad (5.21b)$$

in which the matrix exponential,  $\exp(\mathbf{X})$ , can be expressed by the power series as

$$\exp(\mathbf{X}) = \sum_{j=1}^{\infty} \frac{\mathbf{X}^j}{j!}. \quad (5.22)$$

Elastic and piezoelectric modal transfer matrices can be obtained, by implementing the continuity of  $\mathbf{v}_n$  and  $\mathbf{V}_n$  between all interface layers in the way that, the state's components at the outer radii of the elastic and the piezoelectric layers are related to the states variables at the inner radii of the elastic and the piezoelectric layers via global transfer matrices,  $\mathbf{t}_n$ , and  $\mathbf{T}_n$ , respectively such that

$$\mathbf{v}_n(r_a, \omega) = \mathbf{t}_n(\omega) \mathbf{v}_n(r_{in}, \omega), \quad (5.23a)$$

$$\mathbf{t}_n(\omega) = \prod_{i=1}^{n_o} \exp \left( \mathbf{g}_n(\bar{r}_i, \omega) \hat{h}_o \right), \quad (5.23b)$$

for the elastic layer, whereas

$$\mathbf{V}_n(r_{ex}, \omega) = \mathbf{T}_n(\omega) \mathbf{V}_n(r_a, \omega), \quad (5.23c)$$

$$\mathbf{T}_n(\omega) = \prod_{i=1}^{n_a} \exp \left( \mathbf{G}_n(\bar{r}_i, \omega) \hat{h}_a \right), \quad (5.23d)$$

for the piezoelectric layer where  $\mathbf{t}_n(\omega)$  and  $\mathbf{T}_n(\omega)$  are  $6 \times 6$  and  $8 \times 8$  matrices, respectively. The ultimate transfer matrices will be obtained in the next subsection.

### 5.3.1 Ultimate Transfer Matrices

At this point, the transfer matrix of the elastic and piezoelectric layer should be amalgamated in order to obtain the ultimate transfer matrix. Thus, by applying the perfect bonding conditions between the elastic and piezoelectric layers, the state variable vector at the inner surface of the elastic layer,  $\mathbf{v}_n(r_{in}, \omega)$ , augmented with the electrical potential and radial electrical displacement at the inner layer of the piezoelectric actuator may advantageously be related to the state variable vector at the outer surface of the actuator,  $\mathbf{V}_n(r_{ex}, \omega)$  using  $8 \times 8$  global matrix,  $\mathbf{\Theta}_n$  in the form of

$$\mathbf{V}_n(r_{ex}, \omega) = \mathbf{\Theta}_n(\omega) \mathbf{\Upsilon}_n(\omega), \quad (5.24a)$$

$$\mathbf{\Theta}_n(\omega) = [\mathbf{T}_n(:, 1 : 6) \mathbf{t}_n \quad \mathbf{T}_n(:, 7 : 8)], \quad (5.24b)$$

$$\mathbf{\Upsilon}_n(\omega) = [\mathbf{v}_n^{\mathbf{Tr}}(r_{in}, \omega) \quad D_r^n(r_a, \omega) \quad \phi_n(r_a, \omega)] \quad (5.24c)$$

in which, the superscript  $\mathbf{Tr}$  is the operator which flips a matrix over its diagonal. Furthermore, it should be mentioned that  $\mathbf{T}_n(:, 1 : 6)$  includes the first six columns of  $\mathbf{T}_n$ , whereas  $\mathbf{T}_n(:, 7 : 8)$  includes only the last two columns of  $\mathbf{T}_n$ .

## 5.4 Fluid-solid Coupling and Electrical Boundary Conditions

### 5.4.1 Fluid-solid Interaction

Keeping in mind the fully coupled nature of the fluid-solid interaction problem, the relevant mechanical boundary conditions that must be satisfied at the internal and external surface of the cylinder are as follow

- The acoustic fluid model is assumed to be an inviscid flow. Consequently, the tangential stress at the inner and outer of the cylinder can be written as

$$\sigma_{rz}^n(r_j, \omega) = \Sigma_{rz}^n(r_j, \omega) = 0, \quad j = in, ex, \quad (5.25a)$$

$$\sigma_{r\theta}^n(r_j, \omega) = \Sigma_{r\theta}^n(r_j, \omega) = 0, \quad j = in, ex; \quad (5.25b)$$

- Equilibrium of the total external and internal acoustic pressures with normal stress at the traction surfaces (i.e., solid/fluid stress coupling) can be given as

$$\sigma_{rr}^n(r_{in}, \omega) = -p_n^T(r_{in}, \omega), \quad (5.25c)$$

$$\Sigma_{rr}^n(r_{ex}, \omega) = -p_n^I(r_{ex}, \omega) - p_n^R(r_{ex}, \omega); \quad (5.25d)$$

- The relationships between the radial solid Lagrangian displacement components and the radial fluid displacements (i.e., solid/fluid displacement coupling) at

the traction surfaces are written as [12]

$$u_r^n(r_{in}, \omega) = \frac{1}{\rho_{in}\omega^2} \left. \frac{\partial p_n^T(r, \omega)}{\partial r} \right|_{r=r_{in}}, \quad (5.25e)$$

$$U_r^n(r_{ex}, \omega) = \frac{1}{\rho_{ex}\omega^2} \left. \frac{\partial [p_n^I(r, \omega) + p_n^R(r, \omega)]}{\partial r} \right|_{r=r_{ex}}. \quad (5.25f)$$

### 5.4.2 Electrical Boundary Conditions

The short-circuited electrical boundary conditions for the inner and outer surface of the piezoelectric cylinder can be enforced as [95]

$$\phi_n(r_i, \omega) = 0, \quad i = a, ex, \quad (5.26)$$

while, the open-circuited electrical boundary condition can be written as

$$D_r^n(r_i, \omega) = 0, \quad i = a, ex, \quad (5.27)$$

similarly, the compatibility of the electrical boundary condition for the applied voltage on the inner and outer surface of the piezoelectric electrodes can be given as

$$\phi_n(r_i, \omega) = \Phi_n(r_i, \omega), \quad i = a, ex, \quad (5.28)$$

in which the applied modal voltage,  $\Phi_n$  can be written using the Fourier expansion as

$$\Phi_n(r_i, \omega) = \frac{1}{\pi} \int_{-\pi}^{\pi} \Phi_n(r_i, \omega) \cos(n\theta) d\theta, \quad (5.29)$$

for the angular shape of the electrode with the angle,  $2\beta$ , and voltage amplitude  $\varphi$ , Equation 5.29 emerges as

$$\Phi_n(r_i, \omega) = \frac{1}{\pi} \int_{-\beta}^{\beta} \varphi \cos(n\theta) d\theta = \begin{cases} 2\varphi\beta/\pi, & n = 0, \\ [2\varphi \sin(n\beta)]/(n\pi), & n > 0. \end{cases} \quad (5.30)$$

## 5.5 Final Solution

The final solution can be obtained by direct substitution of mechanical and electrical boundary conditions given in subsection 5.4.2 into the ultimate transfer matrix of Equation 5.24 in the form of a linear system of the algebraic equation as

$$\mathbf{A}_n \mathbf{x}_n = \mathbf{b}_n, \quad (5.31)$$

in which  $\mathbf{A}_n$ ,  $\mathbf{x}_n$ , and  $\mathbf{b}_n$  for the short-circuited, open-circuited, and active applied voltage are given in section B.4.

### 5.5.1 STL

The STL is a measure of the capability of a cylinder to stop the incoming acoustics wave from being transmitted through the cylinder. It can be expressed as

$$TL = 10 \log_{10} \left( \frac{\Pi_I}{\Pi_T} \right) \quad (5.32)$$

in which  $\Pi_I$  and  $\Pi_T$  are incident and transmitted acoustic power, respectively. Furthermore,  $\log_{10}(x)$  indicates the common logarithm with base 10. The incident and transmitted acoustic power shall be determined before the calculation of TL. The acoustic power of a plane incident wave impinged on a cylindrical shell can be evaluated as

$$\Pi_I = \frac{1}{2} Re \left( \int_A p^I \nu^* dA \right) = \frac{\sin \alpha |p_0^2| r_{ex}}{\rho_{ex} c_{ex}} \quad (5.33)$$

where  $Re(z)$ ,  $\nu$ , and  $A$  indicate the real part of complex number  $z$ , the radial particle velocity, and the domain of integration over the surface of the cylinder,



respectively. Moreover, the superscript “\*” denotes the complex conjugate of a complex number. Similarly, the transmitted power is written as

$$\Pi_T = \frac{1}{2} \text{Re} \left( \int_A p^T \nu^* dS \right) = \frac{1}{2} \text{Re} \left[ \int_A p^T \frac{\partial(u_r)^*}{\partial t} dS \right] \quad (5.34)$$

Next by substituting the transmitted acoustic pressure expansion Equation 5.6 and radial displacement expansion Equation 5.18a into the Equation 5.34 and performing integration over the internal surface of the cylinder along with using orthogonality of trigonometric function one can obtain

$$\Pi_T = \frac{1}{2} \sum_{n=0}^{\infty} \text{Re} \{ B_n(\omega) H_n^1(k_r^{in} r_{in}) [\mathbb{i} \omega u_r^n(r_{in}, \omega)]^* \int_0^{2\pi} \cos^2(n\theta) r_{in} d\theta \}. \quad (5.35)$$

The simplification of the latter equation can be achieved by performing exact analytical integration in the form of

$$\Pi_T = \sum_{n=0}^{\infty} \frac{\pi r_{in}}{\varepsilon_n} \text{Re} \{ B_n(\omega) H_n^1(k_r^{in} r_{in}) [\mathbb{i} \omega u_r^n(r_{in}, \omega)]^* \}. \quad (5.36)$$

Next, by direct substitution of Equation 5.38 and Equation 5.33 into the Equation 5.32 result in

$$TL = -10 \log_{10}(\Psi) \quad (5.37)$$

in which

$$\Psi = \sum_{n=0}^{\infty} \frac{\text{Re} \{ B_n(\omega) H_n^1(k_r^{in} r_{in}) [\mathbb{i} \omega u_r^n(r_{in}, \omega)]^* r_{in} \pi \rho_{ex} c_{ex}}{|p_0^2| \varepsilon_n \sin(\alpha) r_{ex}}. \quad (5.38)$$

## 5.6 Model Validation

A general MATLAB<sup>®</sup> code is optimized to execute the parallel clusters in order to calculate the TL from the cylinder as well as obtaining the solution of Equation 5.31.

The calculation was carried out on a cluster of INTEL<sup>®</sup> XENON<sup>®</sup> Processor G4400 v4 desktop computer (15M Cache, 3.31 GHz, 7.20 GT/s), which benefits from Multi-core architectures and Hyper-Threading Technology for intensive parallel applications. The MATLAB PARALLEL COMPUTING TOOLBOX was engaged in taking advantage of the ultimate calculation power of multi-thread desktops by performing tasks on 8 workers in the parallel pool (MATLAB computational engines) that run locally [208]. The validity of the proposed analytical solution shall be confirmed by fixing the variables of the problem according to one specific example.

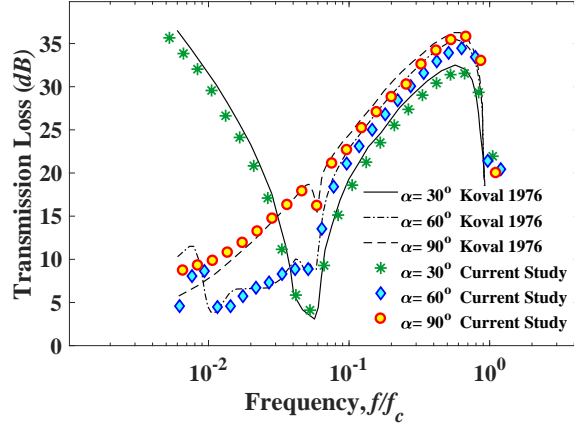
Figure 5.2a shows the TL comparison between the Flugge-Lure-Byrne thin-walled shell theory and the 3D theory of elasticity under no-flow condition (Mach=0) for three different attack angles ( $\alpha = \pi/6; \pi/3; \pi/2$ ). The general MATLAB code was used to calculate the cylinder TL defined by Equation 5.37. Figure 5.2a demonstrates a good agreement with the results presented in Figure 3 of Ref.[2].

Figure 5.2b displays the cylinder TL comparison between Love's shell theory and the 3D theory of elasticity. The cylinder is subjected to an incident plane wave with pressure magnitude of  $p_0 = 1 \text{ Pa}$  for various incident angles ( $\alpha = \pi/6; \pi/4; \pi/3$ ). Equation 5.37 has been employed to calculate the TL from the cylinder. There is no piezoelectric layer in the proposed model provided by Ref.[66], thus in order to make a comparison between the two models possible, the thickness of the piezoelectric actuator layer was set to  $h_a = 0.000001 \text{ m}$ . The outcome, as shown in Figure 5.2b, displays an acceptable agreement with that result presented in Fig. 9 of [66].

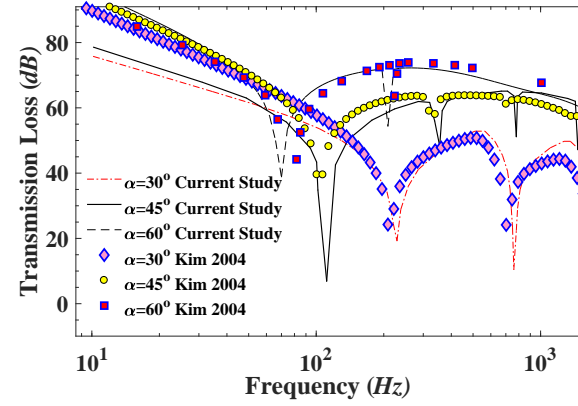
Figure 5.2c shows the cylinder TL comparison between Donnel and Mushtari shell theory and the 3D theory of elasticity. The cylinder is assumed to be filled with ( $\rho_{in} = 1.29 \text{ kg/m}^3$ ;  $c_{in} = 343 \text{ m/s}$ ) and submerged in the external air with

( $\rho_{ex} = 1.29 \text{ kg/m}^3$ ;  $c_{ex} = 343 \text{ m/s}$ ). The structure is made of ( $n_o = 30$ ;  $r_{in} = 1.9970 \text{ m}$ ;  $r_a = 2.003 \text{ m}$ ) with isotropic material property  $c^* = c(1 - i\eta)$  for two different structural damping ( $\eta = 0.1; 0.01$ ). The outcome, as shown in Figure 5.2c, displays a good agreement with the result presented in Ref.[64].

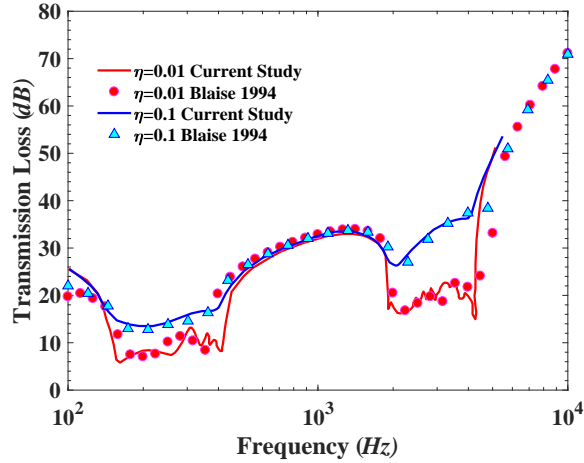
Figure 5.2d shows the cylinder TL comparison between the Mixed 3D-Shell analytical model and the current solution without the piezo-coupling effect. Therefore, the thickness of the piezoelectric layer was set to zero. The cylindrical shell is made of the aluminum material ( $n_o = 10$ ;  $r_{in} = 2.1610 \text{ m}$ ;  $r_a = 2.164 \text{ m}$ ) with an isotropic material property  $\mathbf{c}^* = \mathbf{c}(1 - i\eta)$  and structural damping  $\eta = 5 \%$ . The structure is filled and surrounded by air ( $\rho_{in} = \rho_{ex} = 1.284 \text{ kg/m}^3$ ;  $c_{in} = c_{ex} = 340 \text{ m/s}$ ) and is excited by an oblique incident plane wave with an angle ( $\alpha = \pi/4$ ). See Ref.[69] for more structural details. The final results depicted in Figure 5.2d demonstrate an excellent agreement between the current study and the mixed 3D-Shell model presented in Ref. [69] .



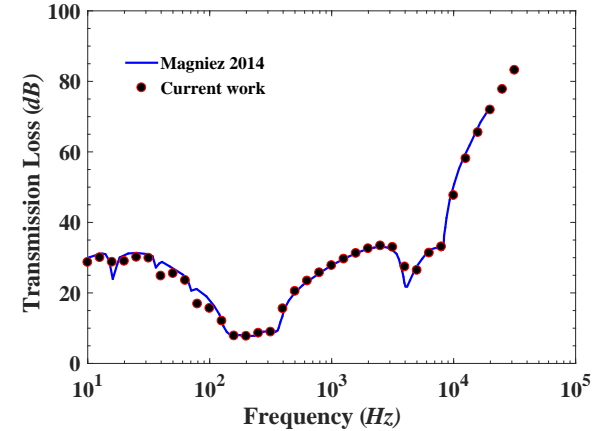
(a) TL comparison between Flugge-Lure-Byrne thin walled theory and the 3D theory of elasticity for three different incident angles ( $\alpha = \pi/6; \pi/3; \pi/2$ ) at Mach=0.



(b) STL comparison between the Love's bending shell theory and 3D theory of elasticity with respect to three different incident angles (\*  $30^\circ$ ; O  $45^\circ$ ; □  $60^\circ$ ).



(c) Cylinder TL comparison between Donnel and Mushtari shell theory (Ref. [64]) and the 3D theory of elasticity for different structural damping ( $O, \eta = 0.1$ ;  $\Delta, \eta = 0.1$ ).



(d) Cylinder TL comparison between the current study and mixed 3D-Shell model presented in Ref. [69] excited by  $45^\circ$  oblique incident plane wave.

Figure 5.2: STL validations.

	$C_{ij}$	PZT4	$Ba_2NaNb_5O_{15}$		Aluminum
$\mathbf{c}_{ij}, \mathbf{C}_{ij} (N/m^2)$	$C_{11}$	$13.9 \times 10^{10}$	$23.9 \times 10^{10}$	$c_{11}$	$9.692 \times 10^{10}$
	$C_{12}$	$7.8 \times 10^{10}$	$10.4 \times 10^{10}$	$c_{12}$	$4.153 \times 10^{10}$
	$C_{13}$	$7.43 \times 10^{10}$	$5.2 \times 10^{10}$	$c_{13}$	$4.153 \times 10^{10}$
	$C_{22}$	$13.9 \times 10^{10}$	$24.7 \times 10^{10}$	$c_{22}$	$9.692 \times 10^{10}$
	$C_{23}$	$7.43 \times 10^{10}$	$5.2 \times 10^{10}$	$c_{23}$	$4.153 \times 10^{10}$
	$C_{33}$	$11.5 \times 10^{10}$	$13.5 \times 10^{10}$	$c_{33}$	$9.692 \times 10^{10}$
	$C_{44}$	$2.56 \times 10^{10}$	$6.5 \times 10^{10}$	$c_{44}$	$2.769 \times 10^{10}$
	$C_{55}$	$2.56 \times 10^{10}$	$6.6 \times 10^{10}$	$c_{55}$	$2.769 \times 10^{10}$
	$C_{66}$	$3.06 \times 10^{10}$	$7.6 \times 10^{10}$	$c_{66}$	$2.769 \times 10^{10}$
$\rho (kg/m^3)$	$\rho_{pz}$	7500	5300	$\rho$	2750

Table 5.1: Mechanical properties of  $Ba_2NaNb_5O_{15}$ , PZT4, and Aluminum.

	$e_{ij}$	PZT4(Axial)	$Ba_2NaNb_5O_{15}$ (Axial)		PZT4(Radial)
$\mathbf{e}_{ij} (C/m^2)$	$e_{31}$	-5.2	-0.4	$e_{11}$	15.1
	$e_{32}$	-5.2	-0.3	$e_{21}$	-5.2
	$e_{33}$	15.1	4.3	$e_{31}$	-5.2
	$e_{15}$	12.7	2.8	$e_{53}$	12.7
	$e_{24}$	12.7	4.3	$e_{62}$	12.7
$\mathbf{\varepsilon}_{ij} (F/m)$	$\varepsilon_{11}$	$650 \times 10^{-11}$	$196 \times 10^{-11}$	$\varepsilon_{11}$	$560 \times 10^{-11}$
	$\varepsilon_{22}$	$650 \times 10^{-11}$	$201 \times 10^{-11}$	$\varepsilon_{22}$	$650 \times 10^{-11}$
	$\varepsilon_{33}$	$560 \times 10^{-11}$	$28 \times 10^{-11}$	$\varepsilon_{33}$	$650 \times 10^{-11}$

Table 5.2: Piezoelectric coupling and dielectric permittivity constants for axially and radially polarized piezoelectric materials.

Next, the cylinder TL has been studied for a single thick layer of the piezoelectric shell. The thickness of the elastic layer was set to zero in the general MATLAB code, which calculates the TL from Equation 5.37. The structure is assumed to be made of axially polarized PZT4 ( $n_a = 10$ ) and excited by an incoming incident plane wave ( $p_0 = 1 Pa$ ) with a normal incident angle ( $\alpha = \pi/2$ ). See more structural details in Table 5.1 and Table 5.2. The cylinder is filled with air ( $\rho_{in} = 1.29 kg/m^3$ ;  $c_{in} = 343 m/s$ ) and surrounded by external air-fluid ( $\rho_{ex} = 1.29 kg/m^3$ ;  $c_{ex} = 343 m/s$ ). Various cylinder thicknesses have been considered in order to show the validity of the proposed analytical solution for the thin and thick geometries. The TL was

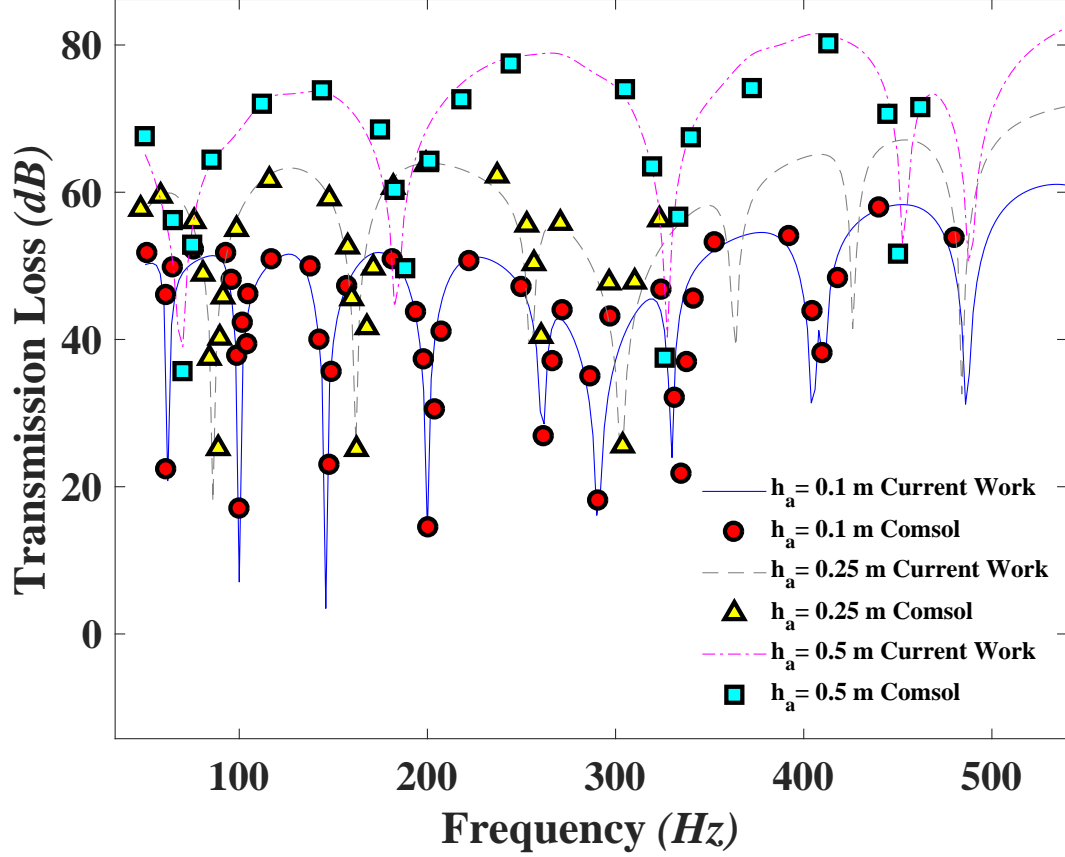


Figure 5.3: Cylinder TL comparison between the current study and FEM (COMSOL MULTIPHYSICS) for the thin, moderately thick, and very thick thicknesses ( $h_a = 0.1\text{ m}, 0.25\text{ m}, 0.5\text{ m}$ ). The cylinder is assumed to be made of a single layer of axially polarized non-graded PZT4 filled and surrounded by air, excited by a normal incident plane wave while the short-circuited boundary condition is applied at the inner and outer surfaces of the cylinder.

computed for the thin (*e.g.*,  $h_a = 0.1\text{ m}$ ), moderately thick (*e.g.*,  $h_a = 0.25\text{ m}$ ) and very thick (*e.g.*,  $h_a = 0.5\text{ m}$ ) cylinder.

Due to the lack of results in the literature for the TL of a piezoelectric cylindrical shell, COMSOL MULTIPHYSICS<sup>®</sup> have been utilized to check the validity of the

	<b>Water</b>	<b>Air</b>
$c \text{ (} m/s^2 \text{)}$	1500	340
$\rho \text{ (} Kg/m^3 \text{)}$	1.2	1000

Table 5.3: Acoustics properties of Water and Air.

proposed close form solution considering the piezo-electric coupling effect studied in this work. COMSOL MULTIPHYSICS<sup>®</sup> has been used to describe specific multiple physical models, including acoustic, elastic, and piezoelectric medium [209]. Like all finite element packages, COMSOL has both its pros and cons. The main pores are difficulty in modeling infinitely large domains, running-time cost, and numerical instability at high frequencies. In contrast, the proposed closed-form solution can tackle all the mentioned issues without difficulty. As an illustration of this, consider the following example. The external acoustic equation can be solved using the Bessel functions with enforcing the boundary condition at  $r = \infty$ , while COMSOL uses the Perfectly Matched Layer (PLM), which is an artificial boundary condition that absorbs the majority of the refracted waves. Nevertheless, there is always a partial reflection of waves from the PLM layer, which is the inevitable result of truncate computational regions in numerical methods. The FEM model includes the internal and external pressure acoustic media which are attached to the piezo-laminated cylinder as can be seen from Figure 5.4. The external acoustic pressure model is surrounded by cylindrical type of PML layer to ensure that the acoustic waves are not reflecting from the boundaries.

In order to find the optimized mesh size, a cylindrical shell with only one layer of isotropic materials were constructed in the FEM software. Next, the element size was decreased in the FEM model and the STL results were checked against the analytical results in Ref. [2] for the sound transmission loss through a cylinder made

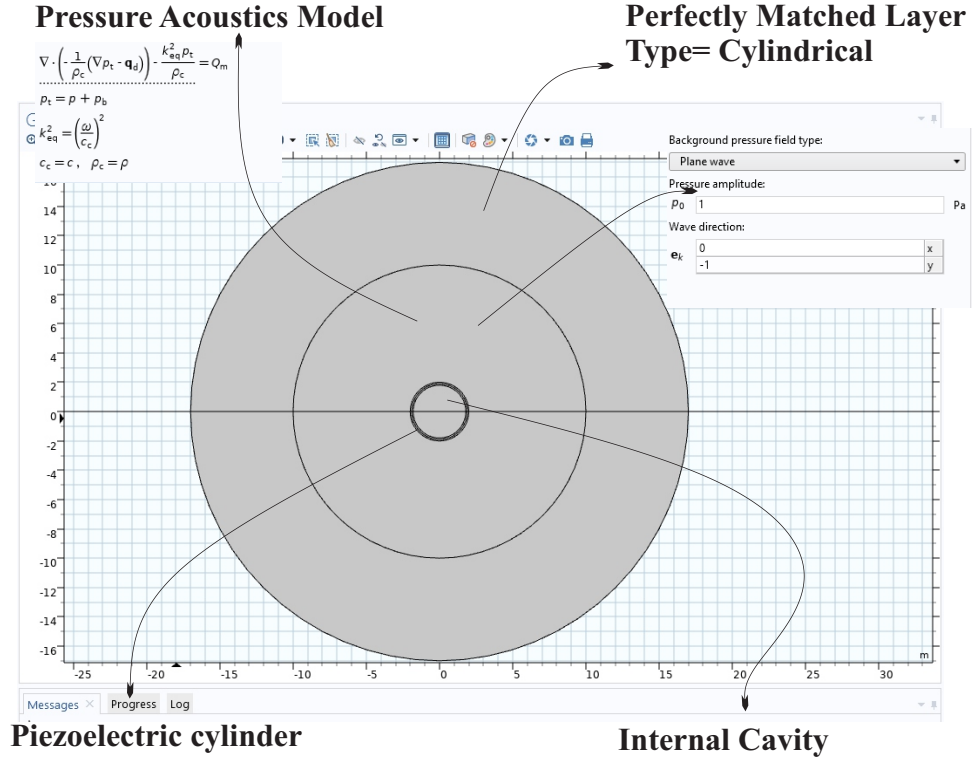


Figure 5.4: FEM modeling of the problem using COMSOL MULTIPHYSICS®.

of one elastic isotropic layer. At this step, the optimized mesh size was found. In the next step, the new FEM model with a single layer of axially polarized non-graded PZT4 materials with the same mesh size were constructed in the FEM software. Now, the results from the new FEM model were checked against the results from the current study. Figure 7.2 shows an excellent agreement between the current study and the commercial finite element package, COMSOL MULTIPHYSICS 4.4 [209]. The free triangular mesh type was used to generate the mesh for different areas as can be seen in Figure 5.5. In order to perform finite element simulation, about 430 mapped elements were used to model the PZT4 layers, about 20,402 free triangular elements were employed to model the internal and external acoustic fluids and 33420



elements were used to model the cylindrical PML layer. The numerical results will be discussed in the next section.

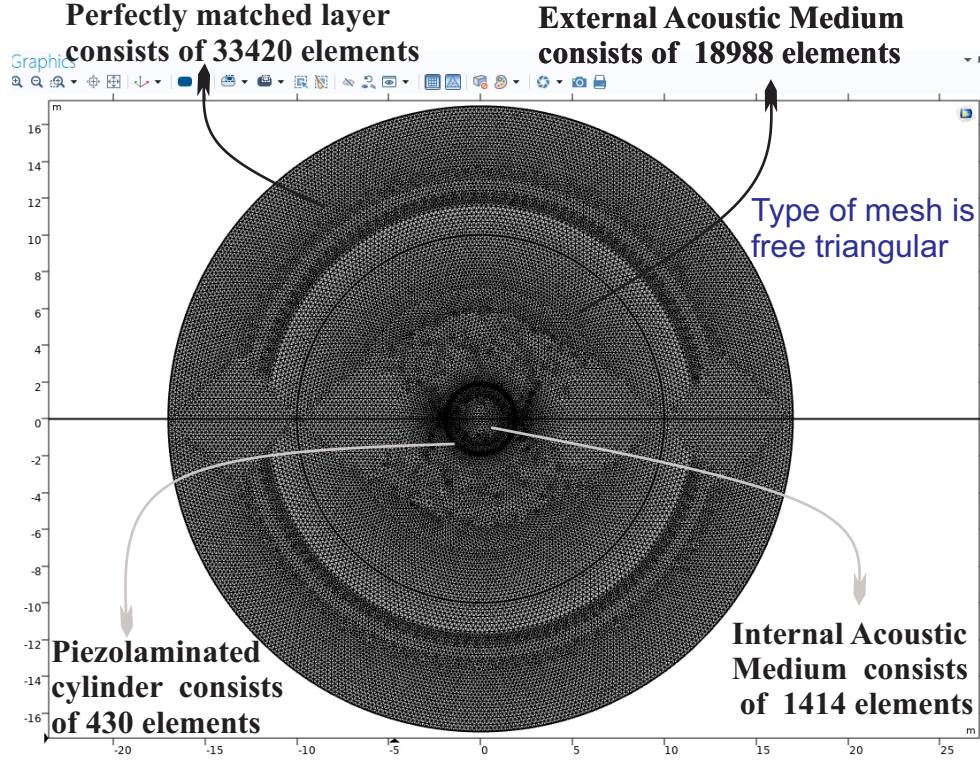


Figure 5.5: Mesh modeling of the problem using COMSOL MULTIPHYSICS®.

## 5.7 Results and discussion

In this section, the case studies will be discussed; before addressing the main results, it should be mentioned that due to the large number of variables involved in the proposed analytical solution, while keeping in mind the computational limitations, we shall focus on some logically selected examples. Accordingly, the elastic layer is considered to be made of a single aluminum layer ( $h_o = 0.1 \text{ m}$  and  $r_{in} = 1.8 \text{ m}$ ).

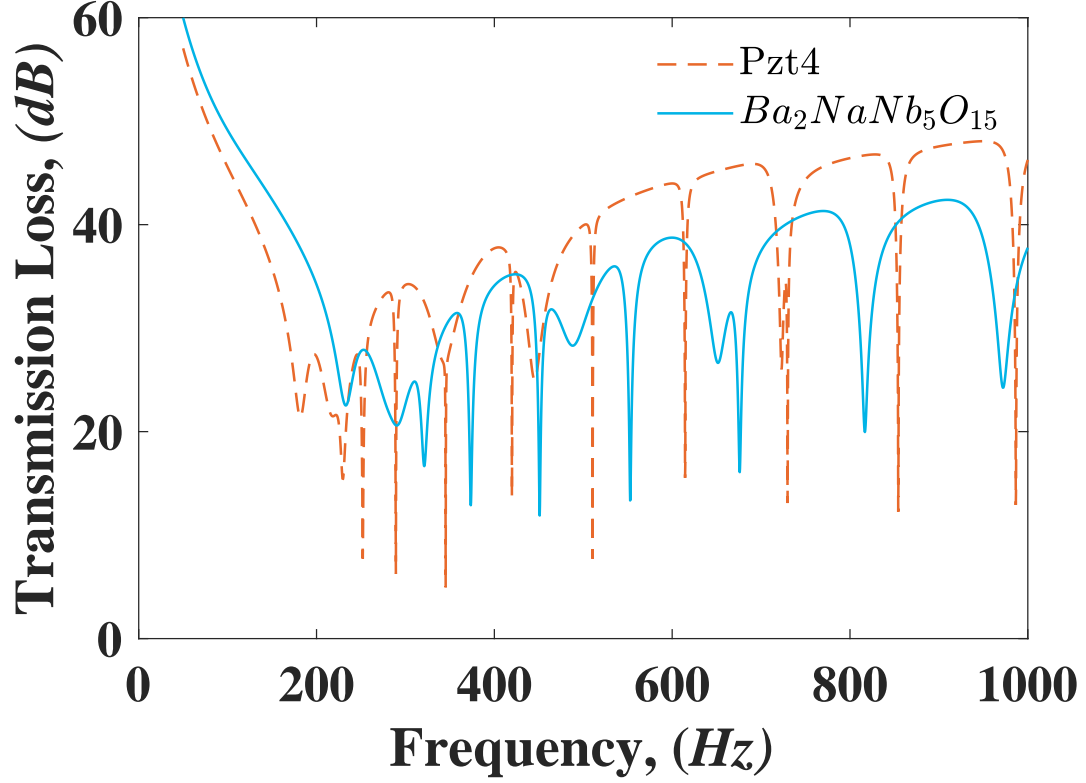


Figure 5.6: Effect of piezoelectric layer on the STL of the piezocylinder. The cylinder is filled with air and submerged in the water. The elastic layer of the cylinder is made of Aluminum, while the piezoelectric layer is axially polarized ( $r_{in} = 1.8 \text{ m}$ ,  $r_a = 1.9 \text{ m}$  and  $r_{ex} = 2 \text{ m}$ ). The short-circuited boundary condition was applied at the internal and external surfaces of the piezoelectric cylinder.

The actuator layer ( $h_a = 0.1 \text{ m}$  and  $r_a = 1.9 \text{ m}$ ) is perfectly bonded to the host structure with the material properties as given in Table 5.1 and Table 5.2. The piezo-composite cylinder is filled with air and submerged in water with the acoustic properties of the constituent material given in Table 5.3. The amplitude of the normal plane incident wave is considered to be  $1 \text{ Pa}$  in all our calculations. In all the following figures, the geometry and material properties of the piezo-composite structure are according to the above-mentioned values, unless specified otherwise.

Figure 5.6 shows the effect of the piezoelectric layer on the cylinder TL. The

$Pzt4$  and  $Ba_2NaNb_5O_{15}$  are axially polarized piezoelectric materials that have been chosen for the comparison. See more mechanical and electrical properties in Table 5.1 and Table 5.2. The results show that  $Ba_2NaNb_5O_{15}$  is more effective in the low-frequency range. This is an expected result because  $Ba_2NaNb_5O_{15}$  has a higher elastic constant than the  $Pzt4$ . Please keep in mind that the effect of stiffness on the TL is dominant in the low-frequency range, especially at frequency ranges between 20 Hz to 0.2 kHz. In contrast, the  $Pzt4$  displays better performance in the high-frequency range, specifically at frequency ranges from 0.25 kHz to 1kHz except for the frequency resonance. This is due to the fact that the density of  $Pzt4$  is higher than the  $Ba_2NaNb_5O_{15}$ , which makes it more efficient in the mass controlled high-frequency ranges. Therefore,  $Ba_2NaNb_5O_{15}$  is a better sound absorber in the low-frequency range, especially at frequency ranges between 20 Hz to 0.2 kHz, while the PZT leads to higher TL in the high-frequency range especially at 0.2 kHz to 1 kHz. This can be important guidance for choosing a piezoelectric sensor/actuator when lower or higher TL is preferred with a specific operating frequency range.

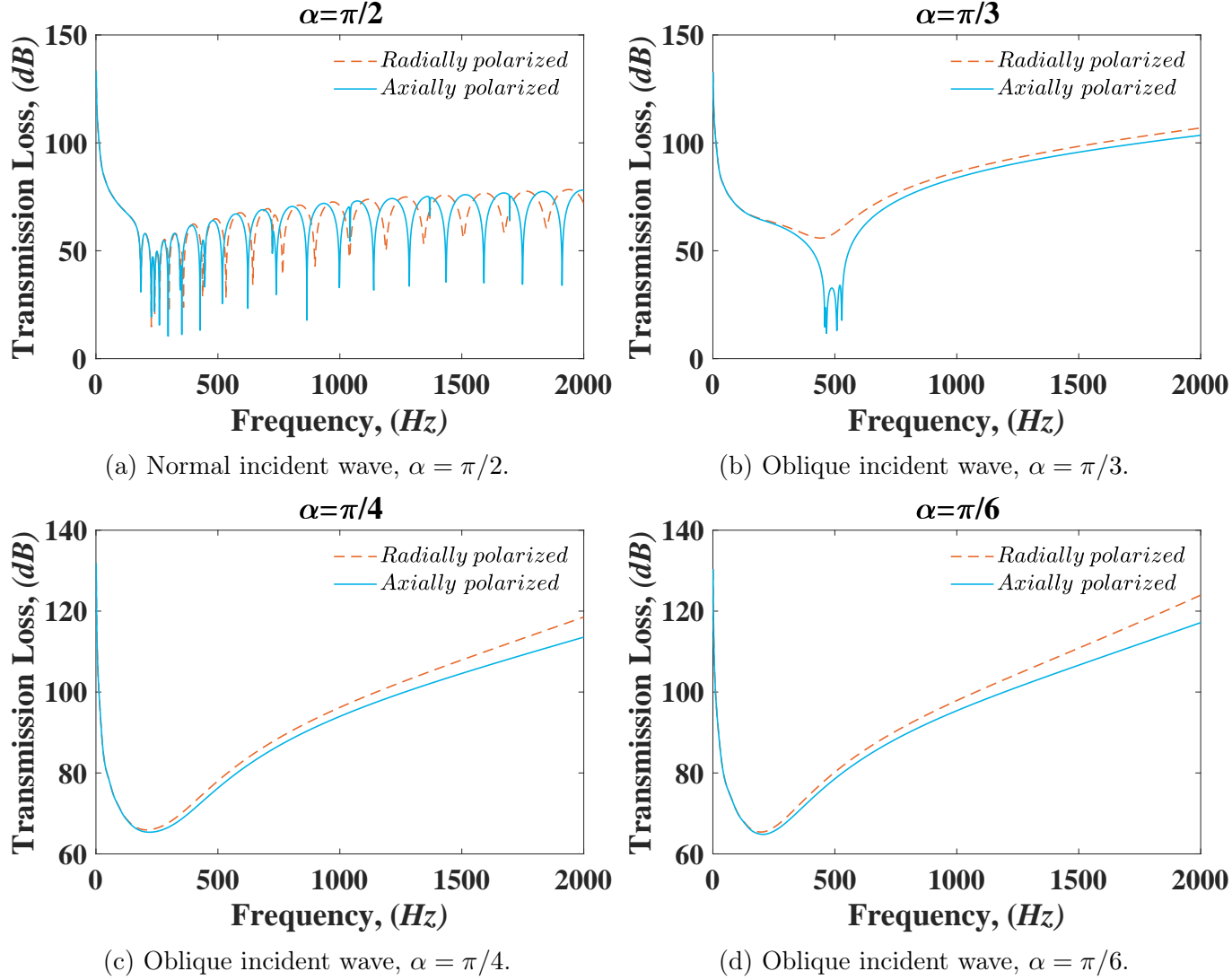


Figure 5.7: STL versus the frequency for different piezoelectric polarization, when the cylinder is filled with air and submerged in water subjected to different angles of the plane incident waves. The cylinder is made of Aluminum and PZT4 with  $r_{in} = 1.8 \text{ m}$ ,  $r_m = 1.9 \text{ m}$  and  $r_{ex} = 2 \text{ m}$ . The cylinder is filled and surrounded by air, and the short-circuited boundary condition is enforced at the inner and outer surface of the piezoelectric cylindrical shell.

Figure 6.6 shows the variation of TL versus the frequency for different polarization of piezoelectric materials and angles of plane incident wave in the frequency range of 0-2 kHz. The structure is filled and surrounded by air. The elastic layer is considered to be made of a single aluminum layer ( $h_o = 0.1 \text{ m}$  and  $r_{in} = 1.8 \text{ m}$ ). The actuator layer ( $h_a = 0.1 \text{ m}$  and  $r_a = 1.9 \text{ m}$ ) is perfectly bonded to the host structure. The short-circuited electrical boundary condition is enforced at the inner and outer surface of the piezoelectric cylindrical shell. It is observed from Figure 6.5a that there is no significant improvement of TL for a different direction of polarization in

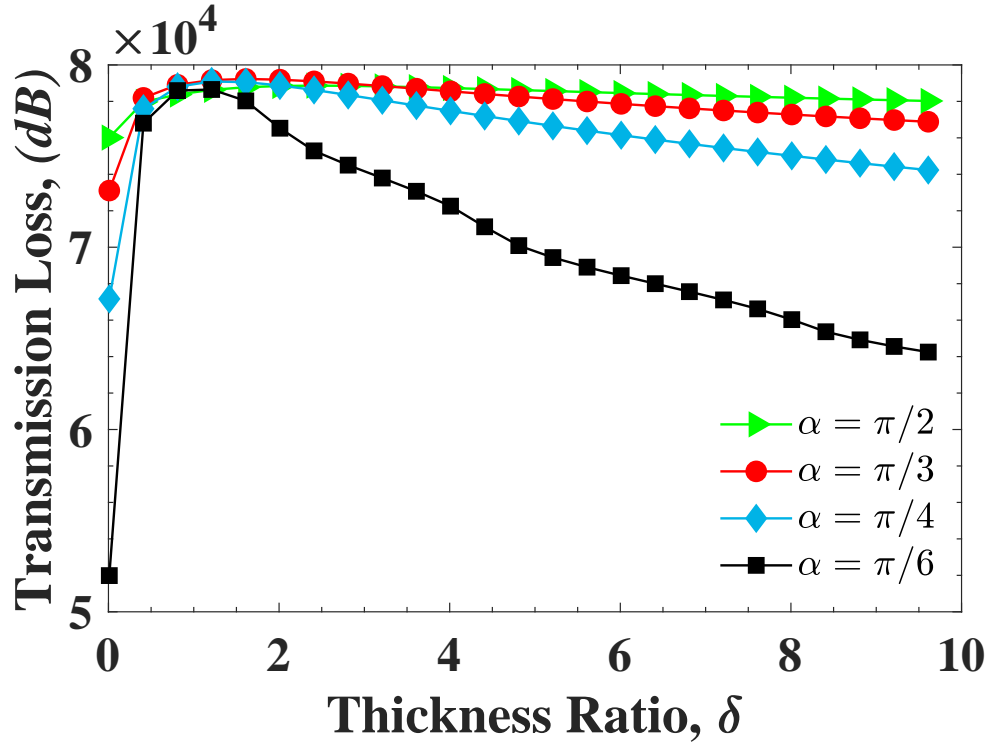


Figure 5.8: Accumulated cylinder TL versus the thickness ratio between the piezo-layer and host material,  $\delta = \frac{h_a}{h_o}$ , for the selected incident angles. The cylinder is made of Aluminum, and radially polarized PZT4 ( $r_{in} = 1.8 \text{ m}$  and  $r_{ex} = 2 \text{ m}$ ) surrounded and filled with air-fluid while the short-circuited boundary condition was enforced at the inner and outer surface of the piezoelectric layer.

the low-frequency ranges, while the TL moderately improves beyond a frequency of 1.5 kHz. The radially polarized piezoelectric layer also shows a higher value of TL, especially in the resonant frequencies indicating a better soundproof performance compared to the axially polarized piezoelectric material beyond a frequency of 1.5 kHz for the case of radially polarized piezoelectric materials. Figure 6.6c displays the TL for the incident angle,  $\alpha = \pi/3$ . It is interesting to see that the TL significantly improves for the radially polarized piezoelectric layer in comparison to the axially polarized case in the frequency 0.5 kHz, while there is no significant improvement at the low and high range frequencies. This is probably due to the fact that the dipoles of radially polarized piezoelectric materials are more sensitive in the direction of the applied forces resulting in a better performance in the case of the higher value of the incident angle. In addition, the radially polarized case does not have a dip with low TL at around 500 Hz. This is an important finding to avoid low TL at a specific resonance frequency. In other words, by choosing the proper piezo-electric polarization direction, a sudden TL drop can be avoided at a specific incident angle.

Figure 6.5c and Figure 6.6b did not show a significant difference in the low-frequency ranges ( $Freq. < 500 \text{ Hz}$ ), but more substantial improvement can be noticed at the higher frequency range ( $Freq. > 500 \text{ Hz}$ ) for the case of radially polarized piezoelectric materials. A comparison of all subplots given in Figure 6.6 clearly indicates that by decreasing the angle of the incident plane wave,  $\alpha$ , both radially and axially polarized cases show similar behavior, making both piezoelectric polarization practically ineffective for passive sound radiation isolation in the low value of incident angles. Moreover, the TL is more apparent, especially in the high-frequency ranges from 0.2 kHz to 2 kHz for radially polarized piezoelectric

materials. Another interesting finding is that there is no cylinder resonance frequency when the angle of the incident wave is smaller than  $\pi/4$ . This is because the cylinder resonances occur when the projection of the impinging wave's airborne wavelength along the axial direction into the cylinder and frequency match with the appropriate value of circumferential wave number,  $n$ . In the case of incident waves smaller than  $\pi/4$ , frequencies did not match, and that is why no resonance frequency can be seen (Koval [2]).

Figure 5.8 describes the effect of thickness ratio,  $\delta = \frac{h_a}{h_o}$ , on the accumulated TL for the different incident angles. The inner and outer radius of the cylinder is kept constant ( $r_{in} = 1.8 \text{ m}$ ;  $r_{ex} = 2 \text{ m}$ ) while the thickness ratio changes from 0.01 to 10. The piezoelectric material is considered to be PZT4 with the radial direction of polarization, while the core elastic layer is made of Aluminum, as given in Table 5.1. The accumulated TL is obtained by performing integration of Equation 5.37 over the frequency bounds from 1 Hz to 2 kHz. The vectorized adaptive quadrature built-in function of MATLAB<sup>®</sup> with default error tolerances is used to perform numerical integration in the frequency domain [210]. It is very interesting to see that by increasing the thickness ratio from zero to one, the TL reaches the maximum value, while further increasing the thickness ratio of piezoelectric layer over elastic layer cannot help to improve the TL beyond the optimal value of the thickness ratio regardless of the angles of the incident wave. The optimal thickness ratio given in Figure 5.8 can be used in the passive sound reduction of piezo-composite shells. In addition, the best performance of the sound isolation can be seen for the normal incident angle, while the worst case of sound isolation is corresponding to the incident angle of  $\alpha = \pi/6$  with low (thickness ratio smaller than 1) and high (thickness ratio

larger than 2) thickness ratios.

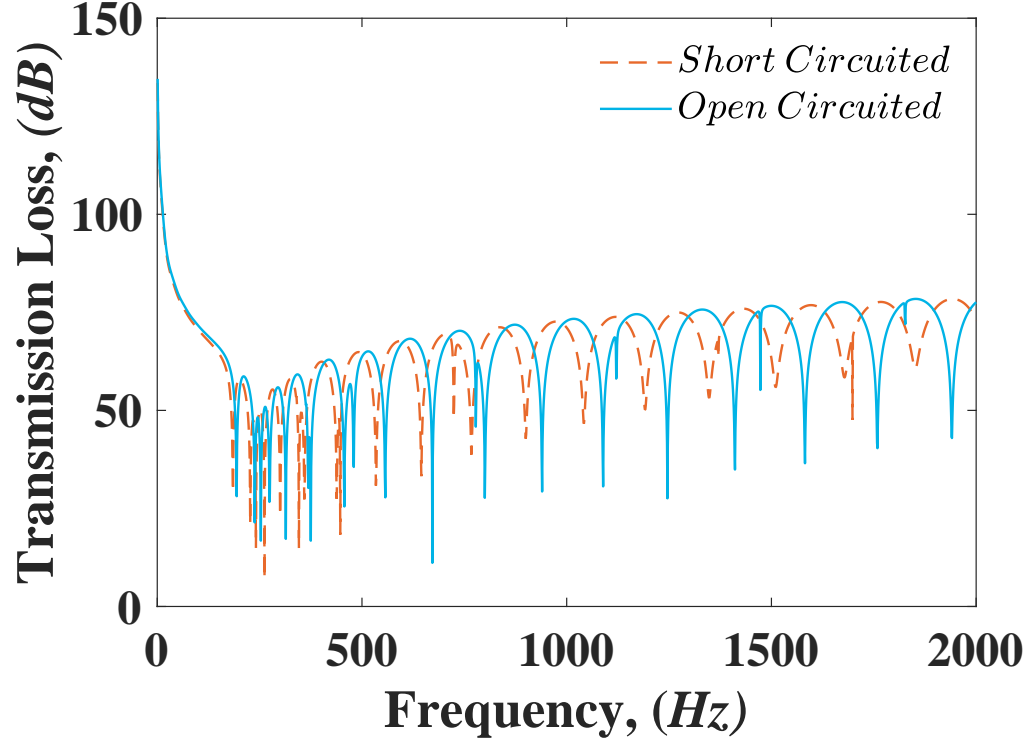


Figure 5.9: Cylinder TL versus the frequency for the short and open circuited electrical boundary conditions. The cylinder is radially polarized, made of PZT4 piezoelectric material and Aluminum ( $r_{in} = 1.8 \text{ m}$ ,  $r_m = 1.9 \text{ m}$  and  $r_{ex} = 2 \text{ m}$ ), filled and surrounded with air acted upon by a plane normal incident wave.

Figure 5.9 displays the effect of electrical boundary conditions on the STL of a radially polarized piezo-composite cylindrical shell. The cylinder is made of Aluminum, and PZT4 ( $r_{in} = 1.8 \text{ m}$ ,  $r_m = 1.9 \text{ m}$  and  $r_{ex} = 2 \text{ m}$ ) which is surrounded and filled by air as the acoustic properties of the fluid medium are given in Table 5.3. The angle of the incoming incident plane wave was assumed to be normal ( $\alpha = \pi/2$ ). The analysis of the figure shows several impressive results. Comparison between the short and open-circuited electrical boundary conditions in the low-frequency ranges shows no significant difference in the TL, while the TL becomes different for the two



boundary conditions in the range of frequency beyond the 0.5 kHz. Moreover, the dips with small values for the case of an open-loop boundary condition show a lower magnitude of TL indicating the fact that the open-circuited boundary condition is not quite effective for sound isolation in high-frequency ranges specifically at frequency ranges beyond 1 kHz, while the closed-circuit boundary condition leads to higher TL especially at the resonance frequencies, showing better performance in sound isolation in high-frequency ranges. In the case of open-circuit boundary conditions, the piezoelectric layer is stiffer. In contrast, in the short circuit boundary condition, the piezoelectric layer absorbs more energy due to the energy dissipation during charging. In other words, after impinging the plane incident wave on the surface of the cylinder, the acoustic power of the incident wave converts to the mechanical vibrations of the piezoelectric coupled structure. These mechanical vibrations will be converted to electrical charges using the direct piezoelectric effect (the generation of electricity when stress is applied) and then dissipates from the system by the short circuit electrical boundary condition. By this process, more acoustic energy of incident waves will be dissipated from the system system, resulting in a higher value of TL considering the piezoelectric effects.

Figure 5.11 shows the effect of the material gradient profile on the STL of an axially polarized cylinder for the selected type of piezoelectric composition. The elastic layer of the cylinder is made of non-graded aluminum materials  $\mu = 0$  (given in Equation 5.13), while the piezoelectric layer is made of axially polarized piezoelectric considering FGM properties along the radial direction with the total concentration of PZT4 materials (PZT-rich composition) in the inner layer of the piezoelectric shell and full concentration of  $Ba_2NaNb_5O_{15}$  (Ban-rich composition)

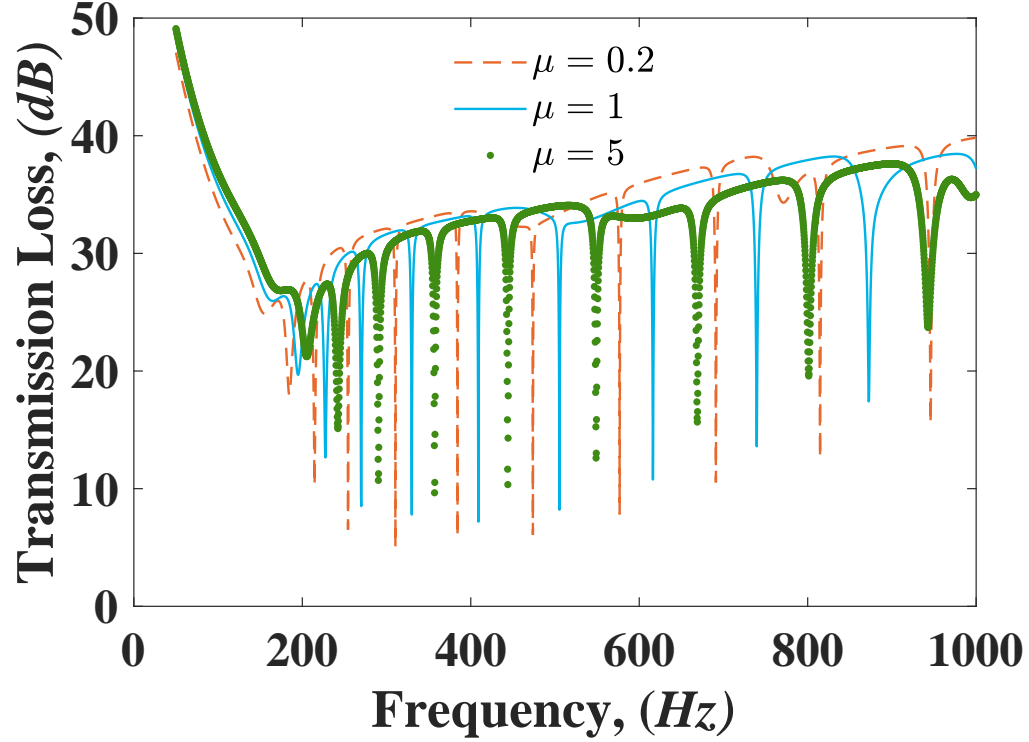


Figure 5.10: Variation of STL as a function of frequency for the selected material gradient profiles ( $\mu = 0.2, 1, 5$ ). The cylinder is axially polarized, made of FGPM perfectly bonded to the internal shell made of aluminum ( $r_{in} = 1.8 \text{ m}$ ,  $r_m = 1.9 \text{ m}$ , and  $r_{ex} = 2 \text{ m}$ ), filled with air and fully submerged in the water acted upon by a normal plane incident wave.

at the outermost laminated layer of the piezoelectric shell ( $r_{in} = 1.8 \text{ m}$ ,  $r_a = 1.9 \text{ m}$  and  $r_{ex} = 2 \text{ m}$ ). Please note that all the mechanical and electrical properties of the functionally graded piezoelectric layer are changing along the radial direction with different concentrations of PZT4 and  $Ba_2NaNb_5O_{15}$ . The short-circuited electrical boundary condition was applied at the internal and external surfaces of the piezoelectric cylinder. The cylinder is filled with air and fully submerged in the water subjected to a normal incident plane wave. It can be clearly seen that the STL is notably higher for the Ban-rich composition profile (i.e.  $\mu = 5$ ) than the case

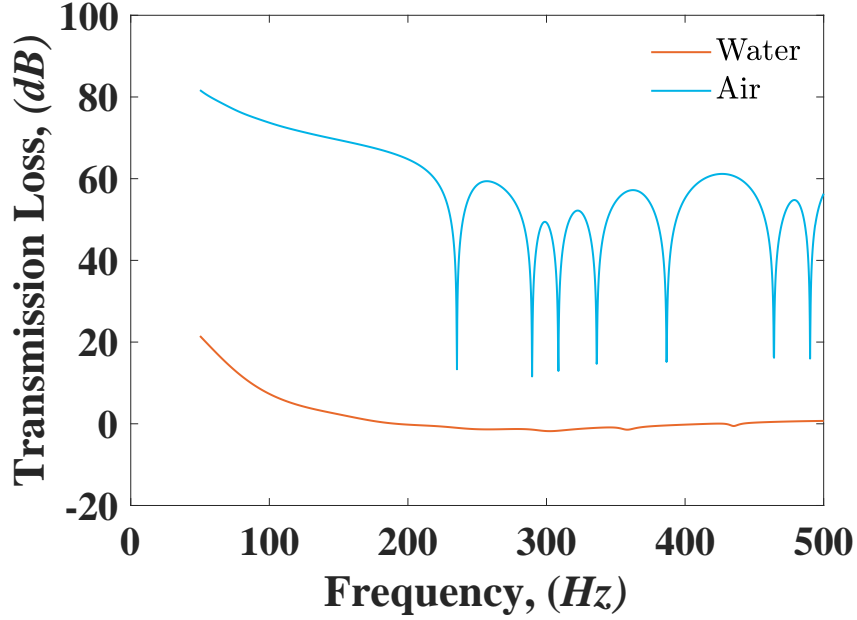


Figure 5.11: STL spectrum for the selected acoustic fluids. The cylinder is axially polarized, made of PZT4 perfectly bonded to the internal shell made of aluminum ( $r_{in} = 1.8 \text{ m}$ ,  $r_m = 1.9 \text{ m}$ , and  $r_{ex} = 2 \text{ m}$ ), insonified by a normal plane incident wave, filled with and submerged in water/air.

of PZT4-rich composition in a frequency lower than 0.2 kHz. This can be linked to the higher material stiffness of the Ban-rich profile in comparison to the PZT4-rich one because the stiffness is dominant in the lower frequency ranges. Moreover, the PZT-rich composition displays slightly better performance in the sound isolation in the frequency range between the 0.2 kHz to 1 kHz except for the dip low values. This can be related to the higher spatial density of the PZT4-rich composition to the Ban-rich counterpart which makes the PZT4-rich a more practical sound absorber in the high-frequency regions [66].

Figure 5.11 shows the effect of fluid characteristics on the STL of an axially polarized cylinder. The cylinder is axially polarized, made of PZT4 materials, perfectly bonded to the internal shell made of aluminum ( $r_{in} = 1.8 \text{ m}$ ,  $r_m = 1.9 \text{ m}$ ,

and  $r_{ex} = 2 \text{ m}$  ), insonified by a normal plane incident wave. The cylinder is considered to be filled and submerged with either water (with considerable low compressibility compared with air) or air in order to study the effect of fluid properties on the STL. The acoustic properties of the fluid medium are given in Table 5.3. The results show that the acoustic TL is higher for air in comparison to water. Water is a more incompressible fluid compare to air result in having a higher speed of sound. Consequently, for the case of water, more fraction of incoming incident waves will be transferred through the cylinder due to the low comparability of water resulting in a low TL. This is also evident from Equation 5.38, which shows the reverse relationship between STL and speed of sound. It can also be concluded that TL is higher for compressible fluids than incompressible fluids. Another interesting observation is that the dips of negative are very small in the case of water compared to the air one. With water (low compressibility) in and out the shell, the natural modes of the shell structure are hard to be excited compared with air, resulting in very small dips of negative. This phenomenon can be found in the literature as well ([211]).

## 5.8 Conclusion

The study presented here concentrates on the theoretical modeling and estimation of TL of an arbitrary thick infinite piezo-composite cylindrical shell. The 3D theory of piezo-elasticity, state-space approach, and transfer matrix method have been employed to capture the dynamics of the thick cylindrical shell model. Two different piezoelectric polarizations have been considered. The validity of the presented analytical solution was cross-checked by simplified models available in the literature.

Due to the lack of available results for the TL of the piezoelectric cylinder, a finite element simulation has been carried out to double-check the result of a purely piezoelectric cylindrical shell. The final result shows an excellent agreement between the FEM and the proposed analytical solution. The main findings of this research are as follows:

- By increasing the thickness of the cylinder, the magnitude of TL increases while the number of minimum values decreases.
- The radially polarized piezoelectric shows a better performance in the cylinder isolation compared to the axially polarized one, especially in the high value of incident angles at a high frequency larger than 500Hz.
- PZT4 shows a better sound isolation performance in comparison to  $Ba_2NaNb_5O_{15}$  in high-frequency ranges, while the  $Ba_2NaNb_5O_{15}$  provides more isolation in low-frequency ranges.
- Short-circuited electrical boundary conditions can be used to improve the sound isolation performance of the piezo-composite cylinder in high-frequency ranges considering the energy dissipation during the charging and discharging process.
- The best sound isolation performance of the piezo-composite cylinder can be achieved by fixing the thickness ratio of the piezoelectric to the elastic layer to approximately one, regardless of the angle of the incoming incident plane wave.
- Fluids with higher compressibility characteristics show a higher value of TL compares to low compressibility fluids.

The proposed analytical model has three main advantages over the FEM. It can easily handle the TL for high-frequency range, low computational cost, and covering infinite acoustics domains. It is worth noting that the proposed solution can easily handle fully anisotropic material with the different piezoelectric polarization directions. In addition, the presented model can be easily employed to investigate active and passive TL control from the piezo-composite cylindrical shells.

## Chapter 6

# Active Broadband STL Control Through an Arbitrary Thick Smart Piezo-composite Cylinder

*“All science is concerned with the  
relationship of cause and effect.  
Each scientific discovery increases  
man’s ability to predict the  
consequences of his actions and thus  
his ability to control future events..”*

---

Laurence J. Peter

Sound isolation is one of the most vital issues in the structural enhancement of engineering structures. Designing, studying and enhancement of sound isolation methods and associated techniques have been widely investigated by many scholars (Li and Zhang [28], Dong and Wang [32], Young and Crocker [34], Oba and Finette [35], Moore and Lyon [37]). The most common technique that has been widely investigated is based on the passive sound isolation technique by adding absorption

treatments to the main structure such as using shunt piezoelectric, viscoelastic, blocking masses and porous materials (Fu et al. [78], Arunkumar et al. [83], Fu et al. [79], Pietrzko and Mao [80], Talebitooti et al. [82], Talebitooti and Zarastvand [81], Daneshjou et al. [72], Chronopoulos et al. [73]). However, these methods have disadvantages, such as the increase in the structural weight, decline in the sound attenuation performance of insulation materials due to aging, temperature or frequency variation. Recent advancements in the field of intelligent structure offer significant progress in dealing with air-borne noise control problems [96, 39]. The use of smart piezoelectric structures is an attractive choice. Piezoelectric materials have advantages such as low cost, reliability, durability, high performance, and low weight. However, there are relatively few works that use piezoelectric materials to control the airborne noise of cylindrical structures. The current work is aimed to fill this gap in the literature by using the 3D theory of elasticity and piezoelectricity to give highly accurate results even in high-frequency ranges by considering the peripheral waves of higher order. The 3D theory of elasticity used in the current work, unlike the shell theories, can describe the refraction of acoustics waves from the internal and external surface of the cylinder Veksler [185]. Unlike the shell theories that apply the boundary conditions on the middle surface, the 3D theory of elasticity and piezoelectricity used to model the current problem imposes the boundary condition on the real external and internal surfaces [185]. This study also takes advantage of the direct piezoelectric effect, which uses the piezoelectric layer as a sensor and can easily be implemented with minimal modification of the original structure compared to other pressure sensors. The analytical solution is accomplished, first by modeling the corresponding vibro-acoustic problem and then by sending a control signal from



the distributed piezoelectric sensor through a controller process to drive the outer piezoelectric actuator. In other words, the vibroacoustic response of an elastic cylinder can be actively mitigated via the smart alteration of damping characteristics of the piezo-composite external actuator layer with suitable control signals. Here, the STL convergence for different incident angles is studied. Also, the effect of different controller gain parameters on the STL spectra of radially/axially polarized piezo-composite cylinder for four different angles of incident waves are investigated.

The current study is of paramount importance as a fundamental problem in many interdisciplinary fields for active sound isolation enhancement of structures with solid-fluid interaction. It can help acoustic engineers to design structures with impressive noise isolation performance in a wide range of frequencies that can not be achieved by passive sound suppression techniques. Such an intelligent structure has a widespread application in noise abatement in the fuselage (Krakers et al. [5]) and marine applications (Caresta [4]). Finally, the frequency domain closed-form solution can be used as a reliable benchmark for confirming results evaluated by the approximate or numerical method, particularly in the cases that there is a lack of experimental data.

## 6.1 Problem Description for STL Control Through an Smart Piezo-composite Cylinder

In this section, a distributed sensor layer is augmented to the structure given in chapter 5, in order to send a control signal through a controller with certain feedback gain to drive the external piezoelectric actuators.

Here, we consider a hollow piezoelectric laminated cylinder with infinite length, a core layer made of orthotropic materials with thickness  $H_o$  which is coated by a piezoelectric actuator and sensor on its outside and inside surfaces. The thickness of the piezoelectric sensor and actuator layers are  $H_s$  and  $H_a$ , while the electrodes, as well as the electrical connection between the sensor and actuators, are shown in Figure 8.1. The cylinder is assumed to be filled and submerged in the fluid with acoustic characteristics of  $(\rho_{in}, c_{in})$  and  $(\rho_{ex}, c_{ex})$ , respectively. The cylinder is considered to be excited by a progressive incident plane wave. Such a smart sensor/actuator structure will later be used to attain impressive wave isolation performance. Before addressing the control strategy, we shall concisely describe the elasto-acoustic model of the piezo-composite cylinder structure coupled with the internal cavity and external fluid medium.

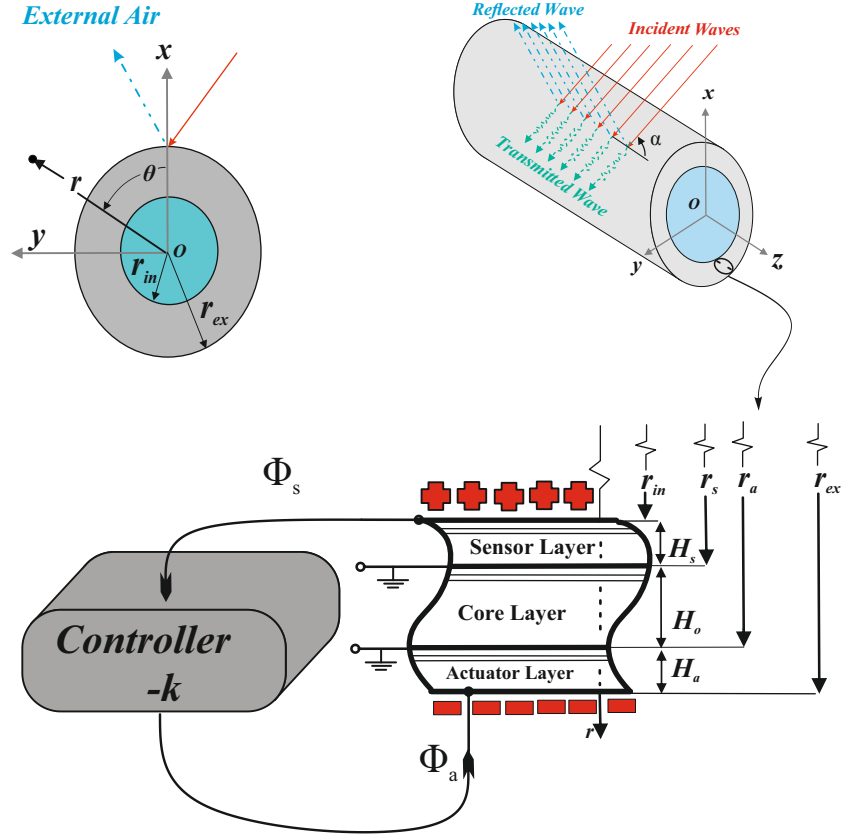


Figure 6.1: Schematic of feedback controller for piezo-laminated cylindrical shell.

## 6.2 Sensor Layer Modeling

The structural modeling for the actuator and core layer is thoroughly discussed in section 4.1. The only difference is considering the transfer matrices for the sensor layer, which will be addressed in the following section. The acoustic model and calculation of STL are comprehensively discussed and explained in section 3.1.1 and subsection 5.5.1. The boundary conditions and controller implementation will be discussed next.

### 6.2.1 Modal Spatial State Equations

Now, by straight use of Equation 5.8 to Equation 5.18b the following uncoupled modal state-space equations emerge as ([19])

$$\frac{d\mathbf{v}_n(r, \omega)}{dr} = \mathbf{g}_n(r, \omega)\mathbf{v}_n(r, \omega), \quad (6.1a)$$

$$\frac{d\mathbf{V}_n(r, \omega)}{dr} = \mathbf{G}_n(r, \omega)\mathbf{V}_n(r, \omega), \quad (6.1b)$$

where  $\mathbf{g}_n(r, \omega)$  is  $6 \times 6$  modal coefficient matrix whose elements are given in Equation B.3.1, whereas  $\mathbf{G}_n(r, \omega)$  is  $8 \times 8$  modal coefficient matrix whose arrays for the axially and radially polarized piezoelectric materials are provided in subsection B.3.2 and subsection B.3.3, respectively. The direct solution for Equation 6.1 is very complex as the matrix coefficients are radially dependent ([19]). So, an adaptive laminated technique should be implemented to solve the Ordinary Differential Equations (ODE) given in Equation 6.1. The details of the solution procedure of Equation 6.1 are given in subsection 4.1.2 ([3, 159]). After implementing the adaptive laminated model considering perfect bounding condition at the interfaces, the global transfer matrix,  $\mathbf{\Theta}_n$ , can be obtained in the form of ([159])

$$\mathbf{Y}_n(\omega) = \mathbf{\Theta}_n(\omega)\mathbf{\Upsilon}_n(\omega), \quad (6.2a)$$

$$\mathbf{Y}_n(\omega) = [\mathbf{V}_n^a(r_{ex}, \omega)^{Tr} \ D_r^n(r_s, \omega) \ \phi_n(r_s, \omega)]^{Tr}, \quad (6.2b)$$

$$\mathbf{\Upsilon}_n(\omega) = [\mathbf{V}_n^s(r_{in}, \omega)^{Tr} \ D_r^n(r_a, \omega) \ \phi_n(r_a, \omega)]^{Tr}, \quad (6.2c)$$

$$\mathbf{\Theta}_n(\omega) = \begin{pmatrix} \mathbf{S}_n(:, 1:6)\mathbf{T}_n^s(1:6,:) & \mathbf{S}_n(:, 7:8) \\ \mathbf{T}_n^s(7:8,:) & 0 \end{pmatrix}, \quad (6.2d)$$

$$\mathbf{S}_n(\omega) = [\mathbf{T}_n^a(:, 1:6)\mathbf{t}_n \ \mathbf{T}_n^a(:, 7:8)], \quad (6.2e)$$

where  $\mathbf{T}^t$  indicates the transpose of the matrix while the superscript  $s$  and  $a$  show the sensor and actuator layers, respectively. Moreover, it should be specified that  $\mathbf{T}_n(:, 1 : 6)$  contains all the first six columns of  $\mathbf{T}_n$ . In addition,  $\mathbf{T}_n(:, 7 : 8)$  contains the last two columns of  $\mathbf{T}_n$ .

## 6.2.2 Boundary Conditions and Controller Implementation

The fluid-solid compatibility conditions that must be enforced at the internal and external surfaces of the piezo-composite cylinder are expressed as follows ([12])

$$\Sigma_{r\theta}^n(r_j, \omega) = \Sigma_{rz}^n(r_j, \omega) = 0, \quad j = in, ex, \quad (6.3a)$$

$$\Sigma_{rr}^n(r_{in}, \omega) = -p_n^T(r_{in}, \omega), \quad (6.3b)$$

$$\Sigma_{rr}^n(r_{ex}, \omega) = -p_n^I(r_{ex}, \omega) - p_n^R(r_{ex}, \omega), \quad (6.3c)$$

$$U_r^n(r_j, \omega) = \frac{1}{\rho_j \omega^2} \left. \frac{\partial p_n^j(r, \omega)}{\partial r} \right|_{r=r_j}, \quad j = in, ex. \quad (6.3d)$$

The grounded electrical boundary conditions must be enforced at the external and internal layer of sensor and actuator, respectively, as [95]

$$\phi_n(r_i, \omega) = 0, \quad i = a, s, \quad (6.4)$$

where,  $\phi_n$  is the modal electric potential. The negative feedback velocity is implemented to enhance the sound isolation performance of the cylindrical structure by sending the electrical charge created over the electrode of the sensor layer into a controller with an appropriate closed-loop gain amplifier that generates a suitable electrical charge. The electrical charge that derives the actuator can be written as

([212])

$$\phi_n(r_{ex}, \omega) = -k \phi_n(r_{in}, \omega), \quad (6.5)$$

with the direct substitution of boundary conditions presented in subsection 6.2.2 into the global transfer matrix of Equation 6.2, after some tedious manipulation, the final solution emerges as

$$\mathbf{A}_n \mathbf{x}_n = \mathbf{b}_n, \quad (6.6)$$

in which,  $\mathbf{A}_n$ ,  $\mathbf{x}_n$  and  $\mathbf{b}_n$  are provided in subsection B.4.3.

## 6.3 Model Validation

Considering our computational limitations besides the wide diversity of physical parameters engaged in the proposed vibroacoustic formulation, some practical examples shall be deliberated here. The speed of sound waves and densities of the internal and external fluids are given in Table 5.3.

The internal and external piezoelectric layers are both considered to be made of either axially or radially polarized PZT4. The mechanical and electrical properties of the piezoelectric layers are given in Table 5.1 and Table 5.2, respectively. The amplitude of the acoustic incident wave is considered to be equal to one ( $|p_0| = 1 \text{ Pa}$ ) in all calculations.

A general MATLAB<sup>®</sup> code is scripted to calculate the TL for the piezo-composite cylinder as well as obtaining the solution of Equation 6.6. The computations were performed on a cluster of INTEL<sup>®</sup> Core(TM) i5-7500 CPU @ 3.40 GHz desktop

computer (32.0 GB Ram DDR4) capable of exhaustive parallel calculations. The MATLAB PARALLEL COMPUTING TOOLBOX was utilized to expedite our calculation of STL [208]. Before addressing the main results of simulations, the correctness of the above described analytical solution shall be briefly verified.

Thus, we used our general MATLAB code to calculate the STL through the piezo-composite cylinder ( $r_{in} = 1.95 \text{ m}$ ,  $r_s = 1.98 \text{ m}$ ,  $r_a = 1.99 \text{ m}$ ,  $r_{ex} = 2 \text{ m}$ ) with actuator and sensor layers made of axially polarized PZT4 (see Table 5.2) while the core layer is made of Aluminum material as its mechanical properties given in Table 5.1. The cylinder is surrounded and filled with air and excited by a normal incident plane wave ( $\alpha = \pi/2$ ). There was no result in the literature for comparison of our model even for the case of the thin piezoelectric cylinder. Consequently, a finite element model was constructed in COMSOL MULTIPHYSICS<sup>®</sup> to verify the accuracy of the proposed solution considering both the sensor and actuator piezoelectric layer. In order to simulate the infinite acoustic space surrounding the cylinder, a PLM is used to let the scattered waves pass through the boundary without any reflection back to the main domain. The advantage of our model compared to the finite element package is that in our model, the Hankel function is utilized to enforce the infinite domain while in the finite element package, there is always a partial reflection of waves from the truncated region, which causes inaccuracy in the calculation of scattered pressures.

In addition to the accuracy of the proposed solution, our code is faster compared to the Finite Element models. It takes about 21.086 seconds to get the result using the proposed model while we used only one core to get the result, whereas it takes about 1376 seconds for the FEM to get the result, while the FEM benefits from

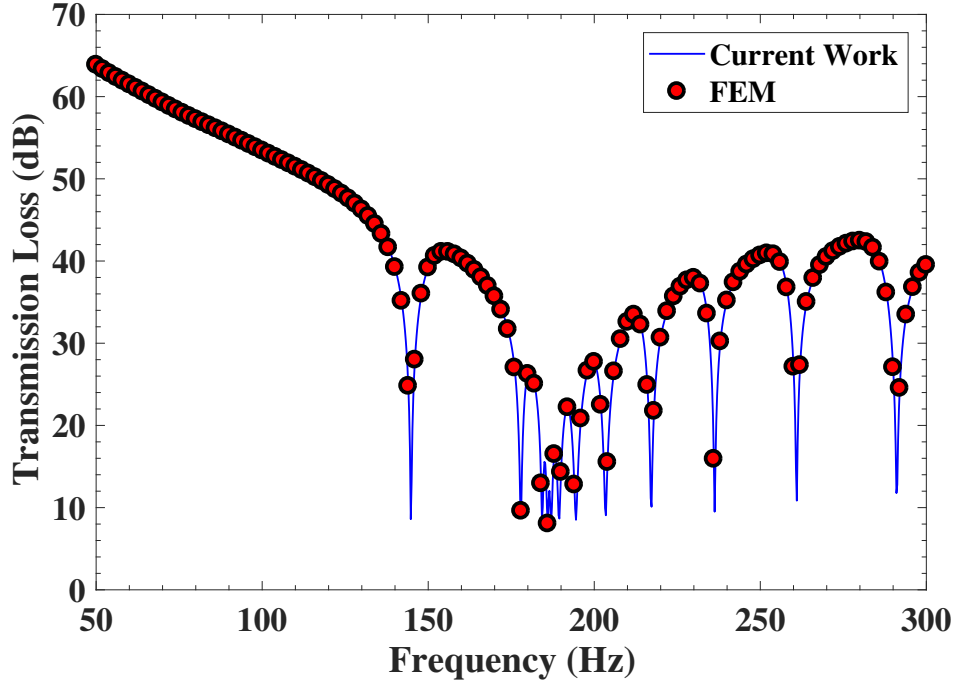


Figure 6.2: Comparison of STL with FEM (COMSOL MULTIPHYSICS) for a tri-layer piezoelectric cylinder. The cylinder is assumed to be made of axially polarized PZT4 ( $r_{in} = 1.95 \text{ m}$ ,  $r_s = 1.98 \text{ m}$ ,  $r_a = 1.99 \text{ m}$ ,  $r_{ex} = 2 \text{ m}$ ) with closed-loop electrical boundary condition applied to both of the sensor and actuator layers whereas the core layer is made of Aluminum material. The structure is surrounded and filled with air and excited by a normal incident plane wave ( $\alpha = \pi/2$ ).

the parallel computation of four logical cores. Consequently, the proposed model can generate results about 65 times faster than the FEM. High computation cost in FEM is because it needs to refine mesh for the whole domain, in this case, the area of surrounded fluid should be big enough for better accuracy in the results, and also, the PLM layer should be thick enough to absorb all scattered waves, which results in having big mesh with a high number of degrees of freedom. Please note that 347085 degrees of freedom are used in our FEM. Finally, the result, as shown in Figure 7.2, displays a good agreement between the proposed model and COMSOL



MULTIPHYSICS 4.4 simulation results [209].

## 6.4 Results and discussion

Before addressing the main results, we shall check the convergence of our solution. The convergence of our solution was achieved by increasing the value of the series truncation constant,  $N$ , while the stability of the calculated STL values was investigated. The code was programmed in a way to repeat the calculation until the difference between the values of two consecutive STL falls into a predefined error bound ( $\Delta TL \leq 2.22 \times 10^{-16}$ ). When the above criterion was satisfied, the calculation of STL was terminated and the new value of STL was believed to be converged. The maximum value of truncated constant correspondent to the converged value of STL was considered to be optimal truncated constant ( $N_{opt}$ ).

Figure 6.3 shows the convergence study of STL for four selected incident wave frequencies and different angles of the acoustic incident plane wave ( $\alpha = \pi/18, \pi/4, \pi/3, \pi/2$ ). The piezo-composite cylinder is considered to be made of a radially polarized PZT4, filled and submerged in water. The values of converged truncated mode numbers beyond which, the value of STL becomes stable are shown in every sub-figure. It is evident that the convergence rate of STL significantly deteriorates as the frequency of excitation increases. For instance, considering Figure 6.3a the fastest STL convergence ( $N = 1$ ) happens at the lowest excitation frequency ( $f = 100 \text{ Hz}$ ,  $\alpha = \pi/18$ ) while the worst-case scenario occurs at high frequency ( $f = 10 \text{ kHz}$ ). As it is evident, there is an infinite number of modes for a continuous system, when the frequency of interest is low, the less number of natural frequencies are excited result in satisfying the stability in the calculation of STL by considering the low value of truncated

constant ([213]). Furthermore, considering the constant excitation frequency, the highest optimal truncated constant can be seen for normal incident angles ( $\alpha = \pi/2$ ). As the value of the incident angle decreases with a specific frequency, the value of the optimal truncated constant decreases. For example, the lowest value of truncated constant at the frequency of  $f = 10 \text{ kHz}$  for reasonable convergence is  $N = 15$  and  $N = 57$ , with the wave angles of  $\alpha = \pi/18$  and  $\alpha = \pi/2$ , respectively.

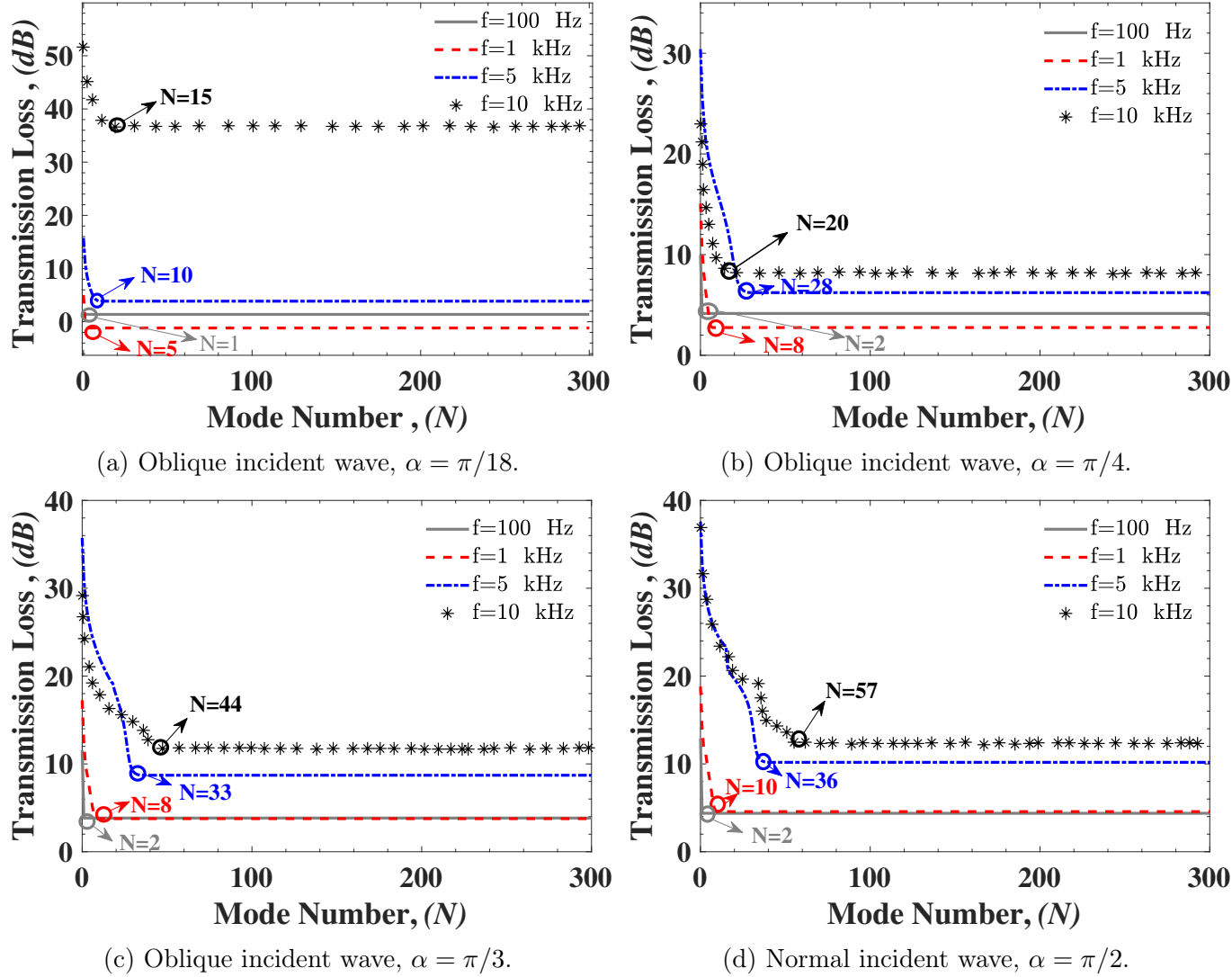


Figure 6.3: Convergence study for selected incident wave frequencies and different angles of an acoustic incident plane wave. The piezo-composite cylinder is assumed to be made of radially polarized PZT4, filled and submerged in water.

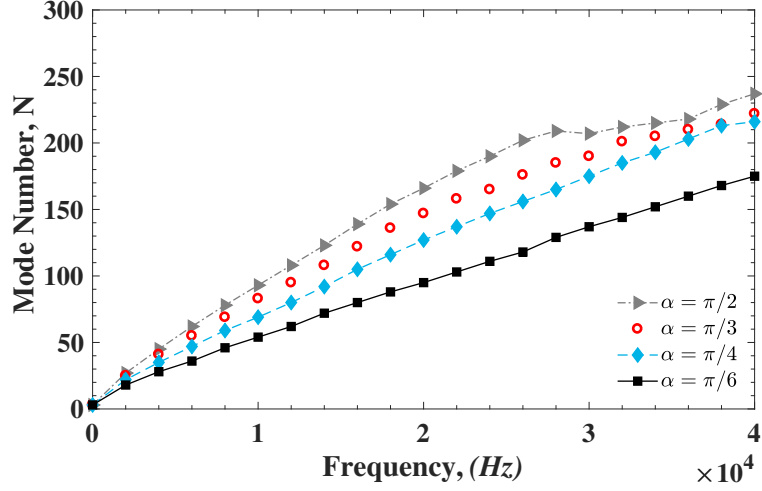


Figure 6.4: Variation of converged truncated mode number with respect to the frequency for selected angles of incident waves. The piezo-composite cylinder is assumed to be made of radially polarized PZT4, surrounded and filled with water.

Figure 6.4 shows the variation of optimal truncation constant versus the frequency for different values of the incident plane wave angles. The cylinder is assumed to be made of radially polarized PZT4 materials for sensor and actuator layers ( $r_{in} = 1.7 \text{ m}, r_s = 1.8 \text{ m}, r_a = 1.9 \text{ m}, r_{ex} = 2 \text{ m}$ ) while the core layer is made from aluminum material (See Table 5.1 and Table 5.2). The cylinder is filled and submerged in the water (See Table 5.3). Generally, the value of the optimal truncated mode number increases as the frequency of incident wave excitation increases. In other words, a higher number of modes should be included in our calculation to achieve an acceptable accuracy in the calculation of STL for a higher range of incident wave frequencies. In addition, as the value of incident wave angle increases, a higher number of modes should be included to satisfy the convergence criteria regardless of the frequency of excitation. The extreme cases can be seen between  $\alpha = \pi/6$  and  $\alpha = \pi/2$  as the results shown in Figure 6.4.

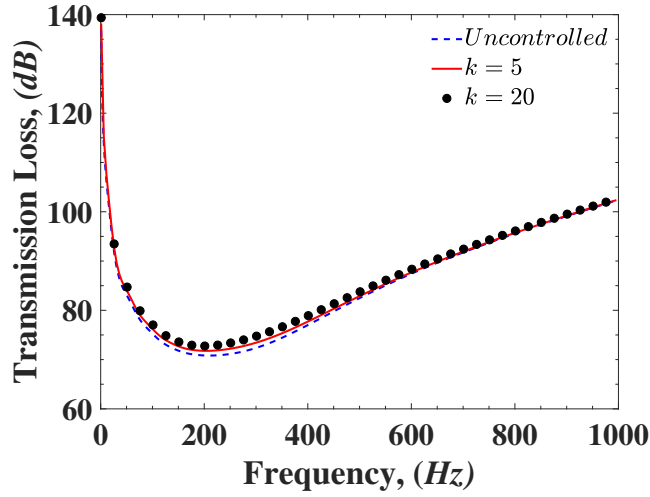
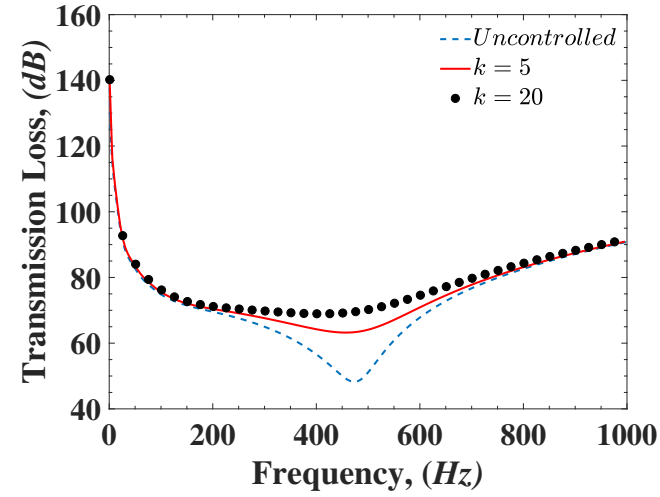
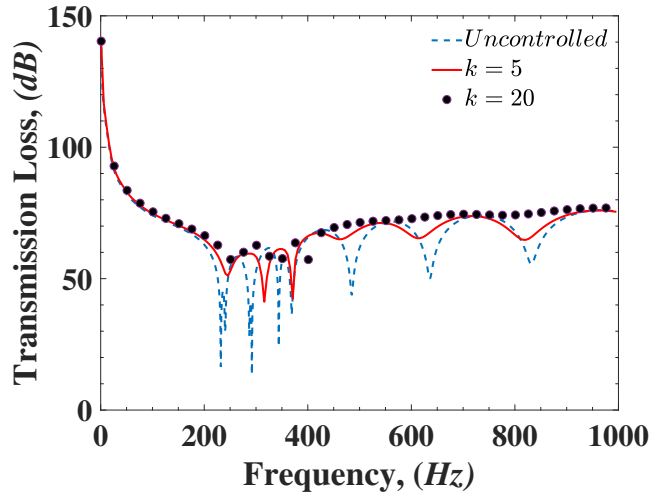
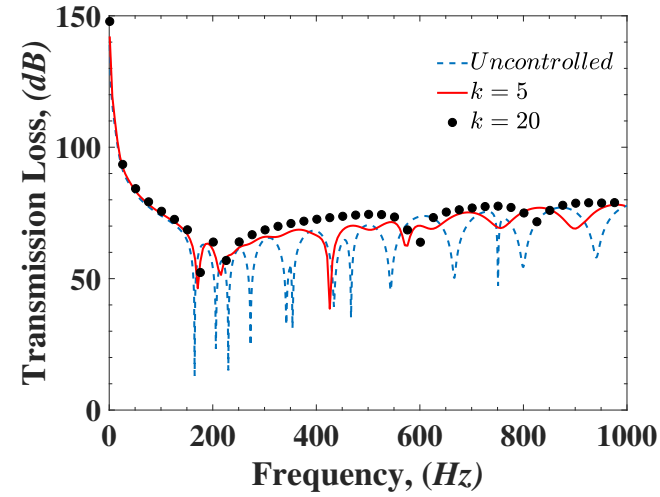
(a) Oblique incident wave,  $\alpha = \pi/4$ .(b) Oblique incident wave,  $\alpha = \pi/3$ .(c) Oblique incident wave,  $\alpha = 5\pi/12$ .(d) Normal incident wave,  $\alpha = \pi/2$ .

Figure 6.5: STL spectra of the radially polarized piezo-composite cylinder for four different angles of incident waves, based on the negative feedback control strategy with four different gain controls.

Figure 6.5 shows the STL spectra of the radially polarized piezo-composite cylinder for four different angles of incident waves ( $\alpha = \pi/4, \pi/3, 5\pi/12, \pi/2$ ), within the frequency range of ( $1 < f < 10^3 \text{ Hz}$ ) based on the negative feedback control strategy with four different gain controls. The external and internal layers of the cylinder are assumed to be made of radially polarized PZT4 ( $r_{in} = 1.7 \text{ m}, r_s = 1.8 \text{ m}, r_a = 1.9 \text{ m}, r_{ex} = 2 \text{ m}$ ) material, whereas the core layer is made of Aluminum (See Table 5.1 and Table 5.2).

As evident in the figure, for the un-controlled case, the total magnitude of the STL decreases as the value of the angle of the incident wave increases with the highest reduction observed in the normal angle of the incident wave. As the incident angle increases, the higher fraction of incident wave power contributes to the normal stress generated inside the cylinder leading to a lower STL. Regardless of the angle of incident waves, the controlled STL plots follow the uncontrolled variation trend in a smooth way. Generally, the negative control feedback strategy provides significant enhancement of the STL at resonance frequencies for the normal incident angle case ( $\alpha = \pi/2$ ).

As the value of the feedback gain,  $k$ , increases, the more undesirable STL resonance dips can be avoided, especially when the plane incident wave angle is close to the normal angle. The desirable effect of active control feedback declines as the incident wave angle approaches more inclined angles, such as the case for  $\alpha = \pi/4$ .

In the case of  $\alpha = \pi/2$ , as the incident plane wave impinges on the cylinder, it creates a significant uniform radial strain inside the cylinder, which generates a considerable electrical voltage in the internal sensor layer,  $E_r$ . (please see the constitutive Equation B.1.5). This electrical voltage will then drive the actuator layer

via the proper feedback gain. The electrical voltage applied to the actuator layer creates a strong radial electrical field,  $E_r * (-k)$ . By observing the Equation B.1.4, it can be concluded that the significant magnitude of the radial electric field,  $E_r$ , multiplying by the feedback gain,  $k$ , and the corresponding piezoelectric coupling constant,  $e_{11}$ , can create strong radial structural stress,  $\Sigma_{rr}$ , to cancel the incident wave normal pressure ( $\Sigma_{rr} = k e_{11} E_r$ ).

Here, for the normal angle of the incident wave, the magnitude of  $E_z$  is zero ( $E_z = \frac{\partial \phi}{\partial z}$ ) and the axial wave-number becomes zero according to Equation 5.3. When the axial wave-number is zero, the shear stress in the  $rz$  plane of the cylinder is not significant, and the potential function,  $\phi$ , is not a function of  $z$  anymore having zero electrical fields in the  $z$  direction; hence the feedback-controlled stress mainly depends on the electrical field in the radial direction, which is also the polling direction of the piezoelectric layers in this case study. This way, by controlling the magnitude of radial structural stress,  $\Sigma_{rr}$ , the feedback piezoelectric control will be able to provide superior STL performance when the incident wave is normal to the cylinder. However, as the angle of incident wave decreases, the effect of feedback control strategy with the radially polarized piezo-layers becomes less significant. The reason is that as the value of the incident wave angle decreases, the magnitude of axial wave number,  $k_z$ , is getting larger leading to more significant axial direction stress/pressure variation on the cylinder surface. The axial stress is not zero anymore and could cancel certain radial direction electrical field generated by the radial direction stress leading to relatively weak feedback-controlled stress to cancel the incident wave pressure. Even though the TL effect with feedback-controlled piezoelectric layers is still good in the frequency range between 300-500 Hz. But when the wave angle is

smaller than  $\pi/4$ , the TL effect is not clear. In addition, with a small wave angle ( $\pi/4$ ), there are no clear resonant wave modes excited. In this case, the controller does not properly detect the impinging of the acoustic wave on the cylinder, and the actuator is not able to provide the corresponding controlling voltage to enhance the STL. Moreover, the dipoles of radially polarized piezoelectric materials are more or less aligned in the radial direction.

Figure 6.6 displays the STL spectra of the axially polarized piezo-composite cylinder for four different angles of incident waves ( $\alpha = \pi/12, \pi/6, \pi/3, 5\pi/12$ ), within the frequency range of ( $1 < f < 10^3 \text{ Hz}$ ) with four different control gains. The actuator and sensor layers ( $r_{in} = 1.7 \text{ m}, r_s = 1.8 \text{ m}, r_a = 1.9 \text{ m}, r_{ex} = 2 \text{ m}$ ) are considered to be fabricated of axially polarized PZT4 materials while the central layer is made of Aluminum materials (See Table 5.1 and Table 5.2).



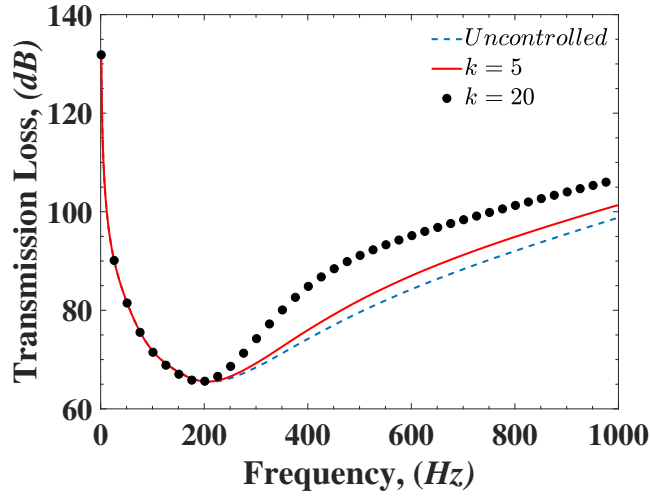
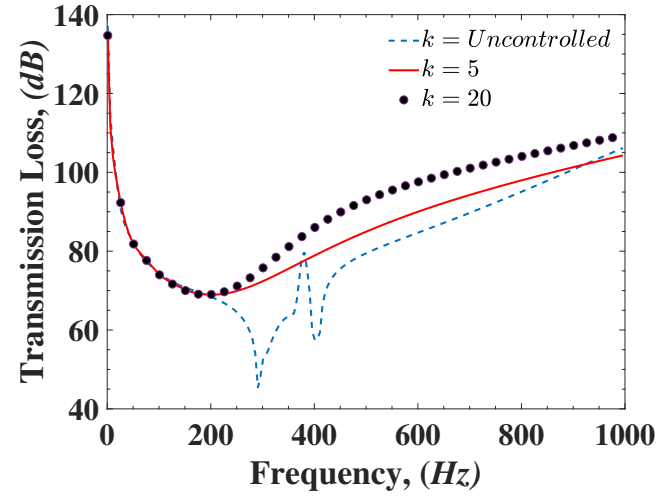
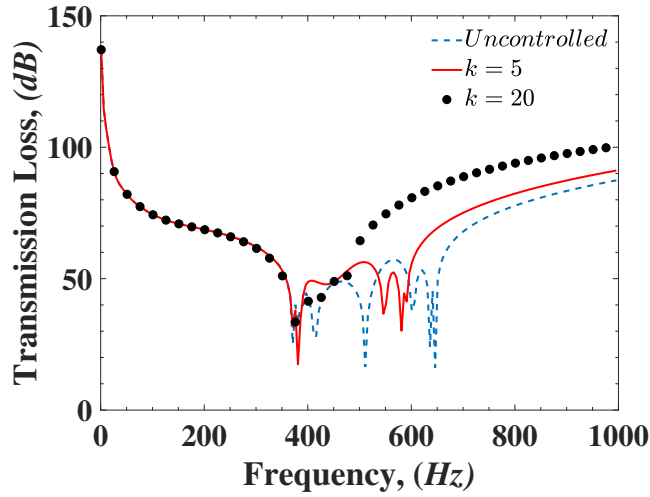
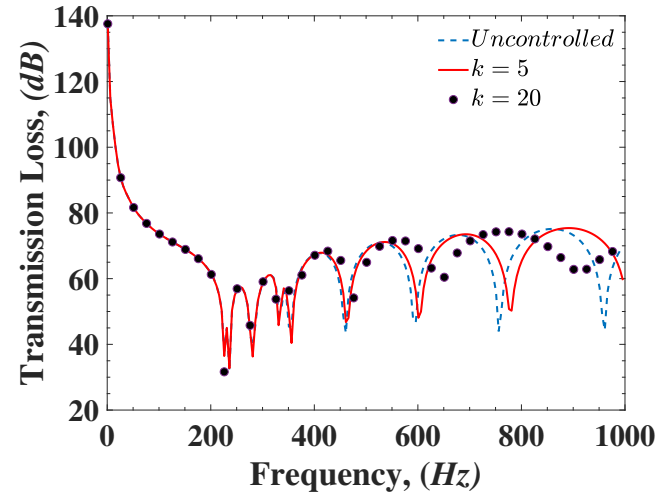
(a) Oblique incident wave,  $\alpha = \pi/12$ .(b) Oblique incident wave,  $\alpha = \pi/6$ .(c) Oblique incident wave,  $\alpha = \pi/3$ .(d) Oblique incident wave,  $\alpha = 5\pi/12$ .

Figure 6.6: STL spectra of the axially polarized piezo-composite cylinder for four different angles of incident waves, based on the negative feedback control strategy with four different gain controls.

As evident in Figure 6.6, the control feedback strategy reduces the unfavorable oscillatory motion of the cylinder in addition to providing a superior sound isolation enhancement, particularly for near-grazing incident angles ( $\alpha = \pi/12$  &  $\pi/6$ ). It can be observed that by increasing the value of feedback gain,  $k$ , the controller can effectively enhance the STL, especially in the case with a small angle of incident waves, whereas the effectiveness of the feedback controller reduces severely for incident angles close to normal ( $\alpha = 5\pi/12$ ).

For the case of  $\alpha = 5\pi/12$ , the value of the axial wavenumber given in Equation 5.3b becomes extremely small. This makes the stress/strain to be almost independent of the z-direction leading to having a relatively small value of the axial electrical field,  $E_z$ . By looking at the axially polarized piezoelectric constitutive equation (B.1.2) one can conclude that only the axial piezoelectric field,  $E_z$ , and the corresponding piezoelectric coupling constant,  $e_{31}$ , can contribute to increasing the controlled radial stress in the cylinder.

When the value of the axial electrical field is very small, it may lead to creating relatively small radial stress by applying a feedback-controlled voltage to the actuator. This way, the controller cannot effectively reduce the detrimental effect of normal incident waves, resulting in having unfavorable dips of the STL even by applying high feedback gain as it is shown in Figure 6.6d. On the other hand, when the angle of the incident wave is small, the value of axial wave number,  $k_z$ , increases, resulting in having more significant axial direction stress/strain and a powerful axial electrical field. The axial electric field, in conjunction with the piezoelectric coupling constant,  $e_{31}$ , can generate relatively high radial stress in the cylinder. Consequently, the actuator can adjust the radial stress in a way to decrease the

acoustic power transmitted inside the cylinder. Furthermore, the dipoles of the axially polarized piezoelectric cylinder are lined up in the axial direction. This means that by applying a proper voltage with well-designed layouts of the piezoelectric elements and electrodes, the actuator is able to cancel some of the small angled incident waves in the cylinder, resulting in having better sound isolation performance.

## 6.5 Conclusions

A fully-coupled analytical formulation is accomplished for the STL control of a thick piezo-composite cylinder by utilizing the acoustic wave equation, the 3D exact theory of elasticity and piezoelectricity. The active control strategy is achieved by sending the control signal from the distributed piezoelectric sensor layer through a controller to drive the external piezoelectric actuator. The final result shows an excellent agreement between the FEM and the proposed analytical solution. The main findings of this research are as follows:

- As the angle of the incident wave increases approaching the normal wave case, a higher number of modes should be included to satisfy the convergence criteria regardless of the frequency of excitation.
- A significant wave isolation effect is realized at the resonant frequencies on the STL spectra for a radially/axially polarized piezo-composite cylinder with different feedback gains.
- In the case of the radially polarized piezoelectric actuator and sensor layers, the feedback control provides significant STL enhancement.

- For the incident wave close to the normal angle, the desirable effect of the active control feedback declines as the value of the incident wave angle approaches to more inclined angles.
- In the case of the axially polarized piezoelectric actuator and sensor, the control feedback strategy reduces the unfavorable oscillatory motion of the cylinder in addition to providing a superior sound isolation enhancement, particularly for near-grazing incident angles ( $\alpha = \pi/12$  &  $\pi/6$ ).

## Chapter 7

# Effect of Electrode Size and Configuration on the Sound Transmission Loss of Smart Piezo-laminated Structures

*“It is strange that only extraordinary men make the discoveries, which later appear so easy and simple.”*

---

Georg C. Lichtenberg

In the traditional design of the piezoelectric layer, the entire surface of the cylinder is covered in piezoelectric materials and metal electrode layers with no consideration for the size and location of the electrodes. The current chapter is aimed to use different sizes and configurations of piezoelectric electrode patches to increase the sound transmission loss (STL) through thick-walled piezo-laminated cylindrical shells. Therefore, designing a model that can take into account the partial piezoelectric

electrodes with various configurations while dealing with the structural with various thicknesses, is very important in acoustic quieting applications. In the following chapter the proper boundary condition for discrete electrodes will be discussed and explained.

## 7.1 Problem Description for Different Size and Configuration of Electrodes

In this section, the structure given in chapter 5 is modified, so instead of having a distributed piezoelectric electrode, individually separated electrodes with different sizes and configurations will be modelled.

Let us consider an infinitely long piezo-laminated cylindrical shell that is submerged in an infinite inviscid acoustic medium with the acoustic properties  $(\rho_{ex}, c_{ex})$  indicating the spatial material density and the speed of the sound in the external acoustic medium, as depicted in Figure 8.1. The structure is assumed to be filled with inviscid acoustic fluid with the physical parameters  $(\rho_{in}, c_{in})$ , indicating the spatial material density and the speed of sound of the internal acoustic cavity, respectively. The core layer of the cylinder is assumed to be made of an anisotropic material with the spatial material density  $\rho_o$  and the thickness,  $H_o = r_a - r_{in}$ . The core layer is covered with a continuously distributed smart piezoelectric material with a spatial density of  $\rho_{pz}$  and thickness  $H_a = r_{ex} - r_a$ . The piezoelectric cylinder is then can be charged via different size and configurations of electrodes as depicted in Figure 8.1. The smart cylinder is experiencing an oblique incident shock wave,  $\phi^{inc}(r, \theta, z; \omega)$ , with the arbitrary oblique incident angle of  $\alpha$ , where  $r, \theta$  and  $z$  are

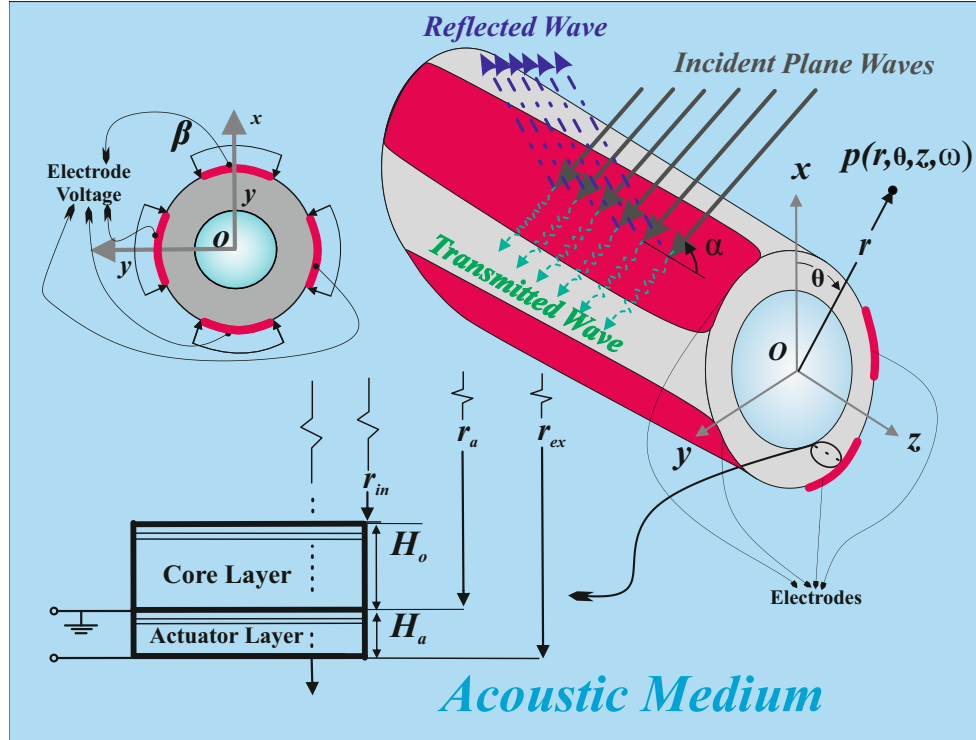


Figure 7.1: Schematic diagram of smart piezo-laminated cylinder embedded with discrete electrodes submerged in an inviscid acoustic fluid excited by an arbitrary oblique incident plane wave.

the radials, tangential and axial coordinates in the cylindrical coordinate system, respectively.

## 7.2 Mathematical Modeling

Acoustic field equation and smart structure modeling are comprehensively discussed and explained in section 5.1. In order to consider the effect of the partial piezoelectric electrode on STL, the spatial Fourier transform will be used to model the partial discrete electrodes. The details of the electro-mechanical boundary conditions will be discussed in the next section.

### 7.2.1 Electro-mechanical Boundary Conditions

For an inner and outer surface of the piezo-composite cylinder, appropriate fluid-solid boundary conditions are listed as follows:

$$v_j(r = r_{in}, \theta, z, \omega) = -i\omega u_j(r = r_{in}, \theta, z, \omega), \quad j = r, \theta, z. \quad (7.1a)$$

$$v_j(r = r_{ex}, \theta, z, \omega) = -i\omega U_j(r = r_{ex}, \theta, z, \omega), \quad j = r, \theta, z. \quad (7.1b)$$

$$\sigma_j^f(r_{in}, \omega) = \sigma_j(r_{in}, \omega), \quad j = rr, r\theta, rz. \quad (7.1c)$$

$$\sigma_j^f(r_{ex}, \omega) = \sigma_j(r_{ex}, \omega), \quad j = rr, r\theta, rz. \quad (7.1d)$$

It is possible to apply the electrical boundary condition for the short-circuited case at both the inner and outer surfaces of the cylinder as described below [95]

$$\phi_n(r_i, \omega) = 0, \quad i = a, ex. \quad (7.2)$$

The spatial Fourier transform for the case of partial discrete electrodes can be written as ([159])

$$\Phi_n(r_i, \theta, z, \omega) = \sum_{n=0}^{\infty} \phi_n(r_i, \omega) \cos(n\theta) e^{\mathbf{i}(\omega t - k_z^{ex} z)}, \quad (7.3)$$

where the modal expansion for the case of partial discrete electrode can be given as ([159])

$$\phi_n(r_i, \omega) = \frac{1}{2\pi} \int_{-\pi}^{\pi} \Phi_n(r_i, \theta, z, \omega) \cos(n\theta) d\theta, \quad (7.4)$$



in which , i indicate the inner or outer radius of the piezoelectric cylinder.

By substitution of electro-mechanical boundary conditions presented in Equation 7.1, Equation 7.2 and Equation 7.4 into the global transfer matrix of Equation 5.24, eventually, after extensive manipulation, the final result appeared as

$$\mathbf{A}_n \mathbf{x}_n = \mathbf{b}_n, \quad (7.5)$$

in which  $\mathbf{A}_n$ ,  $\mathbf{x}_n$  and  $\mathbf{b}_n$  are given in section B.4. Finally, the STL can be easily calculated using the procedure given in subsection 5.5.1.

### 7.3 Model Validation

We shall confirm the validity of the solution before describing the general nature and behavior of the problem. An optimized MATLAB<sup>®</sup> code is used in order to compute the TL from the cylinder as well as to solve Equation 7.5 with parallel clustering. By using the built-in Matlab functions, "besselj" and "besselh", one can calculate exact Bessel and Hankel functions corresponding to the first and second kinds of complex arguments. By using the specialized math function "diff", which provides differentiated symbolic expressions, we were able to find the derivatives of Bessel and Hankel functions. In order to perform calculations, we used the cluster of INTEL<sup>®</sup> XENON<sup>®</sup> Processor G4400 v4 desktop computer (15M Cache, 3.31 GHz, 7.20 GT/s) which utilize intense parallel computing via Multi-core architectures and Hyper-Threading technology. It was decided to use MATLAB PARALLEL COMPUTING TOOLBOX to run 26 parallel pools so as to take advantage of the high calculation power available on multi-threading desktops [208]. By examining an example specific

to the problem, we can confirm the validity of the analytical solution that has been proposed.

Since no results have been found in the literature regarding the TL through a piezoelectric cylindrical shell with discrete electrodes, COMSOL MULTIPHYSICS<sup>®</sup> have been used to validate the proposed close form solution with the piezoelectric coupling effect that was investigated in this study. A series of physical models were described in the software, including elastic, acoustic, and piezoelectric models [209]. As with all finite element packages, COMSOL has its pros and cons. There are three main pores with modeling with COMSOL: difficulty in modeling infinitely large domains, high computational costs, and numerical instability at high frequencies. With the proposed closed-form solution, though, none of the issues above will be a problem. To illustrate this, let's look at the following example. With the boundary condition enforced at  $r = \infty$ , the external acoustic equation can be solved with Bessel functions, whereas, COMSOL uses perfectly matched layer (PML), which are artificial boundary conditions that absorb the majority of the refracted waves. With the boundary condition enforced at  $r = \infty$ , it is possible to solve the external acoustic equation by using Bessel functions. However, COMSOL uses the perfectly matched layer (PML), which is a boundary condition that is artificial and prevents most of the scattered waves from entering the surface. Nevertheless, waves are always partially reflected from the PLM layer, which is the inevitable consequence when numerical methods truncate the computational regions. To simulate the smart piezo-laminated cylinder, 25200 mapped elements were used, with approximately 200464 free triangular elements to model the acoustic fluids, both internal cavity and external fluid medium.

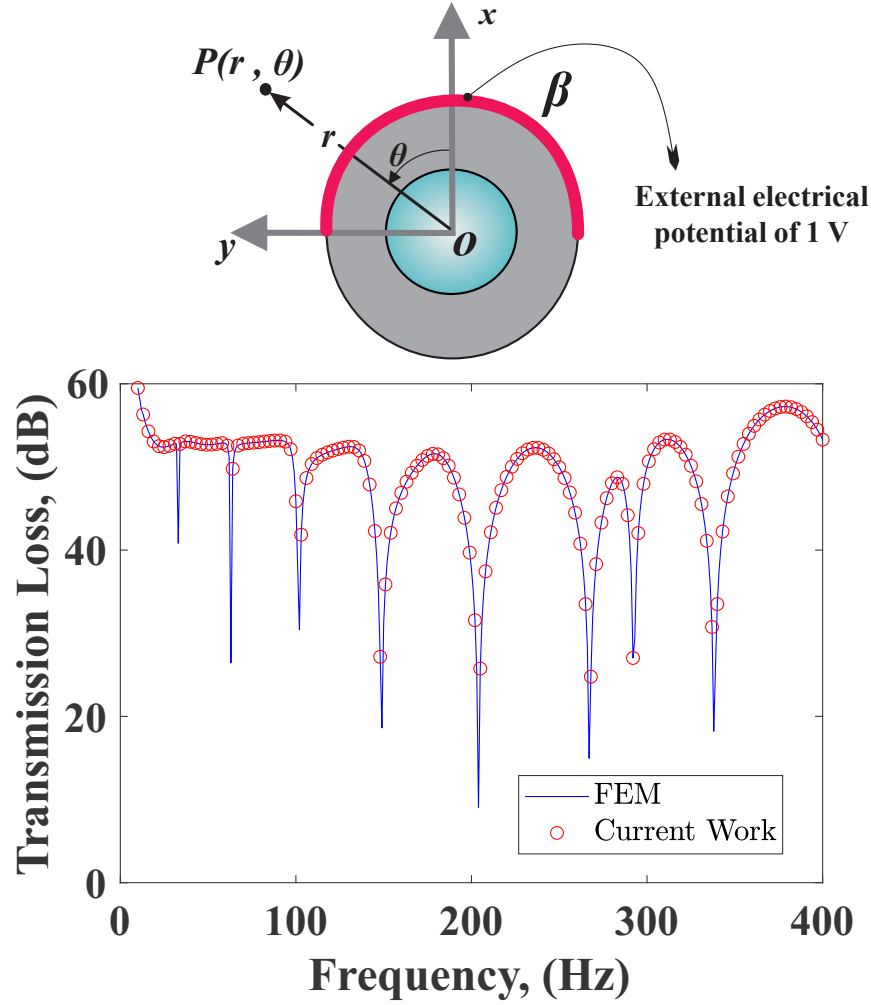


Figure 7.2: Comparison of STL with finite element method (COMSOL MULTIPHYSICS) for a piezo-composite cylinder. The cylinder is assumed to be made of radially polarized PZT4 ( $r_{in} = 1.8 \text{ m}$ ,  $r_a = 1.9 \text{ m}$ ,  $r_{ex} = 2 \text{ m}$ ) with closed-loop electrical boundary condition applied to the internal layer of the actuator, whereas the external layer of the piezoelectric cylinder is attached to  $90^\circ$  electrode at the top with the external electrical potential of 1 V as excitation. The core layer of piez-composite cylinder is made of Aluminum material. The structure is surrounded and filled with air and excited by a normal incident plane wave ( $\alpha = \pi/2$ ).

Figure 7.2 shows the comparison of STL with finite element method (COMSOL

MULTIPHYSICS) for a piezo-composite cylinder. The cylinder is assumed to be made of radially polarized PZT4 ( $r_{in} = 1.8 \text{ m}$ ,  $r_a = 1.9 \text{ m}$ ,  $r_{ex} = 2 \text{ m}$ ) with closed-loop electrical boundary condition applied on the internal layer of the actuator, whereas the external layer of the piezoelectric cylinder is attached to  $90^\circ$  electrode at the top with the external electrical potential of 1 V as excitation as it depicted in the Figure 7.2. The mechanical and electrical properties of the piezoelectric materials are given in Table 5.1 and Table 5.2, respectively. The core layer of the piez-composite cylinder is made of Aluminum material. The mechanical properties of Aluminum are given in Table 5.1. The structure is surrounded and filled with air and excited by a normal incident plane wave ( $\alpha = \pi/2$ ). The acoustic properties of the fluid medium are given in Table 5.3. Based on Figure 7.2, the current study is in an excellent agreement with the commercial finite element package COMSOL MULTIPHYSICS 4.4 [209]. The next section will address the numerical results.

## 7.4 Results and Discussion

In this section the case studies will be discussed; before addressing the main results, it should be mentioned that due to the large number of variables involved in the proposed analytical solution, while keeping in mind the computational limitations, we shall focus on some logically selected examples. Accordingly, the elastic layer is considered to be made of a single aluminum layer ( $h_o = 0.1 \text{ m}$  and  $r_{in} = 1.8 \text{ m}$ ). The actuator layer ( $h_a = 0.1 \text{ m}$  and  $r_a = 1.9 \text{ m}$ ) is made of radially polarized PZT4, perfectly bonded to the host structure with the material properties as given in Table 5.1 and Table 5.2. The piezo-composite cylinder is filled and surrounded with air as the acoustic properties of the constituent material are given in Table 5.3.

The amplitude of the normal plane incident wave is considered to be  $1 \text{ Pa}$  whereas the piezoelectric cylinder is considered to be grounded in its internal surface in all our calculations. In all following figures, the geometry and material properties of the piezo-composite structure are according to the above-mentioned values, unless specified otherwise.

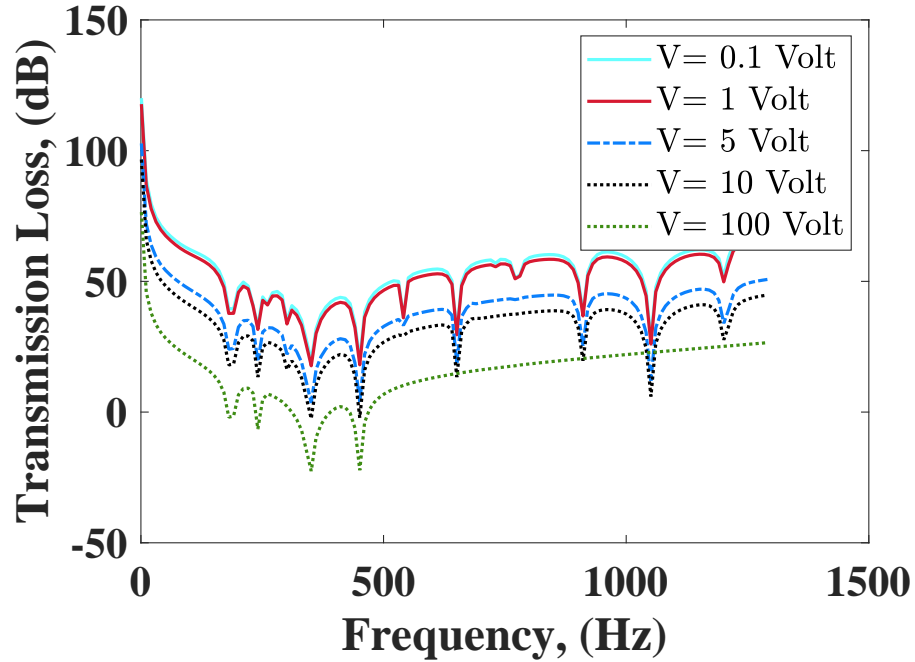


Figure 7.3: Sound transmission loss through a piezo-composite cylinder for different electrical potential excited by a normal incident plane wave. The cylinder is made of Aluminum and radially polarized Pzt4 ( $r_{in} = 1.8 \text{ m}$  and  $r_{ex} = 2 \text{ m}$ ) surrounded and filled with air-fluid. The piezoelectric cylinder is considered to be grounded in its internal surface.

#### 7.4.1 Voltage effect

Figure 7.3 shows the sound transmission loss through a piezo-composite cylinder for different electrical potential excited by a normal incident plane wave. The outer

surface of the piezoelectric cylinder is considered to be covered with  $180^\circ$  electrode at the top. In addition, the electrodes on the external surface of the cylinder are supplied with different electrical potentials as excitation. As seen from Figure 7.3, the sound transmission loss decreases by increasing the value of the external electric potential. The reason is that, by increasing the value of external electric potential, more electrical energy converts to mechanical energy. The mechanical energy then will increase the value of normal stress which results in increasing the magnitude of the pressure value inside the cylinder. As we can see from the definition of the sound transmission loss given in Equation 5.32, by increasing the acoustic transmitted pressure inside the cylinder, the value of sound transmission loss decreases, resulting in providing less soundproofing abilities. In conclusion, the value of external electrical potential has a significant effect on STL in areas far from resonance frequencies.

#### **7.4.2 Electrode size effect**

Figure 7.4 shows the sound transmission loss through a piezo-composite cylinder for different sizes of electrodes excited by a normal incident plane wave. The outer surface of the piezoelectric cylinder is considered to be covered with an electrode at its apex. In addition, the electrodes are supplied with an external electrical potential of 1 V as excitation.

As evident in Figure 7.4, the sound transmission loss is very dependent on the frequency of the excitation and the size of the electrode. While at a low frequency of excitation, the size of electrodes doesn't have too much influence on the level of sound transmission loss possibly in the frequency range between 0 to 500 Hz. By increasing the frequency of excitation beyond 500 Hz, one can recognize different

effects of electrode size on the sound transmission loss of the cylinder. For example at the frequency of 5 kHz, the electrode with size  $\beta = \pi/12$  shows the lowest STL, while the electrode with size  $\beta = \pi/4$  shows higher sound transmission loss which indicates more sound isolation quality for this size of electrodes. However, this trend cannot be generalized to all ranges of frequencies. For instance by increasing the frequency of excitation to 6.5 KHz, one can distinguish the fact that the electrode with size  $\beta = \pi/12$  shows higher STL than the electrode with size  $\beta = \pi/4$ . The same fact can be seen for the electrode with the size of  $\beta = \pi/12$  around the frequency of 2 kHz. At this frequency, the green plot associated with the electrode size  $\beta = \pi/12$  shows the highest level of the STL. This indicated that the level of sound isolation can be adjusted by using the proper size of the electrode at a specific frequency.

Besides, by proper choice of electrode size, one can avoid the resonance frequency of the cylinder to provide higher sound transmission loss. For instance, by looking at the frequencies such as 2.75, 5, and 6.25, we can clearly see that the red plot associated with the  $\beta = \pi/12$  shows the lowest sound transmission loss due to the resonance at the specified frequency while the other plot associated with the electrode size  $\beta = \pi/4$  and  $\beta = \pi/2$  avoid the resonance frequency and shows higher sound transmission loss. This pattern is not unique and can be seen for other plots as well. This shows the fact that by the smart choice of electrode size, the designer can avoid a sharp decrease in sound transmission loss at the resonance frequency which results in the better acoustic quieting ability of the smart structure.

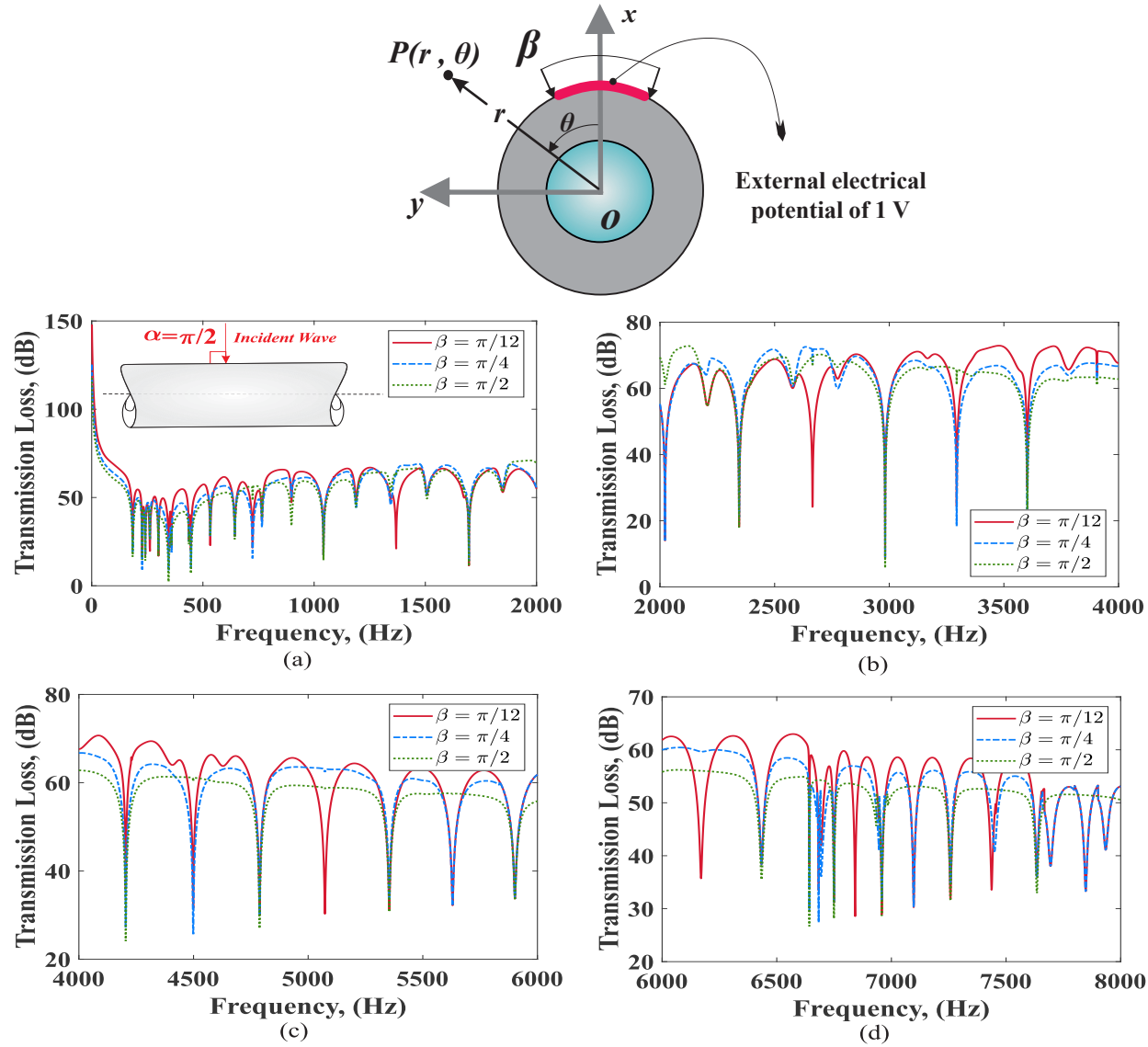


Figure 7.4: Sound transmission loss through a piezo-composite cylinder for different sizes of electrodes excited by a normal incident plane wave. The cylinder is made of Aluminum and radially polarized Pzt4 ( $r_{in} = 1.8\text{ m}$  and  $r_{ex} = 2\text{ m}$ ) surrounded and filled with air-fluid with external electrical potential of 1 V as excitation. The piezoelectric cylinder is considered to be grounded in its internal surface.



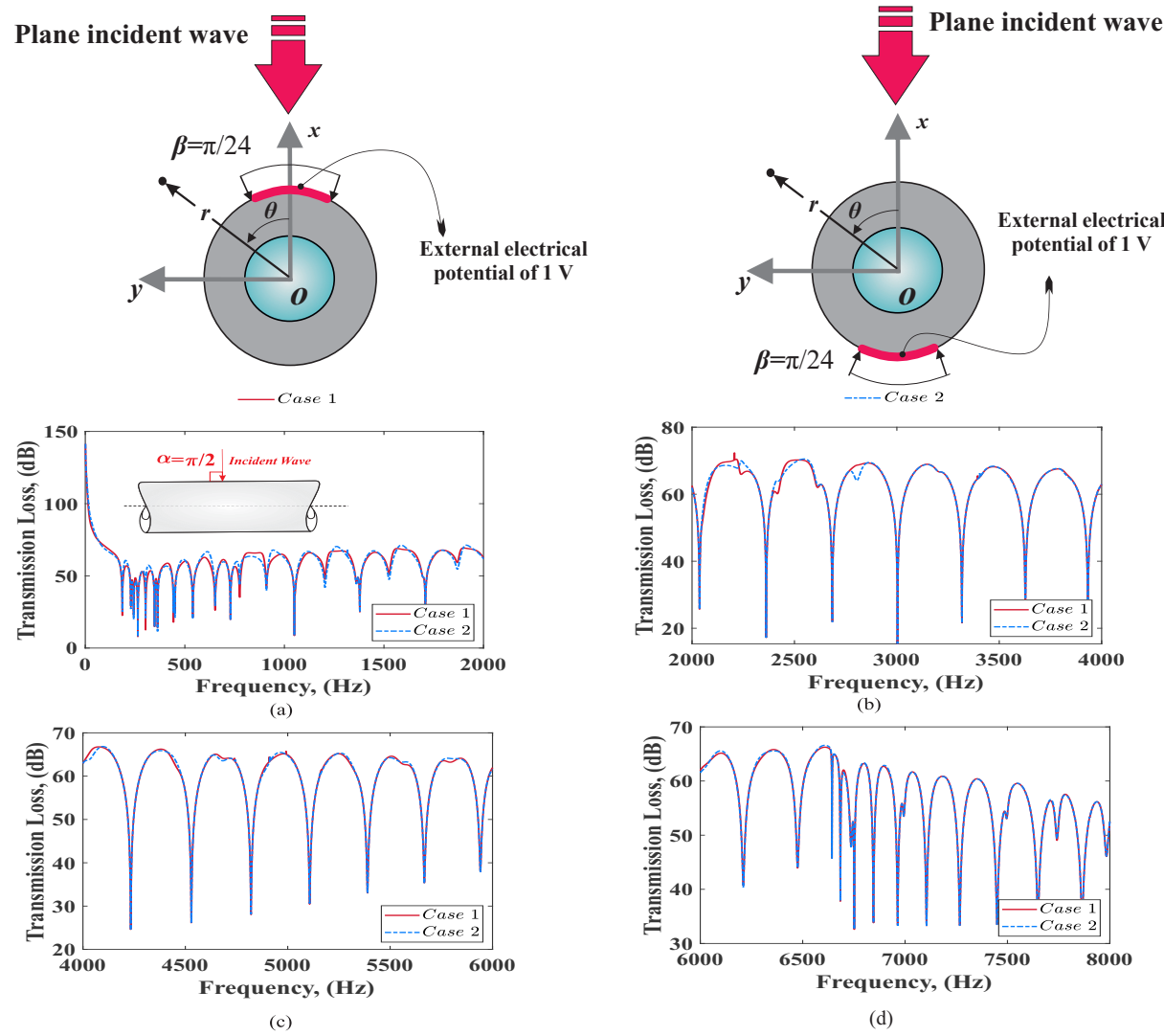


Figure 7.5: The sound transmission loss through a piezo-composite cylinder at different positions of the electrode patch in relation to an incident plane wave. The cylinder is made of Aluminum and radially polarized Pzt4 ( $r_{in} = 1.8\text{ m}$  and  $r_{ex} = 2\text{ m}$ ) surrounded and filled with air-fluid while the internal surface of the cylinder is grounded. In addition, the electrodes are supplied with an external electrical potential of 1 V as excitation.

### 7.4.3 Electrode location effect

Figure 7.5 displays the sound transmission loss through a piezo-composite cylinder for different positions of the electrode patch with respect to the excitation by a normal incident plane wave. The cylinder is made of Aluminum and radially polarized Pzt4 ( $r_{in} = 1.8 \text{ m}$  and  $r_{ex} = 2 \text{ m}$ ) surrounded and filled with air-fluid while the internal surface of the cylinder is grounded. In addition, the electrodes are supplied with an external electrical potential of 1 V as excitation. By comparing the plots for the case with electrode patch at the apex to the case with electrode patch at the bottom against the plane incident wave, one can recognize the fact that the position of the electrode patch with respect to the direction of the incident wave has a minor effect on the sound transmission loss of the smart cylinder. This pattern is also uniform through all different ranges of frequencies. Thus, the higher sound transmission loss can not be achieved only by changing the position of the piezoelectric patches with respect to the direction of the plane incident wave.

### 7.4.4 Electrode asymmetric effect

Figure 7.6 shows sound transmission loss comparison for different asymmetric patches of electrodes through a piezo-composite cylinder, excited by a normal incident plane wave. The size of the top electrode is equal to  $\beta = \pi/3$  while the size of the asymmetric electrode is equal to  $\beta' = \pi/12$ . The cylinder is made of Aluminum and radially polarized Pzt4 ( $r_{in} = 1.8 \text{ m}$  and  $r_{ex} = 2 \text{ m}$ ) surrounded and filled with air-fluid. In addition, the electrodes are supplied with an external electrical potential of 1 V as excitation. It can be seen from the Figure 7.6 that the degree of asymmetry in the configuration of electrodes does have some influence on the

sound transmission loss at some specific frequency. For example, at a frequency around 6.5 kHz, the first case shows lower sound transmission loss compared to the second case. However, in general, the two cases don't show a major difference at many frequency ranges. For instance, there is no major difference between the two cases in the frequency ranges between 0 to 4 kHz. This indicates that the degree of asymmetry in the configuration of electrodes has less effect on sound transmission loss compared to the size of electrodes as shown in Figure 7.4.

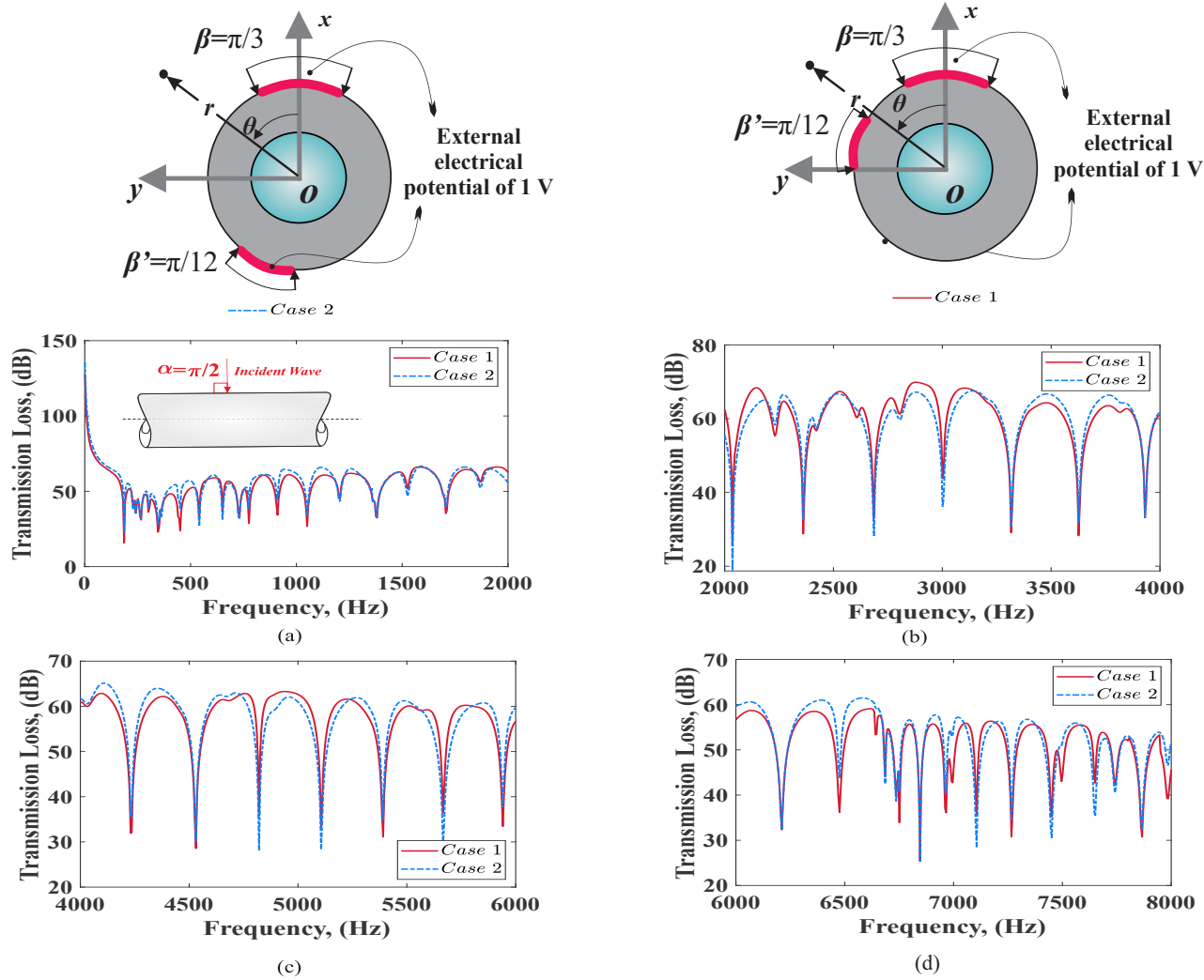


Figure 7.6: Sound transmission loss through a piezo-composite cylinder for different asymmetric patches of electrodes, excited by a normal incident plane wave. The size of the top electrode is equal to  $\beta = \pi/3$  while the size of the asymmetric electrode is equal to  $\beta' = \pi/12$ . The cylinder is made of Aluminum and radially polarized Pzt4 ( $r_{in} = 1.8\text{ m}$  and  $r_{ex} = 2\text{ m}$ ) surrounded and filled with air-fluid while the piezoelectric cylinder is considered to be grounded in its internal surface. The external electrodes are supplied with an external electrical potential of 1 V as excitation.

#### 7.4.5 Electrode number effect

Figure 7.7 shows sound transmission loss through a piezo-composite cylinder with different configurations of electrode patches, excited by a normal incident plane wave. Three different cases of electrode patches are considered for comparison purposes. The size of all electrodes is considered the same with the angle of  $\beta = \pi/6$ . For the first case, there is only one patch of the electrode at the apex of the cylinder where the incident plane wave impinges. In the second case, there are two patches of electrodes at the top and bottom of the piezoelectric cylinder. The third case has four patches of electrodes placed at an equal distance of  $90^\circ$  from each other. In addition, the electrodes are supplied with an external electrical potential of 1 V as excitation.

As it is evident from the Figure 7.7, the configuration of the electrode patches has a minor effect on the sound transmission loss in the lower frequency ranges between 0 to 1 kHz. However, by increasing the frequency of the incident plane wave, different patterns on the sound transmission loss can be distinguished for different configurations of the electrode patches. For instance, the third case shows higher sound transmission loss at the frequency of 2 kHz compared to the first and second configurations. However, the third case shows the lowest sound transmission loss at the frequency of 4 kHz. This reveals that providing a higher level of sound quieting abilities can not be achieved only by increasing the number of piezoelectric patches. In fact, the higher sound transmission loss can be achieved by the intelligent choice of electrode patches for the specific excitation frequency of the plane incident wave. Besides, in some cases, different configurations of electrode patches can avoid resonance frequency in different cases. For example, the plot of sound transmission

loss for case 2 and case 3 passes the frequency of 6.5 kHz without a sharp decrease in STL, however, a sharp dip of negatives can be seen for the first case at this frequency. This indicated that using the proper configuration of electrode patches, the designers can prevent the transmission of noise into the structure by avoiding the resonance frequencies.

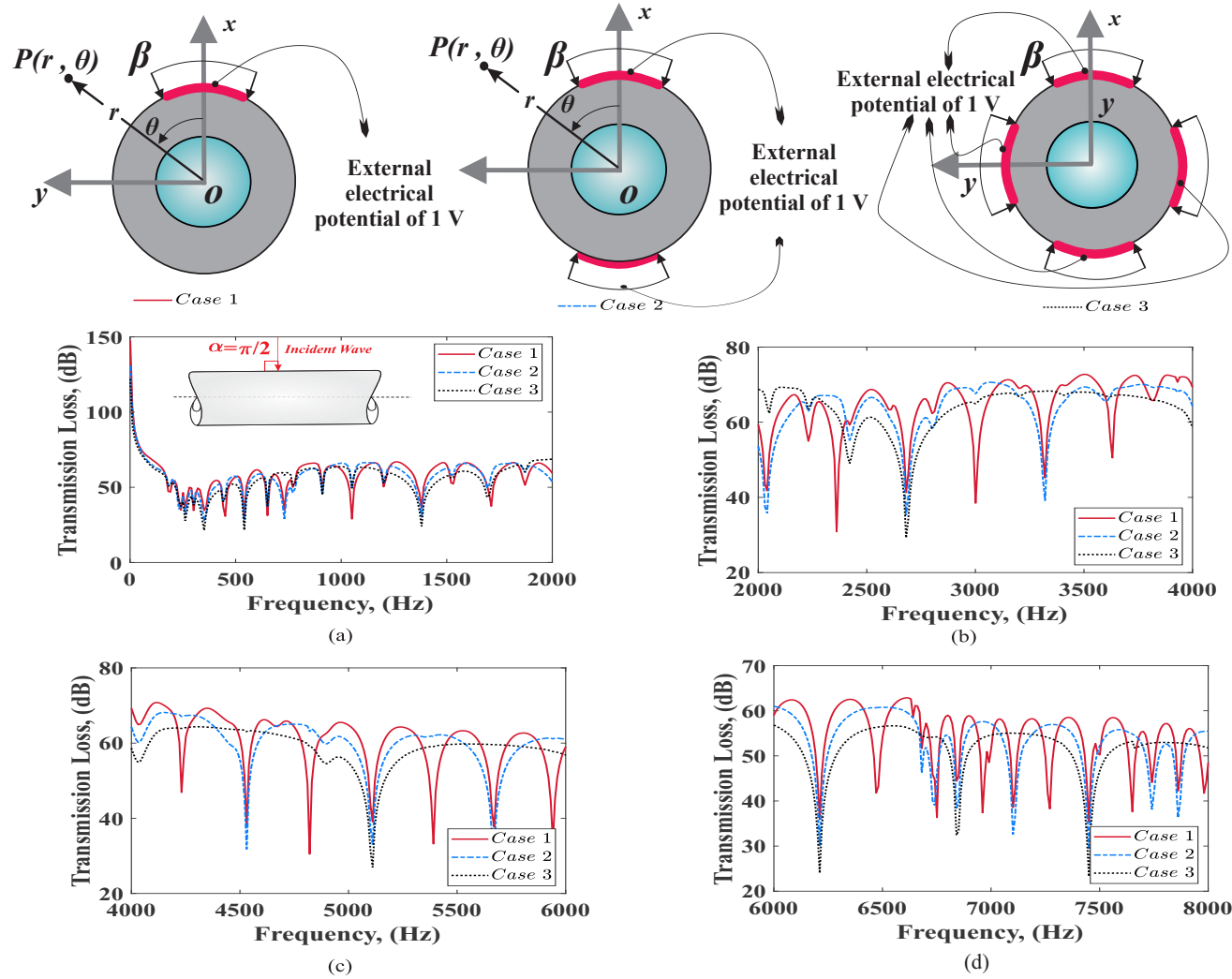


Figure 7.7: Sound transmission loss through a piezo-composite cylinder for different arrangements of electrodes, excited by a normal incident plane wave. The size of all electrodes is equal to  $\beta = \pi/6$ . The cylinder is made of Aluminum and radially polarized Pzt4 ( $r_{in} = 1.8\text{ m}$  and  $r_{ex} = 2\text{ m}$ ) surrounded and filled with air-fluid. In addition, the electrodes are supplied with an external electrical potential of 1 V as excitation. In addition, the internal surface of the cylinder is grounded.

## 7.5 Conclusions

This study is focused on rigorously examining the influence of size and configuration of piezoelectric electrodes on sound transmission loss (STL) through thick-walled piezo-laminated cylindrical shells, excited by a plane wave incident obliquely. The cylindrical shell is modeled using the three-dimensional (3D) exact theory of elasticity and piezoelectricity, and the Helmholtz equation is used for the propagation of waves inside the acoustic cavity as well as through the surrounding fluids. A closed-form solution is generated by enforcing the proper boundary conditions and expanding the harmonic field. COMSOL MULTIPHYSICS software is used to verify the validity of the analytical solution. Parameter studies are conducted to investigate the effects of size and configurations of electrodes on STL. Results are presented with specific recommendations regarding the size and configuration of piezoelectric electrodes for active sound absorption. Based on the findings of this research, the following conclusions can be drawn:

- The level of sound isolation can be adjusted by using the proper size of the electrode at each specific frequency
- Increasing the number of electrode patches may not necessarily provide higher soundproofing abilities
- By proper choice of electrode size, one can avoid the resonance frequency of the cylinder to provide higher sound transmission loss
- The position of the electrode patch with respect to the direction of the incident wave has a minor effect on the sound transmission loss of the smart cylinder



- The higher sound transmission loss can be achieved by the intelligent choice of electrode configurations for each specific excitation frequency
- The degree of asymmetry in the configuration of electrodes has less effect on sound transmission loss compared to the size of electrodes

## Chapter 8

# Effect of Fluid Viscosity on the Sound Transmission Loss of Smart Piezo-laminated Structures

*“The whole of science is nothing more than a refinement of everyday thinking.”*

---

Albert Einstein

When the sound waves impinge on the wall of a cylinder, the sound wave attenuates because of the boundary layer effects. These losses can be significant when the structure is quite small compared to the surrounding media and submerged in a viscous fluid. This chapter aims to rigorously investigate the effects of fluid viscosity on the STL through a submerged thick smart anisotropic piezo-composite cylinder subject to an oblique incident plane wave. The three-dimensional (3D) theory of elasticity and piezoelectricity are used to model a solid smart piezo-composite cylinder, while the Navier-Stokes equation is employed to describe the surrounding

viscous acoustic medium as well as the internal acoustic cavity. The Helmholtz decomposition is used to resolve the velocity field of fluid into longitudinal and transverse vectors, whereas the state space method and transfer matrix approach are used to model the smart cylindrical structure. Subsequently, the closed-form solution is derived by enforcing mechanical and electrical boundary conditions along with a proper wave harmonic field expansion. The validity of the proposed closed-form solutions is investigated using different data from a simplified analytical model found in the literature as well as finite element modeling by making simplified assumptions. Parametric studies are carried out to investigate the effect of fluid viscosity (dynamic viscosity and bulk viscosity), shell anisotropy and piezoelectric boundary conditions on the STL through a piezo-composite cylinder submerged in a viscous fluid. The results show that the magnitude of STL linearly increases as the value of bulk and dynamic viscosities increases, which results in providing a better soundproofing ability.

## 8.1 Problem Description For Transmission Loss in Viscous Fluid

In this section the structure given in chapter 5 will be used to model the piezo-laminated cylinder. However, instead of using inviscid fluid, the viscous acoustic model will be used to model the internal cavity and surrounding fluid.

Let us consider an infinitely-long smart piezo-composite cylinder with an internal cavity filled with a viscous acoustic fluid, as depicted in Figure 8.1. The radius of the internal cavity is  $r_{in}$ , while  $\rho_{in}$  and  $c_{in}$  denote the spatial density and speed of sound in the internal cavity.  $\mu_{in}$  and  $\lambda_{in}$  describe the dynamic viscosity and the expansive (bulk) viscosity of the viscous fluid filling the internal cavity, respectively. The core layer of the smart structure is assumed to be made of isotropic/anisotropic materials with thickness  $H_o$  and density of  $\rho_o$ . The core layer of the structure is coated with a piezoelectric actuator layer. The continuously distributed outer smart layer of the cylinder is made of piezoelectric materials with a thickness of  $H_a$  and density of  $\rho_{pz}$ . The smart piezo-composite structure is assumed to be submerged in an infinite viscous fluid with the physical parameters  $(\rho_{ex}, c_{ex}, \mu_{ex}, \lambda_{ex})$  referring respectively to the spatial density, speed of sound, dynamic viscosity and the bulk viscosity of the surrounding viscous fluid. Furthermore, the stationary but flexible elasto-acoustic smart structure (not moving in whole in the fluid) is obliquely insonified by a monochromatic harmonic progressive plane incident wave,  $\phi^{inc}(r, \theta, z; \omega)$ , with the oblique incident angle of  $\alpha$  and the cylindrical coordinate system  $(r, \theta, z)$  as set in Figure 8.1. Before describing the smart elastic structure, we shall concisely describe the viscous acoustic model for the internal cavity and external fluid medium. Please

note that, the detail of smart structure modeling is discussed in section 5.1.

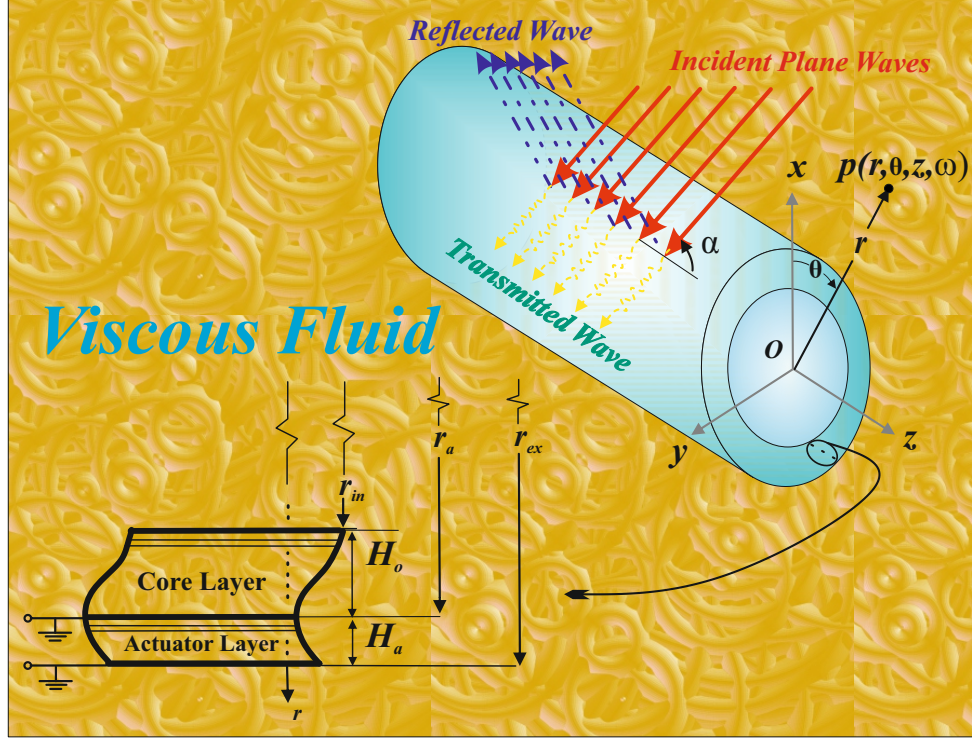


Figure 8.1: Schematic diagram of a smart piezo-composite cylinder submerged in a viscous fluid excited by an oblique incident plane wave.

### 8.1.1 Viscous Acoustic Model

Equation 3.20 can be used to solve the acoustic fields inside the internal cavity and outside of the cylinder. Considering the radiation boundary conditions and the unbounded surrounding fluid, the scattered acoustic waves can be expressed as ([18])

$$\phi_c^{ex}(r, \theta, z, \omega) = \sum_{n=0}^{\infty} A_n(\omega) H_n^2(\Gamma_c^{ex} r) \cos(n\theta) e^{ik_z z}, \quad (8.1a)$$

$$\psi_r^{ex}(r, \theta, z, \omega) = \sum_{n=1}^{\infty} B_n(\omega) H_{(n+1)}^2(\Gamma_s^{ex} r) \sin(n\theta) e^{ik_z z}, \quad (8.1b)$$

$$\psi_\theta^{ex}(r, \theta, z, \omega) = - \sum_{n=0}^{\infty} B_n(\omega) H_{(n+1)}^2(\Gamma_s^{ex} r) \cos(n\theta) e^{ik_z z}, \quad (8.1c)$$

$$\psi_z^{ex}(r, \theta, z, \omega) = \sum_{n=1}^{\infty} C_n(\omega) H_n^2(\Gamma_s^{ex} r) \sin(n\theta) e^{ik_z z}, \quad (8.1d)$$

where  $H_n^1(\mathbb{Z})$  is the Hankel functions of the first kind,  $\Gamma_i^{ex} = \sqrt{(k_i^{ex})^2 - k_z^2}$  in which ( $i = c, s$ ), and  $k_z = \mathbb{R}[k_c^{ex} \sin(\alpha)]$  in which  $\alpha$  is the angle of oblique incident wave. Furthermore, the superscript “*ex*” indicates the external viscous fluid medium. In addition,  $A_n(\omega)$ ,  $B_n(\omega)$  and  $C_n(\omega)$  are the modal scattered coefficients. Similarly, the transmitted waves inside the internal acoustic cavity can be given by [18]

$$\phi_c^{in}(r, \theta, z, \omega) = \sum_{n=0}^{\infty} D_n(\omega) H_n^1(\Gamma_c^{in} r) \cos(n\theta) e^{ik_z z}, \quad (8.2a)$$

$$\psi_r^{in}(r, \theta, z, \omega) = \sum_{n=1}^{\infty} E_n(\omega) H_{(n+1)}^1(\Gamma_s^{in} r) \sin(n\theta) e^{ik_z z}, \quad (8.2b)$$

$$\psi_\theta^{in}(r, \theta, z, \omega) = - \sum_{n=0}^{\infty} E_n(\omega) H_{(n+1)}^1(\Gamma_s^{in} r) \cos(n\theta) e^{ik_z z}, \quad (8.2c)$$

$$\psi_z^{in}(r, \theta, z, \omega) = \sum_{n=1}^{\infty} F_n(\omega) H_n^1(\Gamma_s^{in} r) \sin(n\theta) e^{ik_z z}, \quad (8.2d)$$

where  $D_n(\omega)$ ,  $E_n(\omega)$  and  $F_n(\omega)$  are the unknown transmitted coefficients, and  $H_n^2(\mathbb{Z})$  is the Hankel function of the second kind. Moreover, the superscript “*in*” indicates

the internal fluid medium and  $\Gamma_i^{in} = \sqrt{(\kappa_i^{in})^2 - \kappa_z^2}$  in which ( $i = c, s$ ).

Next, the modal expansion of the oblique incident plane wave impinging on the external surface of the cylinder can be expressed in the cylindrical coordinate as [214]

$$\phi^{inc}(r, \theta, z, \omega) = \sum_{n=0}^{\infty} \phi_0 \varepsilon_n (-\mathbf{i})^n J_n(\Gamma_c^{ex} r) \cos(n\theta) e^{\mathbf{i}(k_z z)}, \quad (8.3)$$

where  $J_n(\mathbb{Z})$  is the Bessel function of the first kind ([215]),  $\phi_0$  is the magnitude of the incident plane wave, and

$$\varepsilon_n = \begin{cases} 1 & n = 0, \\ 2 & n \geq 1. \end{cases}$$

The stress components in the viscous fluid is given by [16, 17]

$$\sigma_{rr}^f = -p + \left( \lambda - 2\frac{\mu}{3} \right) \Delta + 2\mu \frac{\partial u_r}{\partial r}, \quad (8.4a)$$

$$\sigma_{r\theta}^f = \mu \left( \frac{1}{r} \frac{\partial u_r}{\partial \theta} + \frac{\partial u_\theta}{\partial r} - \frac{u_\theta}{r} \right), \quad (8.4b)$$

$$\sigma_{rz}^f = \mu \left( \frac{\partial u_r}{\partial z} + \frac{\partial u_z}{\partial r} \right), \quad (8.4c)$$

in which

$$p = -\mathbf{i}\omega\rho\phi + \left( \lambda + \frac{4}{3}\mu \right) \Delta, \quad (8.5)$$

where  $\Delta = k_c^2 \phi$  and  $\phi = \phi^{inc} + \phi_c$ .

### 8.1.2 Electro-mechanical Boundary Conditions

The appropriate fluid-solid boundary conditions that must be imposed at the inner and outer surfaces of the piezo-composite cylinder are written as follows [194]

$$v_j(r = r_{in}, \theta, z, \omega) = -i\omega u_j(r = r_{in}, \theta, z, \omega), \quad j = r, \theta, z. \quad (8.6a)$$

$$v_j(r = r_{ex}, \theta, z, \omega) = -i\omega U_j(r = r_{ex}, \theta, z, \omega), \quad j = r, \theta, z. \quad (8.6b)$$

$$\sigma_j^f(r_{in}, \omega) = \sigma_j(r_{in}, \omega), \quad j = rr, r\theta, rz. \quad (8.6c)$$

$$\sigma_j^f(r_{ex}, \omega) = \sigma_j(r_{ex}, \omega), \quad j = rr, r\theta, rz. \quad (8.6d)$$

The compatibility of the electrical boundary condition for the short-circuited case can be applied at the inner and outer surface of the piezo-composite cylinder as

$$\phi_n(r_i, \omega) = 0, \quad i = a, ex. \quad (8.7)$$

Likewise, the open-circuited electrical boundary condition can be given as

$$D_r^n(r_i, \omega) = 0, \quad i = a, ex, \quad (8.8)$$

By substituting electro-mechanical boundary conditions presented in Equation 8.6, Equation 8.7 and Equation 8.8 into the global transfer matrix of Equation 5.24, after some algebraic manipulations, the final solution can be derived as

$$\mathbf{A}_n \mathbf{x}_n = \mathbf{b}_n, \quad (8.9)$$

in which  $\mathbf{A}_n$ ,  $\mathbf{x}_n$  and  $\mathbf{b}_n$  are provided in section C.1.

## 8.2 Model Validation

Before discussing the numerical results, we shall investigate the convergence of the proposed analytical solution. The convergence of the current solution is attained by



Parameters	Glycerine	Olive oil	Water	FC-75	Air
$c(m/s)$	1910	1440	1497	613.77	343
$\rho(kg/m^3)$	1250	900	1000	1730	1.21
$\mu(kg/m.s)$	0.95	0.084	0.000894	0.00079	$1.825 \times 10^{-5}$
$\lambda(kg/m.s)$	0.95	0.084	0.00250	0.00079	$1.825 \times 10^{-5}$

Table 8.1: Acoustic parameters for several Newtonian fluids at  $25^\circ C$ .

checking the stability of the estimated value of the STL while increasing the value of the series truncation constant,  $N$  in Equation 5.38. The Matlab m-file is coded in a way to allow the code to be executed repeatedly until the difference between two consecutive calculated STL becomes smaller than the predefined error bounds ( $\Delta TL \leq 10^{-15}$ ). When the loop check becomes false, the iteration is terminated, and the final value of the STL is considered to be converged. The flowchart diagram of the solution procedure is displayed in Figure 8.2.

Before illustrating the nature and general behavior of the problem, we shall confirm the validity of the solution. A general MATLAB<sup>®</sup> code is scripted to calculate the TL for the piezo-composite cylinder as well as obtaining the solution of Equation 8.9. The exact calculation of Bessel functions, Hankel functions of the first and the second kinds of the complex argument is attained by taking advantage of Matlab “besselj” and “besselh” built-in functions. The derivatives of the Bessel and Hankel functions were achieved using the specialized math function “diff” which provides differentiate symbolic expression. The computations were performed on a cluster of INTEL<sup>®</sup> Core(TM) i5-7500 CPU @ 3.40 GHz desktop computer (32.0 GB Ram DDR4) capable of exhaustive parallel calculations. The MATLAB PARALLEL COMPUTING TOOLBOX was utilized to expedite our calculation of STL [208].

Noting the large number of parameters involved in the problem that affects the

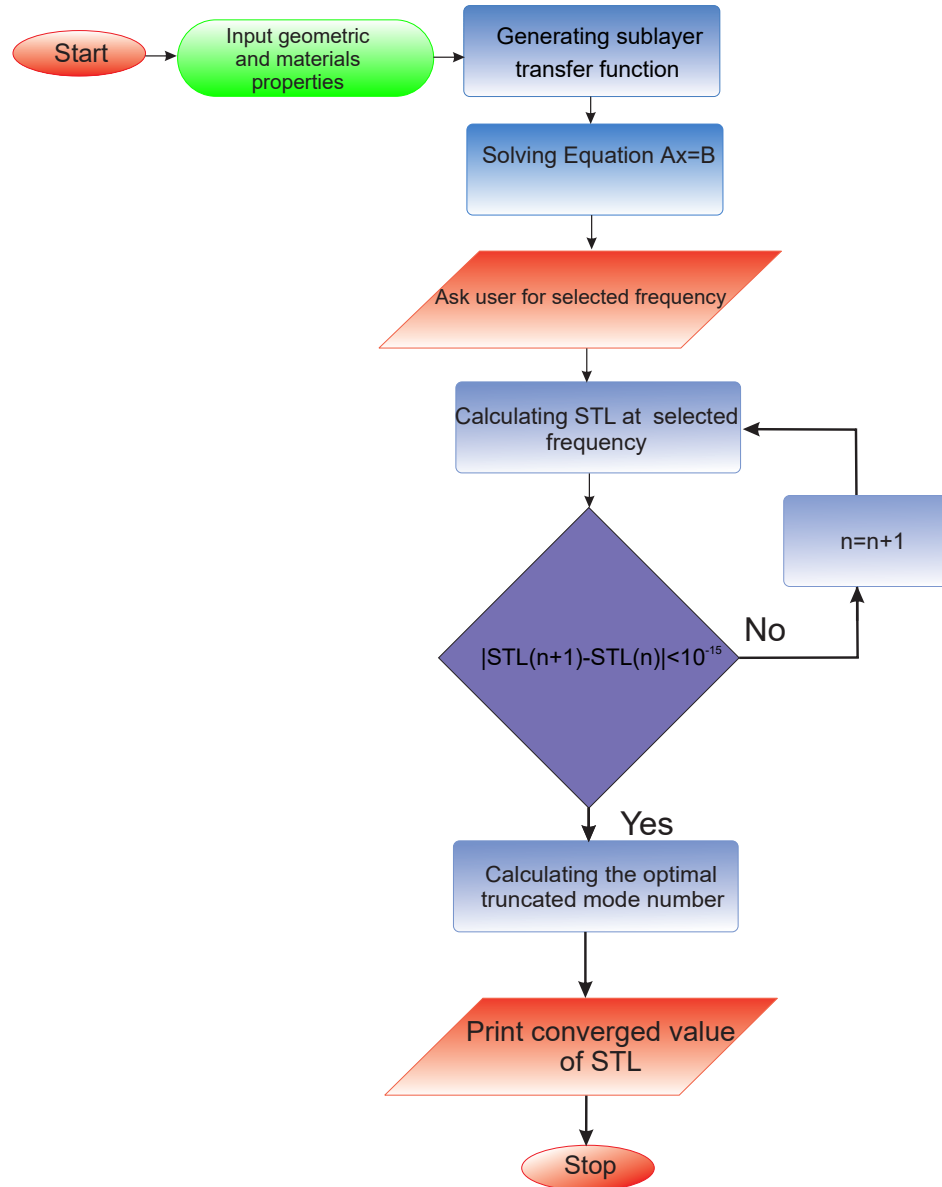


Figure 8.2: Flowchart diagram followed for the calculation of STL.

STL and keeping in mind the intensive computational cost, we shall focus our attention on some specific examples. In all calculations, the material properties and structural geometry of the smart cylinder are considered as follows, unless specified

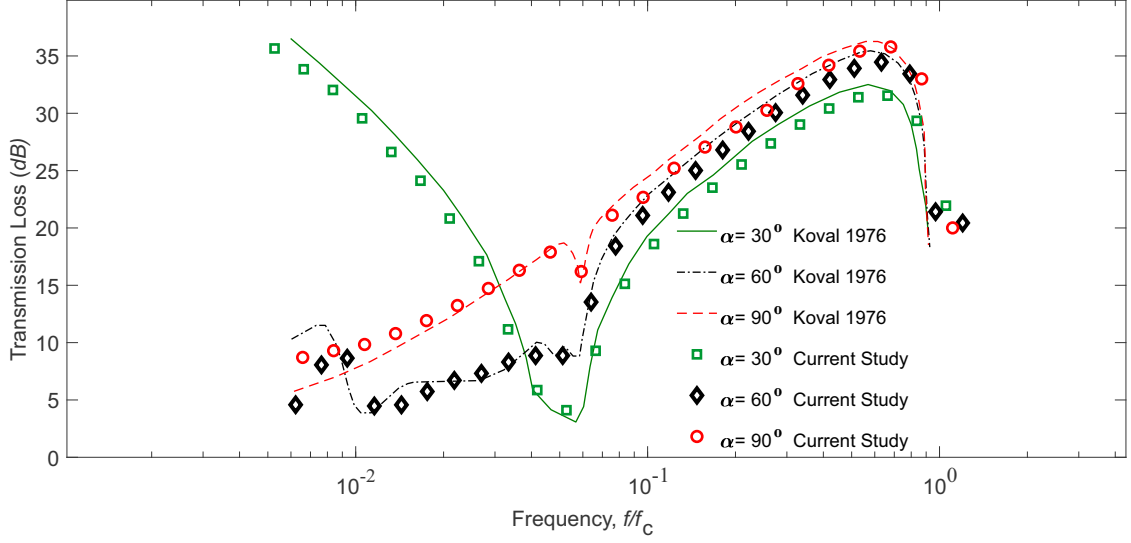


Figure 8.3: STL comparison between Flugge-Lure-Byrne thin walled theory as presented in [2] and the current study for three different incident angles ( $\alpha = \pi/6; \pi/3; \pi/2$ ) at Mach=0 for a cylinder submerged in an inviscid fluid.

Parameters	Temperature $^{\circ}C$				
	0	20	40	60	100
$\mu$ (Centipoise)	9390	1150	234	68	13
$\lambda$ (Centipoise)	12000	1410	283	81	14

Table 8.2: Viscosity of Glycerol solution in different temperatures ([1]).

otherwise. The smart piezo-composite cylinder is assumed to be submerged in a viscous acoustic fluid with its acoustic properties given are Table 8.1 and Table 8.2 [1, 194]. The material used in the core layer of the piezo-composite cylinder is made of Aluminium, while the actuator layer is made of piezoelectric materials. The mechanical and electrical properties of the smart piezo-composite cylinder are given in Table 5.1 and Table 5.2, respectively. The amplitude of the incident plane wave pressure is considered to be 1 Pa. In this section, firstly, the viscous effect of fluid on the STL will be discussed, followed by the temperature effect, and anisotropic

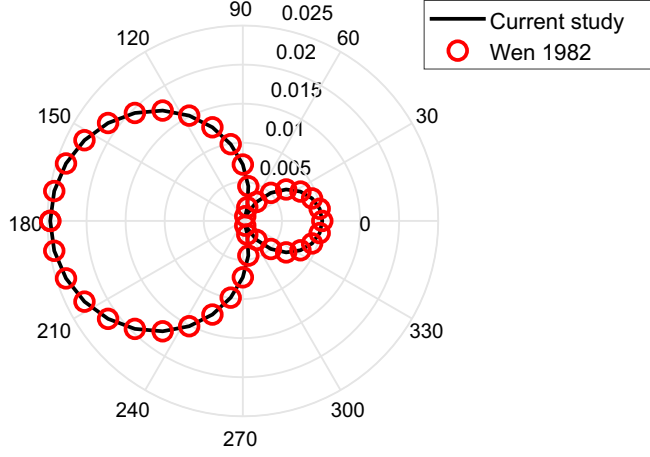


Figure 8.4: Angular distributions of the scattering patterns of pressures at a far-field for a brass cylinder submerged in glycerine at  $77^\circ F$  ( $\Re[k_c]r_{in} = 0.1$ ) .

material property effect. Finally, the effect of piezoelectric boundary conditions on the STL will be discussed and explained.

Figure 8.3 shows the TL through a single layer of cylinder calculated by the Flugge-Lure-Byrne thin-walled shell theory and the 3D theory of elasticity under no-flow condition ( $\text{Mach}=0$ ) for three different attack angles ( $\alpha = \pi/6; \pi/3; \pi/2$ ). The shear and bulk coefficient of viscosity was set to zero in Equation 8.2d in order to calculate the STL for non-viscous fluids. The cylinder is assumed to be made of Aluminium, filled and surrounded with air as the acoustics properties of the fluid medium and the mechanical properties of the Aluminium materials are given in Table 8.1, and Table 5.1, respectively. Figure 8.3 demonstrates a good agreement with the results presented in Ref.[2].

The most relevant acoustic field parameter is the far-field scattered pressure. The

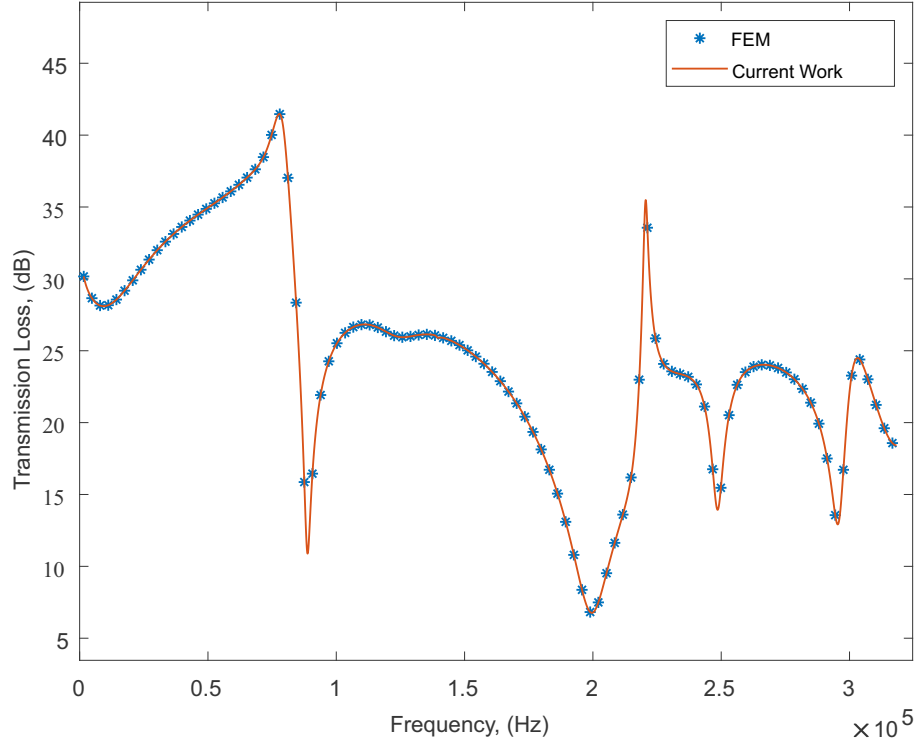


Figure 8.5: STL comparison between the current study and FEM model for a piezo-composite cylinder, filled and submerged in Glycerol at  $40^{\circ}C$ . The cylinder is assumed to be made of a single layer of Aluminium coated with radially polarized PZT4 piezoelectric material. Besides, the cylinder is excited by a normal incident plane wave while the open-loop electrical boundary condition is enforced at the internal and external surface of the cylinder.

scattered far-field pressure amplitude can be defined using Equation 8.5 as [216],

$$|p_{\infty}^{scat}(r, \theta, z, \omega)| = \lim_{r \rightarrow +\infty} \left| -i\omega\rho\phi_c(r, \theta, z, \omega) + k_c^2 \left( \lambda + \frac{4}{3}\mu \right) \phi_c(r, \theta, z, \omega) \right|. \quad (8.10)$$

Figure 8.4 demonstrates the angular distribution of the scattered pressures at far-field for a single layer brass cylinder, fully submerged in glycerine at  $77^{\circ}F$ , excited by a normal incident plane wave at a selected dimensionless wave number of  $\mathbb{R}([k_c]r_{in}) = 0.1$ . The acoustic properties of glycerine are given in Table 8.1.

The angular distribution of the scattered pressures at the far field was calculated by setting the thickness of the piezoelectric layer equal to zero. The results for the angular distribution of the scattered pressures at far-field shown in Figure 8.4, displays an excellent agreement with results presented in Ref.[16].

Figure 8.5 shows the STL comparison between the current study and FEM model (COMSOL MULTIPHYSICS) for a piezo-composite cylinder, filled and submerged in Glycerol at  $40^{\circ}C$ . The dynamic viscosity and expansive viscosity of Glycerol at different temperatures are given in Table 8.2, while the acoustic properties of Glycerol are given in Table 8.1. The cylinder is assumed to be made of a single layer of Aluminium coated with radially polarized PZT4 piezoelectric material. The mechanical properties of the constituent materials are given in Table 5.1, whereas the electrical properties of the radially polarized PZT4 are shown in Table 5.2. Besides, the cylinder is excited by a normal incident plane wave while the closed-loop electrical boundary condition is enforced at the internal and external surface of the cylinder.

In order to simulate the boundless domain of an acoustic medium in finite element software, a PLM is used to truncate the domain. PLM is an artificial absorbing layer that prevents the reflection of outgoing acoustic waves back into the internal domain. Nevertheless, there is always a partial reflection of outgoing waves from the PLM layer, which is the inevitable result of truncated computational regions in numerical methods. In order to perform FEM simulation, 51648 tetrahedron mesh were used to model the piezo-composite cylinder in addition to the internal and external acoustic fluids. Moreover, the mesh size sensitivity analysis was carried out for checking numerical convergence. The outcome, as shown in Figure 8.5, displays

an excellent agreement between the current study and FEM modelling results.

## 8.3 Results and discussion

in this section, we will perform a parametric study to investigate the effect of viscosity, anisotropy and piezoelectricity on the STL.

### 8.3.1 Effect of Viscosity on STL

In this section, the effect of the viscosity of the surrounding acoustic fluid on the STL will be discussed and explained. Most calculations are performed in the frequency range of  $f < 1$  MHz due to the slow convergence of the series solution.

Figure 8.6 displays STL comparison between inviscid and viscous models at different frequency spectra. The short-circuited electrical boundary condition is applied at the outer and inner layers of the piezoelectric cylinder, while the cylinder is excited by a normal incident plane wave with the amplitude of 1 Pa. The core layer of the cylinder is made of Aluminum, while the piezoelectric layer is made of radially polarized PZT4 ( $r_{in} = 19$  mm,  $r_a = 20$  mm and  $r_{ex} = 21$  mm). The mechanical properties for the Aluminum and PZT4 are given in Table 5.1, whereas the electrical properties of the radially polarized PZT4 are given in Table 5.2. The internal cavity of the piezo-composite cylinder is filled with Glycerol; also, the piezo-composite cylinder is submerged in Glycerol at 0°C. The dynamic viscosity and expansive viscosity of Glycerol at different temperatures are given in Table 8.2. Furthermore, the acoustic properties of Glycerol at 0°C are given in Table 8.1.

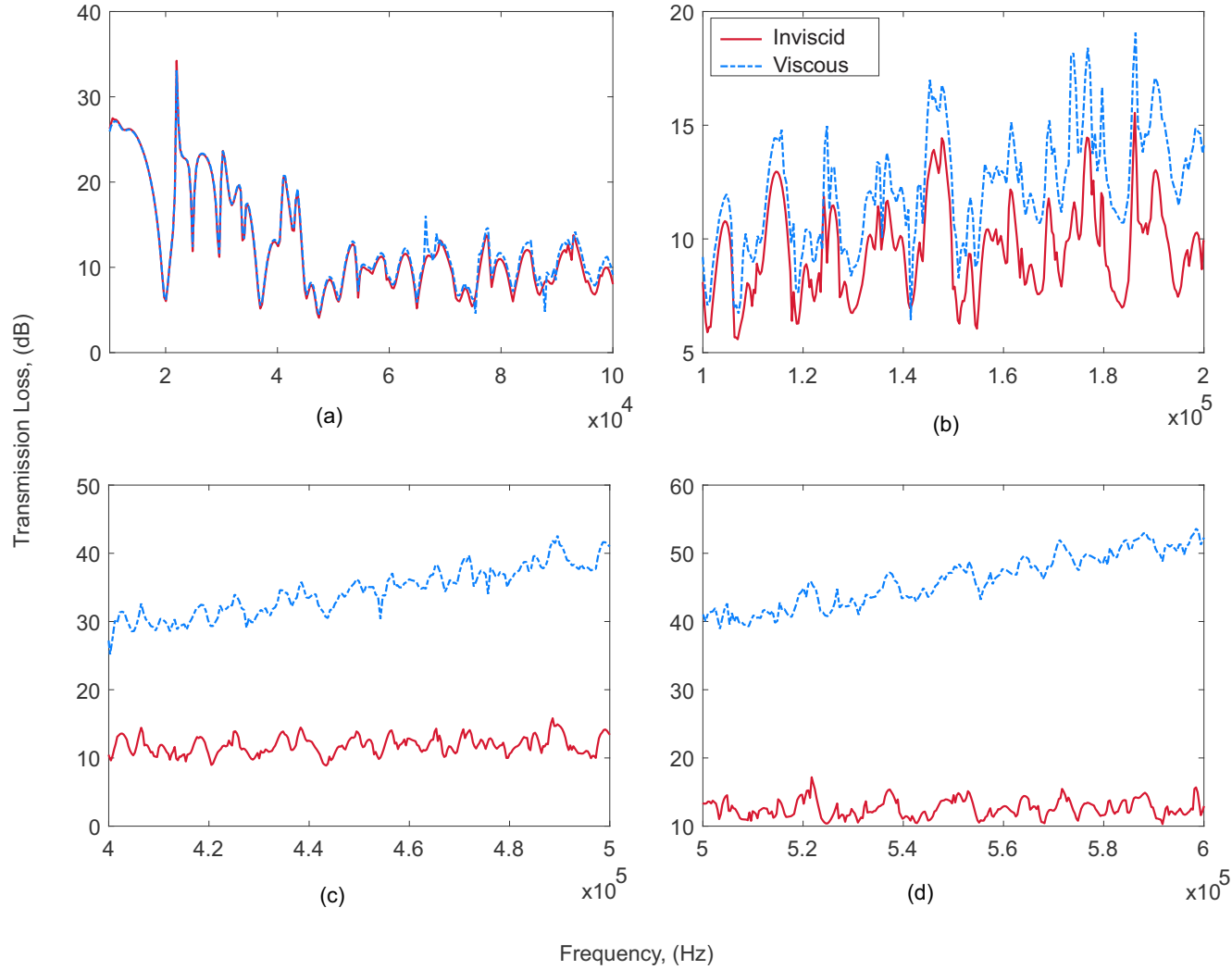


Figure 8.6: STL comparison between inviscid and viscous model at different frequency spectra for the short-circuited electrical boundary conditions. The cylinder is excited by a normal incident plane wave ( $\alpha = \pi/2$ ). The core layer of the cylinder is made of Aluminum, while the piezoelectric layer is made of radially polarized PZT4 ( $r_{in} = 19$  mm,  $r_a = 20$  mm and  $r_{ex} = 21$  mm). The Piezo-composite cylinder is filled with and submerged in Glycerol at  $0^\circ\text{C}$ .



As seen in Figure 8.6, the effect of fluid viscosity is not dominant on the STL at the frequency range between 0 to 10 kHz. Consequently, the difference between the STL obtained when the fluid is non-viscous or viscous is insignificant. This shows that the non-viscous model can only be used when the value of the excitation frequency is relatively low (here the excitation frequency should be lower than 40 kHz) and the non-viscous model should not be used for relatively high frequencies; otherwise the final result for the STL will be underestimated. As the frequency of the incident wave increases to a higher value in the range between 400 to 600 kHz, the viscous model shows a different behavior compared to the non-viscous model; the higher the frequency of the incident wave is, the bigger the difference is. The reason is that the value of shear and compressional wave numbers given in Equation 3.21 becomes a complex number for the viscous model, while the value of the compressional wave is a real number in the non-viscous model. Due to the lack of viscosity, there is no shear wave number in the non-viscous model.

As shown in Equation 3.21, for a low value of excitation frequency, the imaginary part of both shear and compressional waves are small and can be neglected. This is why the non-viscous and viscous plot shows the same behavior in low-frequency ranges. However, as the value of excitation frequency of the incident wave increases, the imaginary part of the compressional and shear wave becomes significant, especially the imaginary part of the compressional wave increases with power 2 of frequency. This is why, as the excitation frequency increases, we can see more differences in the results of the STL. So, the imaginary part of the compressional and shear waves numbers plays an important role at high frequencies. Furthermore, the value of STL shows a higher magnitude of STL compare to the non-viscous model in the

frequency range between 100 to 600 kHz. This indicates that viscosity decreases the acoustic power transmitting inside the cylinder. The reason is that some of the acoustic waves are attenuated due to viscous loss before entering the cylinder, and as result, it increases the soundproofing performance of the structure.

Figure 8.7 shows the STL versus dynamic viscosity of the fluid for the cylinder submerged in Glycerol at 0°C. The cylinder is made of a single layer of Aluminum excited by a normal incident plane wave with the amplitude of 1 Pa ( $r_{in} = 19$  mm,  $r_a = 20$  mm). The mechanical properties for Aluminum are given in Table 5.1. As seen from the figure, the effect of viscosity is insignificant in lower frequencies such as  $f = 100$  kHz, however, the effect of dynamic viscosity becomes significant at a higher excitation frequency such as  $f = 300$  kHz and  $f = 400$  kHz. In addition, the STL linearly increases as the value of dynamic viscosity increases, especially for the case of  $f = 400$  kHz. The reason is that as the value of dynamic viscosity increases at a higher range of excitation, the imaginary part of the compressional wave number increases by the exponent two of the excitation frequency as it is given in Equation 3.21b. As result, the imaginary part of the compressional wave number will have a higher magnitude compared to the real part. The higher value of compressional wave number results in viscous dissipation [217]. As more incident, acoustic waves attenuated due to the high value of dynamic viscosity, the magnitude of STL increases, which results in providing a better soundproofing ability for the fluid with higher dynamic viscosity.

Figure 8.8 compares the effect of dynamic viscosity and bulk viscosity on the STL of the cylinder submerged in glycerol. The frequency of the incident plane wave is set to 100 kHz. As seen from the figure, it is obvious that the value of the

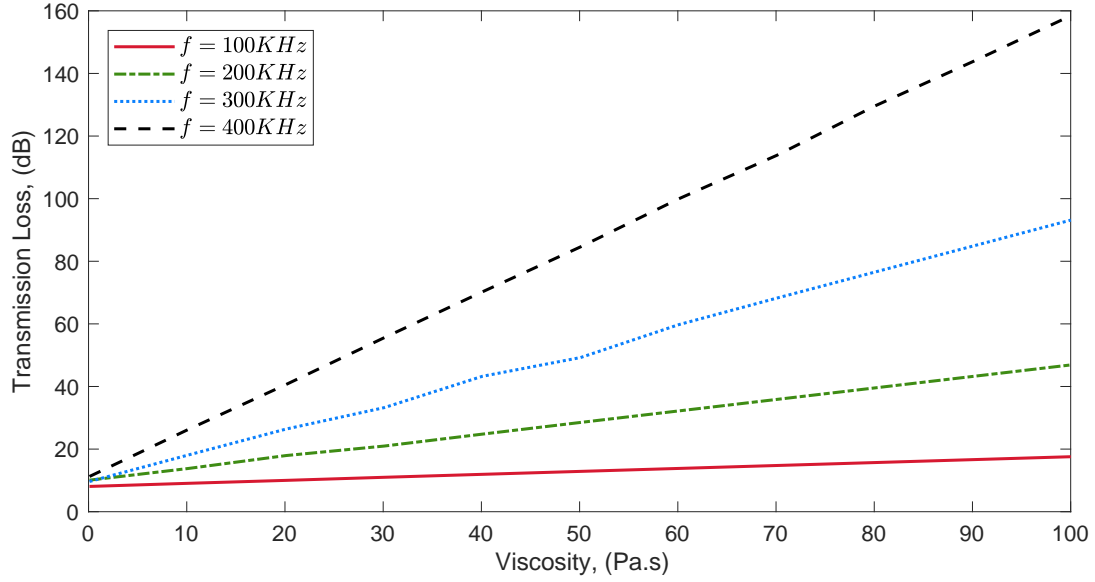


Figure 8.7: STL versus dynamic viscosity for a cylinder submerged in glycerol at 0°C. The cylinder is made of a single layer of Aluminum excited by a normal incident plane wave with the amplitude of 1 Pa ( $r_{in} = 19$  mm,  $r_a = 20$  mm).

dynamic viscosity of the surrounding fluid has more effect on the STL compared to the bulk viscosity of the fluid. The plot for the dynamic viscosity also shows a higher slope compared to the plot associated with the bulk viscosity. The reason is that the complex part of the compressional wave has a linear relation with the dynamic viscosity and bulk viscosity, as described in Equation 3.21b. However, the slope for the dynamic viscosity is  $\frac{4}{3}$ , whereas this coefficient is 1 for the case of bulk viscosity. This way, the effect of dynamic viscosity on the imaginary part of the compressional wave number is slightly higher than the bulk viscosity. This results in a higher attenuation of acoustic waves due to a viscous loss. This is why the STL is slightly more sensitive to the changes in the dynamic viscosity compared to the bulk viscosity.

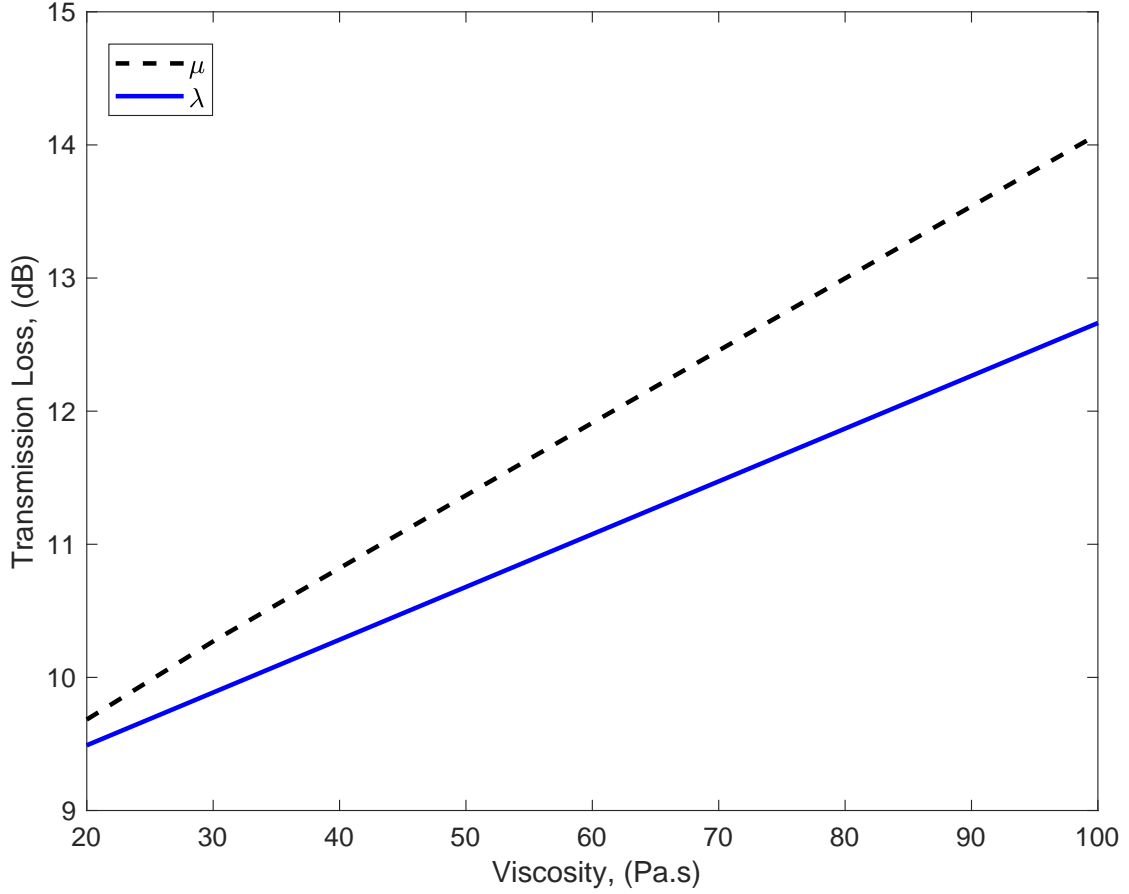


Figure 8.8: Comparison of the effect of dynamic viscosity and bulk viscosity on the STL of the cylinder submerged in glycerol. The cylinder is made of a single layer of Aluminum excited by a normal incident plane wave with the amplitude of 1 Pa ( $r_{in} = 19$  mm,  $r_a = 20$  mm). The frequency of the incident plane wave is set to 100 kHz

### 8.3.2 Effect of temperature on the STL

Figure 8.9 shows the effect of fluid temperature on the STL through a piezo-composite cylinder at different frequency spectra for the short-circuited electrical boundary conditions. The cylinder is excited by a normal incident plane wave ( $\alpha = \pi/2$ ).

As seen from the figure, the differences between the values of the STL for glycerol

at 0°C and glycerol at 40°C are very close in the frequency range between 1 to 100 kHz, while the differences are more dominant as the frequency of excitation increases to a higher value such as the frequency range between 300 to 500 kHz. Also, as the temperature increases, the value of STL decreases especially when the excitation frequency of the incident wave is high. The reason is that as the temperature of the surrounding fluid increases, the dynamic viscosity and expansive (volume) viscosity of the fluid decreases accordingly. When the temperature of the fluid increases, there is an increase in the molecular interaction because the molecules travel faster in high temperatures [218, 219]. In addition to the molecular interchange, cohesive forces between the molecules contribute to liquid viscosity [219]. As fluid temperature increases, cohesive forces are decreased and molecular interactions are increased, which results in a reduction in the shear viscosity of the fluid [219]. On the other hand, by decreasing the temperature, the cohesive forces become dominant and the molecular interactions decrease; this leads to an increase in the shear viscosity of the fluid. Increasing the viscosity of the fluid at low temperatures results in a more significant attenuation of acoustic waves. As a result of these losses, less acoustic power can be transmitted inside the cylinder, which leads to increasing the STL. So, the lower the temperature is, the higher the STL becomes and vice versa.

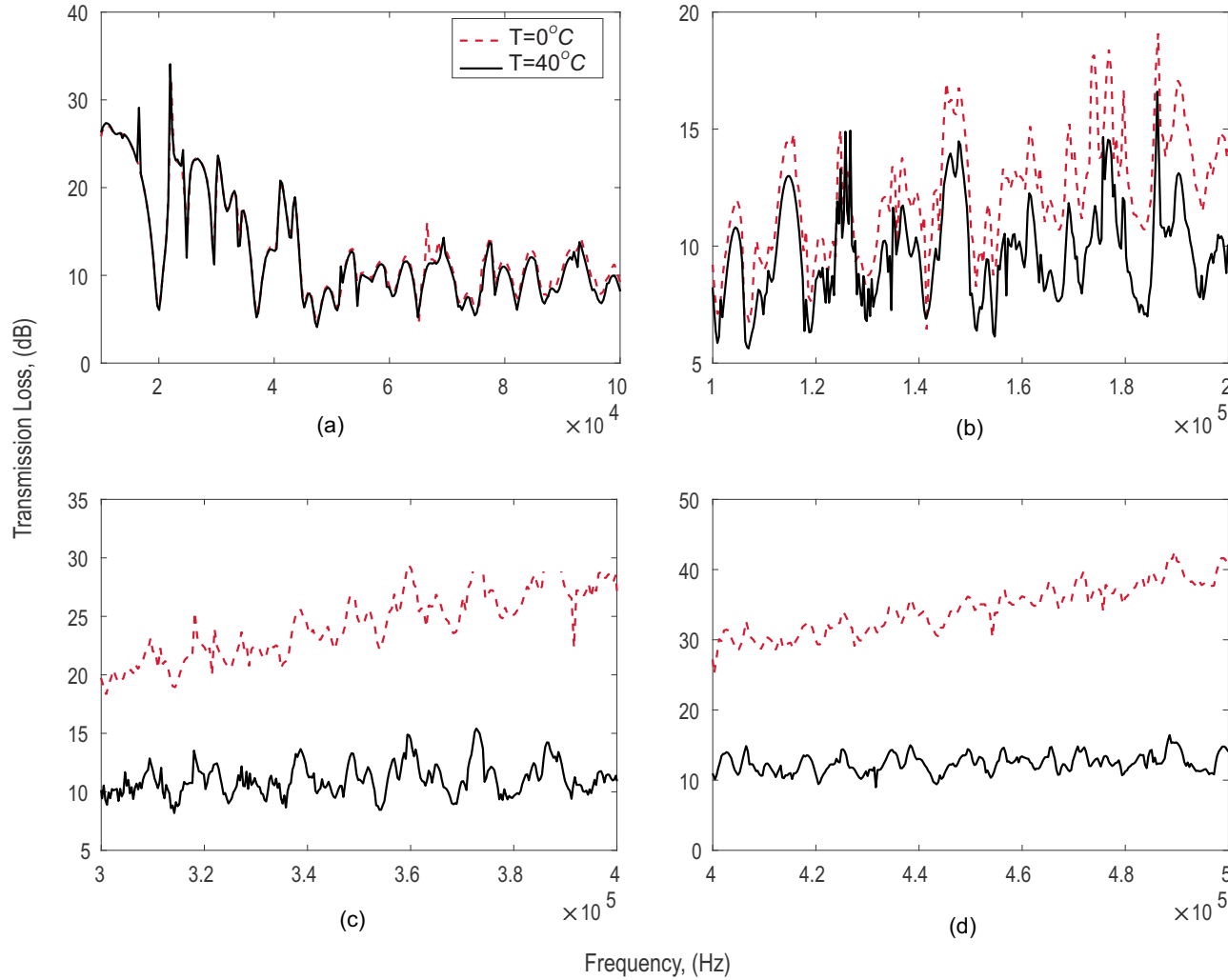


Figure 8.9: Effect of fluid temperature on the STL through a piezo-composite cylinder at different frequency spectra for the short circuited electrical boundary conditions; the cylinder is excited by a normal incident plane wave ( $\alpha = \pi/2$ ). The core layer of the cylinder is made of Aluminum, while the piezoelectric layer is made of radially polarized PZT4 ( $r_{in} = 19$  mm,  $r_a = 20$  mm and  $r_{ex} = 21$  mm). The Piezo-composite cylinder is filled with and submerged in Glycerol at different temperatures ( $T = 0^{\circ}\text{C}$ ,  $\mu = 9390$  cp,  $\lambda = 12000$  cp;  $T = 40^{\circ}\text{C}$ ,  $\mu = 234$  cp,  $\lambda = 238$  cp).

### 8.3.3 Effect of anisotropy on the STL considering fluid viscosity

In this section, the effect of anisotropy of a cylindrical shell submerged in a viscous fluid on the STL will be discussed. Most calculations are performed in the frequency range of  $f < 500$  kHz due to the slow convergence of the solution.

Figure 8.10 shows the effect of anisotropy of the piezoelectric actuator layer with three different levels of anisotropy on the STL spectra for the short-circuited piezo-composite cylinder submerged in Fluorocarbon (FC-75) at  $25^\circ C$  at different ranges of frequencies. The acoustic properties of Fluorocarbon (FC-75) are given in Table 8.1. The cylinder is excited by a normal incident plane wave ( $\alpha = \pi/2$ ) with a pressure amplitude of 1 Pa. The elastic layer of the cylinder is made of Aluminum ( $r_{in} = 19$  mm,  $r_a = 20$  mm and  $r_{ex} = 100$  mm). The actuator layer of the cylinder is changed for three different materials with isotropic, orthotropic, and triclinic mechanical properties. For the triclinic case, the actuator is constituted of one layer of Lithium niobate ( $LiNbO_3$ ) with the crystalline Z axis along z and the crystalline Y axis along r and the second layer is made up Lithium tantalate ( $LiTaO_3$ ) with crystalline X axis along z and the crystalline Y along r, in order to show the triclinic effect on the STL (see Akcakaya and Farnell [199]). The mechanical and electrical properties of the triclinic piezoelectric materials are given in Table 4.1.

The actuator layer with orthotropic mechanical properties is made of the same triclinic material by allocating all the nonzero elastic constants to zero in a way that it alternates from a triclinic material to an orthotropic piezoelectric material with only 9 distinct elastic constants (see [3] for more details). Lastly, the same approach

was used to model the isotropic actuator layer by adjusting the non-zero orthotropic stiffness constants in the stiffness matrix, which includes only two independent material constants with 12 nonzero terms.



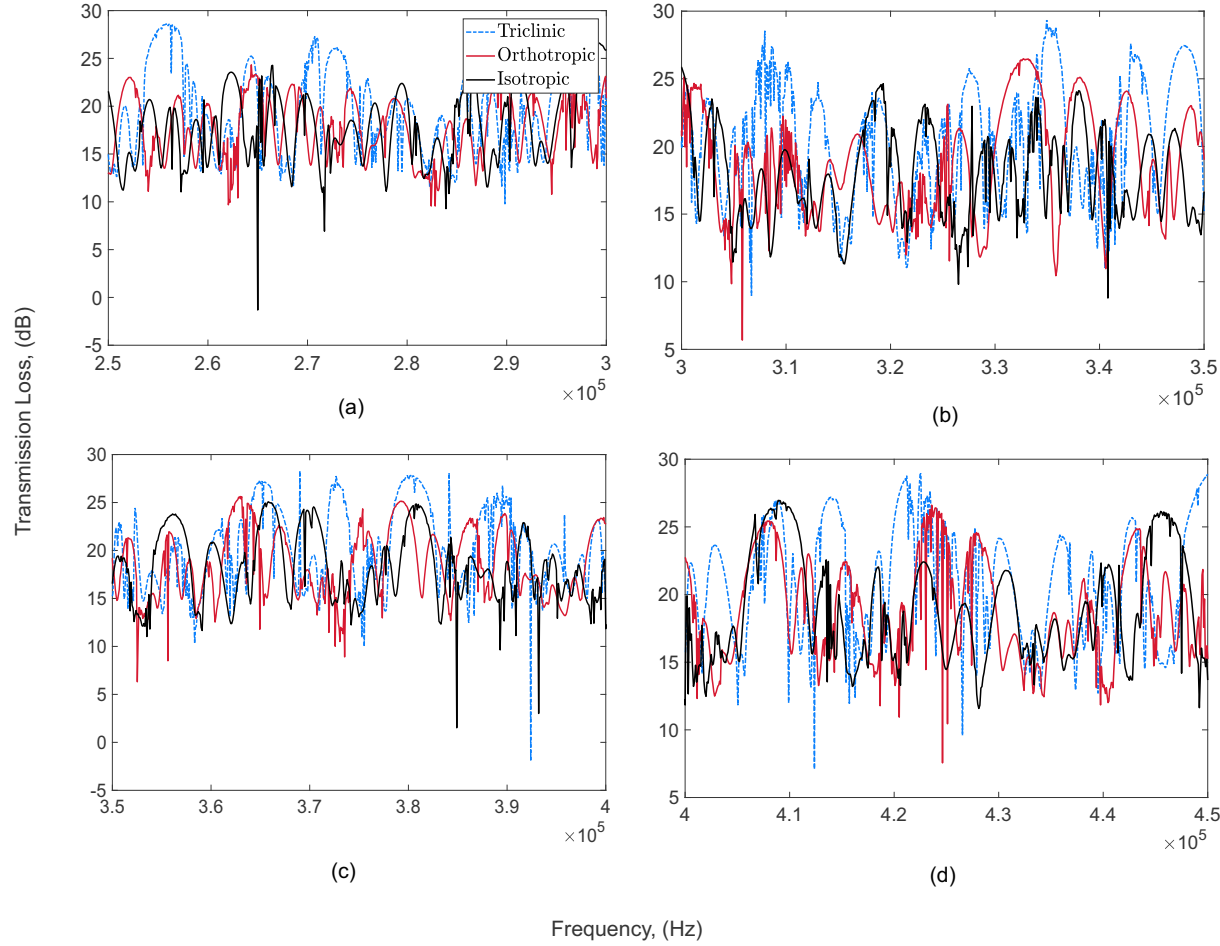


Figure 8.10: Effect of anisotropy of actuator layer on the STL spectra for the short-circuited piezo-composite cylinder submerged in Fluorocarbon (FC-75) at 25°C at different frequency ranges. The cylinder is excited by a normal incident plane wave ( $\alpha = \pi/2$ ) with a pressure amplitude of 1 Pa. The elastic layer of the cylinder is made of Aluminum, while three different actuator layers are considered to be made of isotropic, orthotropic, or triclinic materials. The triclinic case is constituted of one layer of Lithium niobate ( $LiNbO_3$ ), and the second type of layer is made of Lithium tantalate ( $LiTaO_3$ ) ( $r_{in} = 19$  mm,  $r_a = 20$  mm and  $r_{ex} = 100$  mm). The mechanical and electrical properties of the triclinic piezoelectric materials are given in Table 4.1. The cylinder is also considered to be short-circuited at both its external and internal layers.

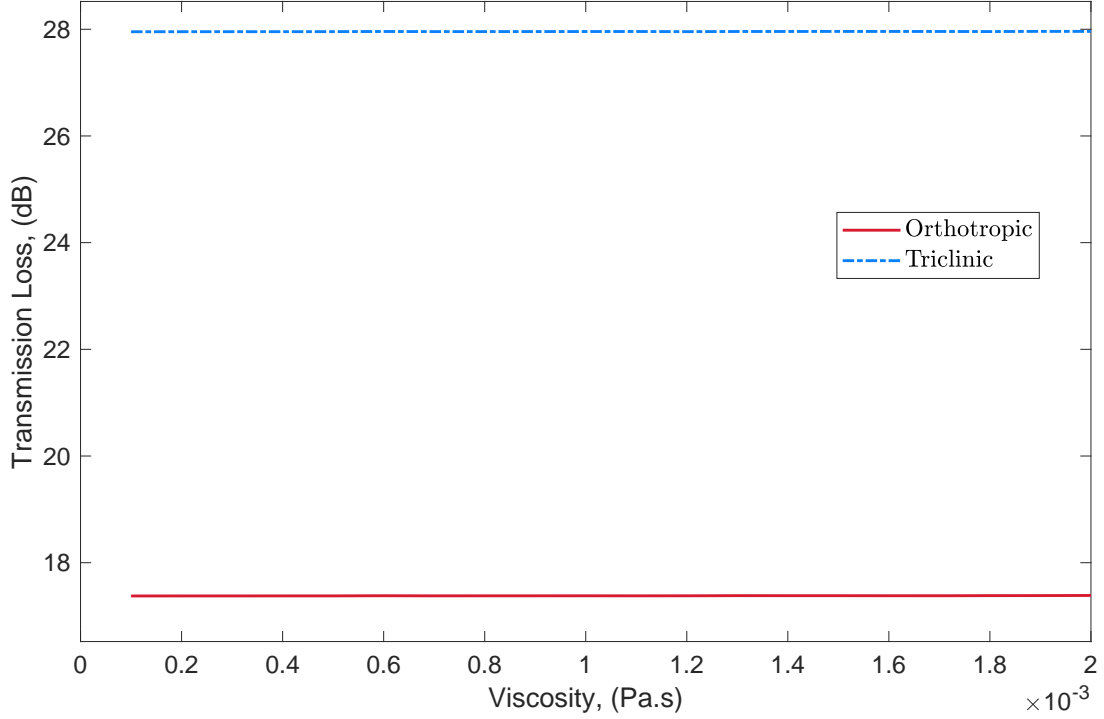


Figure 8.11: Comparison of the effect of anisotropy on the STL of a piezo-laminated cylinder submerged in Fluorocarbon (FC-75) at 25°C for different ranges of dynamic viscosity. The frequency of the incident plane wave is set to 250 kHz. The core layer of the cylinder is made of Aluminum, while the external layer is made of anisotropic piezoelectric material constituting of one layer of Lithium niobate ( $LiNbO_3$ ), and the second type of layer is made up of Lithium tantalate ( $LiTaO_3$ ) ( $r_{in} = 19$  mm,  $r_a = 20$  mm and  $r_{ex} = 100$  mm). The cylinder is considered to be short-circuited on both its external and internal layers. The cylinder is excited by a normal incident plane wave ( $\alpha = \pi/2$ ) with a pressure amplitude of 1 Pa. The mechanical and electrical properties of the triclinic piezoelectric materials are given in Table 4.1. [3].

As seen from the Figure 8.10, there is a shift between the resonance frequency of the triclinic, orthotropic, and isotropic materials. Also, the triclinic material has a higher value of the STL compared to the orthotropic and isotropic cases. It is worth noting that the triclinic materials have 21 independent elastic constants, while the orthotropic materials have only 9 distinct elastic constants whereas the isotropic

materials have only 2 independent material constants. It means that the triclinic materials have a higher elastic stiffness compared to the orthotropic and isotropic materials. In particular, if the elastic cylinder is stiffer, the outer layer and the inner layer of the shell would move less, which would reduce the acoustic power of the waves that were transmitted. Consequently, the STL will increase because a lower acoustic power is transmitted into the cylinder. As a result, the cylinder can provide better sound isolation if the piezoelectric layer is made of triclinic materials with a higher level of anisotropy.

Figure 8.11 shows the effect of anisotropy on the STL of a piezo-laminated cylinder submerged in Fluorocarbon (FC-75) at 25°C for different ranges of dynamic viscosity. The excitation frequency of the incident plane wave is set to 250 kHz. The core layer of the cylinder is made of Aluminum, while the external layer is made of anisotropic piezoelectric material constituting of one layer of Lithium niobate ( $LiNbO_3$ ), and the second type of layer is made up of Lithium tantalate ( $LiTaO_3$ ) ( $r_{in} = 19$  mm,  $r_a = 20$  mm and  $r_{ex} = 100$  mm).

As seen from Figure 8.11, the triclinic materials show a higher value of STL compare to the orthotropic materials. This shows that the triclinic materials, which have a higher level of anisotropy, submerged in a fluid with a higher value of dynamic viscosity provide better performance for the sound isolation.

### 8.3.4 Effect of piezoelectricity on the STL with the viscous fluid

In this section, the effect of piezoelectric boundary conditions on the STL will be discussed. The calculations are performed in the frequency range of  $f < 1$  MHz due

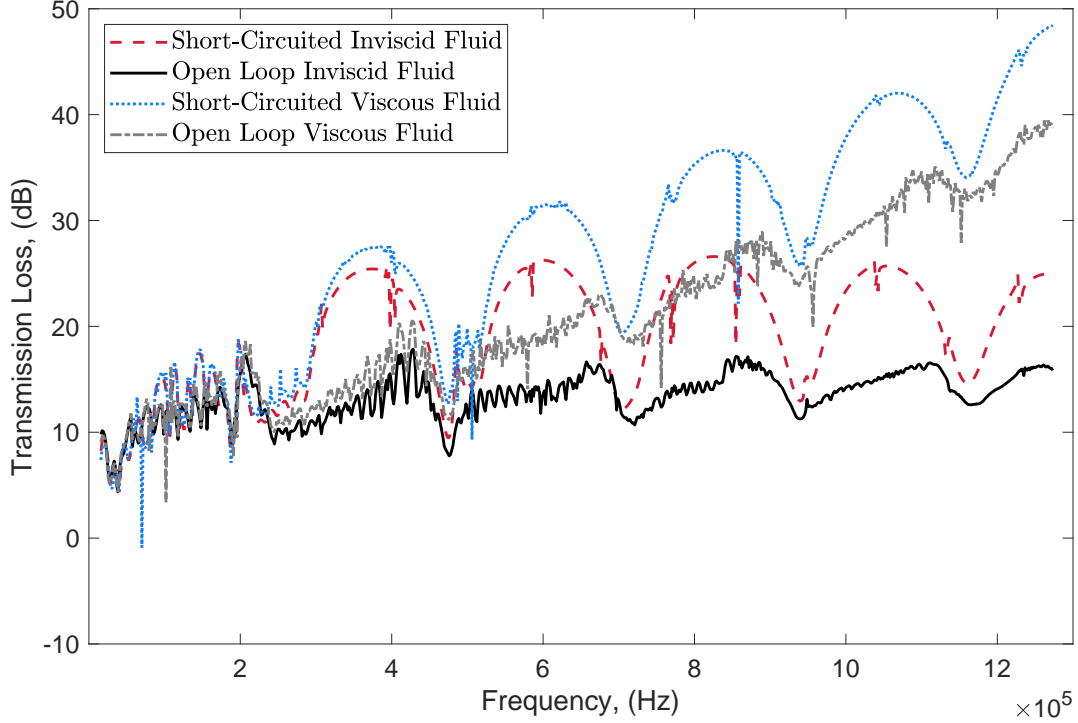


Figure 8.12: Comparison of viscous and inviscid models for the effect of piezoelectric boundary conditions on the STL spectra for the short-circuited and open-circuited piezo-composite cylinder submerged in glycerin at  $0^{\circ}\text{C}$  at different ranges of frequencies. The cylinder is excited by a normal incident plane wave ( $\alpha = \pi/2$ ) with the pressure amplitude of 1 Pa. The core layer of the cylinder is made of Aluminum, while the external layer is made of radially polarized PZT4 ( $r_{in} = 19$  mm,  $r_a = 20$  mm and  $r_{ex} = 30$  mm).

to the slow convergence of the series solution.

Figure 8.12 shows the comparison of viscous and inviscid model for the effect of piezoelectric electrical boundary condition on the STL spectra for the short-circuited and open-circuited piezo-composite cylinder submerged in Glycerin at  $0^{\circ}\text{C}$  at different ranges of frequency. As seen from the figure, the effect of the piezoelectric boundary conditions is not dominant on the STL at the frequency ranges between 0 to 200 kHz. Consequently, the difference between the STL calculated for the

open-loop and short-circuited electrical boundary conditions for both viscous and inviscid models is insignificant. However, as the excitation frequency increases to higher values such as 1 MHz, the difference between the calculated values becomes significant. Particularly, the short-circuited cylinder submerged in a viscous fluid shows a higher STL than the open-loop smart cylinder submerged in an inviscid fluid. In addition, the dips of negatives for the open-loop case show a lower STL than the short-circuited boundary condition, especially at the frequency ranges beyond 1.2 MHz. This means that short-circuited electrical boundary conditions absorb more energy during the charging and discharging process. Additionally, we see that viscosity also affects STL in the case of inviscid and viscous models.. For example, the short-circuited inviscid plot shows a lower STL compared to the viscous one at high-frequency ranges (1.2 MHz). Thus, viscosity contributes a significant amount to higher STL values in comparison to short circuit electrical boundary conditions, particularly at high frequencies.

Figure 8.13 shows the effect of different electrical boundary conditions on the STL of piezo-laminated cylinder submerged in oil at 25°C for different ranges of dynamic viscosity. The frequency of the incident plane wave is set to 400 kHz. As seen from Figure 8.13, by increasing the value of dynamic viscosity the magnitude of the STL increases for both the open-loop and short-circuited electrical boundary conditions. However, the short-circuited electrical boundary conditions show a higher value of the STL compare to the open-loop boundary conditions. The higher value of STL for the short-circuited electrical boundary condition makes this type of electrical boundary condition to be suitable for sound isolation purposes.

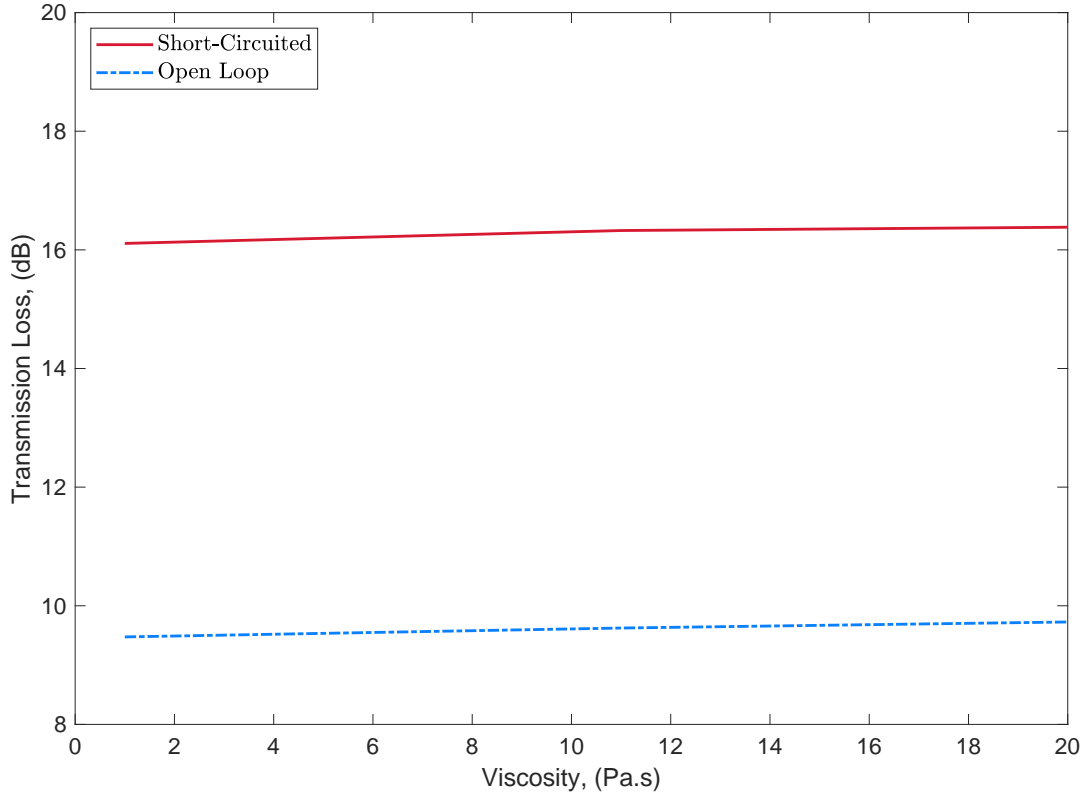


Figure 8.13: Comparison of the effect of different electrical boundary conditions on the STL of piezo-laminated cylinder submerged in the Oil at 25°C for a different range of dynamic viscosity. The frequency of the incident plane wave is set to 400 kHz. The elastic layer of the cylinder is made of Aluminum, while the external layer is made of radially polarized PZT4 ( $r_{in} = 19$  mm,  $r_a = 20$  mm and  $r_{ex} = 30$  mm). The cylinder is excited by a normal incident plane wave ( $\alpha = \pi/2$ ) with a pressure amplitude of 1 Pa.

## 8.4 Conclusions

The current study is aimed to rigorously investigate the effects of fluid viscosity, electrical boundary condition, and anisotropy on the STL through a thick smart anisotropic piezo-composite cylinder, excited by an oblique incident plane wave. The 3D theory of elasticity and piezoelectricity are used to model the smart piezo-composite cylinder, while the Navier-Stokes equation is employed to describe the viscous acoustic

medium. The Helmholtz decomposition is used to resolve the velocity field of fluid into longitudinal and transverse vectors, whereas the state space method and transfer matrix approach are used to model the smart cylindrical structure. Subsequently, the closed-form solution is developed by enforcing appropriate boundary conditions along with proper wave harmonic field expansion. The validity of the proposed closed-form solutions is checked with different data from the simplified model given in the literature as well as a finite element package known as COMSOL MULTIPHYSICS. Parameter studies are carried out to investigate the effect of fluid viscosity (dynamic viscosity and bulk viscosity), shell anisotropy, and piezoelectric boundary conditions on the STL through a piezo-composite cylinder submerged in a viscous fluid. The main findings of this research are as follows:

- The non-viscous model can only be used when the value of the excitation frequency is relatively low (Less than 20 kHz). The inviscid model should not be used for a broad range of frequencies when the submerging fluid has a high value of dynamic and expansive viscosities, otherwise, the final result for STL will not be accurate.
- An acoustic power transmitting within the cylinder can be decreased when the fluid has a high dynamic viscosity and a high bulk viscosity.
- As the temperature of the surrounding fluid increases, the value of STL decreases and vice versa, especially, when the excitation frequency of the incident wave is relatively high.
- With an increase in dynamic viscosity, the magnitude of STL linearly increases, which leads to a greater degree of soundproofing for fluids.

- There is a shift between the resonance frequency of the triclinic, the orthotropic, and isotropic materials. The triclinic materials have a higher value of the STL compare to the isotropic and orthotropic materials.
- The cylinder submerged in a viscous fluid with short-circuited electrical boundary conditions provides a higher sound isolation performance. The viscosity effect on STL is more significant than the effect of electrical boundary conditions at a higher frequency range (for the specific structure of this work, the frequency should be approximately greater than 200 kHz).

As suggestions of the important future works, the exact size effect should be studied to reveal the possible application of our idea to practical applications like underwater vehicles. In addition, the proposed model is based on special assumptions that the whole structure is not running in the fluid or the fluid is not flowing in and outside the solid. To make the STL study closer to some practical operations, the relative motions between the solid and fluid can be considered in the following works.



# Chapter 9

## Conclusions and Future Works

### 9.1 Conclusions

Dynamic studies of thick smart cylindrical piezo-composite structures are studied in an effort to use an-isotropic piezoelectric materials to design structures with superior soundproofing performances. A robust mathematical approach is used to address the multiphysics nature of the problem.

Firstly, the free vibration of the general form of an anisotropic piezoelectric material which is known as triclinic materials with all possible material constants is analytically modeled and studied to cover a broad range of anisotropic piezoelectric materials. The current model can handle piezoelectric materials with stronger anisotropy such as lead Lithium Tantalate, Lithium Niobate, and Oxyborate crystals of  $YCa_4O(BO_3)_3$  (YCOB). The main findings of this investigation are as follows

- The orthotropic model can only be used to model triclinic piezoelectric materials when the circumferential wave number, axial wave number, and the value of the lowest natural frequency are all relatively small.

- The results of the orthotropic piezoelectric model can not be extended to investigate the behavior of the triclinic piezoelectric materials in high-frequency ranges.

Next, the first study was extended to investigate sound transmission through a thick-walled FGM piezo-laminated cylindrical shell filled with and submerged in compressible inviscid fluids. STL is calculated by exact integration over the shell's outer surface. Parameter studies are conducted to investigate the effects of piezoelectric material properties, piezoelectric polarization direction, shell thickness ratio, electrical boundary conditions, and FGPM on the STL due to the piezoelectricity. This study shows several important findings such as:

- The radially polarized piezoelectric shows a better performance in the cylinder isolation compared to the axially polarized one, especially in the high value of incident angles at a high frequency larger than 500Hz.
- Short-circuited electrical boundary conditions can be used to improve the sound isolation performance of the piezo-composite cylinder in high-frequency ranges considering the energy dissipation during the charging and discharging process.

In order to provide higher STL at the resonance frequency, the previous model was utilized to control STL through the piezo-composite cylinder. The active control strategy is achieved by sending a control signal from the distributed piezoelectric sensor layer through a controller with specific feedback gain to drive the external piezoelectric actuators. The mechanical stress generated by the piezo-actuator layer cancels the parts of the input incident wave to enhance the STL. Comprehensive

numerical studies are carried out to investigate the poling direction, and feedback gain effects on the STL. This study shows new distinguished findings such as:

- A significant wave isolation effect is realized at the resonant frequencies on the STL spectra for a radially/axially polarized piezo-composite cylinder with different feedback gains.
- In the case of the axially polarized piezoelectric actuator and sensor, the control feedback strategy reduces the unfavorable oscillatory motion of the cylinder in addition to providing a superior sound isolation enhancement, particularly for near-grazing incident angles ( $\alpha = \pi/12$  &  $\pi/6$ ).

Next, our model was improved to consider the influence of size and configuration of piezoelectric electrodes on sound transmission loss (STL) through thick-walled piezo-laminated cylindrical shells. A closed-form solution is generated by enforcing the proper boundary conditions and expanding the harmonic field.

- Increasing the number of electrode patches may not necessarily provide higher soundproofing abilities
- By proper choice of electrode size, one can avoid the resonance frequency of the cylinder to provide higher sound transmission loss

Finally, due to the failure of the inviscid model when the structure is submerged in the fluid with a high level of viscosity, the acoustic viscous model was used to study the sound transmission loss through the smart piezo-laminated cylindrical shell. The main findings of this study are as follows:

- The non-viscous model can only be used when the value of the excitation frequency is relatively low (Less than 20 KHz). The inviscid model should not be used for a broad range of frequencies when the submerging fluid has a high value of dynamic and expansive viscosities, otherwise, the final result for STL will not be accurate.
- An acoustic power transmitting within the cylinder can be decreased when the fluid has a high dynamic viscosity and a high bulk viscosity.
- With an increase in dynamic viscosity, the magnitude of STL linearly increases, which leads to a greater degree of soundproofing for fluids.

More detailed conclusions can be found at the end of each previous chapter.

## 9.2 Possible Future Works

This work presented a very robust mathematical model to investigate the effect of anisotropy of piezoelectric materials in addition to studying the STL through the piezo-composite cylindrical structure. The model was later on used to control the STL in order to provide engineering structures with better sound isolation performances. Unquestionably, this powerful complex model can be further extended to consider other effects. In our future work, we are interested in studying Auxetic materials. Auxetics are structures or materials that have a negative Poisson's ratio. This means when these materials are subjected to the applied force, they become thicker in the perpendicular direction of the applied force. Auxetics can be structured on a macroscopic scale, in crystals, or molecules. These materials can show high energy absorption and fracture resistance. In future works, we will

investigate the effect of Auxetic materials on the STL from cylindrical structures in order to predict the sound isolation performance of these new materials. Such a study can have a widespread application in the development of products with enhanced sound absorption characteristics, which can be used for sound attenuation purposes. Auxetic materials also have a very low density, which makes them a better candidate when the weight of the structure is of concern, for instance, sound isolation in airplane cabins.

The current model can be used for data transmission through a thick-walled tunnel. As we know the majority of tunnels are steel-containing structures. In order to protect electronic equipment, shielding the radio waves with steel-containing structures is desirable. However, it is detrimental to receiving telecommunication signals. This means that radio waves that are used in the cell phone can not pass through the tunnel for communication purposes. This problem can be solved by using acoustic waves. Acoustic waves can easily propagate through concrete, metal, etc. Therefore, acoustic waves can be used for the transmission of multimedia data includes images and videos. The current work provides a suitable framework for using acoustic waves to transfer data through the tunnel. The incident wave can propagate through the concrete tunnel and the transmitted wave can be used to transfer multimedia data. In order to amplify the transmitted signal, the data should be transferred at a frequency with lower sound transmission loss in order to increase the power of the transmitted signal.

In addition, in order to make structures with superior soundproofing abilities, pro-elastic materials can be used in the core layer of the cylinder. The use of porous materials for noise control is increasing due to their sound-absorbing properties.

They are frequently used in a structure-lined design, bonded, unbounded, or mounted close to the vibrating component. The piezo-laminated shell can be made of the internal layer of poroelastic materials bound to the internal sensor and an external actuator layer made of piezoelectric materials. The controller system like the one given in Chapter 6 can be used to derive the external actuator in order to increase the sound transmission loss from the cylinder. The poroelastic layer can be developed based on Biot's theory of poroelasticity. Then, by using the transfer matrix given in Equation 6.2, and considering the continuity of different layers, the global transfer matrix for the new structure integrated with poroelastic material can be achieved. Using proper mechanical and electrical boundary conditions, the sound transmission loss through the new structure can be obtained. Such structure would show higher sound transmission loss and can be used when there is a great need for a quieter composite structure.

In order to check the results from this work, an experimental setup should be considered. A cylindrical shell with a poroelastic layer should be constructed. To eliminate direct sound transmission from the inside when measuring TL, the ends of the shell should be closed with thick end caps, which should be snugly fitted and sealed with tapes [66]. In order to avoid the reflection of the sound scattered waves from the walls of confined space in order to simulate the infinite medium, the structure should be placed in an anechoic chamber [66]. An anechoic chamber is a room designed to eliminate reflections of electromagnetic or sound waves. Such rooms are often also isolated from other sources of energy. TL can be calculated by installing two microphone pairs on the inside surface and the outside of the shell at the same position [66]. White noise should be used to drive the external

sound sources. Sound waves from the external sound source are reflected both inside and outside the space [66]. The difficult point is to match the assumption in the introduced STL model that only the inward wave on the two surfaces of the solid shell is precisely measured to accurately evaluate the STL value.

It is evident that TL is calculated differently depending on the incident angle of the plane wave used in the analysis [66]. TL can be averaged across all possible incident angles to remove this dependency [66]. The average power transmission coefficient  $\tau$  can be calculated based on the Paris formula [203] and Equation 5.38 as

$$\tau = 2 \int_0^{\alpha_{max}} \Psi(\alpha) \sin(\alpha) \cos(\alpha) d\alpha$$

According to the Mulholland et al. [220], the maximum incident angle should be chosen 80. The cost of such an experimental setup will be 16.44 Cad for 1 m of poroelastic soundproofing foam. The piezoelectric cylinder should cost 129.59 cads for 25 mm with an 18 mm diameter. A DS3 Dodecahedron Loudspeaker needs to be used to send plane wave incident waves which cost approximately around 2,963.84 Cad , if the inward wave can be precisely measured on the solid shell surfaces with the finely prepared experimental setup.

# List of Publication

## Journal Papers

- i. V. Rabbani, A. Bahari, M. Hodaei, P. Maghoul, and N. Wu, Three-dimensional free vibration analysis of triclinic piezoelectric hollow cylinder, *CompositesPart B: Engineering* 158 (2019a) 352–363.
- ii. V. Rabbani, M. Hodaei, X. Deng, H. Lu, D. Hui, and N. Wu, Sound transmission through a thick-walled fgm piezo-laminated cylindrical shell filled with and submerged in compressible fluids, *Engineering Structures* 197 (2019b) 109-323.
- iii. V. Rabbani and N. Wu, Active broadband sound transmission loss control through an arbitrary thick smart piezo-laminated cylinder, *Aerospace Science and Technology*, 110 (2021) 106-515.
- iv. V. Rabbani, N. Wu, P. Maghoul, and D. Hui. Effect of Fluid Viscosity on the Sound Transmission Loss of Smart Piezo-laminated Structures, Submitted to *Journal of Wave Motion*.
- v. V. Rabbani, N. Wu, and P. Maghoul, Effect of Electrode Size and Configuration on the Sound Transmission Loss of Smart Piezo-laminated Structures, Submitted to *International Journal of Mechanical Science*.



## List of Copyrighted Materials

Materials used in chapter 1, chapter 2, and chapter 3 of this thesis are reproduced, with modifications from:

- i. V. Rabbani, A. Bahari, M. Hodaei, P. Maghoul, N. Wu, Three-dimensional free vibration analysis of triclinic piezoelectric hollow cylinder, *CompositesPart B: Engineering* 158 (2019a) 352–363.
- ii. V. Rabbani, M. Hodaei, X. Deng, H. Lu, D. Hui, N. Wu, Sound transmission through a thick-walled fgm piezo-laminated cylindrical shell filled with and submerged in compressible fluids, *Engineering Structures* 197 (2019b) 109323.
- iii. V. Rabbani and N. Wu, Active broadband sound transmission loss control through an arbitrary thick smart piezo-laminated cylinder, *Aerospace Science and Technology*, 110 (2021) 106-515.
- iv. V. Rabbani and N. Wu, P. Maghoul, D. Hui, Effect of Electrode Size and Configuration on the Sound Transmission Loss of Smart Piezo-laminated Structures, *Journal of Sound and Vibration*, submitted.

Upon transferring the copyright to Elsevier Publishing Company, the right to include the final published version of the mentioned records was granted back to the authors for the purpose of inclusion in the thesis.

# Appendices

# A

## A.1 Anisotropic Piezoelectric Constitutive Model

The constitutive equation for a triclinic piezoelectric material in an expanded matrix form can be written as

$$\begin{Bmatrix} \sigma_{rr} \\ \sigma_{\theta\theta} \\ \sigma_{zz} \\ \sigma_{\theta z} \\ \sigma_{rz} \\ \sigma_{r\theta} \end{Bmatrix} = \begin{pmatrix} C_{11} & C_{12} & C_{13} & C_{14} & C_{15} & C_{16} \\ . & C_{22} & C_{23} & C_{24} & C_{25} & C_{26} \\ . & . & C_{33} & C_{34} & C_{35} & C_{36} \\ . & . & . & C_{44} & C_{45} & C_{46} \\ . & . & . & . & C_{55} & C_{56} \\ . & . & . & . & . & C_{66} \end{pmatrix} \begin{Bmatrix} \epsilon_{rr} \\ \epsilon_{\theta\theta} \\ \epsilon_{zz} \\ \epsilon_{\theta z} \\ \epsilon_{rz} \\ \epsilon_{r\theta} \end{Bmatrix} - \begin{pmatrix} e_{11} & e_{21} & e_{31} \\ e_{12} & e_{22} & e_{32} \\ e_{13} & e_{23} & e_{33} \\ e_{14} & e_{24} & e_{34} \\ e_{15} & e_{25} & e_{35} \\ e_{16} & e_{26} & e_{36} \end{pmatrix} \begin{Bmatrix} E_r \\ E_\theta \\ E_z \end{Bmatrix} \quad (\text{A.1.1})$$

and

$$\begin{Bmatrix} D_r \\ D_\theta \\ D_z \end{Bmatrix} = \begin{pmatrix} e_{11} & e_{12} & e_{13} & e_{14} & e_{15} & e_{16} \\ e_{21} & e_{22} & e_{23} & e_{24} & e_{25} & e_{26} \\ e_{31} & e_{32} & e_{33} & e_{34} & e_{35} & e_{36} \end{pmatrix} \begin{Bmatrix} \epsilon_{rr} \\ \epsilon_{\theta\theta} \\ \epsilon_{zz} \\ \epsilon_{\theta z} \\ \epsilon_{rz} \\ \epsilon_{r\theta} \end{Bmatrix} + \begin{pmatrix} \kappa_{11} & \kappa_{12} & \kappa_{13} \\ . & \kappa_{22} & \kappa_{23} \\ . & . & \kappa_{33} \end{pmatrix} \begin{Bmatrix} E_r \\ E_\theta \\ E_z \end{Bmatrix}. \quad (\text{A.1.2})$$

Equation A.1.1 and Equation A.1.2 are corresponding to those of Equation 4.1.

## A.2 Differential Operator

The cylindrical gradient operator,  $\nabla$ , is

$$\nabla = \frac{\partial}{\partial r} e_r + \frac{1}{r} \frac{\partial}{\partial \theta} e_\theta + \frac{\partial}{\partial z} e_z. \quad (\text{A.2.1})$$

### A.3 Kinematic Relations

The Cauchy-Green infinitesimal deformation tensor in an expanded matrix form becomes

$$\begin{pmatrix} \epsilon_{rr} & \epsilon_{r\theta} & \epsilon_{rz} \\ \cdot & \epsilon_{\theta\theta} & \epsilon_{\theta z} \\ \cdot & \cdot & \epsilon_{zz} \end{pmatrix} = \begin{pmatrix} \frac{\partial u_r}{\partial r} & \frac{1}{2} \left( \frac{1}{r} \frac{\partial u_r}{\partial \theta} - \frac{u_\theta}{r} + \frac{\partial u_\theta}{\partial r} \right) & \frac{1}{2} \left( \frac{\partial u_z}{\partial r} + \frac{\partial u_r}{\partial z} \right) \\ \cdot & \frac{1}{r} \frac{\partial u_\theta}{\partial \theta} + \frac{u_r}{r} & \frac{1}{2} \left( \frac{\partial u_\theta}{\partial z} + \frac{\partial u_z}{r \partial \theta} \right) \\ \cdot & \cdot & \frac{\partial u_z}{\partial z} \end{pmatrix}. \quad (\text{A.3.1})$$

Equation A.3.1 corresponds to the one of Equation 4.3.

### A.4 Conservation Laws

The expanded matrix form of conservation of linear momentum in the absence of body force is given as

$$\frac{1}{r} \frac{\partial}{\partial r} (r \sigma_{rr}) + \frac{1}{r} \frac{\partial \sigma_{r\theta}}{\partial \theta} + \frac{\partial \sigma_{rz}}{\partial z} - \frac{\sigma_{\theta\theta}}{r} = \rho \ddot{u}_r, \quad (\text{A.4.1a})$$

$$\frac{1}{r} \frac{\partial}{\partial r} (r \sigma_{r\theta}) + \frac{1}{r} \frac{\partial \sigma_{\theta\theta}}{\partial \theta} + \frac{\partial \sigma_{\theta z}}{\partial z} + \frac{\sigma_{r\theta}}{r} = \rho \ddot{u}_\theta, \quad (\text{A.4.1b})$$

$$\frac{1}{r} \frac{\partial}{\partial r} (r \sigma_{rz}) + \frac{1}{r} \frac{\partial \sigma_{\theta z}}{\partial \theta} + \frac{\partial \sigma_{zz}}{\partial z} = \rho \ddot{u}_z, \quad (\text{A.4.1c})$$

where a double over-dot represents the second-order differentiation with respect to time. Equation A.4.1 corresponds to the one of Equation 4.4. The electrostatic charge equilibrium of a piezoelectric material in the absence of free charge density is written as

$$\frac{1}{r} \frac{\partial (r D_r)}{\partial r} + \frac{1}{r} \frac{\partial D_\theta}{\partial \theta} + \frac{\partial D_z}{\partial z} = 0. \quad (\text{A.4.2})$$

Equation A.4.2 corresponds to the one of Equation 4.5.

## A.5 Modal Coefficient Matrices

The modal coefficient elements of the piezoelectric medium,  $\Xi$ , can be written as

$$\Xi_{8 \times 8} = \begin{bmatrix} \Xi(1, 1) & \cdots & \Xi(1, 8) \\ \vdots & \ddots & \vdots \\ \Xi(8, 1) & \cdots & \Xi(8, 8) \end{bmatrix}, \quad (\text{A.5.1})$$

where

$$\begin{aligned} \Xi(1, 1) = & (-C_{25}C_{66}e_{11}e_{51} - C_{15}C_{66}e_{21}e_{51} - C_{16}C_{26}e_{51}^2 + C_{12}C_{66}e_{51}^2 + C_{16}C_{25}e_{51} \\ & e_{61} + C_{15}C_{26}e_{51}e_{61} - C_{15}C_{25}e_{61}^2 - C_{15}C_{25}C_{66}\epsilon_{11} - C_{56}^2(C_{12}\epsilon_{11} + e_{11}e_{21}) + C_{55}(e_{61}(-C_{16} \\ & e_{21} + C_{12}e_{61}) + C_{66}(C_{12}\epsilon_{11} + e_{11}e_{21}) - C_{26}(C_{16}\epsilon_{11} + e_{11}e_{61})) + C_{56}((C_{25}e_{11} + C_{15}e_{21} \\ & - 2C_{12}e_{51})e_{61} + C_{26}(C_{15}\epsilon_{11} + e_{11}e_{51}) + C_{16}(C_{25}\epsilon_{11} + e_{21}e_{51}))) / (r(2C_{15}C_{66}e_{11}e_{51} \\ & C_{56}^2(C_{11}\epsilon_{11} + e_{11}^2) + C_{15}^2e_{61}^2 - 2C_{16}C_{15}e_{51}e_{61} + C_{16}^2e_{51}^2 - C_{11}C_{66}e_{51}^2 + C_{66}C_{15}^2\epsilon_{11} - C_{55}C_{66} \\ & (C_{11}\epsilon_{11} + e_{11}^2) - 2C_{16}e_{11}e_{61} + C_{11}e_{61}^2 + C_{16}^2(-\epsilon_{11}) - 2C_{56}(e_{61}(C_{15}e_{11} - C_{11}e_{51}) + C_{16} \\ & (C_{15}\epsilon_{11} + e_{11}e_{51})), \end{aligned}$$

$\vdots$



$$\begin{aligned}
\Xi(8, 1) = & \left( -C_{12}C_{56}^2e_{11} + C_{12}C_{55}C_{66}e_{11} + C_{11}C_{56}^2e_{21} - C_{11}C_{55}C_{66}e_{21} - C_{11}C_{26}C_{56} \right. \\
& e_{51} + C_{11}C_{25}C_{66}e_{51} + C_{16}^2(C_{55}e_{21} - C_{25}e_{51}) + C_{11}(C_{26}C_{55} - C_{25}C_{56})e_{61} + C_{15}^2(C_{66}e_{21} - \\
& C_{26}e_{61} + C_{16}(C_{56}(C_{25}e_{11} - 2C_{15}e_{21} + C_{12}e_{51}) + C_{26}(C_{15}e_{51} - C_{55}e_{11}) + (C_{15}C_{25} - \\
& C_{12}C_{55}e_{61} + C_{15}(C_{26}C_{56}e_{11} - C_{66}(C_{25}e_{11} + C_{12}e_{51}) + C_{12}C_{56}e_{61}))/ (r(2C_{15}C_{66}e_{11} \\
& e_{51} + C_{16}^2e_{51}^2 - C_{11}C_{66}e_{51}^2 - 2C_{15}C_{16}e_{51}e_{61} + C_{15}^2e_{61}^2 + C_{15}^2C_{66}\epsilon_{11} + C_{56}^2(C_{11}\epsilon_{11} + e_{11}^2) - C_{55} \\
& (C_{66}(C_{11}\epsilon_{11} + e_{11}^2) - 2C_{16}e_{11}e_{61} + C_{11}e_{61}^2 + C_{16}^2(-\epsilon_{11})) - 2C_{56}(e_{61}(C_{15}e_{11} - C_{11}e_{51} \\
& \left. + C_{16}(C_{15}\epsilon_{11} + e_{11}e_{51}))))),
\end{aligned}$$

⋮

$$\begin{aligned}
\Xi(8, 8) = - \big( & i \left( C_{15} C_{66} e_{12} e_{51} n + C_{15} C_{66} e_{13} e_{51} \zeta r + C_{15} C_{66} e_{11} e_{52} n + C_{16}^2 e_{51} e_{52} n \right. \\
& - C_{11} C_{66} e_{51} e_{52} n + C_{15} C_{66} e_{11} e_{53} \zeta r + C_{16}^2 e_{51} e_{53} \zeta r - C_{11} C_{66} e_{51} e_{53} \zeta r - C_{15} C_{16} e_{52} e_{61} n - \\
& C_{15} C_{16} e_{53} e_{61} \zeta r - C_{15} C_{16} e_{51} e_{62} n + C_{15}^2 e_{61} e_{62} n - C_{15} C_{16} e_{51} e_{63} \zeta r + C_{15}^2 e_{61} e_{63} \zeta r + C_{15}^2 C_{66} \\
& n \epsilon_{12} + C_{15}^2 C_{66} \zeta r \epsilon_{13} + C_{56}^2 (C_{11} (n \epsilon_{12} + \zeta r \epsilon_{13}) + e_{11} (e_{12} n + e_{13} \zeta r)) + C_{55} (-C_{11} e_{61} (e_{62} \\
& n + e_{63} \zeta r + C_{16} (e_{11} (e_{62} n + e_{63} \zeta r) + e_{12} e_{61} n + e_{13} e_{61} \zeta r) + C_{16}^2 (n \epsilon_{12} + \zeta r \epsilon_{13}) - C_{66} ( \\
& C_{11} (n \epsilon_{12} + \zeta r \epsilon_{13}) + e_{11} (e_{12} n + e_{13} \zeta r))) - C_{56} (C_{15} (e_{11} (e_{62} n + e_{63} \zeta r) + e_{12} e_{61} n + \\
& e_{13} e_{61} \zeta r - C_{11} (e_{51} (e_{62} n + e_{63} \zeta r) + e_{52} e_{61} n + e_{53} e_{61} \zeta r) + (C_{15} (e_{11} (e_{62} n + e_{63} \zeta r) + \\
& e_{12} e_{61} n + e_{13} e_{61} \zeta r - C_{11} (e_{51} (e_{62} n + e_{63} \zeta r) + e_{52} e_{61} n + e_{53} e_{61} \zeta r) + C_{16} (e_{12} e_{51} n + n \\
& (2C_{15} \epsilon_{12} + e_{11} e_{52}) + r \zeta (2C_{15} \epsilon_{13} + e_{13} e_{51} + e_{11} e_{53})))))) / (r (2C_{15} C_{66} e_{11} e_{51} + C_{16}^2 e_{51}^2 \\
& - C_{11} C_{66} e_{51}^2 - 2C_{15} C_{16} e_{51} e_{61} + C_{15}^2 e_{61}^2 + C_{15}^2 C_{66} \epsilon_{11} + C_{56}^2 (C_{11} \epsilon_{11} + e_{11}^2) - C_{55} (C_{66} ( \\
& C_{11} \epsilon_{11} + e_{11}^2 - 2C_{16} e_{11} e_{61} + C_{11} e_{61}^2 + C_{16}^2 (-\epsilon_{11}) - 2C_{56} (e_{61} (C_{15} e_{11} - C_{11} e_{51}) + C_{16} (C_{15} \\
& \epsilon_{11} + e_{11} e_{51})))))).
\end{aligned}$$

Hint: The rest of the arrays of Matrix  $\Xi$  can be found on the supplementary files.



## A.6 Final System of Linear Algebraic Equation

The expanded matrix form of the transformed modal coefficients of Equation 4.18 can be expressed as

$$\begin{pmatrix} \Theta(1,1) & \Theta(1,2) & \Theta(1,3) & -1 & 0 & 0 & \Theta(1,7) & 0 \\ \Theta(2,1) & \Theta(2,2) & \Theta(2,3) & 0 & -1 & 0 & \Theta(1,7) & 0 \\ \Theta(3,1) & \Theta(3,2) & \Theta(3,3) & 0 & 0 & -1 & \Theta(1,7) & 0 \\ \Theta(4,1) & \Theta(4,2) & \Theta(4,3) & 0 & 0 & 0 & \Theta(4,7) & 0 \\ \Theta(5,1) & \Theta(5,2) & \Theta(5,3) & 0 & 0 & 0 & \Theta(5,7) & 0 \\ \Theta(6,1) & \Theta(6,2) & \Theta(6,3) & 0 & 0 & 0 & \Theta(6,7) & 0 \\ \Theta(7,1) & \Theta(7,2) & \Theta(7,3) & 0 & 0 & 0 & \Theta(7,7) & -1 \\ \Theta(8,1) & \Theta(8,2) & \Theta(8,3) & 0 & 0 & 0 & \Theta(8,7) & 0 \end{pmatrix} \begin{Bmatrix} u_r(a, \omega) \\ u_\theta(a, \omega) \\ u_z(a, \omega) \\ u_r(b, \omega) \\ u_\theta(b, \omega) \\ u_z(b, \omega) \\ D_r(a, \omega) \\ D_r(b, \omega) \end{Bmatrix} = 0_{8 \times 1}. \quad (\text{A.6.1})$$

## B

### B.1 Constitutive Relations

#### B.1.1 Constitutive relation of the orthotropic materials

As a specific case of the anisotropic material, the expanded form of the orthotropic constitutive model can be written as

$$\begin{Bmatrix} \sigma_{rr} \\ \sigma_{\theta\theta} \\ \sigma_{zz} \\ \sigma_{\theta z} \\ \sigma_{rz} \\ \sigma_{r\theta} \end{Bmatrix} = \begin{pmatrix} c_{11} & c_{12} & c_{13} & 0 & 0 & 0 \\ . & c_{22} & c_{23} & 0 & 0 & 0 \\ . & . & c_{33} & 0 & 0 & 0 \\ . & . & . & c_{44} & 0 & 0 \\ . & . & . & . & c_{55} & 0 \\ . & . & . & . & . & c_{66} \end{pmatrix} \begin{Bmatrix} \gamma_{rr} \\ \gamma_{\theta\theta} \\ \gamma_{zz} \\ \gamma_{\theta z} \\ \gamma_{rz} \\ \gamma_{r\theta} \end{Bmatrix}. \quad (\text{B.1.1})$$

Equation B.1.1 is the expanded form of Equation 5.8.

### B.1.2 Constitutive relation of axially polarized piezoelectric materials

The constitutive relation of axially polarized piezoelectric materials can be written as

$$\begin{Bmatrix} \Sigma_{rr} \\ \Sigma_{\theta\theta} \\ \Sigma_{zz} \\ \Sigma_{\theta z} \\ \Sigma_{rz} \\ \Sigma_{r\theta} \end{Bmatrix} = \begin{pmatrix} C_{11} & C_{12} & C_{13} & 0 & 0 & 0 \\ \cdot & C_{22} & C_{23} & 0 & 0 & 0 \\ \cdot & \cdot & C_{33} & 0 & 0 & 0 \\ \cdot & \cdot & \cdot & C_{44} & 0 & 0 \\ \cdot & \cdot & \cdot & \cdot & C_{55} & 0 \\ \cdot & \cdot & \cdot & \cdot & \cdot & C_{66} \end{pmatrix} \begin{Bmatrix} \Gamma_{rr} \\ \Gamma_{\theta\theta} \\ \Gamma_{zz} \\ \Gamma_{\theta z} \\ \Gamma_{rz} \\ \Gamma_{r\theta} \end{Bmatrix} - \begin{pmatrix} 0 & 0 & e_{31} \\ 0 & 0 & e_{32} \\ 0 & 0 & e_{33} \\ 0 & e_{24} & 0 \\ e_{15} & 0 & 0 \\ 0 & 0 & 0 \end{pmatrix} \begin{Bmatrix} E_r \\ E_\theta \\ E_z \end{Bmatrix}, \quad (\text{B.1.2})$$

Equation B.1.4 is corresponding to the one of Equation 5.9. The direct piezoelectric effect can be expressed as

$$\begin{Bmatrix} D_r \\ D_\theta \\ D_z \end{Bmatrix} = \begin{pmatrix} 0 & 0 & 0 & 0 & e_{51} & 0 \\ 0 & 0 & 0 & e_{42} & 0 & 0 \\ e_{13} & e_{23} & e_{33} & 0 & 0 & 0 \end{pmatrix} \begin{Bmatrix} \Gamma_{rr} \\ \Gamma_{\theta\theta} \\ \Gamma_{zz} \\ \Gamma_{\theta z} \\ \Gamma_{rz} \\ \Gamma_{r\theta} \end{Bmatrix} + \begin{pmatrix} \epsilon_{11} & 0 & 0 \\ \cdot & \epsilon_{22} & 0 \\ \cdot & \cdot & \epsilon_{33} \end{pmatrix} \begin{Bmatrix} E_r \\ E_\theta \\ E_z \end{Bmatrix}. \quad (\text{B.1.3})$$

Equation B.1.3 is corresponding to the one of Equation 5.11.

### B.1.3 Constitutive relation of radially polarized piezoelectric materials

The constitutive relation of radially polarized piezoelectric materials can be written as

$$\begin{Bmatrix} \Sigma_{rr} \\ \Sigma_{\theta\theta} \\ \Sigma_{zz} \\ \Sigma_{\theta z} \\ \Sigma_{rz} \\ \Sigma_{r\theta} \end{Bmatrix} = \begin{pmatrix} C_{11} & C_{12} & C_{13} & 0 & 0 & 0 \\ . & C_{22} & C_{23} & 0 & 0 & 0 \\ . & . & C_{33} & 0 & 0 & 0 \\ . & . & . & C_{44} & 0 & 0 \\ . & . & . & . & C_{55} & 0 \\ . & . & . & . & . & C_{66} \end{pmatrix} \begin{Bmatrix} \Gamma_{rr} \\ \Gamma_{\theta\theta} \\ \Gamma_{zz} \\ \Gamma_{\theta z} \\ \Gamma_{rz} \\ \Gamma_{r\theta} \end{Bmatrix} - \begin{pmatrix} e_{11} & 0 & 0 \\ e_{21} & 0 & 0 \\ e_{31} & 0 & 0 \\ 0 & 0 & 0 \\ 0 & 0 & e_{53} \\ 0 & e_{62} & 0 \end{pmatrix} \begin{Bmatrix} E_r \\ E_\theta \\ E_z \end{Bmatrix}, \quad (\text{B.1.4})$$

Equation B.1.4 is corresponding to the one of Equation 5.9. The direct piezoelectric effect can be expressed as

$$\begin{Bmatrix} D_r \\ D_\theta \\ D_z \end{Bmatrix} = \begin{pmatrix} e_{11} & e_{21} & e_{31} & 0 & 0 & 0 \\ 0 & 0 & 0 & 0 & 0 & e_{62} \\ 0 & 0 & 0 & 0 & e_{53} & 0 \end{pmatrix} \begin{Bmatrix} \Gamma_{rr} \\ \Gamma_{\theta\theta} \\ \Gamma_{zz} \\ \Gamma_{\theta z} \\ \Gamma_{rz} \\ \Gamma_{r\theta} \end{Bmatrix} + \begin{pmatrix} \epsilon_{11} & 0 & 0 \\ . & \epsilon_{22} & 0 \\ . & . & \epsilon_{33} \end{pmatrix} \begin{Bmatrix} E_r \\ E_\theta \\ E_z \end{Bmatrix}. \quad (\text{B.1.5})$$

Equation B.1.5 is corresponding to the one of Equation 5.11.

## B.2 Matrix Operators

The matrix operator,  $\mathbf{K}$  that relates the strain field to the Lagrangian deformation is given as

$$\mathbf{K} = \begin{pmatrix} \frac{\partial}{\partial r} & 0 & 0 \\ \frac{1}{r} & \frac{1}{r} \frac{\partial}{\partial \theta} & 0 \\ 0 & 0 & \frac{\partial}{\partial z} \\ 0 & \frac{1}{2} \frac{\partial}{\partial z} & \frac{1}{2r} \frac{\partial}{\partial \theta} \\ \frac{1}{2} \frac{\partial}{\partial z} & 0 & \frac{1}{2} \frac{\partial}{\partial r} \\ \frac{1}{2r} \frac{\partial}{\partial \theta} & \frac{1}{2} \frac{\partial}{\partial r} - \frac{1}{2r} & 0 \end{pmatrix}. \quad (\text{B.2.1})$$

Equation B.2.1 is corresponding to those in Equation 5.14 and Equation 5.15.

The expanded form of matrix operators,  $\mathbf{m}$  and  $\mathbf{M}$  are given as

$$\mathbf{m} = \begin{pmatrix} \frac{\partial}{\partial r} + \frac{1}{r} & 0 & 0 & 0 & \frac{\partial}{\partial z} & \frac{1}{r} \frac{\partial}{\partial \theta} - \frac{1}{r} \\ 0 & \frac{1}{r} \frac{\partial}{\partial \theta} & 0 & \frac{\partial}{\partial z} & 0 & \frac{\partial}{\partial r} + \frac{2}{r} \\ 0 & 0 & \frac{\partial}{\partial z} & \frac{1}{r} \frac{\partial}{\partial \theta} & \frac{\partial}{\partial r} + \frac{1}{r} & 0 \end{pmatrix}, \quad (\text{B.2.2})$$

and

$$\mathbf{M} = \begin{pmatrix} \frac{\partial}{\partial r} + \frac{1}{r} & 0 & 0 & 0 & \frac{\partial}{\partial z} & \frac{1}{r} \frac{\partial}{\partial \theta} - \frac{1}{r} & 0 & 0 & 0 \\ 0 & \frac{1}{r} \frac{\partial}{\partial \theta} & 0 & \frac{\partial}{\partial z} & 0 & \frac{\partial}{\partial r} + \frac{2}{r} & 0 & 0 & 0 \\ 0 & 0 & \frac{\partial}{\partial z} & \frac{1}{r} \frac{\partial}{\partial \theta} & \frac{\partial}{\partial r} + \frac{1}{r} & 0 & 0 & 0 & 0 \\ 0 & 0 & 0 & 0 & 0 & 0 & \frac{\partial}{\partial r} + \frac{1}{r} & \frac{1}{r} \frac{\partial}{\partial \theta} & \frac{\partial}{\partial z} \end{pmatrix}. \quad (\text{B.2.3})$$

Matrix operators,  $\mathbf{m}$  and  $\mathbf{M}$  given in Equation B.2.2 and Equation B.2.3 are corresponding to those in Equation 5.16 and Equation 5.17.

## B.3 Modal Coefficient Matrices

### B.3.1 Elastic Modal Coefficient Matrices

Modal coefficient elements of elastic medium are as follows

$$\mathbf{g}_n(r, \omega) = \begin{pmatrix} S_n^{(1,1)}(r, \omega) & S_n^{(1,2)}(r, \omega) & S_n^{(1,3)}(r, \omega) \\ S_n^{(2,1)}(r, \omega) & S_n^{(2,2)}(r, \omega) & S_n^{(2,3)}(r, \omega) \end{pmatrix} \quad (\text{B.3.1})$$

where  $S_n^{(i,j)} \equiv S_n^{(i,j)}(r, \omega)$  are

$$S_n^{(1,1)} = \begin{pmatrix} -\frac{c_{12}}{rc_{11}} & -\frac{inc_{12}}{rc_{11}} \\ -\frac{in}{r} & \frac{1}{r} \\ -ik_z & 0 \end{pmatrix}, \quad S_n^{(1,2)} = \begin{pmatrix} -\frac{ik_z c_{13}}{c_{11}} & \frac{1}{c_{11}} \\ 0 & 0 \\ 0 & 0 \end{pmatrix},$$

$$S_n^{(2,1)} = \begin{pmatrix} \frac{c_{22} - \frac{(c_{12})^2}{c_{11}}}{r^2} - \omega^2 \rho & \frac{\text{i}n(c_{11}c_{22} - (c_{12})^2)}{r^2 c_{11}} \\ \frac{\text{i}n((c_{12})^2 - c_{11}c_{22})}{r^2 c_{11}} & c_{44}k_z^2 + \frac{n^2(c_{11}c_{22} - (c_{12})^2)}{r^2 c_{11}} - \omega^2 \rho \\ \frac{\text{i}k_z(c_{12}c_{13} - c_{11}c_{23})}{rc_{11}} & \frac{k_z n(c_{11}(c_{23} + c_{44}) - c_{12}c_{13})}{rc_{11}} \end{pmatrix},$$

$$S_n^{(2,2)} = \begin{pmatrix} \frac{\text{i}k_z(c_{11}c_{23} - c_{12}c_{13})}{rc_{11}} & \frac{\frac{c_{12}}{c_{11}} - 1}{r} \\ \frac{k_z n(c_{11}(c_{23} + c_{44}) - c_{12}c_{13})}{rc_{11}} & -\frac{\text{i}nc_{12}}{rc_{11}} \\ \left(c_{33} - \frac{(c_{13})^2}{c_{11}}\right)k_z^2 + \frac{n^2 c_{44}}{r^2} - \omega^2 \rho & -\frac{\text{i}k_z c_{13}}{c_{11}} \end{pmatrix},$$

$$S_n^{(1,3)} = \begin{pmatrix} 0 & 0 \\ \frac{1}{c_{66}} & 0 \\ 0 & \frac{1}{c_{55}} \end{pmatrix}, \quad S_n^{(2,3)} = \begin{pmatrix} -\frac{\text{i}n}{r} & -\text{i}k_z \\ -\frac{2}{r} & 0 \\ 0 & -\frac{1}{r} \end{pmatrix}.$$

Equation B.3.1 corresponds to the one of Equation 6.1a.

### B.3.2 Modal Matrix of Axially Polarized Piezoelectric Material

Modal coefficient elements of axially polarized piezoelectric material can be written as

$$\mathbf{G}_n(r, \omega) = \begin{pmatrix} W_n^{(1,1)}(r, \omega) & W_n^{(1,2)}(r, \omega) & W_n^{(1,3)}(r, \omega) & W_n^{(1,4)}(r, \omega) \\ W_n^{(2,1)}(r, \omega) & W_n^{(2,2)}(r, \omega) & W_n^{(2,3)}(r, \omega) & W_n^{(2,4)}(r, \omega) \end{pmatrix} \quad (\text{B.3.2})$$

in which  $W_n^{(i,j)} \equiv W_n^{(i,j)}(r, \omega)$  are

$$W_n^{(1,1)} = \begin{pmatrix} -\frac{C_{12}}{rC_{11}} & -\frac{\text{i}nC_{12}}{rC_{11}} \\ -\frac{\text{i}n}{r} & \frac{1}{r} \\ -\text{i}k_z & 0 \\ \frac{C_{22} - \frac{(C_{12})^2}{C_{11}}}{r^2} - \omega^2 \rho_{pz} & \frac{\text{i}n(C_{11}C_{22} - (C_{12})^2)}{r^2 C_{11}} \end{pmatrix},$$

$$W_n^{(1,2)} = \begin{pmatrix} -\frac{ik_z C_{13}}{C_{11}} & \frac{1}{C_{11}} \\ 0 & 0 \\ 0 & 0 \\ \frac{ik_z(C_{11}C_{23}-C_{12}C_{13})}{rC_{11}} & \frac{\frac{C_{12}}{C_{11}}-1}{r} \end{pmatrix}, \quad W_n^{(1,3)} = \begin{pmatrix} 0 & 0 \\ \frac{1}{C_{66}} & 0 \\ 0 & \frac{\epsilon_{11}}{e_{15}^2+C_{55}\epsilon_{11}} \\ -\frac{in}{r} & -ik_z \end{pmatrix},$$

$$W_n^{(1,4)} = \begin{pmatrix} 0 & -\frac{ik_z e_{31}}{C_{11}} \\ 0 & 0 \\ \frac{e_{15}}{e_{15}^2+C_{55}\epsilon_{11}} & 0 \\ 0 & \frac{ik_z(C_{11}e_{32}-C_{12}e_{31})}{rC_{11}} \end{pmatrix},$$

$$W_n^{(2,1)} = \begin{pmatrix} \frac{in((C_{12})^2-C_{11}C_{22})}{r^2C_{11}} & C_{44}k_z^2 + \frac{n^2(C_{11}C_{22}-(C_{12})^2)}{r^2C_{11}} - \omega^2\rho_{pz} \\ \frac{ik_z(C_{12}C_{13}-C_{11}C_{23})}{rC_{11}} & \frac{k_z n(C_{11}(C_{23}+C_{44})-C_{12}C_{13})}{rC_{11}} \\ \frac{ik_z(C_{12}e_{31}-C_{11}e_{32})}{rC_{11}} & \frac{k_z n(C_{11}(e_{24}+e_{32})-C_{12}e_{31})}{rC_{11}} \\ 0 & 0 \end{pmatrix},$$

$$W_n^{(2,2)} = \begin{pmatrix} \frac{k_z n(C_{11}(C_{23}+C_{44})-C_{12}C_{13})}{rC_{11}} & -\frac{inC_{12}}{rC_{11}} \\ \left(C_{33} - \frac{(C_{13})^2}{C_{11}}\right)k_z^2 + \frac{n^2C_{44}}{r^2} - \omega^2\rho_{pz} & -\frac{ik_z C_{13}}{C_{11}} \\ \left(e_{33} - \frac{C_{13}e_{31}}{C_{11}}\right)k_z^2 + \frac{n^2e_{24}}{r^2} & -\frac{ik_z e_{31}}{C_{11}} \\ 0 & 0 \end{pmatrix},$$

$$W_n^{(2,3)} = \begin{pmatrix} -\frac{2}{r} & 0 \\ 0 & -\frac{1}{r} \\ 0 & 0 \\ 0 & \frac{e_{15}}{e_{15}^2+C_{55}\epsilon_{11}} \end{pmatrix},$$

$$W_n^{(2,4)} = \begin{pmatrix} 0 & \frac{k_z n(C_{11}(e_{24}+e_{32})-C_{12}e_{31})}{rC_{11}} \\ 0 & \left(e_{33} - \frac{C_{13}e_{31}}{C_{11}}\right)k_z^2 + \frac{n^2e_{24}}{r^2} \\ -\frac{1}{r} & -\epsilon_{33}k_z^2 - \frac{e_{31}^2k_z^2}{C_{11}} - \frac{n^2\epsilon_{22}}{r^2} \\ -\frac{C_{55}}{e_{15}^2+C_{55}\epsilon_{11}} & 0 \end{pmatrix}.$$

Equation B.3.2 corresponds to the one of Equation 6.1b.

### B.3.3 Modal Matrix of Radially Polarized Piezoelectric Materials

Modal coefficient elements of a radially polarized piezoelectric material can be written as

$$\begin{aligned}
\mathbf{G}_n^{(1,1)}(r, \omega) &= -\frac{C_{12}\epsilon_{11} + e_{11}e_{21}}{C_{11}\epsilon_{11}r + e_{11}^2}, \quad \mathbf{G}_n^{(1,2)}(r, \omega) = -\frac{C_{12}\epsilon_{11}n + e_{11}e_{21}n}{C_{11}\epsilon_{11}r + e_{11}^2}, \\
\mathbf{G}_n^{(1,3)}(r, \omega) &= -\frac{\mathfrak{i}k_z(C_{13}\epsilon_{11} + e_{11}e_{31})}{C_{11}\epsilon_{11} + e_{11}^2}, \quad \mathbf{G}_n^{(1,4)}(r, \omega) = \frac{\epsilon_{11}}{C_{11}\epsilon_{11} + e_{11}^2}, \\
\mathbf{G}_n^{(1,5)}(r, \omega) &= 0, \quad \mathbf{G}_n^{(1,6)}(r, \omega) = 0, \quad \mathbf{G}_n^{(1,7)}(r, \omega) = \frac{e_{11}}{C_{11}\epsilon_{11} + e_{11}^2}, \\
\mathbf{G}_n^{(1,8)}(r, \omega) &= 0, \quad \mathbf{G}_n^{(2,1)}(r, \omega) = \frac{n}{r}, \quad \mathbf{G}_n^{(2,2)}(r, \omega) = \frac{1}{r}, \quad \mathbf{G}_n^{(2,3)}(r, \omega) = 0, \\
\mathbf{G}_n^{(2,4)}(r, \omega) &= 0, \quad \mathbf{G}_n^{(2,5)}(r, \omega) = \frac{1}{C_{66}}, \quad \mathbf{G}_n^{(2,6)}(r, \omega) = 0, \quad \mathbf{G}_n^{(2,7)}(r, \omega) = 0, \\
\mathbf{G}_n^{(2,8)}(r, \omega) &= \frac{e_{62}n}{C_{66}r}, \quad \mathbf{G}_n^{(3,1)}(r, \omega) = -\mathfrak{i}k_z, \quad \mathbf{G}_n^{(3,2)}(r, \omega) = 0, \quad \mathbf{G}_n^{(3,3)}(r, \omega) = 0, \\
\mathbf{G}_n^{(3,4)}(r, \omega) &= 0, \quad \mathbf{G}_n^{(3,5)}(r, \omega) = 0, \quad \mathbf{G}_n^{(3,6)}(r, \omega) = \frac{1}{C_{55}}, \quad \mathbf{G}_n^{(3,7)}(r, \omega) = 0, \\
\mathbf{G}_n^{(3,8)}(r, \omega) &= -\frac{\mathfrak{i}e_{53}k_z}{C_{55}}, \\
\mathbf{G}_n^{(4,1)}(r, \omega) &= \frac{C_{11}e_{21}^2 + C_{12}^2(-\epsilon_{11}) - 2C_{12}e_{11}e_{21}}{r^2(C_{11}\epsilon_{11} + e_{11}^2)} + \frac{C_{22}}{r^2} + \omega^2(-\rho_p), \\
\mathbf{G}_n^{(4,2)}(r, \omega) &= -\frac{C_{12}^2\epsilon_{11}n}{r^2(C_{11}\epsilon_{11} + e_{11}^2)} - \frac{2C_{12}e_{11}e_{21}n}{r^2(C_{11}\epsilon_{11} + e_{11}^2)} + \\
&\quad \frac{C_{11}e_{21}^2n}{r^2(C_{11}\epsilon_{11} + e_{11}^2)} + \frac{C_{22}n}{r^2},
\end{aligned}$$

$$\mathbf{G}_n^{(4,3)}(r, \omega) = -\frac{\mathfrak{i}C_{13}k_z(C_{12}\epsilon_{11} + e_{11}e_{21})}{r(C_{11}\epsilon_{11} + e_{11}^2)} - \frac{\mathfrak{i}C_{12}e_{11}e_{31}k_z}{r(C_{11}\epsilon_{11} + e_{11}^2)} +$$

$$\frac{\mathfrak{i}C_{11}e_{21}e_{31}k_z}{r(C_{11}\epsilon_{11} + e_{11}^2)} + \frac{\mathfrak{i}C_{23}k_z}{r},$$

$$\mathbf{G}_n^{(4,4)}(r, \omega) = \frac{\epsilon_{11}(C_{12} - C_{11}) + e_{11}(e_{21} - e_{11})}{r(C_{11}\epsilon_{11} + e_{11}^2)}, \quad \mathbf{G}_n^{(4,5)}(r, \omega) = -\frac{n}{r},$$

$$\mathbf{G}_n^{(4,6)}(r, \omega) = -\mathfrak{i}k_z, \quad \mathbf{G}_n^{(4,7)}(r, \omega) = \frac{C_{12}e_{11} - C_{11}e_{21}}{C_{11}\epsilon_{11}r + e_{11}^2r}, \quad \mathbf{G}_n^{(4,8)}(r, \omega) = 0,$$

$$\mathbf{G}_n^{(5,1)}(r, \omega) = -\frac{C_{12}^2\epsilon_{11}n}{r^2(C_{11}\epsilon_{11} + e_{11}^2)} - \frac{2C_{12}e_{11}e_{21}n}{r^2(C_{11}\epsilon_{11} + e_{11}^2)} +$$

$$\frac{C_{11}e_{21}^2n}{r^2(C_{11}\epsilon_{11} + e_{11}^2)} + \frac{C_{22}n}{r^2},$$

$$\mathbf{G}_n^{(5,2)}(r, \omega) = \frac{n^2(C_{11}e_{21}^2 + C_{12}^2(-\epsilon_{11}) - 2C_{12}e_{11}e_{21})}{r^2(C_{11}\epsilon_{11} + e_{11}^2)} + \frac{C_{22}n^2}{r^2} +$$

$$C_{44}k_z^2 - \omega^2\rho_p,$$

$$\mathbf{G}_n^{(5,3)}(r, \omega) = -\frac{\mathfrak{i}C_{12}C_{13}\epsilon_{11}k_zn}{r(C_{11}\epsilon_{11} + e_{11}^2)} - \frac{\mathfrak{i}C_{12}e_{11}e_{31}k_zn}{r(C_{11}\epsilon_{11} + e_{11}^2)} -$$

$$\frac{\mathfrak{i}C_{13}e_{11}e_{21}k_zn}{r(C_{11}\epsilon_{11} + e_{11}^2)} + \frac{\mathfrak{i}C_{11}e_{21}e_{31}k_zn}{r(C_{11}\epsilon_{11} + e_{11}^2)} + \frac{\mathfrak{i}C_{23}k_zn}{r} + \frac{\mathfrak{i}C_{44}k_zn}{r},$$

$$\mathbf{G}_n^{(5,4)}(r, \omega) = \frac{C_{12}\epsilon_{11}n + e_{11}e_{21}n}{C_{11}\epsilon_{11}r + e_{11}^2r}, \quad \mathbf{G}_n^{(5,5)}(r, \omega) = -\frac{2}{r}, \quad \mathbf{G}_n^{(5,6)}(r, \omega) = 0,$$

$$\mathbf{G}_n^{(5,7)}(r, \omega) = \frac{C_{12}e_{11}n - C_{11}e_{21}n}{C_{11}\epsilon_{11}r + e_{11}^2r}, \quad \mathbf{G}_n^{(5,8)}(r, \omega) = 0,$$



$$\begin{aligned}
\mathbf{G}_n^{(6,1)}(r, \omega) &= \frac{\mathfrak{i}C_{12}C_{13}\epsilon_{11}k_z}{r(C_{11}\epsilon_{11} + e_{11}^2)} + \frac{\mathfrak{i}C_{12}e_{11}e_{31}k_z}{r(C_{11}\epsilon_{11} + e_{11}^2)} + \\
&\quad \frac{\mathfrak{i}C_{13}e_{11}e_{21}k_z}{r(C_{11}\epsilon_{11} + e_{11}^2)} - \frac{\mathfrak{i}C_{11}e_{21}e_{31}k_z}{r(C_{11}\epsilon_{11} + e_{11}^2)} - \frac{\mathfrak{i}C_{23}k_z}{r}, \\
\mathbf{G}_n^{(6,2)}(r, \omega) &= \frac{\mathfrak{i}C_{12}C_{13}\epsilon_{11}k_z n}{r(C_{11}\epsilon_{11} + e_{11}^2)} + \frac{\mathfrak{i}C_{12}e_{11}e_{31}k_z n}{r(C_{11}\epsilon_{11} + e_{11}^2)} + \\
&\quad \frac{\mathfrak{i}C_{13}e_{11}e_{21}k_z n}{r(C_{11}\epsilon_{11} + e_{11}^2)} - \frac{\mathfrak{i}C_{11}e_{21}e_{31}k_z n}{r(C_{11}\epsilon_{11} + e_{11}^2)} - \frac{\mathfrak{i}C_{23}k_z n}{r} - \frac{\mathfrak{i}C_{44}k_z n}{r}, \\
\mathbf{G}_n^{(6,3)}(r, \omega) &= -\frac{C_{13}^2\epsilon_{11}k_z^2}{C_{11}\epsilon_{11} + e_{11}^2} - \frac{2C_{13}e_{11}e_{31}k_z^2}{C_{11}\epsilon_{11} + e_{11}^2} + \frac{C_{33}e_{11}^2k_z^2}{C_{11}\epsilon_{11} + e_{11}^2} + \\
&\quad \frac{C_{11}C_{33}\epsilon_{11}k_z^2}{C_{11}\epsilon_{11} + e_{11}^2} + \frac{C_{44}e_{11}^2n^2}{r^2(C_{11}\epsilon_{11} + e_{11}^2)} + \frac{C_{11}C_{44}\epsilon_{11}n^2}{r^2(C_{11}\epsilon_{11} + e_{11}^2)} + \\
&\quad \frac{C_{11}e_{31}^2k_z^2}{C_{11}\epsilon_{11} + e_{11}^2} - \frac{e_{11}^2\omega^2\rho_p}{C_{11}\epsilon_{11} + e_{11}^2} - \frac{C_{11}\epsilon_{11}\omega^2\rho_p}{C_{11}\epsilon_{11} + e_{11}^2}, \\
\mathbf{G}_n^{(6,4)}(r, \omega) &= -\frac{\mathfrak{i}k_z(C_{13}\epsilon_{11} + e_{11}e_{31})}{C_{11}\epsilon_{11} + e_{11}^2}, \quad \mathbf{G}_n^{(6,5)}(r, \omega) = 0, \quad \mathbf{G}_n^{(6,6)}(r, \omega) = -\frac{1}{r}, \\
\mathbf{G}_n^{(6,7)}(r, \omega) &= -\frac{\mathfrak{i}k_z(C_{13}e_{11} - C_{11}e_{31})}{C_{11}\epsilon_{11} + e_{11}^2}, \quad \mathbf{G}_n^{(6,8)}(r, \omega) = 0, \quad \mathbf{G}_n^{(7,1)}(r, \omega) = 0, \\
\mathbf{G}_n^{(7,2)}(r, \omega) &= 0, \quad \mathbf{G}_n^{(7,3)}(r, \omega) = 0, \quad \mathbf{G}_n^{(7,4)}(r, \omega) = 0, \quad \mathbf{G}_n^{(7,5)}(r, \omega) = -\frac{2e_{62}n}{C_{66}r}, \\
\mathbf{G}_n^{(7,6)}(r, \omega) &= -\frac{2\mathfrak{i}e_{53}k_z}{C_{55}}, \quad \mathbf{G}_n^{(7,7)}(r, \omega) = -\frac{1}{r}, \\
\mathbf{G}_n^{(7,8)}(r, \omega) &= -\frac{k_z^2(C_{55}\epsilon_{33} + 2e_{53}^2)}{C_{55}} - \frac{n^2(C_{66}\epsilon_{22} + 2e_{62}^2)}{C_{66}r^2},
\end{aligned}$$

$$\mathbf{G}_n^{(8,1)}(r, \omega) = \frac{C_{11}e_{21} - C_{12}e_{11}}{r(C_{11}\epsilon_{11} + e_{11}^2)}, \quad \mathbf{G}_n^{(8,2)}(r, \omega) = \frac{C_{11}e_{21}n - C_{12}e_{11}n}{r(C_{11}\epsilon_{11} + e_{11}^2)},$$

$$\mathbf{G}_n^{(8,3)}(r, \omega) = \frac{\mathfrak{i}(C_{11}e_{31}k_z - C_{13}e_{11}k_z)}{C_{11}\epsilon_{11} + e_{11}^2}, \quad \mathbf{G}_n^{(8,4)}(r, \omega) = \frac{\mathfrak{i}(C_{11}e_{31}k_z - C_{13}e_{11}k_z)}{C_{11}\epsilon_{11} + e_{11}^2},$$

$$\mathbf{G}_n^{(8,5)}(r, \omega) = 0, \quad \mathbf{G}_n^{(8,6)}(r, \omega) = 0, \quad \mathbf{G}_n^{(8,7)}(r, \omega) = -\frac{C_{11}}{C_{11}\epsilon_{11} + e_{11}^2},$$

$$\mathbf{G}_n^{(8,8)}(r, \omega) = -\frac{C_{11}}{C_{11}\epsilon_{11} + e_{11}^2},$$

subsection B.3.3 corresponds to the one of Equation 6.1b.

## B.4 Final Solution

### B.4.1 Short Circuited and Active Electrical Boundary Conditions

The matrix of coefficients,  $\mathbf{A}_n$  given in Equation 6.6 is expanded for the active applied boundary conditions in the form of

$$\mathbf{A}_n = \begin{pmatrix} -\zeta_5 & [\Theta_n^{(1,1)}\zeta_6 - \Theta_n^{(1,4)}\zeta_3] & \Theta_n^{(1,2)} & \Theta_n^{(1,3)} & 0 & 0 & \Theta_n^{(1,7)} & 0 \\ 0 & [\Theta_n^{(2,1)}\zeta_6 - \Theta_n^{(2,4)}\zeta_3] & \Theta_n^{(2,2)} & \Theta_n^{(2,3)} & -1 & 0 & \Theta_n^{(2,7)} & 0 \\ 0 & [\Theta_n^{(3,1)}\zeta_6 - \Theta_n^{(3,4)}\zeta_3] & \Theta_n^{(3,2)} & \Theta_n^{(3,3)} & 0 & -1 & \Theta_n^{(3,7)} & 0 \\ \zeta_2 & [\Theta_n^{(4,1)}\zeta_6 - \Theta_n^{(4,4)}\zeta_3] & \Theta_n^{(4,2)} & \Theta_n^{(4,3)} & 0 & 0 & \Theta_n^{(4,7)} & 0 \\ 0 & [\Theta_n^{(5,1)}\zeta_6 - \Theta_n^{(5,4)}\zeta_3] & \Theta_n^{(5,2)} & \Theta_n^{(5,3)} & 0 & 0 & \Theta_n^{(5,7)} & 0 \\ 0 & [\Theta_n^{(6,1)}\zeta_6 - \Theta_n^{(6,4)}\zeta_3] & \Theta_n^{(6,2)} & \Theta_n^{(6,3)} & 0 & 0 & \Theta_n^{(6,7)} & 0 \\ 0 & [\Theta_n^{(7,1)}\zeta_6 - \Theta_n^{(7,4)}\zeta_3] & \Theta_n^{(7,2)} & \Theta_n^{(7,3)} & 0 & 0 & \Theta_n^{(7,7)} & -1 \\ 0 & [\Theta_n^{(8,1)}\zeta_6 - \Theta_n^{(8,4)}\zeta_3] & \Theta_n^{(8,2)} & \Theta_n^{(8,3)} & 0 & 0 & \Theta_n^{(8,7)} & 0 \end{pmatrix}, \quad (\text{B.4.1})$$

where

$$\zeta_1 = p_0 \epsilon_n (-\mathbf{i})^n J_n(k_r^{ex} r_{ex}), \zeta_2 = H_n^2(k_r^{ex} r_{ex}), \zeta_3 = H_n^1(k_r^{in} r_{in}), \quad (\text{B.4.2a})$$

$$\zeta_4 = \frac{1}{\rho_{ex} \omega^2} \frac{\partial p_n^I(r, \omega)}{\partial r} \Big|_{r=r_{ex}}, \zeta_5 = \frac{1}{\rho_{ex} \omega^2} \frac{\partial p_n^R(r, \omega)}{\partial r}, \quad (\text{B.4.2b})$$

$$\zeta_6 = \frac{1}{\rho_{in} \omega^2} \frac{\partial p_n^T(r, \omega)}{\partial r} \Big|_{r=r_{in}}. \quad (\text{B.4.2c})$$

The unknowns modal vector  $\mathbf{x}_n$  is written as

$$\mathbf{x}_n = \begin{pmatrix} A_n(\omega) \\ B_n(\omega) \\ u_\theta^n(r_{in}, \omega) \\ u_z^n(r_{in}, \omega) \\ U_\theta^n(r_{ex}, \omega) \\ U_z^n(r_{ex}, \omega) \\ D_r^n(r_{in}, \omega) \\ D_r^n(r_{ex}, \omega) \end{pmatrix}. \quad (\text{B.4.3})$$

The expanded form of the constants vector,  $b_n$  is given as

$$b_n = \begin{pmatrix} -\Phi(r_a, \omega) \Theta_n^{(1,8)} + \zeta_4 \\ -\Phi(r_a, \omega) \Theta_n^{(2,8)} \\ -\Phi(r_a, \omega) \Theta_n^{(3,8)} \\ -\Phi(r_a, \omega) \Theta_n^{(4,8)} - \zeta_1 \\ -\Phi(r_a, \omega) \Theta_n^{(5,8)} \\ -\Phi(r_a, \omega) \Theta_n^{(6,8)} \\ -\Phi(r_a, \omega) \Theta_n^{(7,8)} \\ -\Phi(r_a, \omega) \Theta_n^{(8,8)} + \Phi(r_a, \omega) \end{pmatrix}. \quad (\text{B.4.4})$$

For the short circuited boundary condition case, the modal electrical voltage,  $\Phi_n(r_i, \omega)$ , shall be equal to zero in the Equation C.1.6 (i.e.  $\Phi(r_a, \omega) = \Phi(r_{ex}, \omega) = 0$ ).

### B.4.2 Open Circuited Electrical Boundary Condition

The matrix of coefficients,  $\mathbf{A}_n$  given in Equation 6.6 is expanded for the case of open-circuited electrical boundary condition in the form of

$$\mathbf{A}_n = \begin{pmatrix} -\zeta_5 & [\Theta_n^{(1,1)}\zeta_6 - \Theta_n^{(1,4)}\zeta_3] & \Theta_n^{(1,2)} & \Theta_n^{(1,3)} & 0 & 0 & \Theta_n^{(1,8)} & 0 \\ 0 & [\Theta_n^{(2,1)}\zeta_6 - \Theta_n^{(2,4)}\zeta_3] & \Theta_n^{(2,2)} & \Theta_n^{(2,3)} & -1 & 0 & \Theta_n^{(2,8)} & 0 \\ 0 & [\Theta_n^{(3,1)}\zeta_6 - \Theta_n^{(3,4)}\zeta_3] & \Theta_n^{(3,2)} & \Theta_n^{(3,3)} & 0 & -1 & \Theta_n^{(3,8)} & 0 \\ \zeta_2 & [\Theta_n^{(4,1)}\zeta_6 - \Theta_n^{(4,4)}\zeta_3] & \Theta_n^{(4,2)} & \Theta_n^{(4,3)} & 0 & 0 & \Theta_n^{(4,8)} & 0 \\ 0 & [\Theta_n^{(5,1)}\zeta_6 - \Theta_n^{(5,4)}\zeta_3] & \Theta_n^{(5,2)} & \Theta_n^{(5,3)} & 0 & 0 & \Theta_n^{(5,8)} & 0 \\ 0 & [\Theta_n^{(6,1)}\zeta_6 - \Theta_n^{(6,4)}\zeta_3] & \Theta_n^{(6,2)} & \Theta_n^{(6,3)} & 0 & 0 & \Theta_n^{(6,8)} & 0 \\ 0 & [\Theta_n^{(7,1)}\zeta_6 - \Theta_n^{(7,4)}\zeta_3] & \Theta_n^{(7,2)} & \Theta_n^{(7,3)} & 0 & 0 & \Theta_n^{(7,8)} & 0 \\ 0 & [\Theta_n^{(8,1)}\zeta_6 - \Theta_n^{(8,4)}\zeta_3] & \Theta_n^{(8,2)} & \Theta_n^{(8,3)} & 0 & 0 & \Theta_n^{(8,8)} & -1 \end{pmatrix}, \quad (\text{B.4.5})$$

where  $\zeta_i$  (i.e.  $i = 1, 2, \dots, 6$ ) is given in subsection B.4.1.

The unknowns modal vector  $\mathbf{x}_n$  is written as

$$\mathbf{x}_n = \begin{pmatrix} A_n(\omega) \\ B_n(\omega) \\ u_\theta^n(r_{in}, \omega) \\ u_z^n(r_{in}, \omega) \\ U_\theta^n(r_{ex}, \omega) \\ U_z^n(r_{ex}, \omega) \\ \phi_r^n(r_{in}, \omega) \\ \phi_r^n(r_{ex}, \omega) \end{pmatrix}. \quad (\text{B.4.6})$$

The expanded form of the constants vector,  $b_n$  is given as

$$b_n = \begin{pmatrix} \zeta_4 \\ 0 \\ 0 \\ -\zeta_1 \\ 0 \\ 0 \\ 0 \\ 0 \end{pmatrix}. \quad (\text{B.4.7})$$

### B.4.3 Feedback Control With a Closed-loop Gain Amplifier

The matrix of coefficients,  $\mathbf{A}_n$  given in Equation 6.6 is expanded for the case of the feedback control condition in the form of

$$\mathbf{A}_n = \begin{pmatrix} -\zeta_5 & [\Theta_n^{(1,1)}\zeta_6 - \Theta_n^{(1,4)}\zeta_3] & \Theta_n^{(1,2)} & \Theta_n^{(1,3)} & 0 & 0 & \Theta_n^{(1,8)} & \Theta_n^{(1,9)} & 0 & 0 \\ 0 & [\Theta_n^{(2,1)}\zeta_6 - \Theta_n^{(2,4)}\zeta_3] & \Theta_n^{(2,2)} & \Theta_n^{(2,3)} & -1 & 0 & \Theta_n^{(2,8)} & \Theta_n^{(2,9)} & 0 & 0 \\ 0 & [\Theta_n^{(3,1)}\zeta_6 - \Theta_n^{(3,4)}\zeta_3] & \Theta_n^{(3,2)} & \Theta_n^{(3,3)} & 0 & -1 & \Theta_n^{(3,8)} & \Theta_n^{(3,9)} & 0 & 0 \\ \zeta_2 & [\Theta_n^{(4,1)}\zeta_6 - \Theta_n^{(4,4)}\zeta_3] & \Theta_n^{(4,2)} & \Theta_n^{(4,3)} & 0 & 0 & \Theta_n^{(4,8)} & \Theta_n^{(4,9)} & 0 & 0 \\ 0 & [\Theta_n^{(5,1)}\zeta_6 - \Theta_n^{(5,4)}\zeta_3] & \Theta_n^{(5,2)} & \Theta_n^{(5,3)} & 0 & 0 & \Theta_n^{(5,8)} & \Theta_n^{(5,9)} & 0 & 0 \\ 0 & [\Theta_n^{(6,1)}\zeta_6 - \Theta_n^{(6,4)}\zeta_3] & \Theta_n^{(6,2)} & \Theta_n^{(6,3)} & 0 & 0 & \Theta_n^{(6,8)} & \Theta_n^{(6,9)} & 0 & 0 \\ 0 & [\Theta_n^{(7,1)}\zeta_6 - \Theta_n^{(7,4)}\zeta_3] & \Theta_n^{(7,2)} & \Theta_n^{(7,3)} & 0 & 0 & \Theta_n^{(7,8)} & \Theta_n^{(7,9)} & -1 & 0 \\ 0 & [\Theta_n^{(8,1)}\zeta_6 - \Theta_n^{(8,4)}\zeta_3] & \Theta_n^{(8,2)} & \Theta_n^{(8,3)} & 0 & 0 & k + \Theta_n^{(8,8)} & \Theta_n^{(8,9)} & 0 & 0 \\ 0 & [\Theta_n^{(9,1)}\zeta_6 - \Theta_n^{(9,4)}\zeta_3] & \Theta_n^{(9,2)} & \Theta_n^{(9,3)} & 0 & 0 & \Theta_n^{(9,8)} & \Theta_n^{(9,9)} & 0 & -1 \\ 0 & [\Theta_n^{(10,1)}\zeta_6 - \Theta_n^{(10,4)}\zeta_3] & \Theta_n^{(10,2)} & \Theta_n^{(10,3)} & 0 & 0 & \Theta_n^{(10,8)} & \Theta_n^{(10,9)} & 0 & 0 \end{pmatrix}, \quad (\text{B.4.8})$$

where  $\zeta_i$  (i.e.  $i = 1, 2, \dots, 6$ ) is given in subsection B.4.1 ([3]).

The unknowns modal vector  $\mathbf{x}_n$  is written as

$$\mathbf{x}_n = \begin{pmatrix} A_n(\omega) \\ B_n(\omega) \\ u_\theta^n(r_{in}, \omega) \\ u_z^n(r_{in}, \omega) \\ U_\theta^n(r_{ex}, \omega) \\ U_z^n(r_{ex}, \omega) \\ \phi_r^n(r_{in}, \omega) \\ D_r^n(r_a, \omega) \\ D_r^n(r_{ex}, \omega) \\ D_r^n(r_s, \omega) \end{pmatrix}. \quad (\text{B.4.9})$$

The expanded form of the constants vector,  $b_n$  is given as

$$b_n = (\zeta_4 \ 0 \ 0 \ -\zeta_1 \ 0 \ 0 \ 0 \ 0 \ 0 \ 0)^T. \quad (\text{B.4.10})$$

# C

## C.1 Final Solution of Viscous Model

### C.1.1 Open Circuited Electrical Boundary Conditions

The matrix of coefficients,  $\mathbf{A}_n$  given in Equation 8.9 is expanded for the open circuited boundary conditions in the form of

$$\mathbf{A}_n = \begin{pmatrix} \Omega_n[1, 1] & \Omega_n[1, 2] & \Omega_n[1, 3] & \Omega_n[1, 4] & \Omega_n[1, 5] & \Omega_n[1, 6] & \Omega_n[1, 7] & \Omega_n[1, 8] \\ \Omega_n[2, 1] & \Omega_n[2, 2] & \Omega_n[2, 3] & \Omega_n[2, 4] & \Omega_n[2, 5] & \Omega_n[2, 6] & \Omega_n[2, 7] & \Omega_n[2, 8] \\ \Omega_n[3, 1] & \Omega_n[3, 2] & \Omega_n[3, 3] & \Omega_n[3, 4] & \Omega_n[3, 5] & \Omega_n[3, 6] & \Omega_n[3, 7] & \Omega_n[3, 8] \\ \Omega_n[4, 1] & \Omega_n[4, 2] & \Omega_n[4, 3] & \Omega_n[4, 4] & \Omega_n[4, 5] & \Omega_n[4, 6] & \Omega_n[4, 7] & \Omega_n[4, 8] \\ \Omega_n[5, 1] & \Omega_n[5, 2] & \Omega_n[5, 3] & \Omega_n[5, 4] & \Omega_n[5, 5] & \Omega_n[5, 6] & \Omega_n[5, 7] & \Omega_n[5, 8] \\ \Omega_n[6, 1] & \Omega_n[6, 2] & \Omega_n[6, 3] & \Omega_n[6, 4] & \Omega_n[6, 5] & \Omega_n[6, 6] & \Omega_n[6, 7] & \Omega_n[6, 8] \\ \Omega_n[7, 1] & \Omega_n[7, 2] & \Omega_n[7, 3] & \Omega_n[7, 4] & \Omega_n[7, 5] & \Omega_n[7, 6] & \Omega_n[7, 7] & \Omega_n[7, 8] \\ \Omega_n[8, 1] & \Omega_n[8, 2] & \Omega_n[8, 3] & \Omega_n[8, 4] & \Omega_n[8, 5] & \Omega_n[8, 6] & \Omega_n[8, 7] & \Omega_n[8, 8] \end{pmatrix}, \quad (\text{C.1.1})$$

where,

$$\Omega_n[1, 1] = \frac{i\Gamma_c^{\text{ex}} (H_n^2)' (r_{\text{ex}}\Gamma_c^{\text{ex}})}{\omega},$$

$$\Omega_n[1, 2] = \frac{k_z H_{n+1}^2 (r_{\text{ex}}\Gamma_s^{\text{ex}})}{\omega},$$

$$\Omega_n[1, 3] = -\frac{inH_n^2 (r_{\text{ex}}\Gamma_s^{\text{ex}})}{\omega r_{\text{ex}}},$$

$$\begin{aligned}\Omega_n[1, 4] = & H_n \left( r_{\text{in}} \Gamma_c^{\text{in}} \right) \left( r_{\text{in}}^2 \left( k_z \Theta_n(1, 3) + i\omega \Theta_n(1, 4) \left( \omega \rho_{\text{in}} + 2i\mu_{\text{in}} k_c^{2\text{in}} \right) \right) - 2n\omega \mu_{\text{in}} \right. \\ & \Theta_n(1, 5) + inr_{\text{in}} \eta a_n(1, 2) + r_{\text{in}} \Gamma_c^{\text{in}} H'_n \left( r_{\text{in}} \Gamma_c^{\text{in}} \right) (2n\omega \mu_{\text{in}} \Theta_n(1, 5) - ir_{\text{in}} (2\omega \\ & \left. \mu_{\text{in}} k_z \Theta_n(1, 6) + \Theta_n(1, 1) - 2\omega \mu_{\text{in}} r_{\text{in}}^2 \Theta_n(1, 4) \Gamma_c^{2\text{in}} H''_n \left( r_{\text{in}} \Gamma_c^{\text{in}} \right) / \omega r_{\text{in}}^2, \end{aligned}$$

$$\begin{aligned}\Omega_n[1, 5] = & -ir_{\text{in}} \Gamma_s^{\text{in}} H'_{n+1} \left( r_{\text{in}} \Gamma_s^{\text{in}} \right) \left( r_{\text{in}} \left( \Theta_n(1, 3) - \omega \mu_{\text{in}} k_z (2\Theta_n(1, 4) + \Theta_n(1, 5)) \right) - \right. \\ & i(n+1)\omega \mu_{\text{in}} \Theta_n(1, 6) + H_{n+1} \left( r_{\text{in}} \Gamma_s^{\text{in}} \right) \left( r_{\text{in}}^2 (-k_z) (\omega \mu_{\text{in}} k_z \Theta_n(1, 6) + \Theta_n(1, 1) + \right. \\ & \left. \Theta_n(1, 2) - i(n+1)r_{\text{in}} (\omega \mu_{\text{in}} k_z \Theta_n(1, 5) + \Theta_n(1, 3)) + (n+1)\omega \mu_{\text{in}} \Theta_n(1, 6) - \right. \\ & \left. \left. \omega \mu_{\text{in}} r_{\text{in}}^2 \Theta_n(1, 6) \Gamma_s^{2\text{in}} H''_{n+1} \left( r_{\text{in}} \Gamma_s^{\text{in}} \right) / \omega r_{\text{in}}^2, \end{aligned}$$

$$\begin{aligned}\Omega_n[1, 6] = & inH_n \left( r_{\text{in}} \Gamma_s^{\text{in}} \right) \left( r_{\text{in}} (\omega \mu_{\text{in}} k_z \Theta_n(1, 6) + \Theta_n(1, 1)) + i\omega \mu_{\text{in}} (2\Theta_n(1, 4) \right. \\ & \left. + n\Theta_n(1, 5) + r_{\text{in}} \Gamma_s^{\text{in}} (\omega \mu_{\text{in}} (2n\Theta_n(1, 4) + \Theta_n(1, 5)) - ir_{\text{in}} \Theta_n(1, 2)) H'_n \left( r_{\text{in}} \Gamma_s^{\text{in}} \right) \right. \\ & \left. - \omega \mu_{\text{in}} r_{\text{in}}^2 \Theta_n(1, 5) \Gamma_s^{2\text{in}} H''_n \left( r_{\text{in}} \Gamma_s^{\text{in}} \right) / \omega r_{\text{in}}^2, \end{aligned}$$

$$\Omega_n[1, 7] = \Theta_n(1, 8),$$

$$\Omega_n[1, 8] = 0,$$

$$\Omega_n[2, 1] = -\frac{inH_n^2(r_{\text{ex}}\Gamma_c^{\text{ex}})}{\omega r_{\text{ex}}},$$

$$\Omega_n[2, 2] = \frac{k_z H_{n+1}^2 (r_{\text{ex}} \Gamma_s^{\text{ex}})}{\omega},$$

$$\Omega_n[2, 3] = \frac{i \Gamma_s^{\text{ex}} (H_n^2)' (r_{\text{ex}} \Gamma_s^{\text{ex}})}{\omega},$$

$$\begin{aligned} \Omega_n[2, 4] = & H_n (r_{\text{in}} \Gamma_c^{\text{in}}) (r_{\text{in}}^2 (k_z \Theta_n(2, 3) + i \omega \Theta_n(2, 4) (\omega \rho_{\text{in}} + 2i \mu_{\text{in}} k_c^{2\text{in}})) - \\ & 2n \omega \mu_{\text{in}} \Theta_n(2, 5) + i n r_{\text{in}} \Theta_n(2, 2) + r_{\text{in}} \Gamma_c^{\text{in}} H_n' (r_{\text{in}} \Gamma_c^{\text{in}}) (2n \omega \mu_{\text{in}} \Theta_n(2, 5) - \\ & i r_{\text{in}} (2 \omega \mu_{\text{in}} k_z \Theta_n(2, 6) + \Theta_n(2, 1)) - 2 \omega \mu_{\text{in}} r_{\text{in}}^2 \Theta_n(2, 4) \Gamma_c^{2\text{in}} H_n'' (r_{\text{in}} \Gamma_c^{\text{in}}) / \omega r_{\text{in}}^2, \end{aligned}$$

$$\begin{aligned} \Omega_n[2, 5] = & -i r_{\text{in}} \Gamma_s^{\text{in}} H_{n+1}' (r_{\text{in}} \Gamma_s^{\text{in}}) (r_{\text{in}} (\Theta_n(2, 3) - \omega \mu_{\text{in}} k_z (2 \Theta_n(2, 4) + \Theta_n(2, 5))) \\ & - i(n+1) \omega \mu_{\text{in}} \Theta_n(2, 6) + H_{n+1} (r_{\text{in}} \Gamma_s^{\text{in}}) (r_{\text{in}}^2 (-k_z) (\omega \mu_{\text{in}} k_z \Theta_n(2, 6) + \Theta_n(2, 1) + \\ & \Theta_n(2, 2) - i(n+1) r_{\text{in}} (\omega \mu_{\text{in}} k_z \Theta_n(2, 5) + \Theta_n(2, 3)) + (n+1) \omega \mu_{\text{in}} \Theta_n(2, 6) - \\ & \omega \mu_{\text{in}} r_{\text{in}}^2 \Theta_n(2, 6) \Gamma_s^{2\text{in}} H_{n+1}'' (r_{\text{in}} \Gamma_s^{\text{in}}) / \omega r_{\text{in}}^2, \end{aligned}$$

$$\begin{aligned} \Omega_n[2, 6] = & i n H_n (r_{\text{in}} \Gamma_s^{\text{in}}) (r_{\text{in}} (\omega \mu_{\text{in}} k_z \Theta_n(2, 6) + \Theta_n(2, 1)) + i \omega \mu_{\text{in}} (2 \Theta_n(2, 4) \\ & + n \Theta_n(2, 5) + r_{\text{in}} \Gamma_s^{\text{in}} (\omega \mu_{\text{in}} (2n \Theta_n(2, 4) + \Theta_n(2, 5)) - i r_{\text{in}} \Theta_n(2, 2)) H_n' (r_{\text{in}} \Gamma_s^{\text{in}}) - \\ & \omega \mu_{\text{in}} r_{\text{in}}^2 \Theta_n(2, 5) \Gamma_s^{2\text{in}} H_n'' (r_{\text{in}} \Gamma_s^{\text{in}}) / \omega r_{\text{in}}^2, \end{aligned}$$

$$\Omega_n[2, 7] = \Theta_n(2, 8),$$



$$\Omega_n[2, 8] = 0,$$

$$\Omega_n[3, 1] = -k_z \omega H_n^2 (r_{\text{ex}} \Gamma_c^{\text{ex}}),$$

$$\Omega_n[3, 2] = \frac{i\omega \left( r_{\text{ex}} \Gamma_s^{\text{ex}} (H_{n+1}^2)' (r_{\text{ex}} \Gamma_s^{\text{ex}}) + (n+1) H_{n+1}^2 (r_{\text{ex}} \Gamma_s^{\text{ex}}) \right)}{r_{\text{ex}}},$$

$$\Omega_n[3, 3] = 0,$$

$$\begin{aligned} \Omega_n[3, 4] = & H_n (r_{\text{in}} \Gamma_c^{\text{in}}) (r_{\text{in}}^2 (k_z \Theta_n(3, 3) + i\omega \Theta_n(3, 4) (\omega \rho_{\text{in}} + 2i\mu_{\text{in}} k_c^{2\text{in}})) - 2n\omega \\ & \mu_{\text{in}} \Theta_n(3, 5) + inr_{\text{in}} \Theta_n(3, 2) + r_{\text{in}} \Gamma_c^{\text{in}} H_n' (r_{\text{in}} \Gamma_c^{\text{in}}) (2n\omega \mu_{\text{in}} \Theta_n(3, 5) - ir_{\text{in}} (2\omega \\ & \mu_{\text{in}} k_z \Theta_n(3, 6) + \Theta_n(3, 1) - 2\omega \mu_{\text{in}} r_{\text{in}}^2 \Theta_n(3, 4) \Gamma_c^{2\text{in}} H_n'' (r_{\text{in}} \Gamma_c^{\text{in}}) / \omega r_{\text{in}}^2, \end{aligned}$$

$$\begin{aligned} \Omega_n[3, 5] = & -ir_{\text{in}} \Gamma_s^{\text{in}} H_{n+1}' (r_{\text{in}} \Gamma_s^{\text{in}}) (r_{\text{in}} (\Theta_n(3, 3) - \omega \mu_{\text{in}} k_z (2\Theta_n(3, 4) + \Theta_n(3, 5)) \\ & - i(n+1)\omega \mu_{\text{in}} \Theta_n(3, 6) + H_{n+1} (r_{\text{in}} \Gamma_s^{\text{in}}) (r_{\text{in}}^2 (-k_z) (\omega \mu_{\text{in}} k_z \Theta_n(3, 6) + \Theta_n(3, 1) + \\ & \Theta_n(3, 2) - i(n+1)r_{\text{in}} (\omega \mu_{\text{in}} k_z \Theta_n(3, 5) + \Theta_n(3, 3)) + (n+1)\omega \mu_{\text{in}} \Theta_n(3, 6) - \omega \mu_{\text{in}} \\ & r_{\text{in}}^2 \Theta_n(3, 6) \Gamma_s^{2\text{in}} H_{n+1}'' (r_{\text{in}} \Gamma_s^{\text{in}}) / \omega r_{\text{in}}^2, \end{aligned}$$

$$\begin{aligned} \Omega_n[3, 6] = & inH_n (r_{\text{in}} \Gamma_s^{\text{in}}) (r_{\text{in}} (\omega \mu_{\text{in}} k_z \Theta_n(3, 6) + \Theta_n(3, 1)) + i\omega \mu_{\text{in}} (2\Theta_n(3, 4) \\ & + n\Theta_n(3, 5) + r_{\text{in}} \Gamma_s^{\text{in}} (\omega \mu_{\text{in}} (2n\Theta_n(3, 4) + \Theta_n(3, 5)) - ir_{\text{in}} \Theta_n(3, 2)) H_n' (r_{\text{in}} \Gamma_s^{\text{in}}) \\ & - \omega \mu_{\text{in}} r_{\text{in}}^2 \Theta_n(3, 5) \Gamma_s^{2\text{in}} H_n'' (r_{\text{in}} \Gamma_s^{\text{in}}) / \omega r_{\text{in}}^2, \end{aligned}$$

$$\Omega_n[3, 7] = \Theta_n(3, 8),$$

$$\Omega_n[3, 8] = 0,$$

$$\Omega_n[4, 1] = 2\mu_{\text{ex}}\Gamma_c^{2\text{ex}} (H_n^2)'' (r_{\text{ex}}\Gamma_c^{\text{ex}}) + H_n^2 (r_{\text{ex}}\Gamma_c^{\text{ex}}) (2\mu_{\text{ex}}k_c^{2\text{ex}} - i\omega\rho_{\text{ex}}),$$

$$\Omega_n[4, 2] = -2i\mu_{\text{ex}}k_z\Gamma_s^{\text{ex}} (H_{n+1}^2)' (r_{\text{ex}}\Gamma_s^{\text{ex}}),$$

$$\Omega_n[4, 3] = \frac{2n\mu_{\text{ex}} (H_n^2 (r_{\text{ex}}\Gamma_s^{\text{ex}}) - r_{\text{ex}}\Gamma_s^{\text{ex}} (H_n^2)' (r_{\text{ex}}\Gamma_s^{\text{ex}}))}{r_{\text{ex}}^2},$$

$$\begin{aligned} \Omega_n[4, 4] = & H_n (r_{\text{in}}\Gamma_c^{\text{in}}) (r_{\text{in}}^2 (k_z\Theta_n(4, 3) + i\omega\Theta_n(4, 4) (\omega\rho_{\text{in}} + 2i\mu_{\text{in}}k_c^{2\text{in}})) - \\ & 2n\omega\mu_{\text{in}}\Theta_n(4, 5) + inr_{\text{in}}\Theta_n(4, 2) + r_{\text{in}}\Gamma_c^{\text{in}}H_n' (r_{\text{in}}\Gamma_c^{\text{in}}) (2n\omega\mu_{\text{in}}\Theta_n(4, 5) - ir_{\text{in}} \\ & (2\omega\mu_{\text{in}}k_z\Theta_n(4, 6) + \Theta_n(4, 1) - 2\omega\mu_{\text{in}}r_{\text{in}}^2\Theta_n(4, 4)\Gamma_c^{2\text{in}}H_n'' (r_{\text{in}}\Gamma_c^{\text{in}}) / \omega r_{\text{in}}^2, \end{aligned}$$

$$\begin{aligned} \Omega_n[4, 5] = & -ir_{\text{in}}\Gamma_s^{\text{in}}H_{n+1}' (r_{\text{in}}\Gamma_s^{\text{in}}) (r_{\text{in}} (\Theta_n(4, 3) - \omega\mu_{\text{in}}k_z (2\Theta_n(4, 4) + \Theta_n(4, 5))) \\ & - i(n+1)\omega\mu_{\text{in}}\Theta_n(4, 6) + H_{n+1} (r_{\text{in}}\Gamma_s^{\text{in}}) (r_{\text{in}}^2 (-k_z) (\omega\mu_{\text{in}}k_z\Theta_n(4, 6) + \Theta_n(4, 1) \\ & + \Theta_n(4, 2) - i(n+1)r_{\text{in}} (\omega\mu_{\text{in}}k_z\Theta_n(4, 5) + \Theta_n(4, 3)) + (n+1)\omega\mu_{\text{in}}\Theta_n(4, 6) - \\ & \omega\mu_{\text{in}}r_{\text{in}}^2\Theta_n(4, 6)\Gamma_s^{2\text{in}}H_{n+1}'' (r_{\text{in}}\Gamma_s^{\text{in}}) / \omega r_{\text{in}}^2, \end{aligned}$$

$$\begin{aligned}\Omega_n[4, 6] = & inH_n \left( r_{\text{in}} \Gamma_s^{\text{in}} \right) \left( r_{\text{in}} \left( \omega \mu_{\text{in}} k_z \Theta_n(4, 6) + \Theta_n(4, 1) \right) + i\omega \mu_{\text{in}} \left( 2\Theta_n(4, 4) + \right. \right. \\ & n\Theta_n(4, 5) + r_{\text{in}} \Gamma_s^{\text{in}} \left( \omega \mu_{\text{in}} \left( 2n\Theta_n(4, 4) + \Theta_n(4, 5) \right) - ir_{\text{in}} \Theta_n(4, 2) \right) H'_n \left( r_{\text{in}} \Gamma_s^{\text{in}} \right) - \\ & \left. \left. \omega \mu_{\text{in}} r_{\text{in}}^2 \Theta_n(4, 5) \Gamma_s^{2\text{in}} H''_n \left( r_{\text{in}} \Gamma_s^{\text{in}} \right) / \omega r_{\text{in}}^2, \right.\end{aligned}$$

$$\Omega_n[4, 7] = \Theta_n(4, 8),$$

$$\Omega_n[4, 8] = 0,$$

$$\Omega_n[5, 1] = \frac{2n\mu_{\text{ex}} \left( H_n^2 \left( r_{\text{ex}} \Gamma_c^{\text{ex}} \right) - r_{\text{ex}} \Gamma_c^{\text{ex}} \left( H_n^2 \right)' \left( r_{\text{ex}} \Gamma_c^{\text{ex}} \right) \right)}{r_{\text{ex}}^2},$$

$$\Omega_n[5, 2] = \frac{i\mu_{\text{ex}} k_z \left( (n+1) H_{n+1}^2 \left( r_{\text{ex}} \Gamma_s^{\text{ex}} \right) - r_{\text{ex}} \Gamma_s^{\text{ex}} \left( H_{n+1}^2 \right)' \left( r_{\text{ex}} \Gamma_s^{\text{ex}} \right) \right)}{r_{\text{ex}}},$$

$$\Omega_n[5, 3] = \frac{\mu_{\text{ex}} \left( r_{\text{ex}} \Gamma_s^{\text{ex}} \left( r_{\text{ex}} \Gamma_s^{\text{ex}} \left( H_n^2 \right)'' \left( r_{\text{ex}} \Gamma_s^{\text{ex}} \right) - \left( H_n^2 \right)' \left( r_{\text{ex}} \Gamma_s^{\text{ex}} \right) \right) + n^2 H_n^2 \left( r_{\text{ex}} \Gamma_s^{\text{ex}} \right) \right)}{r_{\text{ex}}^2},$$

$$\begin{aligned}\Omega_n[5, 4] = & H_n \left( r_{\text{in}} \Gamma_c^{\text{in}} \right) \left( r_{\text{in}}^2 \left( k_z \Theta_n(5, 3) + i\omega \Theta_n(5, 4) \left( \omega \rho_{\text{in}} + 2i\mu_{\text{in}} k_c^{2\text{in}} \right) \right) - 2n \right. \\ & \omega \mu_{\text{in}} \Theta_n(5, 5) + inr_{\text{in}} \Theta_n(5, 2) + r_{\text{in}} \Gamma_c^{\text{in}} H'_n \left( r_{\text{in}} \Gamma_c^{\text{in}} \right) \left( 2n\omega \mu_{\text{in}} \Theta_n(5, 5) - ir_{\text{in}} \left( 2\omega \right. \right. \\ & \left. \left. \mu_{\text{in}} k_z \Theta_n(5, 6) + \Theta_n(5, 1) - 2\omega \mu_{\text{in}} r_{\text{in}}^2 \Theta_n(5, 4) \Gamma_c^{2\text{in}} H''_n \left( r_{\text{in}} \Gamma_c^{\text{in}} \right) / \omega r_{\text{in}}^2, \right.\end{aligned}$$

$$\begin{aligned}
\Omega_n[5, 5] = & -ir_{\text{in}}\Gamma_s^{\text{in}}H'_{n+1}(r_{\text{in}}\Gamma_s^{\text{in}})(r_{\text{in}}(\Theta_n(5, 3) - \omega\mu_{\text{in}}k_z(2\Theta_n(5, 4) + \Theta_n(5, 5) \\
& - i(n+1)\omega\mu_{\text{in}}\Theta_n(5, 6) + H_{n+1}(r_{\text{in}}\Gamma_s^{\text{in}})(r_{\text{in}}^2(-k_z)(\omega\mu_{\text{in}}k_z\Theta_n(5, 6) + \Theta_n(5, 1) \\
& + \Theta_n(5, 2) - i(n+1)r_{\text{in}}(\omega\mu_{\text{in}}k_z\Theta_n(5, 5) + \Theta_n(5, 3)) + (n+1)\omega\mu_{\text{in}}\Theta_n(5, 6) - \\
& \omega\mu_{\text{in}}r_{\text{in}}^2\Theta_n(5, 6)\Gamma_s^{2\text{in}}H''_{n+1}(r_{\text{in}}\Gamma_s^{\text{in}}),
\end{aligned}$$

$$\begin{aligned}
\Omega_n[5, 6] = & inH_n(r_{\text{in}}\Gamma_s^{\text{in}})(r_{\text{in}}(\omega\mu_{\text{in}}k_z\Theta_n(5, 6) + \Theta_n(5, 1)) + i\omega\mu_{\text{in}}(2\Theta_n(5, 4) + \\
& n\Theta_n(5, 5) + r_{\text{in}}\Gamma_s^{\text{in}}(\omega\mu_{\text{in}}(2n\Theta_n(5, 4) + \Theta_n(5, 5)) - ir_{\text{in}}\Theta_n(5, 2))H'_n(r_{\text{in}}\Gamma_s^{\text{in}}) \\
& - \omega\mu_{\text{in}}r_{\text{in}}^2\Theta_n(5, 5)\Gamma_s^{2\text{in}}H''_n(r_{\text{in}}\Gamma_s^{\text{in}})/\omega r_{\text{in}}^2,
\end{aligned}$$

$$\Omega_n[5, 7] = \Theta_n(5, 8),$$

$$\Omega_n[5, 8] = 0,$$

$$\Omega_n[6, 1] = 2i\mu_{\text{ex}}k_z\Gamma_c^{\text{ex}}(H_n^2)'(r_{\text{ex}}\Gamma_c^{\text{ex}}),$$

$$\begin{aligned}
\Omega_n[6, 2] = & \mu_{\text{ex}}\left(r_{\text{ex}}\Gamma_s^{\text{ex}}\left((n+1)(H_{n+1}^2)'(r_{\text{ex}}\Gamma_s^{\text{ex}}) + r_{\text{ex}}\Gamma_s^{\text{ex}}(H_{n+1}^2)''(r_{\text{ex}}\Gamma_s^{\text{ex}})\right) - \right. \\
& \left. (r_{\text{ex}}^2(-k_z^2) + n+1H_{n+1}^2(r_{\text{ex}}\Gamma_s^{\text{ex}})/r_{\text{ex}}^2, \right.
\end{aligned}$$

$$\Omega_n[6, 3] = -\frac{in\mu_{\text{ex}}k_zH_n^2(r_{\text{ex}}\Gamma_s^{\text{ex}})}{r_{\text{ex}}},$$

$$\begin{aligned}\Omega_n[6, 4] &= H_n \left( r_{\text{in}} \Gamma_c^{\text{in}} \right) \left( r_{\text{in}}^2 \left( k_z \Theta_n(6, 3) + i\omega \Theta_n(6, 4) \left( \omega \rho_{\text{in}} + 2i\mu_{\text{in}} k_c^{2\text{in}} \right) \right) - 2n \right. \\ &\quad \left. \omega \mu_{\text{in}} \Theta_n(6, 5) + inr_{\text{in}} \Theta_n(6, 2) + r_{\text{in}} \Gamma_c^{\text{in}} H'_n \left( r_{\text{in}} \Gamma_c^{\text{in}} \right) \left( 2n\omega \mu_{\text{in}} \Theta_n(6, 5) - ir_{\text{in}} \left( 2\omega \mu_{\text{in}} \right. \right. \right. \\ &\quad \left. \left. k_z \Theta_n(6, 6) + \Theta_n(6, 1) - 2\omega \mu_{\text{in}} r_{\text{in}}^2 \Theta_n(6, 4) \Gamma_c^{2\text{in}} H''_n \left( r_{\text{in}} \Gamma_c^{\text{in}} \right) / \omega r_{\text{in}}^2, \right. \right.\end{aligned}$$

$$\begin{aligned}\Omega_n[6, 5] &= -ir_{\text{in}} \Gamma_s^{\text{in}} H'_{n+1} \left( r_{\text{in}} \Gamma_s^{\text{in}} \right) \left( r_{\text{in}} \left( \Theta_n(6, 3) - \omega \mu_{\text{in}} k_z \left( 2\Theta_n(6, 4) + \Theta_n(6, 5) \right) \right) \right. \\ &\quad \left. - i(n+1)\omega \mu_{\text{in}} \Theta_n(6, 6) + H_{n+1} \left( r_{\text{in}} \Gamma_s^{\text{in}} \right) \left( r_{\text{in}}^2 \left( -k_z \right) \left( \omega \mu_{\text{in}} k_z \Theta_n(6, 6) + \Theta_n(6, 1) + \right. \right. \right. \\ &\quad \left. \left. \Theta_n(6, 2) - i(n+1)r_{\text{in}} \left( \omega \mu_{\text{in}} k_z \Theta_n(6, 5) + \Theta_n(6, 3) \right) + (n+1)\omega \mu_{\text{in}} \Theta_n(6, 6) - \omega \right. \right. \\ &\quad \left. \left. \mu_{\text{in}} r_{\text{in}}^2 \Theta_n(6, 6) \Gamma_s^{2\text{in}} H''_{n+1} \left( r_{\text{in}} \Gamma_s^{\text{in}} \right) / \omega r_{\text{in}}^2, \right. \right.\end{aligned}$$

$$\begin{aligned}\Omega_n[6, 6] &= inH_n \left( r_{\text{in}} \Gamma_s^{\text{in}} \right) \left( r_{\text{in}} \left( \omega \mu_{\text{in}} k_z \Theta_n(6, 6) + \Theta_n(6, 1) \right) + i\omega \mu_{\text{in}} \left( 2\Theta_n(6, 4) \right. \right. \\ &\quad \left. \left. + n\Theta_n(6, 5) + r_{\text{in}} \Gamma_s^{\text{in}} \left( \omega \mu_{\text{in}} \left( 2n\Theta_n(6, 4) + \Theta_n(6, 5) \right) - ir_{\text{in}} \Theta_n(6, 2) \right) H'_n \left( r_{\text{in}} \Gamma_s^{\text{in}} \right) \right. \right. \\ &\quad \left. \left. - \omega \mu_{\text{in}} r_{\text{in}}^2 \Theta_n(6, 5) \Gamma_s^{2\text{in}} H''_n \left( r_{\text{in}} \Gamma_s^{\text{in}} \right) / \omega r_{\text{in}}^2, \right.\end{aligned}$$

$$\Omega_n[6, 7] = \Theta_n(6, 8),$$

$$\Omega_n[6, 8] = 0,$$

$$\Omega_n[7, 1] = 0,$$

$$\Omega_n[7, 2] = 0,$$

$$\Omega_n[7, 3] = 0,$$

$$\begin{aligned}\Omega_n[7, 4] = & H_n \left( r_{\text{in}} \Gamma_c^{\text{in}} \right) \left( r_{\text{in}}^2 \left( k_z \Theta_n(7, 3) + i\omega \Theta_n(7, 4) \left( \omega \rho_{\text{in}} + 2i\mu_{\text{in}} k_c^{2\text{in}} \right) \right) - 2n \right. \\ & \omega \mu_{\text{in}} \Theta_n(7, 5) + inr_{\text{in}} \Theta_n(7, 2) + r_{\text{in}} \Gamma_c^{\text{in}} H'_n \left( r_{\text{in}} \Gamma_c^{\text{in}} \right) \left( 2n\omega \mu_{\text{in}} \Theta_n(7, 5) - ir_{\text{in}} (2\omega \mu_{\text{in}} k_z \Theta_n(7, 6) \right. \\ & \left. \left. + \Theta_n(7, 1) - 2\omega \mu_{\text{in}} r_{\text{in}}^2 \Theta_n(7, 4) \Gamma_c^{2\text{in}} H''_n \left( r_{\text{in}} \Gamma_c^{\text{in}} \right) / \omega r_{\text{in}}^2, \right.\right.\end{aligned}$$

$$\begin{aligned}\Omega_n[7, 5] = & -ir_{\text{in}} \Gamma_s^{\text{in}} H'_{n+1} \left( r_{\text{in}} \Gamma_s^{\text{in}} \right) \left( r_{\text{in}} \left( \Theta_n(7, 3) - \omega \mu_{\text{in}} k_z (2\Theta_n(7, 4) + \Theta_n(7, 5)) \right) \right. \\ & \left. - i(n+1)\omega \mu_{\text{in}} \Theta_n(7, 6) + H_{n+1} \left( r_{\text{in}} \Gamma_s^{\text{in}} \right) \left( r_{\text{in}}^2 (-k_z) (\omega \mu_{\text{in}} k_z \Theta_n(7, 6) + \Theta_n(7, 1) \right. \right. \\ & \left. \left. + \Theta_n(7, 2) - i(n+1)r_{\text{in}} (\omega \mu_{\text{in}} k_z \Theta_n(7, 5) + \Theta_n(7, 3)) + (n+1)\omega \mu_{\text{in}} \Theta_n(7, 6) - \omega \right. \right. \\ & \left. \left. \mu_{\text{in}} r_{\text{in}}^2 \Theta_n(7, 6) \Gamma_s^{2\text{in}} H''_{n+1} \left( r_{\text{in}} \Gamma_s^{\text{in}} \right) / \omega r_{\text{in}}^2, \right.\right.\end{aligned}$$

$$\begin{aligned}\Omega_n[7, 6] = & inH_n \left( r_{\text{in}} \Gamma_s^{\text{in}} \right) \left( r_{\text{in}} (\omega \mu_{\text{in}} k_z \Theta_n(7, 6) + \Theta_n(7, 1)) + i\omega \mu_{\text{in}} (2\Theta_n(7, 4) + \right. \\ & \left. n\Theta_n(7, 5) + r_{\text{in}} \Gamma_s^{\text{in}} (\omega \mu_{\text{in}} (2n\Theta_n(7, 4) + \Theta_n(7, 5)) - ir_{\text{in}} \Theta_n(7, 2)) H'_n \left( r_{\text{in}} \Gamma_s^{\text{in}} \right) - \right. \\ & \left. \omega \mu_{\text{in}} r_{\text{in}}^2 \Theta_n(7, 5) \Gamma_s^{2\text{in}} H''_n \left( r_{\text{in}} \Gamma_s^{\text{in}} \right) / \omega r_{\text{in}}^2, \right.\end{aligned}$$

$$\Omega_n[7, 7] = \Theta_n(7, 8),$$

$$\Omega_n[7, 8] = 0,$$

$$\Omega_n[8, 1] = 0,$$

$$\Omega_n[8, 2] = 0,$$

$$\Omega_n[8, 3] = 0,$$

$$\begin{aligned}\Omega_n[8, 4] = & H_n \left( r_{\text{in}} \Gamma_c^{\text{in}} \right) \left( r_{\text{in}}^2 \left( k_z \Theta_n(8, 3) + i\omega \Theta_n(8, 4) \left( \omega \rho_{\text{in}} + 2i\mu_{\text{in}} k_c^{2\text{in}} \right) \right) - \right. \\ & 2n\omega\mu_{\text{in}} \Theta_n(8, 5) + inr_{\text{in}} \Theta_n(8, 2) + r_{\text{in}} \Gamma_c^{\text{in}} H'_n \left( r_{\text{in}} \Gamma_c^{\text{in}} \right) \left( 2n\omega\mu_{\text{in}} \Theta_n(8, 5) - ir_{\text{in}} \right. \\ & \left. \left. \left( 2\omega\mu_{\text{in}} k_z \Theta_n(8, 6) + \Theta_n(8, 1) - 2\omega\mu_{\text{in}} r_{\text{in}}^2 \Theta_n(8, 4) \Gamma_c^{2\text{in}} H''_n \left( r_{\text{in}} \Gamma_c^{\text{in}} \right) / \omega r_{\text{in}}^2, \right. \right.\end{aligned}$$

$$\begin{aligned}\Omega_n[8, 5] = & -ir_{\text{in}} \Gamma_s^{\text{in}} H'_{n+1} \left( r_{\text{in}} \Gamma_s^{\text{in}} \right) \left( r_{\text{in}} \left( \Theta_n(8, 3) - \omega\mu_{\text{in}} k_z \left( 2\Theta_n(8, 4) + \Theta_n \right. \right. \right. \\ & \left. \left. \left. (8, 5) - i(n+1)\omega\mu_{\text{in}} \Theta_n(8, 6) + H_{n+1} \left( r_{\text{in}} \Gamma_s^{\text{in}} \right) \left( r_{\text{in}}^2 \left( -k_z \right) \left( \omega\mu_{\text{in}} k_z \Theta_n(8, 6) + \right. \right. \right. \right. \\ & \left. \left. \left. \Theta_n(8, 1) + \Theta_n(8, 2) - i(n+1)r_{\text{in}} \left( \omega\mu_{\text{in}} k_z \Theta_n(8, 5) + \Theta_n(8, 3) \right) + (n+1)\omega\mu_{\text{in}} \right. \right. \right. \\ & \left. \left. \left. \Theta_n(8, 6) - \omega\mu_{\text{in}} r_{\text{in}}^2 \Theta_n(8, 6) \Gamma_s^{2\text{in}} H''_{n+1} \left( r_{\text{in}} \Gamma_s^{\text{in}} \right) / \omega r_{\text{in}}^2, \right. \right.\end{aligned}$$

$$\begin{aligned}\Omega_n[8, 6] = & inH_n \left( r_{\text{in}} \Gamma_s^{\text{in}} \right) \left( r_{\text{in}} \left( \omega\mu_{\text{in}} k_z \Theta_n(8, 6) + \Theta_n(8, 1) \right) + i\omega\mu_{\text{in}} \left( 2\Theta_n(8, 4) \right. \right. \\ & \left. \left. + n\Theta_n(8, 5) + r_{\text{in}} \Gamma_s^{\text{in}} \left( \omega\mu_{\text{in}} \left( 2n\Theta_n(8, 4) + \Theta_n(8, 5) \right) - ir_{\text{in}} \Theta_n(8, 2) \right) H'_n \left( r_{\text{in}} \Gamma_s^{\text{in}} \right) \right. \right. \\ & \left. \left. - \omega\mu_{\text{in}} r_{\text{in}}^2 \Theta_n(8, 5) \Gamma_s^{2\text{in}} H''_n \left( r_{\text{in}} \Gamma_s^{\text{in}} \right) / \omega r_{\text{in}}^2, \right.\end{aligned}$$

$$\Omega_n[8, 7] = \Theta_n(8, 8),$$

$$\Omega_n[8, 8] = -1,$$

The unknowns modal vector  $\mathbf{x}_n$  is written as

$$\mathbf{x}_n = \begin{pmatrix} A_n(\omega) \\ B_n(\omega) \\ C_n(\omega) \\ D_n(\omega) \\ E_n(\omega) \\ F_n(\omega) \\ \phi^n(r_a, \omega) \\ \phi^n(r_{ex}, \omega) \end{pmatrix}. \quad (\text{C.1.2})$$

The expanded form of the constants vector,  $b_n$  is given as

$$b_n = \begin{pmatrix} \frac{(-i)^{n+1} \epsilon_n p_o \Gamma_c^{\text{ex}} J'_n(r_{\text{ex}} \Gamma_c^{\text{ex}})}{\omega} \\ \frac{i(-i)^n n \epsilon_n p_o J_n(r_{\text{ex}} \Gamma_c^{\text{ex}})}{\omega r_{\text{ex}}} \\ (-i)^n e^{izk_z} k_z \epsilon_n p_o \omega e^{-izk_z} J_n(r_{\text{ex}} \Gamma_c^{\text{ex}}) \\ -2(-i)^n \mu_{\text{ex}} \epsilon_n p_o k_c^{2\text{ex}} J_n(r_{\text{ex}} \Gamma_c^{\text{ex}}) - 2(-i)^n \mu_{\text{ex}} \epsilon_n p_o \Gamma_c^{2\text{ex}} J''_n(r_{\text{ex}} \Gamma_c^{\text{ex}}) + \\ i(-i)^n \omega \rho_{\text{ex}} \epsilon_n p_o J_n(r_{\text{ex}} \Gamma_c^{\text{ex}}) \\ - \frac{2(-i)^n n \mu_{\text{ex}} \epsilon_n p_o (J_n(r_{\text{ex}} \Gamma_c^{\text{ex}}) - r_{\text{ex}} \Gamma_c^{\text{ex}} J'_n(r_{\text{ex}} \Gamma_c^{\text{ex}}))}{r_{\text{ex}}^2} \\ -2i(-i)^n \mu_{\text{ex}} k_z \epsilon_n p_o \Gamma_c^{\text{ex}} J'_n(r_{\text{ex}} \Gamma_c^{\text{ex}}) \\ 0 \\ 0 \end{pmatrix}. \quad (\text{C.1.3})$$

### C.1.2 Short Circuited Electrical Boundary Condition

The matrix of coefficients,  $\mathbf{A}_n$  given in Equation 8.9 for the case of short-circuited electrical boundary condition can be written in the form of



$$\mathbf{A}_n = \begin{pmatrix} \Omega_n[1, 1] & \Omega_n[1, 2] & \Omega_n[1, 3] & \Omega_n[1, 4] & \Omega_n[1, 5] & \Omega_n[1, 6] & \Pi_n[1, 7] & \Pi_n[1, 8] \\ \Omega_n[2, 1] & \Omega_n[2, 2] & \Omega_n[2, 3] & \Omega_n[2, 4] & \Omega_n[2, 5] & \Omega_n[2, 6] & \Pi_n[2, 7] & \Pi_n[2, 8] \\ \Omega_n[3, 1] & \Omega_n[3, 2] & \Omega_n[3, 3] & \Omega_n[3, 4] & \Omega_n[3, 5] & \Omega_n[3, 6] & \Pi_n[3, 7] & \Pi_n[3, 8] \\ \Omega_n[4, 1] & \Omega_n[4, 2] & \Omega_n[4, 3] & \Omega_n[4, 4] & \Omega_n[4, 5] & \Omega_n[4, 6] & \Pi_n[4, 7] & \Pi_n[4, 8] \\ \Omega_n[5, 1] & \Omega_n[5, 2] & \Omega_n[5, 3] & \Omega_n[5, 4] & \Omega_n[5, 5] & \Omega_n[5, 6] & \Pi_n[5, 7] & \Pi_n[5, 8] \\ \Omega_n[6, 1] & \Omega_n[6, 2] & \Omega_n[6, 3] & \Omega_n[6, 4] & \Omega_n[6, 5] & \Omega_n[6, 6] & \Pi_n[6, 7] & \Pi_n[6, 8] \\ \Omega_n[7, 1] & \Omega_n[7, 2] & \Omega_n[7, 3] & \Omega_n[7, 4] & \Omega_n[7, 5] & \Omega_n[7, 6] & \Pi_n[7, 7] & \Pi_n[7, 8] \\ \Omega_n[8, 1] & \Omega_n[8, 2] & \Omega_n[8, 3] & \Omega_n[8, 4] & \Omega_n[8, 5] & \Omega_n[8, 6] & \Pi_n[8, 7] & \Pi_n[8, 8] \end{pmatrix}, \quad (\text{C.1.4})$$

where,

$$\Pi_n[1, 7] = \Theta_n(1, 7),$$

$$\Pi_n[1, 8] = 0,$$

$$\Pi_n[2, 7] = \Theta_n(2, 7),$$

$$\Pi_n[2, 8] = 0,$$

$$\Pi_n[3, 7] = \Theta_n(3, 7),$$

$$\Pi_n[3, 8] = 0,$$

$$\Pi_n[4, 7] = \Theta_n(4, 7),$$

$$\Pi_n[4, 8] = 0,$$

$$\Pi_n[5, 7] = \Theta_n(5, 7),$$

$$\Pi_n[5, 8] = 0,$$

$$\Pi_n[6, 7] = \Theta_n(5, 7),$$

$$\Pi_n[6, 8] = 0,$$

$$\Pi_n[7, 7] = \Theta_n(7, 7),$$

$$\Pi_n[7, 8] = -1,$$

$$\Pi_n[8, 7] = \Theta_n(8, 7),$$

$$\Pi_n[7, 8] = 0,$$

The unknowns modal vector  $\mathbf{x}_n$  is written as

$$\mathbf{x}_n = \begin{pmatrix} A_n(\omega) \\ B_n(\omega) \\ C_n(\omega) \\ D_n(\omega) \\ E_n(\omega) \\ F_n(\omega) \\ D_r^n(r_a, \omega) \\ D_r^n(r_{ex}, \omega) \end{pmatrix}. \quad (\text{C.1.5})$$

The expanded form of the constants vector,  $b_n$  is given as

$$b_n = \begin{pmatrix} \frac{(-i)^{n+1} \epsilon_n p_o \Gamma_c^{\text{ex}} J'_n(r_{\text{ex}} \Gamma_c^{\text{ex}})}{\omega} \\ \frac{i(-i)^n n \epsilon_n p_o J_n(r_{\text{ex}} \Gamma_c^{\text{ex}})}{\omega r_{\text{ex}}} \\ (-i)^n e^{izk_z} k_z \epsilon_n p_o \omega e^{-izk_z} J_n(r_{\text{ex}} \Gamma_c^{\text{ex}}) \\ -2(-i)^n \mu_{\text{ex}} \epsilon_n p_o k_c^{2\text{ex}} J_n(r_{\text{ex}} \Gamma_c^{\text{ex}}) - 2(-i)^n \mu_{\text{ex}} \epsilon_n p_o \Gamma_c^{2\text{ex}} J''_n(r_{\text{ex}} \Gamma_c^{\text{ex}}) + \\ i(-i)^n \omega \rho_{\text{ex}} \epsilon_n p_o J_n(r_{\text{ex}} \Gamma_c^{\text{ex}}) \\ - \frac{2(-i)^n n \mu_{\text{ex}} \epsilon_n p_o (J_n(r_{\text{ex}} \Gamma_c^{\text{ex}}) - r_{\text{ex}} \Gamma_c^{\text{ex}} J'_n(r_{\text{ex}} \Gamma_c^{\text{ex}}))}{r_{\text{ex}}^2} \\ -2i(-i)^n \mu_{\text{ex}} k_z \epsilon_n p_o \Gamma_c^{\text{ex}} J'_n(r_{\text{ex}} \Gamma_c^{\text{ex}}) \\ 0 \\ 0 \end{pmatrix}. \quad (\text{C.1.6})$$

# Bibliography

- [1] John Bartlett Segur and Helen E Oberstar. Viscosity of glycerol and its aqueous solutions. *Industrial & Engineering Chemistry*, 43(9):2117–2120, 1951.
- [2] Leslie Robert Koval. On sound transmission into a thin cylindrical shell under “flight conditions”. *Journal of Sound and Vibration*, 48(2):265–275, 1976.
- [3] V Rabbani, A Bahari, M Hodaei, P Maghoul, and N Wu. Three-dimensional free vibration analysis of triclinic piezoelectric hollow cylinder. *Composites Part B: Engineering*, 158:352–363, 2019.
- [4] Mauro Caresta. Active control of sound radiated by a submarine in bending vibration. *Journal of Sound and Vibration*, 330(4):615–624, 2011.
- [5] LA Krakters, MJL Van Tooren, Aet al Beukers, AP Berkhof, and MP De Goeje. *Active noise control in fuselage design*, volume 69. Wit Press, 2003.
- [6] Seyyed M Hasheminejad and Hessam Mousavi-Akbarzadeh. Three dimensional non-axisymmetric transient acoustic radiation from an eccentric hollow cylinder. *Wave Motion*, 50(4):723–738, 2013.
- [7] S Iakovlev, CT Seaton, and J-F Sigrist. Submerged circular cylindrical shell subjected to two consecutive shock waves: Resonance-like phenomena. *Journal of Fluids and Structures*, 42:70–87, 2013.
- [8] S Iakovlev, HAFA Santos, K Williston, R Murray, and M Mitchell. Non-stationary radiation by a cylindrical shell: Numerical modeling using the reissner–mindlin theory. *Journal of Fluids and Structures*, 36:50–69, 2013.

- [9] Seyyed M Hasheminejad and Hemad Keshavarzpour. Robust active sound radiation control of a piezo-laminated composite circular plate of arbitrary thickness based on the exact 3d elasticity model. *Journal of Low Frequency Noise, Vibration and Active Control*, 35(2):101–127, 2016.
- [10] Seyyed M Hasheminejad and Siavash Kazemirad. Dynamic viscoelastic effects on sound wave scattering by an eccentric compound circular cylinder. *Journal of Sound and Vibration*, 318(3):506–526, 2008.
- [11] Edward F Crawley and Javier De Luis. Use of piezoelectric actuators as elements of intelligent structures. *AIAA journal*, 25(10):1373–1385, 1987.
- [12] Seyyed M Hasheminejad and Mahdi Alaei-Varnosfaderani. Vibroacoustic response and active control of a fluid-filled functionally graded piezoelectric material composite cylinder. *Journal of intelligent material systems and structures*, 23(7):775–790, 2012.
- [13] Seyyed M Hasheminejad and Hemad Keshavarzpour. Active sound radiation control of a thick piezolaminated smart rectangular plate. *Journal of Sound and Vibration*, 332(20):4798–4816, 2013.
- [14] V Cutanda Henríquez, P Risby Andersen, J Søndergaard Jensen, P Møller Juhl, and Jose Sánchez-Dehesa. A numerical model of an acoustic metamaterial using the boundary element method including viscous and thermal losses. *Journal of Computational Acoustics*, 25(04):1750006, 2017.
- [15] SV Sorokin and AV Chubinskij. On the role of fluid viscosity in wave propaga-

- tion in elastic plates under heavy fluid loading. *Journal of sound and vibration*, 311(3-5):1020–1038, 2008.
- [16] Wen H Lin and AC Raptis. Acoustic scattering by elastic solid cylinders and spheres in viscous fluids. *The Journal of the Acoustical Society of America*, 73(3):736–748, 1983.
- [17] Wen H Lin and AC Raptis. Sound scattering from a thin rod in a viscous medium. *The Journal of the Acoustical Society of America*, 79(6):1693–1701, 1986.
- [18] Seyyed M Hasheminejad and Naemeh Safari. Dynamic viscoelastic effects on sound wave diffraction by spherical and cylindrical shells submerged in and filled with viscous compressible fluids. *Shock and Vibration*, 10(5, 6):339–363, 2003.
- [19] V Rabbani, M Hodaie, X Deng, H Lu, D Hui, and N Wu. Sound transmission through a thick-walled fgm piezo-laminated cylindrical shell filled with and submerged in compressible fluids. *Engineering Structures*, 197:109323, 2019.
- [20] V Rabbani and N Wu. Active broadband sound transmission loss control through an arbitrary thick smart piezo-laminated cylinder. *Aerospace Science and Technology*, 110:106515, 2021.
- [21] ISO. Underwater acoustics—terminology, 2017.
- [22] Bruno H Zimm. The scattering of light and the radial distribution function of high polymer solutions. *The Journal of Chemical Physics*, 16(12):1093–1099, 1948.

- [23] Yasuji Murakami, Kimio Andou, Kouji Shino, Toshiaki Katagiri, and Satomi Hatano. Design and characteristics of aerial optical drop cable with electric power wires. *IEICE transactions on communications*, 83(1):38–46, 2000.
- [24] Frank J Fahy and Paolo Gardonio. *Sound and structural vibration: radiation, transmission and response*. Elsevier, 2007.
- [25] John M Eargle. Fundamental mathematical and physical concepts in acoustics. In *Music, Sound, and Technology*, pages 1–35. Springer, 1995.
- [26] Manchar Lal Munjal. *Acoustics of ducts and mufflers with application to exhaust and ventilation system design*. John Wiley & Sons, 1987.
- [27] Koichi Furutsu. *On the Statistical Theory of Electromagnetic Waves in a Fluctuating Medium (II) Mathematical Basis of the Analogies to Quantum Field Theory*. US Government Printing Office, 1964.
- [28] Fenghua Li and Renhe Zhang. Bottom sound speed and attenuation inverted by using pulsed waveform and transmission loss. *ACTA ACUSTICA-PEKING-*, 25(4):297–302, 2000.
- [29] Ji-xun Zhou, Xue-zhen Zhang, and Peter H Rogers. Resonant interaction of sound wave with internal solitons in the coastal zone. *The Journal of the Acoustical Society of America*, 90(4):2042–2054, 1991.
- [30] E Suematsu and N Imai. A fiber optic/millimeter-wave radio transmission link using hbt as direct photodetector and an optoelectronic upconverter. *IEEE transactions on microwave theory and techniques*, 44(1):133–143, 1996.

- [31] Shan Jiang and Stavros Georgakopoulos. Electromagnetic wave propagation into fresh water. *Journal of Electromagnetic Analysis and Applications*, 3(07):261, 2011.
- [32] K Dong and X Wang. Wave propagation characteristics in piezoelectric cylindrical laminated shells under large deformation. *Composite structures*, 77(2):171–181, 2007.
- [33] Georg Johann Ernest Goubau. Transmission of electromagnetic wave beams, August 20 1963. US Patent 3,101,472.
- [34] Cheng-I James Young and Malcolm J Crocker. Prediction of transmission loss in mufflers by the finite- element method. *The Journal of the Acoustical Society of America*, 57(1):144–148, 1975.
- [35] Roger Oba and Steven Finette. Acoustic propagation through anisotropic internal wave fields: Transmission loss, cross-range coherence, and horizontal refraction. *The Journal of the Acoustical Society of America*, 111(2):769–784, 2002.
- [36] Hossein Kh Bisheh and Nan Wu. Wave propagation in piezoelectric cylindrical composite shells reinforced with angled and randomly oriented carbon nanotubes. *Composites Part B: Engineering*, 160:10–30, 2019.
- [37] JA Moore and RH Lyon. Sound transmission loss characteristics of sandwich panel constructions. *The Journal of the Acoustical Society of America*, 89(2):777–791, 1991.



- [38] Lumiao Chen, Zhaoye Qin, and Fulei Chu. Dynamic characteristics of rub-impact on rotor system with cylindrical shell. *International journal of Mechanical Sciences*, 133(16):51–64, 2017.
- [39] Seyyed M Hasheminejad, Arash Hakimi, and Hemad Keshavarzpour. Broad-band sound transmission loss enhancement of an arbitrary-thick hybrid smart composite plate using multi-objective particle swarm optimization-based active control. *Journal of Intelligent Material Systems and Structures*, 29(8):1724–1747, 2018.
- [40] Seyyed M Hasheminejad, Masoud Cheraghi, and Ali Jamalpoor. Active damping of sound transmission through an electrorheological fluid-actuated sandwich cylindrical shell. *Journal of Sandwich Structures Materials*, page 1099636218777966, 2018.
- [41] Hossein Kh Bisheh and Nan Wu. Wave propagation characteristics in a piezoelectric coupled laminated composite cylindrical shell by considering transverse shear effects and rotary inertia. *Composite Structures*, 191:123–144, 2018.
- [42] Hossein Bisheh and Nan Wu. On dispersion relations in smart laminated fiber-reinforced composite membranes considering different piezoelectric coupling effects. *Journal of Low Frequency Noise, Vibration and Active Control*, page 1461348418821773, 2019.
- [43] Hossein Kh Bisheh and Nan Wu. Analysis of wave propagation characteristics in piezoelectric cylindrical composite shells reinforced with carbon nanotubes. *International Journal of Mechanical Sciences*, 145:200–220, 2018.

- [44] Hossein Kh Bisheh and Nan Wu. Wave propagation in smart laminated composite cylindrical shells reinforced with carbon nanotubes in hygrothermal environments. *Composites Part B: Engineering*, 162:219–241, 2019.
- [45] CHEN Lu-miao, WANG Hong-yu, QIN Zhao-ye, and CHU Fu-lei. Aerodynamic characteristics analysis of eccentric drum based on three-dimensional model. *Journal of Aerospace Power*, (2):14, 2015.
- [46] ZY Qin, SZ Yan, and FL Chu. Influence of clamp band joint on dynamic behavior of launching system in ascent flight. *Proceedings of the Institution of Mechanical Engineers, Part G: Journal of Aerospace Engineering*, 228(1):97–114, 2014.
- [47] Zhao-Ye Qin, Shao-Ze Yan, and Fu-Lei Chu. Dynamic characteristics of launch vehicle and spacecraft connected by clamp band. *Journal of Sound and Vibration*, 330(10):2161–2173, 2011.
- [48] Changguo Wang, Xingwen Du, Xiaodong He, and Guozhi Song. Vibration characteristics simulation of wrinkled circular annulus-shaped gossamer space structure. *International Journal of Computational Methods*, 5(01):189–198, 2008.
- [49] Jingtian Kang, Changguo Wang, Defeng Li, Ge He, and Huifeng Tan. Nanoscale crosslinking in thermoset polymers: a molecular dynamics study. *Physical Chemistry Chemical Physics*, 17(25):16519–16524, 2015.
- [50] Yat-Sze Choy, Kin-Tak Lau, C Wang, CW Chau, Yang Liu, and D Hui.

Composite panels for reducing noise in air conditioning and ventilation systems. *Composites Part B: Engineering*, 40(4):259–266, 2009.

- [51] Yiren S Wang and Malcolm J Crocker. Direct measurement of transmission loss of aircraft structures using the acoustic intensity approach. 1982.
- [52] JS Sastry and ML Munjal. Response of a multi-layered infinite cylinder to two-dimensional pressure excitation by means of transfer matrices. *Journal of sound and vibration*, 209(1):123–142, 1998.
- [53] Jun Li and Hongxing Hua. Transient vibrations of laminated composite cylindrical shells exposed to underwater shock waves. *Engineering Structures*, 31(3):738–748, 2009.
- [54] Ola Flodén, Juan Negreira, Kent Persson, and Göran Sandberg. The effect of modelling acoustic media in cavities of lightweight buildings on the transmission of structural vibrations. *Engineering Structures*, 83:7–16, 2015.
- [55] Z Tao and AF Seybert. A review of current techniques for measuring muffler transmission loss. Technical report, SAE Technical Paper, 2003.
- [56] TW Wu and GC Wan. Muffler performance studies using a direct mixed-body boundary element method and a three-point method for evaluating transmission loss. *Journal of Vibration and Acoustics*, 118(3):479–484, 1996.
- [57] PW Smith Jr. Sound transmission through thin cylindrical shells. *The Journal of the Acoustical Society of America*, 29(6):721–729, 1957.

- [58] M Lax and H Feshbach. Absorption and scattering for impedance boundary conditions on spheres and circular cylinders. *The Journal of the Acoustical Society of America*, 20(2):108–124, 1948.
- [59] Pritchard H White. Sound transmission through a finite, closed, cylindrical shell. *The Journal of the Acoustical Society of America*, 40(5):1124–1130, 1966.
- [60] Leslie Robert Koval. On sound transmission into an orthotropic shell. *Journal of Sound and Vibration*, 63(1):51–59, 1979.
- [61] Leslie Robert Koval. Sound transmission into a laminated composite cylindrical shell. *Journal of Sound and Vibration*, 71(4):523–530, 1980.
- [62] S Narayanan and RL Shanbhag. Sound transmission through layered cylindrical shells with applied damping treatment. *Journal of Sound and Vibration*, 92(4):541–558, 1984.
- [63] A Blaise, C Lesueur, M Gotteland, and M Barbe. On sound transmission into an orthotropic infinite shell: Comparison with koval’s results and understanding of phenomena. *Journal of Sound and Vibration*, 150(2):233–243, 1991.
- [64] A Blaise and C Lesueur. Acoustic transmission through a " 3-d" orthotropic multi-layered infinite cylindrical shell, part ii: validation and numerical exploitation for large structures. *Journal of Sound and Vibration*, 171(5):665–680, 1994.
- [65] Yvette Tang, Jay Robinson, and Richard Silcox. Sound transmission through a cylindrical sandwich shell with honeycomb core. In *34th Aerospace Sciences Meeting and Exhibit*, page 877, 1996.

- [66] Joon-Hyun Lee and J Kim. Study on sound transmission characteristics of a cylindrical shell using analytical and experimental models. *Applied acoustics*, 64(6):611–632, 2003.
- [67] Sebastian Ghinet, Nouredine Atalla, and Haisam Osman. Diffuse field transmission into infinite sandwich composite and laminate composite cylinders. *Journal of sound and vibration*, 289(4-5):745–778, 2006.
- [68] H Hosseini-Toudeshky, MR Mofakhami, and Sh Hosseini Hashemi. Sound transmission into a thick hollow cylinder with the fixed-end boundary condition. *Applied Mathematical Modelling*, 33(3):1656–1673, 2009.
- [69] Julien Magniez, Jean-Daniel Chazot, Mohamed Ali Hamdi, and Bernard Troclet. A mixed 3d-shell analytical model for the prediction of sound transmission through sandwich cylinders. *Journal of Sound and Vibration*, 333(19):4750–4770, 2014.
- [70] Hossein Bisheh and Nan Wu. On dispersion relations in smart laminated fiber-reinforced composite membranes considering different piezoelectric coupling effects. *Journal of Lows Frequency Noise, Vibration and Active Control*, 38:487–509, 2019.
- [71] Hossein Bisheh, Nan Wu, and David Hui. Polarization effects on wave propagation characteristics of piezoelectric coupled laminated fiber-reinforced composite cylindrical shells. *International Journal of Mechanical Sciences*, 161:105–028, 2019.
- [72] K Daneshjou, A Nouri, and R Talebitooti. Analytical model of sound trans-

- mission through orthotropic cylindrical shells with subsonic external flow. *Aerospace Science and Technology*, 13(1):18–26, 2009.
- [73] D Chronopoulos, M Ichchou, B Troclet, and O Bareille. Thermal effects on the sound transmission through aerospace composite structures. *Aerospace Science and Technology*, 30(1):192–199, 2013.
- [74] Zhaoye Qin, Fulei Chu, and Jean Zu. Free vibrations of cylindrical shells with arbitrary boundary conditions: A comparison study. *International Journal of Mechanical Sciences*, 133:91–99, 2017.
- [75] Zhaoye Qin, Zhengbao Yang, Jean Zu, and Fulei Chu. Free vibration analysis of rotating cylindrical shells coupled with moderately thick annular plates. *International Journal of Mechanical Sciences*, 142:127–139, 2018.
- [76] Zhaoye Qin, Xuejia Pang, Babak Safaei, and Fulei Chu. Free vibration analysis of rotating functionally graded cnt reinforced composite cylindrical shells with arbitrary boundary conditions. *Composite Structures*, 220:847–860, 2019.
- [77] Zhaoye Qin, Babak Safaei, Xuejia Pang, and Fulei Chu. Traveling wave analysis of rotating functionally graded graphene platelet reinforced nanocomposite cylindrical shells with general boundary conditions. *Results in Physics*, 15: 102752, 2019.
- [78] Tao Fu, Zhaobo Chen, Hongying Yu, Xuezhi Zhu, and Yanzheng Zhao. Sound transmission loss behavior of sandwich panel with different truss cores under external mean airflow. *Aerospace Science and Technology*, 86:714–723, 2019.

- [79] Tao Fu, Zhaobo Chen, Hongying Yu, Zhonglong Wang, and Xiaoxiang Liu. An analytical study of sound transmission through stiffened double laminated composite sandwich plates. *Aerospace Science and Technology*, 82:92–104, 2018.
- [80] Stanislaw J Pietrzko and Qibo Mao. New results in active and passive control of sound transmission through double wall structures. *Aerospace science and technology*, 12(1):42–53, 2008.
- [81] R Talebitooti and MR Zarastvand. The effect of nature of porous material on diffuse field acoustic transmission of the sandwich aerospace composite doubly curved shell. *Aerospace Science and Technology*, 78:157–170, 2018.
- [82] R Talebitooti, HD Gohari, and MR Zarastvand. Multi objective optimization of sound transmission across laminated composite cylindrical shell lined with porous core investigating non-dominated sorting genetic algorithm. *Aerospace Science and Technology*, 69:269–280, 2017.
- [83] MP Arunkumar, Jeyaraj Pitchaimani, KV Gangadharan, and MC Leninbabu. Vibro-acoustic response and sound transmission loss characteristics of truss core sandwich panel filled with foam. *Aerospace Science and Technology*, 78: 1–11, 2018.
- [84] Joon-H Lee, J Kim, and Han-J Kim. Simplified method to solve sound transmission through structures lined with elastic porous material. *The Journal of the Acoustical Society of America*, 110(5):2282-2294, 2001.
- [85] Julien Magniez, Mohamed Ali Hamdi, Jean-Daniel Chazot, and Bernard

- Troclet. A mixed “biot–shell” analytical model for the prediction of sound transmission through a sandwich cylinder with a poroelastic core. *Journal of Sound and Vibration*, 360:203–223, 2016.
- [86] Olga Umnova, Keith Attenborough, and Chris M Linton. Effects of porous covering on sound attenuation by periodic arrays of cylinders. *The Journal of the Acoustical Society of America*, 119(1):278–284, 2006.
- [87] H Ramezani and A Saghafi. Optimization of a composite double-walled cylindrical shell lined with porous materials for higher sound transmission loss by using a genetic algorithm. *Mechanics of Composite Materials*, 50(1):71–82, 2014.
- [88] K Daneshjou, R Talebitooti, and M Kornokar. Vibroacoustic study on a multilayered functionally graded cylindrical shell with poroelastic core and bonded-unbonded configuration. *Journal of Sound and Vibration*, 393:157–175, 2017.
- [89] R Talebitooti, AM Choudari Khameneh, MR Zarastvand, and M Kornokar. Investigation of three-dimensional theory on sound transmission through compressed poroelastic sandwich cylindrical shell in various boundary configurations. *Journal of Sandwich Structures & Materials*, 21(7):2113–2357, 2018.
- [90] Mehdi Ahmadian and Kristina M Jeric. On the application of shunted piezoceramics for increasing acoustic transmission loss in structures. *Journal of Sound and Vibration*, 243(2):347–359, 2001.
- [91] P Gardonio, NS Ferguson, and FJ Fahy. A modal expansion analysis of noise



- transmission through circular cylindrical shell structures with blocking masses. *Journal of Sound and Vibration*, 244(2):259–297, 2001.
- [92] Yu Liu and Chuanbo He. On sound transmission through double-walled cylindrical shells lined with poroelastic material: comparison with zhou s results and further effect of external mean flow. *Journal of Sound and Vibration*, 358:192–198, 2015.
- [93] Liu Yu and He Chuanbo. Analytical modelling of acoustic transmission across double-wall sandwich shells: Effect of an air gap flow. *Composite Structures*, 136:149–161, 2016.
- [94] Pouria Oliazadeh, Anooshiravan Farshidianfar, and Malcolm J Crocker. Experimental and analytical investigation on sound transmission loss of cylindrical shells with absorbing material. *Journal of Sound and Vibration*, 434:28–43, 2018.
- [95] Seyyed M Hasheminejad and Mahdi Alaei-Varnosfaderani. Acoustic radiation and active control from a smart functionally graded submerged hollow cylinder. *Journal of Vibration and Control*, 20(14):2202–2220, 2014.
- [96] Ugur Aridogan and Ipek Basdogan. A review of active vibration and noise suppression of plate-like structures with piezoelectric transducers. *Journal of Intelligent Material Systems and Structures*, 26(12):1455–1476, 2015.
- [97] Ali Loghmani, Mohammad Danesh, Moon K Kwak, and Mehdi Keshmiri. Active control of radiated sound power of a smart cylindrical shell based on radiation modes. *Applied Acoustics*, 114:218–229, 2016.

- [98] G Song, V Sethi, and H-N Li. Vibration control of civil structures using piezoceramic smart materials: A review. *Engineering Structures*, 28(11): 1513–1524, 2006.
- [99] JD Jones and Chris R Fuller. Active control of sound fields in elastic cylinders by multicontrol forces. *American Institute of Aeronautics and Astronautics journal*, 27(7):845–852, 1989.
- [100] Chris R Fuller, SD Snyder, CH Hansen, and RJ Silcox. Active control of interior noise in model aircraft fuselages using piezoceramic actuators. *American Institute of Aeronautics and Astronautics journal*, 30(11):2613–2617, 1992.
- [101] JQ Sun, MA Norris, DJ Rossetti, and JH Highfill. Distributed piezoelectric actuators for shell interior noise control. *Journal of Vibration and Acoustics*, 118(4):676–681, 1996.
- [102] C-Y Wang and R Vaicaitis. Active control of vibrations and noise of double wall cylindrical shells. *Journal of Sound and Vibration*, 216(5):865–888, 1998.
- [103] OR Lin, Z-X Liu, and Z-L Wang. Cylindrical panel interior noise control using a pair of piezoelectric actuator and sensor. *Journal of Sound and Vibration*, 246(3):525–541, 2001.
- [104] James Karl Henry and RL Clark. Active control of sound transmission through a curved panel into a cylindrical enclosure. *Journal of Sound and Vibration*, 249(2):325–349, 2002.
- [105] DS Li, L Cheng, and CM Gosselin. Optimal design of pzt actuators in active

- structural acoustic control of a cylindrical shell with a floor partition. *Journal of Sound and Vibration*, 269(3-5):569–588, 2004.
- [106] G Bernardini, C Testa, and M Gennaretti. Optimal design of tonal noise control inside smart-stiffened cylindrical shells. *Journal of Vibration and Control*, 18(8):1233–1246, 2012.
- [107] Shaul Katzir. *The beginnings of piezoelectricity: a study in mundane physics*, volume 246. Springer Science & Business Media, 2007.
- [108] Jacques Curie and Pierre Curie. Développement par compression de l’électricité polaire dans les cristaux hémiedres à faces inclinées. *Bulletin de minéralogie*, 3(4):90–93, 1880.
- [109] Inc Encyclopaedia Britannica et al. *Encyclopaedia britannica*. Encyclopaedia Britannica, Incorporated, 1957.
- [110] Gabriel Lippmann. Principe de la conservation de l’électricité, ou second principe de la théorie des phénomènes électriques. *Journal de Physique Théorique et Appliquée*, 10(1):381–394, 1881.
- [111] Jacques Curie and Pierre Curie. Contractions et dilatations produites par des tensions électriques dans les cristaux hémiedres à faces inclinées. *Compt. Rend*, 93:1137–1140, 1881.
- [112] Richard F Mould. Pierre curie, 1859–1906. *Current oncology*, 14(2):74, 2007.
- [113] Farzad Ebrahimi. *Piezoelectric Materials and Devices: Practice and Applications*. BoD–Books on Demand, 2013.

- [114] Woldemar Voigt et al. *Lehrbuch der kristallphysik*, volume 962. Teubner Leipzig, 1928.
- [115] Shaul Katzir. Who knew piezoelectricity? rutherford and langevin on submarine detection and the invention of sonar. *Notes and Records of the Royal Society*, 66(2):141–157, 2012.
- [116] LE Cross and RE Newnham. History of ferroelectrics. *Ceramics and Civilization*, 3:289–305, 1987.
- [117] GA Smolenskiy. Ferroelectrics and antiferroelectrics. Technical report, ARMY FOREIGN SCIENCE AND TECHNOLOGY CENTER CHARLOTTESVILLE VA, 1972.
- [118] Malcolm E Lines and Alastair M Glass. *Principles and applications of ferroelectrics and related materials*. Oxford university press, 2001.
- [119] Takao Someya. *Stretchable electronics*. John Wiley & Sons, 2012.
- [120] National Research Council et al. *Expanding the vision of sensor materials*. National Academies Press, 1995.
- [121] T Tatsumi. Piezoelectric cigarette lighter, June 18 1974. US Patent 3,817,691.
- [122] Claudia L Bianchi, Carlo Pirola, Marta Stucchi, Giuseppina Cerrato, Federico Galli, Alessandro Di Michele, Serena Biella, Wen-Fan Chen, Pramod Koshy, Charles Sorrell, et al. Photocatalytic tio<sub>2</sub>: from airless jet spray technology to digital inkjet printing. *Yang D (ed, pages 261–279, 2018.*

- [123] Kimberly Ann Cook-Chennault, Nithya Thamby, Mary Anne Bitetto, and EB Hameyie. Piezoelectric energy harvesting: a green and clean alternative for sustained power production. *Bulletin of Science, Technology & Society*, 28 (6):496–509, 2008.
- [124] Robert C Scherer. Electric guitar piezoelectric transducer bridge with replaceable string height adjusters, September 22 1970. US Patent 3,530,228.
- [125] HM Shodja and M Ghazisaeidi. Effects of couple stresses on anti-plane problems of piezoelectric media with inhomogeneities. *European Journal of Mechanics-A/Solids*, 26(4):647–658, 2007.
- [126] Antonio Arnau et al. *Piezoelectric transducers and applications*, volume 2004. Springer, 2004.
- [127] Nader Jalili. *Piezoelectric-Based Vibration-Control Systems: Applications to Micro/Nano Sensors and Actuators*. Springer, 2009.
- [128] Seung-Eek Park and Thomas R Shrout. Characteristics of relaxor-based piezoelectric single crystals for ultrasonic transducers. *IEEE Transactions on Ultrasonics, Ferroelectrics, and Frequency Control*, 44(5):1140–1147, 1997.
- [129] Lewis F Brown. Design considerations for piezoelectric polymer ultrasound transducers. *IEEE transactions on ultrasonics, ferroelectrics, and frequency control*, 47(6):1377–1396, 2000.
- [130] EH Anderson and NW Hagood. Simultaneous piezoelectric sensing/actuation: analysis and application to controlled structures. *Journal of Sound and Vibration*, 174(5):617–639, 1994.

- [131] AS DeReggi, SC Roth, JM Kenney, S Edelman, and GR Harris. Piezoelectric polymer probe for ultrasonic applications. *The Journal of the Acoustical Society of America*, 69(3):853–859, 1981.
- [132] Victor Giurgiutiu and Adrian Cuc. Embedded non-destructive evaluation for structural health monitoring, damage detection, and failure prevention. *Shock and Vibration Digest*, 37(2):83, 2005.
- [133] Josef Krautkrämer and Herbert Krautkrämer. *Ultrasonic testing of materials*. Springer Science & Business Media, 2013.
- [134] Joseph L Rose. *Ultrasonic waves in solid media*, 2000.
- [135] Robert Bickerstaff, Mark Vaughn, Gerald Stoker, Michael Hassard, and Mark Garrett. Review of sensor technologies for in-line inspection of natural gas pipelines. *Sandia National Laboratories, Albuquerque, NM*, 2002.
- [136] Kamal Raj Chapagain, Werner Bjerke, Sanat Wagle, Terje Melands, and Frank Melands. Multilayer piezoelectric pvdF transducers for nondestructive testing of concrete structures. In *Ultrasonics Symposium (IUS), 2017 IEEE International*, pages 1–4. IEEE, 2017.
- [137] D Boucher. Trends and problems in low frequency sonar projectors design. In *Power Sonic and Ultrasonic Transducers Design*, pages 100–120. Springer, 1988.
- [138] Makoto Kobayashi and CK Jen. Piezoelectric thick bismuth titanate/lead zirconate titanate composite film transducers for smart nde of metals. *Smart Materials and Structures*, 13(4):951, 2004.

- [139] Fapeng Yu, Shuai Hou, Shujun Zhang, Qingming Lu, and Xian Zhao. Electro-elastic properties of  $\text{YCa}_4\text{O}(\text{BO}_3)_3$  piezoelectric crystals. *physica status solidi (a)*, 211(3):574–579, 2014.
- [140] Fapeng Yu, Shujun Zhang, Xian Zhao, Duorong Yuan, Lifeng Qin, Qing-Ming Wang, and Thomas R Shrout. Dielectric and electromechanical properties of rare earth calcium oxyborate piezoelectric crystals at high temperatures. *IEEE transactions on ultrasonics, ferroelectrics, and frequency control*, 58(4), 2011.
- [141] Shujun Zhang, Yiting Fei, Bruce HT Chai, Eric Frantz, David W Snyder, Xiaoning Jiang, and Thomas R Shrout. Characterization of piezoelectric single crystal  $\text{YCa}_4\text{O}(\text{BO}_3)_3$  for high temperature applications. *Applied Physics Letters*, 92(20):202905, 2008.
- [142] Shujun Zhang, Yiting Fei, Eric Frantz, David W Snyder, Bruce HT Chai, and Thomas R Shrout. High-temperature piezoelectric single crystal  $\text{YCa}_4\text{O}(\text{BO}_3)_3$  for sensor applications. *IEEE transactions on ultrasonics, ferroelectrics, and frequency control*, 55(12), 2008.
- [143] Fapeng Yu, Shujun Zhang, Xian Zhao, Duorong Yuan, Qingming Wang, and Thomas R Shrout. High temperature piezoelectric properties of yttrium calcium oxyborate single crystals. *physica status solidi (RRL)-Rapid Research Letters*, 4(5-6):103–105, 2010.
- [144] Jeremy A Brown, Kevin Dunphy, Jeff R Leadbetter, Robert BA Adamson, and Olivier Beslin. Fabrication and performance of a single-crystal lead magnesium

- niobate-lead titanate cylindrical hydrophone. *The Journal of the Acoustical Society of America*, 134(2):1031–1038, 2013.
- [145] Krzysztof J Opieliński, Piotr Pruchnicki, Tadeusz Gudra, Przemysław Podgórski, Tomasz Kraśnicki, Jacek Kurcz, and Marek Sąsiadek. Ultrasound transmission tomography imaging of structure of breast elastography phantom compared to us, ct and mri. *Archives of Acoustics*, 38(3):321–334, 2013.
- [146] Krzysztof J Opielinski, Mateusz Celmer, Piotr Pruchnicki, Włodzimierz Roguski, Tadeusz Gudra, Jarosław Majewski, Mariusz Bulkowski, Tomasz Piotrowski, and Andrzej Wiktorowicz. The effect of crosstalk in a circular transducer array on ultrasound transmission tomography of breast. In *Proceedings of Meetings on Acoustics 167ASA*, volume 21, page 075001. ASA, 2014.
- [147] Yi Yang, He Tian, Bing Yan, Hui Sun, Can Wu, Yi Shu, Li-Gang Wang, and Tian-Ling Ren. A flexible piezoelectric micromachined ultrasound transducer. *RSC Advances*, 3(47):24900–24905, 2013.
- [148] Lori Vidal Denham and David A Rice. Ultrasonic resonant modes of piezoelectric balloons under internal pressure. *The Journal of the Acoustical Society of America*, 132(3):1368–1377, 2012.
- [149] HS Tzou and M Gadre. Theoretical analysis of a multi-layered thin shell coupled with piezoelectric shell actuators for distributed vibration controls. *Journal of Sound and Vibration*, 132(3):433–450, 1989.
- [150] Bryan Riley, Mark Bodie, Jack Hoying, Kamal Majeed, and Sanjiv Tewani.



- Active vibration and noise cancellation control of four cylinder engines-an application. Technical report, SAE Technical Paper, 1995.
- [151] Ya A Zhuk and IA Guz. Active damping of the forced vibration of a hinged beam with piezoelectric layers, geometrical and physical nonlinearities taken into account. *International Applied Mechanics*, 45(1):94–108, 2009.
- [152] Guozhong Zhao, Biaosong Chen, and Yuanxian Gu. Control–structural design optimization for vibration of piezoelectric intelligent truss structures. *Structural and Multidisciplinary Optimization*, 37(5):509, 2009.
- [153] IF Kirichok. Control of axisymmetric resonant vibrations and self-heating of shells of revolution with piezoelectric sensors and actuators. *International Applied Mechanics*, 46(8):890–901, 2011.
- [154] VI Kozlov and TV Karnaukhova. Basic equations for viscoelastic laminated shells with distributed piezoelectric inclusions intended to control nonstationary vibrations. *International applied mechanics*, 38(10):1253–1260, 2002.
- [155] Seyyed M Hasheminejad, M Vahedi, and AHD Markazi. Multi-objective robust active vibration control of an arbitrary thick piezolaminated beam. *Mechanics of Advanced Materials and Structures*, 22(11):908–924, 2015.
- [156] Vladimir Ya Shur et al. Kinetics of ferroelectric domains: Application of general approach to linbo3 and litao3. *Journal of Materials Science*, 41(1):199–210, 2006.
- [157] Zhengbao Yang, Zhaoye Qin, and Jean Zu. Charging capacitors using single

- crystal pmn-pt and pzn-pt energy harvesters coupled with the sshi circuit. *Sensors and Actuators A: Physical*, 266:76–84, 2017.
- [158] SP Thompson and J Loughlan. The active buckling control of some composite column strips using piezoceramic actuators. *Composite Structures*, 32(1-4): 59–67, 1995.
- [159] Seyyed M Hasheminejad, Vahid Rabbani, and Mahdi Alaei-Varnosfaderani. Active transient elasto-acoustic response damping of a thick-walled liquid-coupled piezolaminated cylindrical vessel. *Mechanics Based Design of Structures and Machines*, 44(3):189–211, 2016.
- [160] WQ Chen, ZG Bian, CF Lv, and HJ Ding. 3d free vibration analysis of a functionally graded piezoelectric hollow cylinder filled with compressible fluid. *International Journal of Solids and Structures*, 41(3):947–964, 2004.
- [161] Seyyed M Hasheminejad and M Rajabi. Acoustic resonance scattering from a submerged functionally graded cylindrical shell. *Journal of sound and vibration*, 302(1):208–228, 2007.
- [162] Horn-Sen Tzou. *Piezoelectric shells: distributed sensing and control of continua*, volume 19. Springer Science & Business Media, 2012.
- [163] HJ Ding, HM Wang, and PF Hou. The transient responses of piezoelectric hollow cylinders for axisymmetric plane strain problems. *International Journal of Solids and Structures*, 40(1):105–123, 2003.
- [164] A Champa Jayasuriya, Snehasish Ghosh, Jerry I Scheinbeim, Virginia Lubkin, Greg Bennett, and Phillip Kramer. A study of piezoelectric and mechanical

- anisotropies of the human cornea. *Biosensors and Bioelectronics*, 18(4):381–387, 2003.
- [165] JF Haskins and JL Walsh. Vibrations of ferroelectric cylindrical shells with transverse isotropy. i. radially polarized case. *The Journal of the Acoustical Society of America*, 29(6):729–734, 1957.
- [166] Douglas S Drumheller and Arturs Kalnins. Dynamic shell theory for ferroelectric ceramics. *The Journal of the Acoustical Society of America*, 47(5B):1343–1353, 1970.
- [167] AE Babaev, LM But, and VG Savin. Transient vibrations of a thin-walled cylindrical piezoelectric vibrator driven by a nonaxisymmetric electrical signal in a liquid. *International Applied Mechanics*, 26(12):1167–1174, 1990.
- [168] AE Babaev and VG Savin. Nonsteady hydroelasticity of a system of coaxial piezoceramic cylindrical shells during electrical excitation. *Soviet Applied Mechanics*, 24(11):1069–1075, 1988.
- [169] HS Tzou and JP Zhong. A linear theory of piezoelastic shell vibrations. *Journal of Sound and Vibration*, 175(1):77–88, 1994.
- [170] GG Sheng and X Wang. Thermoelastic vibration and buckling analysis of functionally graded piezoelectric cylindrical shells. *Applied mathematical modelling*, 34(9):2630–2643, 2010.
- [171] Santosh Kapuria, S Sengupta, and PC Dumir. Three-dimensional solution for simply-supported piezoelectric cylindrical shell for axisymmetric load.

- Computer Methods in Applied Mechanics and Engineering*, 140(1-2):139–155, 1997.
- [172] Chang-Qing Chen and Ya-Peng Shen. Three-dimensional analysis for the free vibration of finite-length orthotropic piezoelectric circular cylindrical shells. *Transactions-American Society of Mechanical Engineers Journal of Vibration and Acoustics*, 120:194–198, 1998.
- [173] DA Shlyakhin. Nonstationary axisymmetric electroelasticity problem for an anisotropic piezoceramic radially polarized cylinder. *Mechanics of solids*, 44(1):62–69, 2009.
- [174] Ji Wang, Peng Hu, Bin Huang, Sergei Zhgoon, Ju-lian Shen, Min-chiang Chao, Ting-feng Ma, and Jian-ke Du. Free vibrations of finite quartz crystal cylinders with the rayleigh-ritz method. In *Piezoelectricity, Acoustic Waves, and Device Applications (SPAWDA), 2016 Symposium on*, pages 335–338. IEEE, 2016.
- [175] Ronit Kar-Gupta and TA Venkatesh. Electromechanical response of 1-3 piezoelectric composites: Effect of poling characteristics. *Journal of Applied Physics*, 98(5):054102, 2005.
- [176] Pengdi Han and Welling Yan. Electro-optical single crystal element, method for the preparation thereof, and systems employing the same, March 8 2016. US Patent 9,280,006.
- [177] J Luo, SJ Fan, HQ Xie, KC Xiao, SX Qian, ZW Zhong, GX Qiang, RY Sun, and JY Xu. Thermal and nonlinear optical properties of  $\text{Ca}_4\text{Y}_2(\text{BO}_3)_3$ . *Crystal Research and Technology*, 36(11):1215–1221, 2001.

- [178] J Papež, J Liesen, and Z Strakoš. Distribution of the discretization and algebraic error in numerical solution of partial differential equations. *Linear Algebra and its Applications*, 449:89–114, 2014.
- [179] Jerome M Klosner and Howard S Levine. Further comparison of elasticity and shell theory solutions. *AIAA Journal*, 4(3):467–480, 1966.
- [180] Paul Mansour Naghdi. The theory of shells and plates. In *Linear Theories of Elasticity and Thermoelasticity*, pages 425–640. Springer, 1973.
- [181] Chai H Yoo and Sung Lee. *Stability of structures: principles and applications*. Elsevier, 2011.
- [182] Marco Amabili. *Nonlinear vibrations and stability of shells and plates*. Cambridge University Press, 2008.
- [183] K Chandrashekhara and KS Nanjunda Rao. Approximate elasticity solution for a long and thick laminated circular cylindrical shell of revolution. *International journal of solids and structures*, 34(11):1327–1341, 1997.
- [184] Junuthula Narasimha Reddy. *An introduction to continuum mechanics*. Cambridge university press, 2013.
- [185] Naum D Veksler. *Resonance acoustic spectroscopy*, volume 11. Springer Science & Business Media, 2012.
- [186] H Deresiewicz. Mechanics of granular matter. In *Advances in applied mechanics*, volume 5, pages 233–306. Elsevier, 1958.

- [187] Junuthula Narasimha Reddy. *An introduction to continuum mechanics*. Cambridge university press, 2007.
- [188] Thomas Chi-tsai Ting and Thomas Chi-tsai Ting. *Anisotropic elasticity: theory and applications*. Number 45. Oxford University Press on Demand, 1996.
- [189] WQ Chen, LZ Wang, and Y Lu. Free vibrations of functionally graded piezoceramic hollow spheres with radial polarization. *Journal of Sound and Vibration*, 251(1):103–114, 2002.
- [190] Martin H Sadd. *Elasticity: theory, applications, and numerics*. Academic Press, 2009.
- [191] L Govindaraju and TG Sitharam. Applied elasticity for engineers-web course.
- [192] Sjoerd W Rienstra and Avraham Hirschberg. An introduction to acoustics. *Eindhoven University of Technology*, 18:19, 2003.
- [193] Victor A Miroshnikov. *Harmonic Wave Systems: Partial Differential Equations of the Helmholtz Decomposition*. Scientific Research Publishing, Inc. USA, 2017.
- [194] SM Hasheminejad and N Safari. Acoustic scattering from viscoelastically coated spheres and cylinders in viscous fluids. *Journal of Sound and Vibration*, 280(1-2):101–125, 2005.
- [195] Mohamad Hasheminejad and Thomas L Geers. Modal impedances for two spheres in a thermoviscous fluid. *The Journal of the Acoustical Society of America*, 94(4):2205–2214, 1993.

- [196] Inderjit Chopra and Jayant Sirohi. *Smart structures theory*, volume 35. Cambridge University Press, 2013.
- [197] Haojiang Ding and Weiqiu Chen. *Three dimensional problems of piezoelectricity*. Nova Science Publishers, 2001.
- [198] Weiqiu Chen and Haojiang Ding. Natural frequencies of fluid-filled transversely isotropic cylindrical shells. *International journal of mechanical sciences*, 41(6): 677–684, 1999.
- [199] E Akcakaya and GW Farnell. Effective elastic and piezoelectric constants of superlattices. *Journal of applied physics*, 64(9):4469–4473, 1988.
- [200] Elmar J Breitbach and Lucio Flavio Campanile. *13th International Conference on Adaptive Structures and Technologies, 2002*. CRC Press, 2003.
- [201] H Huang. An exact analysis of the transient interaction of acoustic plane waves with a cylindrical elastic shell. *Journal of Applied mechanics*, 37(4): 1091–1099, 1970.
- [202] Chongxin Yuan, Otto Bergsma, and Adriaan Beukers. Sound transmission loss prediction of the composite fuselage with different methods. *Applied Composite Materials*, 19(6):865–883, 2012.
- [203] Allan D Pierce and P Smith. Acoustics: An introduction to its physical principles and applications. *Physics Today*, 34(12):56–57, 1981.
- [204] Yu Jiangong, Wu Bin, and Chen Guoqiang. Wave characteristics in functionally

- graded piezoelectric hollow cylinders. *Archive of Applied Mechanics*, 79(9): 807–824, 2009.
- [205] Fengxiang Xu, Xiong Zhang, and Hui Zhang. A review on functionally graded structures and materials for energy absorption. *Engineering Structures*, 171: 309–325, 2018.
- [206] Zhichao Xu and Qibai Huang. Vibro-acoustic analysis of functionally graded graphene-reinforced nanocomposite laminated plates under thermal-mechanical loads. *Engineering Structures*, 186:345–355, 2019.
- [207] Wang Zikung and Zheng Bailin. The general solution of three-dimensional problems in piezoelectric media. *International Journal of Solids and Structures*, 32(1):105–115, 1995.
- [208] Gaurav Sharma and Jos Martin. Matlab®: a language for parallel computing. *International Journal of Parallel Programming*, 37(1):3–36, 2009.
- [209] COMSOL Multiphysics. User’s guide. *Version*, 4:290–298, 2007.
- [210] Lawrence F Shampine. Vectorized adaptive quadrature in matlab. *Journal of Computational and Applied Mathematics*, 211(2):131–140, 2008.
- [211] Anders C Nilsson. Wave propagation in and sound transmission through sandwich plates. *Journal of Sound and Vibration*, 138(1):73–94, 1990.
- [212] Thomas H Lee. *The design of CMOS radio-frequency integrated circuits*. Cambridge University Press, 2003.



- [213] David Thompson. *Railway noise and vibration: mechanisms, modelling and means of control*. Elsevier, 2008. ISBN 9780080451473.
- [214] Philip McCord Morse and K Uno Ingard. *Theoretical acoustics*. Princeton university press, 1986.
- [215] Milton Abramowitz and Irene A Stegun. *Handbook of mathematical functions with formulas, graphs, and mathematical tables*, volume 55. US Government printing office, 1948.
- [216] VV Varadan, Akhlesh Lakhtakia, and Vijay K Varadan. *Field representations and introduction to scattering*, volume 1. North-Holland, 1991.
- [217] Wilfried Brutsaert. The propagation of elastic waves in unconsolidated unsaturated granular mediums. *Journal of Geophysical Research*, 69(2):243–257, 1964.
- [218] Roland Kjellander. *Thermodynamics Kept Simple-A Molecular Approach: What is the Driving Force in the World of Molecules?* CRC Press, 2015.
- [219] Zuyu Zhao and Chao Wang. *Cryogenic Engineering and Technologies: Principles and Applications of Cryogen-free Systems*. CRC Press, 2019.
- [220] KA Mulholland, HD Parbrook, and A Cummings. The transmission loss of double panels. *Journal of Sound and Vibration*, 6(3):324–334, 1967.